

# **MARICE-E-Report MER-13-2012**

## **Modelling the hydrography of Icelandic waters from 1992 to 2006**

Kai Logemann, Jón Olafsson and Guðrún Marteinsdóttir  
Háskóli Islands

In order to simulate the hydrography of Icelandic waters the workgroup MARICE at the University of Iceland has developed the numerical ocean model CODE. With this report we give a detailed description of the recent model version CODE 9.221 and present its output: the hydrography of Icelandic waters during the time period 1992 to 2006. The model was forced by the 6 hourly NCEP/NCAR re-analysis atmospheric fields. Daily river discharge data of 58 Icelandic rivers, estimated by the hydrological model WaSiM operated by the Icelandic Meteorological Office, were included as well as all available CTD profiles recorded from 1992 to 2006 in Icelandic waters. The CTD data was assimilated into the simulation. I.e. with an iterative procedure correction terms were determined which minimised the deviation between simulated and observed temperature and salinity profiles.

The presentation of the model output is confined to charts of monthly mean flow, temperature and salinity at the depth of 50 m and to overall model error estimations. For a more profound analysis of the data set the reader is referred to the following publications of the authors.

## Contents

<b>1. Model description.....</b>	<b>3</b>
1.1. Equations.....	3
1.1.1. Ocean.....	3
1.1.1.1. Equation of motion and continuity.....	3
1.1.1.2. Turbulence closure.....	4
1.1.1.3. Tides.....	5
1.1.1.4. Wind stress and bottom friction.....	5
1.1.1.5. Equation of state.....	5
1.1.1.6. Heat and salt conservation.....	6
1.1.1.7. Surface heat and freshwater fluxes.....	6
1.1.1.7.1. Absorption of solar (short wave) radiation.....	6
1.1.1.7.2. Long wave radiation balance.....	7
1.1.1.7.3. Thermal conduction and diffusive heat flux at the ice/ocean interface..	8
1.1.1.7.4. Sensible and latent heat flux.....	8
1.1.1.7.5. Fresh water flux.....	9
1.1.2. Sea ice.....	10
1.1.2.1. Thermodynamics.....	10
1.1.2.2. Mechanics.....	11
1.2. Numerics.....	14
1.2.1. Temporal discretisation.....	14
1.2.1.1. Equation of continuity and equation of motion.....	14
1.2.1.2. Advection scheme.....	16
1.2.2. Spatial discretisation.....	19
1.3. Model layout.....	21
1.3.1. Model domain and adaptive mesh refinement.....	21
1.3.2. Forcing data.....	27
1.3.3. CTD data assimilation.....	29
1.3.4. Output data.....	35
 <b>2. Results.....</b>	 <b>36</b>
 <b>3. Validation.....</b>	 <b>217</b>
 <b>4. References.....</b>	 <b>220</b>



# 1. Model description

CODE (*Cartesian coordinates Ocean model with three-Dimensional adaptive mesh adaption an primitive Equations*) is a three-dimensional, primitive equations,  $z$ -level, coupled sea-ice/ocean model. The basic idea behind CODE is the simulation of basin-scale ocean dynamics (length scale in the order of 10000 km) including the small-scale structures, with length scales less than 10 km, of selected areas of interest. Additionally the computational costs of the simulation should be minimised to enable the computation of multi-decadal runs within an acceptable length of time. Both points could be realised using the technique of adaptive mesh refinement. Though this involves more complicated numerical methods the disadvantages of conventional nesting (higher computational effort, missing coupling between several model runs, numerical errors at open boundaries) or finite element (higher computational effort) approaches could be avoided. The simulation presented here – entire North Atlantic/Arctic Ocean with highly resolved (1 km) Icelandic waters – was computed on an Intel Xeon 3.33 GHz CPU and needed 92 hours for the simulation of one year.

## 1.1. Equations

Basically the physical state of the ocean can be described with seven variables. Using a three-dimensional Cartesian coordinate system, where the  $x$ - and  $y$ -axis span a horizontal plane (of constant geopotential) and where the  $z$ -axis points vertically upwards (parallel to the gravitation vector) these variables are: the three-dimensional velocity vector  $(u, v, w)$ , the temperature  $T$ , the salinity  $S$ , the sea surface elevation  $\zeta$  and the density  $\rho$ . The sea ice is described by four basic variables: the two-dimensional drift vector  $(u_i, v_i)$ , the ice thickness  $h_i$  and the ice coverage  $A_i$ .

### 1.1.1. Ocean

#### 1.1.1.1. Equation of motion and continuity

Using the hydrostatic and the Reynolds stress approximation the horizontal acceleration is (e.g. Pedlosky, 1987)

$$\frac{\partial u}{\partial t} = -u \frac{\partial u}{\partial x} - v \frac{\partial u}{\partial y} - w \frac{\partial u}{\partial z} + f v + \frac{\partial}{\partial x} \left( A_H \frac{\partial u}{\partial x} \right) + \frac{\partial}{\partial y} \left( A_H \frac{\partial u}{\partial y} \right) + \frac{\partial}{\partial z} \left( A_V \frac{\partial u}{\partial z} \right) - g \frac{\partial \zeta}{\partial x} - g \frac{1}{\rho_0} \int_{z=z}^{z=\zeta} \frac{\partial \rho}{\partial x} dz' - \frac{1}{\rho_0} \frac{\partial p_{AIR}}{\partial x} - \frac{\partial \Phi_T}{\partial x} \quad (1)$$

and

$$\frac{\partial v}{\partial t} = -u \frac{\partial v}{\partial x} - v \frac{\partial v}{\partial y} - w \frac{\partial v}{\partial z} - f u + \frac{\partial}{\partial x} \left( A_H \frac{\partial v}{\partial x} \right) + \frac{\partial}{\partial y} \left( A_H \frac{\partial v}{\partial y} \right) + \frac{\partial}{\partial z} \left( A_V \frac{\partial v}{\partial z} \right) - g \frac{\partial \zeta}{\partial y} - g \frac{1}{\rho_0} \int_{z=z}^{z=\zeta} \frac{\partial \rho}{\partial y} dz' - \frac{1}{\rho_0} \frac{\partial p_{AIR}}{\partial y} - \frac{\partial \Phi_T}{\partial y}, \quad (2)$$

where  $f$  denotes the Coriolis parameter,  $A_H$ ,  $A_V$  turbulent exchange coefficients,  $g$  the gravitational acceleration,  $\rho_0$  the ocean background density,  $p_{AIR}$  the sea-level air pressure and  $\Phi_T$  the tidal potential. The vertical velocity component  $w$  results from the equation of continuity:

$$w = - \int_{z'=-D}^{z'=z} \left( \frac{\partial u}{\partial x} + \frac{\partial v}{\partial y} \right) dz' \quad (3)$$

where  $D$  denotes the ocean depth. The vertical velocity at the sea surface ( $z = \zeta$ ) defines the temporal change of the sea surface elevation  $\zeta$

$$\frac{\partial \zeta}{\partial t} = w(z = \zeta) \quad (4)$$

### 1.1.1.2. Turbulence closure

The coefficient of horizontal momentum exchange  $A_H$  is estimated using the approach of Smagorinsky (1963):

$$A_H = (c_1 \Delta x)^2 \sqrt{\left(\frac{\partial u}{\partial x}\right)^2 + \left(\frac{\partial v}{\partial y}\right)^2 + \left(\frac{\partial u}{\partial y} + \frac{\partial v}{\partial x}\right)^2 + \left(\frac{\partial u}{\partial y} - \frac{\partial v}{\partial x}\right)^2} \quad (5)$$

with the constant  $c_1 = 0.4$  and the horizontal model resolution  $\Delta x$ .

The coefficient of the vertical momentum exchange  $A_V$  is estimated using the approach of Kochergin (1987) and Pohlmann (1996). Outside of the surface and bottom mixed layer a laminar flow is assumed with only molecular vertical viscosity. The mixed layer thickness  $h_{ML}$  is determined using the criterion  $Ri < 0.22$  (Mellor & Yamada 1974) with  $Ri$  being the Richardson number.

$$Ri = \frac{-\frac{g}{\rho} \frac{\partial \rho}{\partial z}}{\left(\frac{\partial u}{\partial z}\right)^2 + \left(\frac{\partial v}{\partial z}\right)^2} \quad (6)$$

Within the mixed layers the turbulent vertical viscosity is computed with

$$A_V = (c_2 h_{ML})^2 \sqrt{\max(0, \left(\frac{\partial u}{\partial z}\right)^2 + \left(\frac{\partial v}{\partial z}\right)^2 + \frac{1}{S_M} \frac{g}{\rho_0} \frac{\partial \rho}{\partial z})} \quad (7)$$

with  $c_2 = 0.05$  and the Schmidt number  $S_M$  which is estimated after Mellor and Durbin (1975) with

$$S_M = \frac{Ri}{0.725 \left( Ri + 0.186 - \sqrt{Ri^2 - 0.316 Ri + 0.0346} \right)}. \quad (8)$$

### 1.1.1.3. Tides

The current version uses a simple first order approach to the tidal potential. Assuming constant co-declinations of  $90^\circ$  for moon and sun, it follows (e.g. Apel, 1987)

$$\Phi_T = -0.8718 \cdot 3 \cdot \sin(90^\circ - \varphi)^2 \cos(2 \omega_l (t - t_{0l}) + 2 \lambda) - 0.4023 \cdot 3 \cdot \sin(90^\circ - \varphi)^2 \cos(2 \omega_s (t - t_{0s}) + 2 \lambda) \quad (9)$$

where  $\varphi$  denotes the latitude,  $\lambda$  the longitude,  $t$  the time,  $t_{0l}$  and  $t_{0s}$  the time of the moon's and sun's zenith at Greenwich and  $\omega_l, \omega_s$  the radian frequencies of moon and sun.

### 1.1.1.4. Wind stress and bottom friction

At the sea surface the vertical momentum transfer is

$$A_v \frac{\partial u}{\partial z}(z = 0) = \lambda w_x \sqrt{w_x^2 + w_y^2} \quad (10)$$

and

$$A_v \frac{\partial v}{\partial z}(z = 0) = \lambda w_y \sqrt{w_x^2 + w_y^2} \quad (11)$$

with the constant  $\lambda = 1.7 \times 10^{-6}$  whereas  $w_x, w_y$  are  $x$ - and  $y$ -components of the wind speed in 10 m height.

The bottom friction is

$$A_v \frac{\partial u}{\partial z}(z = -D) = -r_B u \sqrt{u^2 + v^2} \quad (12)$$

$$A_v \frac{\partial v}{\partial z}(z = -D) = -r_B v \sqrt{u^2 + v^2} \quad (13)$$

with the constant  $r_B = 0.003$ .

### 1.1.1.5. Equation of state

The density of seawater  $\rho$  is computed using the EOS-80 equations (Millero et al., 1980):

$$\rho = \rho(S, T, p) \approx \rho(S, T, -\rho_0 g z) \quad (14)$$

### 1.1.1.6. Heat and salt conservation

Temperature and salinity changes are computed with (e.g. Pedlosky 1987)

$$\frac{\partial T}{\partial t} = -u \frac{\partial T}{\partial x} - v \frac{\partial T}{\partial y} - w \left( \frac{\partial T}{\partial z} + \Gamma \right) + \frac{\partial}{\partial x} \left( K_{H,T} \frac{\partial T}{\partial x} \right) + \frac{\partial}{\partial y} \left( K_{H,T} \frac{\partial T}{\partial y} \right) + \frac{\partial}{\partial z} \left( K_{V,T} \left( \frac{\partial T}{\partial z} + \Gamma \right) \right) + Q_T \quad (15)$$

$$\frac{\partial S}{\partial t} = -u \frac{\partial S}{\partial x} - v \frac{\partial S}{\partial y} - w \frac{\partial S}{\partial z} + \frac{\partial}{\partial x} \left( K_{H,S} \frac{\partial S}{\partial x} \right) + \frac{\partial}{\partial y} \left( K_{H,S} \frac{\partial S}{\partial y} \right) + \frac{\partial}{\partial z} \left( K_{V,S} \frac{\partial S}{\partial z} \right) + Q_S \quad (16)$$

where  $\Gamma = \Gamma(T, S, p)$  is the adiabatic lapse rate, computed with the equation of Fofonoff and Millard (1983), whereas  $Q_T$  and  $Q_S$  denote the sum of surface heat and freshwater fluxes respectively. These fluxes are computed with bulk formulas (Gill, 1982) applied to the atmospheric and astronomic forcing data (solar altitude, cloudiness, air temperature, humidity, wind speed). The turbulent diffusivity coefficients  $K_{H,T}$ ,  $K_{H,S}$ ,  $K_{V,T}$  and  $K_{V,S}$  are estimated with

$$K_{H,T} = K_{H,S} = \frac{A_H}{Pr} \quad (17)$$

$$K_{V,T} = K_{V,S} = \frac{A_V}{S_M} \quad (18)$$

with an assumed Prandtl number of  $Pr = 10$  and the Schmidt number  $S_M$  given by equation (8).

### 1.1.1.7. Surface heat and freshwater fluxes

The surface heat flux is

$$Q_T = Q_{SW} + Q_{LW} + Q_{SENS} + Q_{LAT} \quad (19)$$

i.e. the sum of the short wave, long wave, sensible and latent heat flux.

The surface freshwater flux is

$$Q_S = Q_{EVA} + Q_{PRE} + Q_{RO} + Q_{ICE} \quad (20)$$

i.e. the sum of freshwater fluxes caused by evaporation, precipitation, run-off and ice formation/melting.

#### 1.1.1.7.1. Absorption of solar (short wave) radiation

The amount of solar radiation  $Q_{SW}$  absorbed by the ocean is computed with

$$Q_{SW} = (1 - A_i) \bar{Q}_{SW} \quad 4 \sin\left(\frac{t - t_0}{12 \text{ h}} \pi - \frac{\pi}{2}\right)^2 \text{ if } |t - t_0| < 6 \text{ h, else } Q_{SW} = 0. \quad (21)$$

where  $A_i$ , between 0 and 1, is the ice coverage,  $\bar{Q}_{SW}$  the absorbed solar radiation averaged over 24 hours,  $t$  the time in hours,  $t_0$  the time of the apex of the sun's motion. After Laevastu (1963) and Pickard & Emery (1982)  $\bar{Q}_{SW}$  is the difference between the arriving short wave radiation  $Q'_{SW}$  and its part which is reflected at the sea surface  $Q_R$ .

$$\bar{Q}_{SW} = Q'_{SW} - Q_R \quad (22)$$

It is

$$Q'_{SW} = 0.28 A_n t_D \frac{W}{m^2} (1 - 0.0012 C^3) \quad (23)$$

where  $A_n$  is the noon altitude of the sun in degrees,  $t_D$  denotes the length of day (sunrise to sunset) in hours and  $C$  the cloud cover in oktas. The reflected amount of radiation is computed with:

$$Q_R = 0.15 Q'_{SW} - (0.01 Q'_{SW})^2 \quad (24)$$

Inside the ocean an attenuation coefficient of 0.17 is assumed. I.e. the ocean layer from 0. to 2.5 m depth absorbs 35% of the incoming short wave radiation, the layer from 2.5 to 5 m 25%, 5 – 10 m 20%, and 10 – 20 m 20%. If the ocean is ice covered the amount of reflected radiation is increased:

$$Q_R = 0.8 Q'_{SW} - (0.01 Q'_{SW})^2 \quad (25)$$

whereas the remaining amount is absorbed by the sea ice.

#### 1.1.1.7.2. Long wave radiation balance

In order to compute the long wave radiation flux  $Q_{LW}$  the Stefan-Boltzmann law (e.g. Gill, 1982) is applied:

$$Q_{LW} = \sigma (\epsilon_2 T_{AIR}^4 - \epsilon_1 T_{SRF}^4) \quad (26)$$

with the Stefan-Boltzmann constant  $\sigma = 5.670 \times 10^{-8} \text{ W m}^{-2} \text{ K}^{-4}$ ,  $T_{AIR}$  = air temperature close to the surface (in K),  $T_{SRF}$  = sea surface temperature or the upper surface temperature of the sea ice (in K),  $\epsilon_1 = 0.97$  the emissivity of the ocean (or sea ice), and after Maykut (1986)

$$\epsilon_2 = 0.7855 (1 + 0.2232 C^{2.75}) \quad (27)$$

the emissivity of the atmosphere, which depends on the cloud cover  $C$  (between 0 and 1). The upper surface temperature  $T_{ice,up}$  of the sea ice depends on the air temperature. It is assumed to be  $-0.27^\circ \text{C}$  - the freezing point of sea water with a salinity of 5 psu, computed with the function of Millero (1978) - if the air temperature is above this freezing point. Otherwise the sea ice is assumed to be in a thermodynamic equilibrium, i.e. the sum of the

short wave, long wave, sensible and conductive heat flux is set to zero. The temperature value which fulfils this condition is determined iteratively.

#### 1.1.1.7.3. Thermal conduction and diffusive heat flux at the ice/ocean interface

The conductive heat flux through the ice is

$$Q_{CON} = \frac{\kappa}{h_{eff}} (T_{ICE,UP} - T_{ICE,DOWN}) \quad (28)$$

with  $\kappa = 2.1 \text{ W m}^{-1} \text{ K}^{-1}$  being the coefficient of thermal conduction,  $h_{eff} = h_i/A_i$  the effective ice thickness ( $h_i$  = mean ice thickness,  $A_i$  = ice coverage). The temperature at the lower side of the ice,  $T_{ICE,DOWN}$  is assumed to be equal to the freezing point of the adjacent sea water. This temperature is also used to compute the diffusive heat flux at the ice/ocean interface. It is

$$Q_{DIF} = \rho_0 c_w K_V \frac{T_{ICE,DOWN} - T_{OCE}}{0.5 \Delta z} \quad (29)$$

with  $c_w$  being the heat capacity of sea water,  $T_{OCE}$  the ocean's temperature at the depth of  $0.5 \Delta z$  and  $K_V = 10^{-3} \text{ m}^2 \text{ s}^{-1}$  the estimated diffusivity below the ice cover.

#### 1.1.1.7.4. Sensible and latent heat flux

After Gill (1982) the sensible heat flux is computed with

$$Q_{SENS} = \rho_{AIR} c_A \beta_{SENS} \sqrt{w_x^2 + w_y^2} (T_{AIR} - T_{SRF}) \quad (30)$$

with the air density  $\rho_{AIR} = 1.28 \text{ kg m}^{-3}$ , the specific heat of dry air  $c_A = 1004 \text{ J kg}^{-1} \text{ K}^{-1}$ , the Stanton-number  $\beta_{SENS} = 0.9 \times 10^{-3}$ , the wind speed components in  $x$ - and  $y$ -direction  $w_x$ ,  $w_y$ , the air temperature (in 2 m height)  $T_{AIR}$  and the sea (or ice) surface temperature  $T_{SRF}$ . The flux of latent heat is

$$Q_{LAT} = \rho_{AIR} L_{VAP} \beta_{LAT} \sqrt{w_x^2 + w_y^2} (s_a - s) \quad (31)$$

over ice-free areas and

$$Q_{LAT} = \rho_{AIR} L_{SUB} \beta_{LAT} \sqrt{w_x^2 + w_y^2} (s_a - s) \quad (32)$$

over ice covered areas.

With  $L_{VAP} = 2.5 \text{ MJ kg}^{-1}$  being the sea water enthalpy of evaporation,  $L_{SUB} = 2.8 \text{ MJ kg}^{-1}$  the sea ice enthalpy of sublimation and  $\beta_{LAT} = 1.5 \times 10^{-1}$  the Dalton number.  $s_a$  denotes the specific humidity in 2 m height and  $s$  the specific humidity close to the sea surface. These values are computed with

$$S = \frac{\gamma E(T_{SRF})}{p_{AIR} - (1-\gamma) E(T_{SRF})} \quad (33)$$

and

$$S_a = \frac{\gamma f E(T_{AIR})}{p_{AIR} - (1-\gamma) f E(T_{AIR})} \quad (34)$$

with  $\gamma = R_L / R_w = 0.622$  being the ratio of the gas constants of air and water vapour,  $f$  the relative humidity in 2 m height and  $E$  the equilibrium vapour pressure. Using the formula of H.G. Magnus, it is (e.g. Möller, 1973)

$$E(T) = 6.107 \times 10^{\frac{7.5T}{237+T}} \text{ hPa} \quad (35)$$

with  $T$  being the air temperature in degree Celsius.

#### 1.1.1.7.5. Fresh water flux

The flux of latent heat  $Q_{LAT}$  also gives us the salinity increase caused by evaporation within a surface layer of the thickness  $\Delta z$ :

$$\frac{\partial S}{\partial t} = (1 - A_i) S \frac{Q_{LAT}}{L_{VAP} \rho_0 \Delta z} \quad (36)$$

where  $A_i$  again denotes the ice coverage between 0 and 1. Analogously the salinity decrease caused by precipitation  $P$  (mass flux per unit area) is computed:

$$\frac{\partial S}{\partial t} = (1 - A_i) S \frac{-P}{\rho_0 \Delta z} \quad (37)$$

whereas over the ice covered areas precipitation (snowfall) is causing an increase of the ice thickness  $h_i$

$$\frac{\partial h_i}{\partial t} = A_i \frac{P}{\rho_{ICE}} \quad (38)$$

Freshwater runoff  $RO$  (volume flux) into a cell of horizontal spacing  $\Delta x$  causes the salinity decrease

$$\frac{\partial S}{\partial t} = S \frac{-RO}{\Delta x^2 \Delta z} \quad (39)$$

and a local increase of the sea surface elevation

$$\frac{\partial \zeta}{\partial t} = \frac{RO}{\Delta x^2} \quad (40)$$

Ice formation or melting, i.e. the thermodynamically caused change of the ice thickness  $h_i$ , -  $\left(\frac{\partial h_i}{\partial t}\right)_{th}$  causes the following salinity change

$$\frac{\partial S}{\partial t} = A_i \frac{(S - S_i) \left(\frac{\partial h_i}{\partial t}\right)_{th} \frac{\rho_i}{\rho_0}}{\Delta z} \quad (41)$$

with the sea ice salinity  $S_i = 5$  psu and the sea ice density  $\rho_i = 930 \text{ kg m}^{-3}$ .

### 1.1.2. Sea ice

#### 1.1.2.1. Thermodynamics

After Hibler (1979) the thermodynamically caused change of the sea ice thickness is subdivided into two terms: The thermodynamically caused change of the existing ice cover  $f_h$  and the new ice formation within ice-free areas  $f_0$ . Hence, it is

$$\left(\frac{\partial h_i}{\partial t}\right)_{th} = A_i f_h + (1 - A_i) f_0 \quad (42)$$

with

$$f_0 = \begin{cases} -\frac{\partial T_{SRF}}{\partial t} \frac{\Delta z \rho_0 c_w}{L_{melt} \rho_i}, & \text{if } (T_{SRF} < T_{fr}) \text{ and } \left(\frac{\partial T_{SRF}}{\partial t} < 0\right) \\ 0, & \text{else} \end{cases} \quad (43)$$

and

$$f_h = \left(\frac{\partial h_i}{\partial t}\right)_{\uparrow} + \left(\frac{\partial h_i}{\partial t}\right)_{\downarrow} \quad (44)$$

where  $L_{melt} = 250 \text{ KJ kg}^{-1}$  denotes the sea ice enthalpy of fusion and  $T_{fr}(S)$  the freezing point of sea water.

$\left(\frac{\partial h_i}{\partial t}\right)_{\uparrow}$  denotes the melting and sublimation at the upper side of the ice. It is



$$\left(\frac{\partial h_i}{\partial t}\right)_\uparrow = \begin{cases} -\frac{Q_{LAT}}{L_{sub}}, & \text{if } T_{AIR} < T_{fr}(S_i) \\ -\frac{(Q_{SW} + Q_{LW} + Q_{SENS} + Q_{CON})}{L_{melt}} - \frac{Q_{LAT}}{L_{sub}}, & \text{else} \end{cases} \quad (45)$$

Melting or freezing at the bottom side of the ice depends on the sum of the diffusive and the conductive heat flux

$$\left(\frac{\partial h_i}{\partial t}\right)_\downarrow = \frac{-Q_{DIF} - Q_{CON}}{L_{melt} \rho_i} \quad (46)$$

The thermodynamically caused change of the ice coverage is

$$\begin{aligned} \left(\frac{\partial A_i}{\partial t}\right)_{th} = & \begin{cases} f_0 \left(\frac{1-A_i}{h_0}\right), & \text{if } f_0 > 0 \\ 0, & \text{else} \end{cases} \\ & + \begin{cases} 0, & \text{if } f_h > 0 \\ f_h \frac{A_i}{2 h_i}, & \text{else} \end{cases} \end{aligned} \quad (47)$$

with the empirical constant  $h_0 = 0.5$  m, interpreted as the “thickness of thin ice” by Hibler (1979).

### 1.1.2.2. Mechanics

The two-dimensional ice drift vector  $(u_i, v_i)$  is computed with the following equations of motion:

$$\frac{\partial u_i}{\partial t} = f v_i + \tau_{a,x} + \tau_{w,x} - g \frac{\partial \zeta}{\partial x} + F_x \quad (48)$$

$$\frac{\partial v_i}{\partial t} = -f u_i + \tau_{a,y} + \tau_{w,y} - g \frac{\partial \zeta}{\partial y} + F_y \quad (49)$$

where  $f$  is again the Coriolis parameter,  $\tau_{a,x}, \tau_{a,y}$  are wind stress terms at the upper side of the ice,  $\tau_{w,x}, \tau_{w,y}$  are shear stress terms at the ice/ocean interface, and  $F_x, F_y$  are internal stress terms resulting from Hibler’s viscous-plastic rheology. Finally, gradients of the sea surface elevation  $\zeta$  are forcing the ice drift.

The wind stress terms are:

$$\tau_{a,x} = \frac{\lambda_{A,I}}{h_{eff}} w_x \sqrt{w_x^2 + w_y^2} \quad (50)$$

$$\tau_{a,y} = \frac{\lambda_{A,I}}{h_{eff}} w_y \sqrt{w_x^2 + w_y^2} \quad (51)$$

with the friction parameter  $\lambda_{A,I} = 1.7 \times 10^{-6}$ , and the effective ice thickness  $h_{eff} = h_i/A_i$ . The shear stress terms at the bottom side depend on the relative velocity between ice ( $u_i, v_i$ ) and ocean ( $u_{srf}, v_{srf}$ ):

$$\tau_{w,x} = -\frac{\lambda_{I,O}}{h_{eff}} (u_i - u_{srf}) |u_i - u_{srf}| \quad (52)$$

$$\tau_{w,y} = -\frac{\lambda_{I,O}}{h_{eff}} (v_i - v_{srf}) |v_i - v_{srf}| \quad (53)$$

with  $\lambda_{I,O} = 5.5 \times 10^{-3}$ . Weighted with the ice coverage  $A_i$  these terms, multiplied with  $-h_{eff}$ , replace the oceanic wind stress terms of equation (8) and (9).

After Hibler (1979) the internal stress terms, which exist only in the case of convergent drift, are:

$$F_x = \begin{cases} \eta \left[ \left(1 + \frac{1}{e^2}\right) \frac{\partial^2 u_i}{\partial x^2} + \frac{\partial^2 v_i}{\partial x \partial y} + \frac{1}{e^2} \frac{\partial^2 u_i}{\partial y^2} \right] - \frac{1}{\rho_i h_{eff}} \frac{\partial}{\partial x} \left( \frac{P}{2} \right) & \text{if } \frac{\partial u_i}{\partial x} + \frac{\partial v_i}{\partial y} < 0 \\ 0, & \text{else} \end{cases} \quad (54)$$

$$F_y = \begin{cases} \eta \left[ \left(1 + \frac{1}{e^2}\right) \frac{\partial^2 v_i}{\partial y^2} + \frac{\partial^2 u_i}{\partial x \partial y} + \frac{1}{e^2} \frac{\partial^2 v_i}{\partial x^2} \right] - \frac{1}{\rho_i h_{eff}} \frac{\partial}{\partial y} \left( \frac{P}{2} \right) & \text{if } \frac{\partial u_i}{\partial x} + \frac{\partial v_i}{\partial y} < 0 \\ 0, & \text{else} \end{cases} \quad (55)$$

with  $e = 2$ ,

$$P = P^* h_i \exp(-C (1 - A_i)) \quad (56)$$

$P^* = 5$  kPa and  $C = 20.0$ .

After Semtner (1987) the viscosity  $\eta$  is estimated with

$$\eta = \frac{P^*}{2 \rho_i \left| \frac{\partial u_i}{\partial x} + \frac{\partial v_i}{\partial y} \right|} \quad (57)$$

The ice drift causes dynamically caused changes of the mean ice thickness and the ice coverage. The following equations describe the conservation of the ice volume:

$$\left( \frac{\partial h_i}{\partial t} \right)_{dyn} = -\frac{\partial}{\partial x} (u_i h_i) - \frac{\partial}{\partial y} (v_i h_i) + K_i \left( \frac{\partial^2 h_i}{\partial x^2} + \frac{\partial^2 h_i}{\partial y^2} \right) \quad (58)$$

$$\left(\frac{\partial A_i}{\partial t}\right)_{dyn} = -\frac{\partial}{\partial x}(u_i A_i) - \frac{\partial}{\partial y}(v_i A_i) + K_i \left( \frac{\partial^2 A_i}{\partial x^2} + \frac{\partial^2 A_i}{\partial y^2} \right) \quad (59)$$

with the mesh size dependent diffusion coefficient  $K_i = 2 \times 10^{-6} \text{ s}^{-1} \Delta x^2$  which ensures numerical stability.

## 1.2. Numerics

The model equations are numerically solved by using the technique of *finite differences*, i.e. the ocean is divided into cubes of finite size, and for each of these boxes the spatial average of the variables mentioned above is computed. This spatial discretisation is performed by using an adaptively refined, staggered Arakawa-C-grid (Mesinger and Arakawa, 1976). The equations' numerical equivalents are formulated centred in space and mostly implicitly in time. In order to avoid numerical diffusion of the advection terms a flux limiter function (van Leer, 1979) is used, which ensures the abidance of the total variation diminishing (TVD) condition.

### 1.2.1. Temporal discretisation

#### 1.2.1.1. Equation of continuity, equation of motion, heat and salt conservation

Some of the model equations are solved with explicit schemes, i.e. the ocean state at time step  $n+1$  is assumed to be a function of the state at time step  $n$ :

$$X^{n+1} = f(X^n). \quad (60)$$

Oceanic surface waves whose length is great compared to the water depth (shallow water waves) travel with the speed

$$c = \sqrt{g D}. \quad (61)$$

Therefore, an explicit scheme for the computation of the sea surface elevation has to fulfil the condition

$$\frac{\Delta x}{\Delta t} > \sqrt{g D}, \quad (62)$$

i.e. the wave must not pass more than one grid cell of horizontal spacing  $\Delta x$  within the time step  $\Delta t$ . Taking a grid spacing of 1 km and a water depth of 3000 m this condition requires a time step smaller than 6 s. In order to avoid such a small time step, which would drastically increase the computational costs, an implicit scheme for the computation of the sea surface elevation is chosen. Here it is assumed:

$$X^{n+1} = f(X^n, X^{n+1}). \quad (63)$$

Inserting equation (3) into equation (4) yields:

$$\frac{\partial \zeta}{\partial t} = - \int_{z=-D}^{z=\zeta} \left( \frac{\partial u}{\partial x} + \frac{\partial v}{\partial y} \right) dz \quad (64)$$

Introducing the temporal discretisation and the implicit scheme this becomes:

$$\frac{\zeta^{n+1} - \zeta^n}{\Delta t} = -(1 - c^*) \int_{z=-D}^{z=\zeta} \left( \frac{\partial u}{\partial x} + \frac{\partial v}{\partial y} \right)^n - c^* \int_{z=-D}^{z=\zeta} \left( \frac{\partial u}{\partial x} + \frac{\partial v}{\partial y} \right)^{n+1} \quad (65)$$

with

$$u^{n+1} = u^{n+2/3} - (1 - c^*) \Delta t g \frac{\partial \zeta^n}{\partial x} - c^* \Delta t g \frac{\partial \zeta^{n+1}}{\partial x} \quad (66)$$

and

$$v^{n+1} = v^{n+2/3} - (1 - c^*) \Delta t g \frac{\partial \zeta^n}{\partial y} - c^* \Delta t g \frac{\partial \zeta^{n+1}}{\partial y}, \quad (67)$$

where  $c^*$  denotes a weight between the time steps  $n$  and  $n+1$ . Setting  $c^*=0$  leads to the unstable explicit form,  $c^*=1$  leads to the stable fully implicit version, which is however overestimating the damping of surface waves. CODE 9.221 uses:

$$c^* = \min \left( 1, 0.6 + 0.4 \sqrt{0.03 \frac{\Delta t}{\Delta x} \sqrt{g D}} \right) \quad (68)$$

i.e. values between 0.6 and 1 depending on the relation between the shallow water wave speed and the quotient  $\Delta x / \Delta t$ .

The sea surface elevation at the new time step  $\zeta^{n+1}$  is obtained by inserting equation (66) and (67) into equation (65) and by solving the resulting system of equations iteratively.

$u^{n+2/3}$  and  $v^{n+2/3}$  are computed with two further steps. The first step, from  $u^n$  to  $u^{n+1/3}$ ,  $v^n$  to  $v^{n+1/3}$ , contains the implicit momentum advection (using a second order, central, flux-corrected scheme, see chapter 1.2.1.2.) and momentum diffusion:

$$u^{n+1/3} = u^n + \Delta t \left[ - \left( u^n \frac{\partial u^{n+1/3}}{\partial x} + v^n \frac{\partial u^{n+1/3}}{\partial y} + w^n \frac{\partial u^{n+1/3}}{\partial z} \right) + \frac{\partial}{\partial x} \left( A_H^n \frac{\partial u^{n+1/3}}{\partial x} \right) + \frac{\partial}{\partial y} \left( A_H^n \frac{\partial u^{n+1/3}}{\partial y} \right) + \frac{\partial}{\partial z} \left( A_V^n \frac{\partial u^{n+1/3}}{\partial z} \right) \right] \quad (69)$$

$$v^{n+1/3} = v^n + \Delta t \left[ - \left( u^n \frac{\partial v^{n+1/3}}{\partial x} + v^n \frac{\partial v^{n+1/3}}{\partial y} + w^n \frac{\partial v^{n+1/3}}{\partial z} \right) + \frac{\partial}{\partial x} \left( A_H^n \frac{\partial v^{n+1/3}}{\partial x} \right) + \frac{\partial}{\partial y} \left( A_H^n \frac{\partial v^{n+1/3}}{\partial y} \right) + \frac{\partial}{\partial z} \left( A_V^n \frac{\partial v^{n+1/3}}{\partial z} \right) \right]. \quad (70)$$

The second step contains the explicit computation of the forces caused by the gradients of the density, air pressure and tidal potential field and an implicit Coriolis rotation:

$$u^{n+2/3} = \alpha u^{n+2/3} + \beta v^{n+2/3} - \Delta t \left[ g \frac{1}{\rho_0} \int_{z'=z}^{z'=\zeta} \frac{\partial \rho}{\partial x} + \frac{1}{\rho_0} \frac{\partial p_{AIR}}{\partial x} + \frac{\partial \Phi_T}{\partial x} \right]^n \quad (71)$$

$$v^{n+2/3} = \alpha v^{n+2/3} - \beta u^{n+2/3} - \Delta t \left[ g \frac{1}{\rho_0} \int_{z'=z}^{z'=\zeta} \frac{\partial \rho}{\partial y} + \frac{1}{\rho_0} \frac{\partial p_{AIR}}{\partial y} + \frac{\partial \Phi_T}{\partial y} \right]^n \quad (72)$$

whereas

$$\alpha = \cos(f \Delta t), \quad (73)$$

$$\beta = \sin(f \Delta t), \quad (74)$$

with  $f$  being the Coriolis parameter. Hence, the Coriolis acceleration is simulated with a energy conserving rotation of the horizontal velocity vector (Backhaus 1985):

$$\begin{pmatrix} u' \\ v' \end{pmatrix} = \begin{pmatrix} \alpha & \beta \\ -\beta & \alpha \end{pmatrix} \begin{pmatrix} u \\ v \end{pmatrix}. \quad (75)$$

The terms of advection and diffusion within the equations of heat and salt conservation, eq. 15 and 16, are also treated with an implicit scheme:

$$T^{n+1} = T^n + \Delta t \left( -u^n \frac{\partial T^{n+1}}{\partial x} - v^n \frac{\partial T^{n+1}}{\partial y} - w^n \left( \frac{\partial T^{n+1}}{\partial z} + \Gamma^n \right) + \frac{\partial}{\partial x} \left( K_H^n \frac{\partial T^{n+1}}{\partial x} \right) + \frac{\partial}{\partial y} \left( K_H^n \frac{\partial T^{n+1}}{\partial y} \right) + \frac{\partial}{\partial z} \left( K_V^n \left( \frac{\partial T^{n+1}}{\partial z} + \Gamma^n \right) \right) + Q_r^n \right), \quad (76)$$

$$S^{n+1} = S^n + \Delta t \left( -u^n \frac{\partial S^{n+1}}{\partial x} - v^n \frac{\partial S^{n+1}}{\partial y} - w^n \frac{\partial S^{n+1}}{\partial z} + \frac{\partial}{\partial x} \left( K_H^n \frac{\partial S^{n+1}}{\partial x} \right) + \frac{\partial}{\partial y} \left( K_H^n \frac{\partial S^{n+1}}{\partial y} \right) + \frac{\partial}{\partial z} \left( K_V^n \frac{\partial S^{n+1}}{\partial z} \right) + Q_s^n \right), \quad (77)$$

whereas the same central advection scheme as in eq. (69) and (70) is used which will be described in the following chapter.

### 1.2.1.2. Advection scheme

In order to avoid the strong numerical diffusion caused by the upstream scheme we chose an FTCS scheme (*forward in time, centred in space*) and transformed it finally into an implicit scheme. The property  $T$  of cell  $i$  within the current  $u$  (fig. 1.2.1.) is updated with:

$$T_i^{n+1} = T_i^n - \frac{u_{i-1}^n \Delta t}{2 \Delta x} (T_i^n - T_{i-1}^n) - \frac{u_i^n \Delta t}{2 \Delta x} (T_{i+1}^n - T_i^n). \quad (78)$$

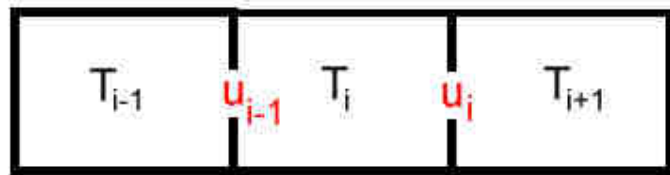


**Fig. 1.2.1.:** Three cells of the C-grid with the property  $T$  within the current  $u$  (directed from left to right or vice versa).

The scheme of equation (76) is unstable but becomes practicable when introducing van Leer's (1979) flux-limiter function which ensures the abidance of the *total variation diminishing* (TVD) condition. This way, the advection scheme will show minimal numerical diffusion and complete avoidance of so called *over-shoots*, i.e. unrealistic high or low values of the advected property caused by numerical dispersion (fig. 1.2.2.).

By considering also the cell's next but one neighbours it is:

$$\Theta_R = \frac{T_i^n - T_{i-1}^n}{T_{i+1}^n - T_i^n} k_1 + \frac{T_{i+2}^n - T_{i+1}^n}{T_{i+1}^n - T_i^n} k_2, \quad (79)$$

and

$$\Theta_L = \frac{T_{i-1}^n - T_{i-2}^n}{T_i^n - T_{i-1}^n} k_1 + \frac{T_{i+1}^n - T_i^n}{T_i^n - T_{i-1}^n} k_2, \quad (80)$$

whereas  $k_1$ , and  $k_2$  indicate the current's direction:

$$k_1 = \begin{cases} 1, & \text{if } (u_{i-1}^n + u_i^n) \geq 0 \\ 0, & \text{else} \end{cases}, \quad k_2 = 1 - k_1. \quad (81)$$

The flux through the right and left wall of cell  $i$  is controlled by the two flux-limiters

$$FL_R = \frac{\Theta_R + |\Theta_R|}{1 + |\Theta_R|}, \quad (82)$$

$$FL_L = \frac{\Theta_L + |\Theta_L|}{1 + |\Theta_L|}. \quad (83)$$

When inserted these into the FTCS-scheme (eq. 78), it follows:

$$\begin{aligned} T_i^{n+1} = & -\frac{\Delta t}{2\Delta x} u_{i-1}^n k_1 (T_{i+1}^n FL_R - T_i^n FL_L) \\ & -\frac{\Delta t}{2\Delta x} u_i^n k_2 (T_i^n FL_R - T_{i-1}^n FL_L) \\ & -\frac{\Delta t}{2\Delta x} u_{i-1}^n k_1 (T_i^n (2 - FL_R) - T_{i-1}^n (2 - FL_L)) \\ & -\frac{\Delta t}{2\Delta x} u_i^n k_2 (T_{i+1}^n (2 - FL_R) - T_i^n (2 - FL_L)). \end{aligned} \quad (84)$$

The flux-limiters mode of operation is to filter out only a minimum of the short wave part of the advected signal and to conserve its shape afterwards (fig 1.2.2.).

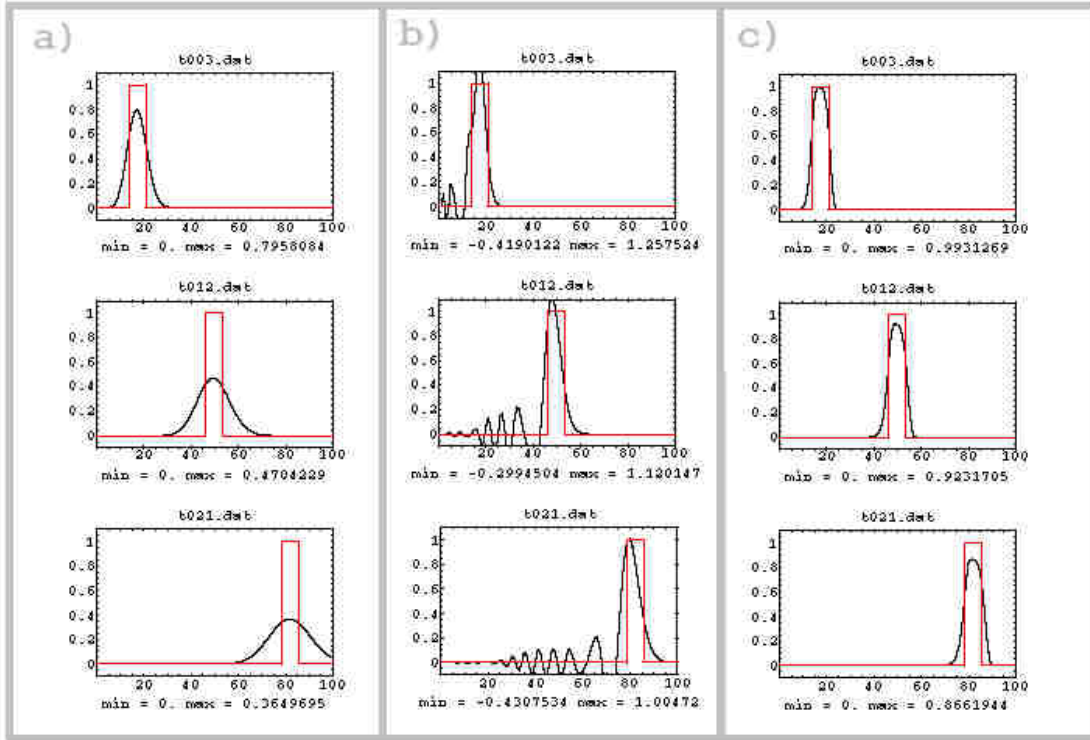


**Fig. 1.2.2.:** Advection of a rectangular signal (width of 7 km) with  $u = 1 \text{ m s}^{-1}$ ,  $\Delta x = 1 \text{ km}$ ,  $\Delta t = 60 \text{ s}$ . The signal after 3, 12, and 21 hours is shown. The red curve shows the analytical solution, the black curves show the numerical solutions – **a)** diffusive upstream scheme, **b)** dispersive Lax-Wendroff-scheme, **c)** FTCS-scheme with van Leer flux-limiter.

The van Leer flux-limiter works well with an implicit scheme as long as the Courant number  $|\Delta t u / \Delta x|$  is less than 0.3. If this condition is not fulfilled the advection scheme is locally changed to an implicit upstream scheme.



### 1.2.2. Spatial discretisation

CODE uses the technique of adaptive mesh refinement. I.e. the size of the cubes, resolving the ocean, can be varied within the same computational mesh. This way the model's spatial resolution can be adapted to the spatial structure of the simulated process. For spatial discretisation and organisation of grid cells the “tree”-algorithm of Khokhlov (1998) is used (fig. 1.2.3.). By defining two connected “Khokhlov trees”, one for the horizontal, the other for the vertical mesh structure, the grid cells formed herein are allocated to pairs of natural numbers ( $n, m$ ) which define the degree of horizontal ( $n$ ) and vertical ( $m$ ) mesh refinement. Hence, a cell has the horizontal size

$$\Delta x = \Delta x_0 \times 2^{-n} \quad (85)$$

and the vertical

$$\Delta z = \Delta z_0 \times 2^{-m}, \quad (86)$$

with  $\Delta x_0$ ,  $\Delta z_0$  being the uniform horizontal and vertical size of the basic cells of adaption level (0,0). At the first step the model domain is resolved with these basic cells. The next steps consist of horizontal, column-wise adaptive mesh refinement. Afterwards the mesh is adaptively refined vertically. This way distinct columns are formed which are necessary for a clear computation of the hydrostatic pressure. The model equations are only solved on the “leaves”, i.e. cells of the final level of adaption. However, the remaining cells are not removed from the computer memory but receive the mean properties of their “children” at each time step.

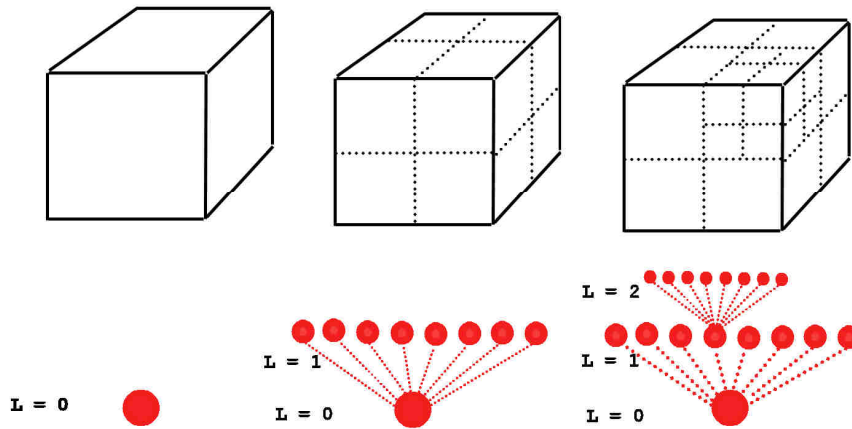


**Fig. 1.2.3:** Schematic process of adaptive grid refinement, following the algorithm of Khokhlov (1998). The large cube on the left side (adaption level 0) is split into 8 “children” of adaption level 1. Hence the model equations are no longer solved on the “parent cell”. However, the “parent cell” is not removed from the computer’s memory. It is obtaining the average properties of its children at each time step instead.

The maximal difference of the adaption level between two adjacent cells is 1. Each cell obtains an index  $i$ . Adjacent cells of the same adaption level or, if not existing, of the next lower level are located with the variable  $nb(i,k)$ , whereas the index  $k = 1,2,\dots,6$  defines the direction (west, east, south, north, down, up). This way, the following difference approximations are formed:

$$\frac{\partial T}{\partial x}(x = x_0 + \frac{1}{2} \Delta x) \approx \frac{T(nb(i,2)) - T(i)}{\Delta x}, \quad (87)$$

$$\frac{\partial^2 T}{\partial x^2}(x = x_0) \approx \frac{T(nb(i,2)) - 2 T(i) + T(nb(i,1))}{\Delta x^2} \quad (88)$$

or

$$\frac{\partial T}{\partial x}(x = x_0 + \frac{3}{2} \Delta x) \approx \frac{T(nb(nb(i,2),2)) - T(nb(i,2))}{\Delta x} . \quad (89)$$

### 1.3. Model layout

A model layout was chosen which shows highly resolved Icelandic waters embedded in the North Atlantic system. This way, also remote large scale structures like the Subtropical Gyre or the Beaufort Sea Ice Gyre and their linkage to the climate of Icelandic waters are included. The model domain is assumed to be closed along the equator and within Bering Strait. A model drift towards unrealistic temperatures or salinities in the low resolved far-field is avoided by a 365 days Newtonian relaxation towards climatologic values.

#### 1.3.1. Model domain and adaptive mesh refinement

With a blending technique between five different stereographic projections, having their projection points on the 40°W meridian between the North Pole and the Equator, the North Atlantic topography (GEBCO 2003 topography (BODC 2003)) is transformed into a Cartesian coordinates system. Afterwards, neglecting the Mediterranean, the North Atlantic/Arctic Ocean basin is subdivided into basic grid cells of 128 km horizontal and 160 m vertical spacing (fig. 1.3.1.).

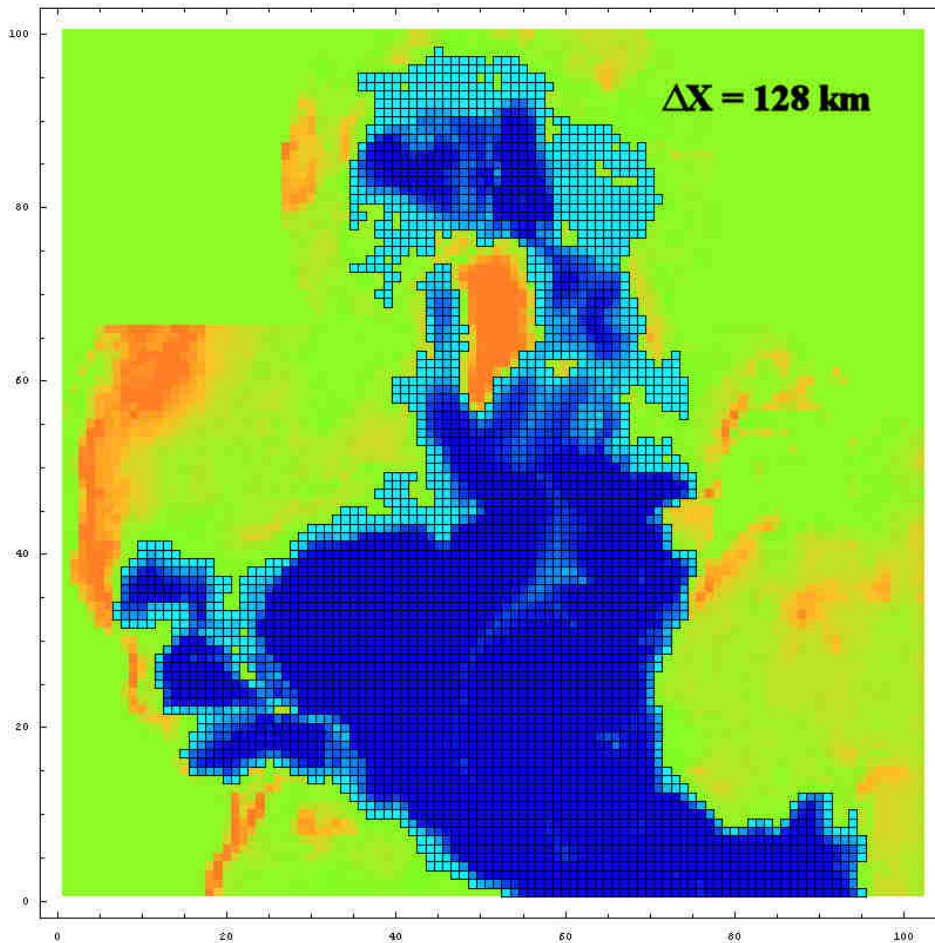


**Fig. 1.3.1:** The model domain in Cartesian coordinates resolved with basic grid cells of 128 km horizontal spacing.

Then, static adaptive mesh refinement, based on topographic structures, is applied. The horizontal refinement level 1 ( $\Delta x = 64$  km) is applied to the Nordic Seas, the North Sea, the Irminger and Iceland basin, the Canadian Archipelago and along the northern Mid-Atlantic ridge. (fig. 1.3.2.).

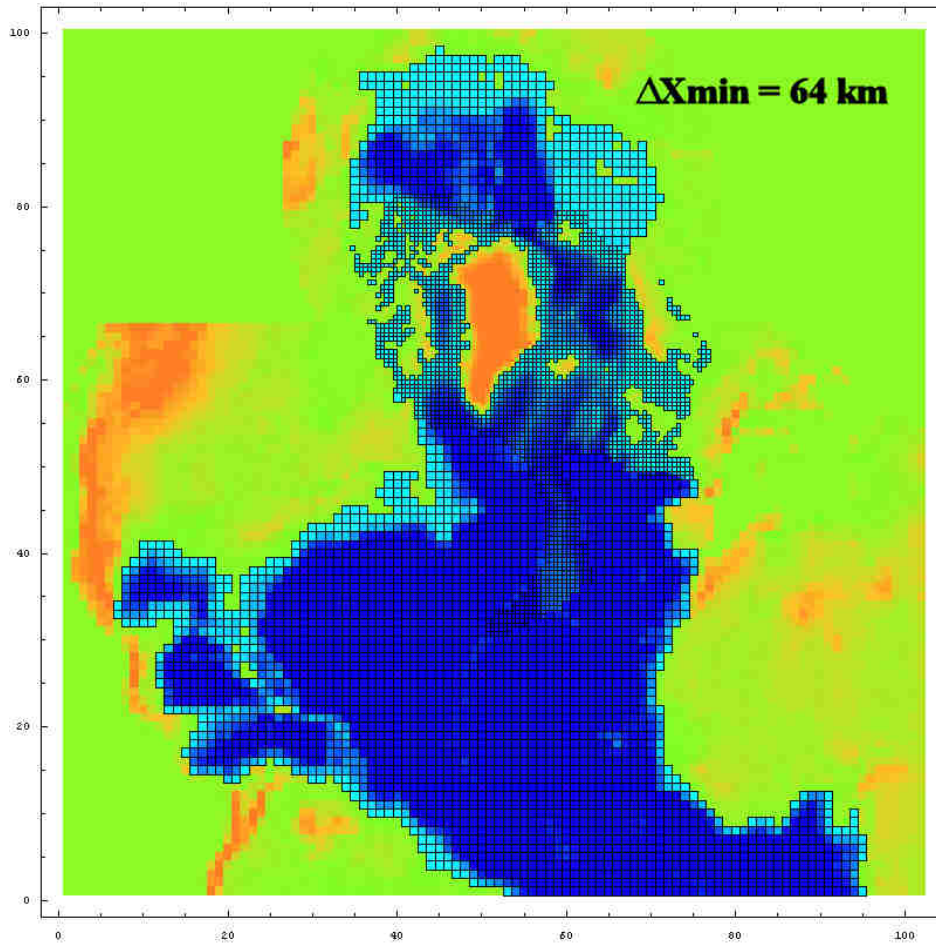


**Fig. 1.3.2:** The computational mesh after the first step of horizontal mesh refinement.

The refinement level 2 ( $\Delta x = 32$  km) is applied along the Greenland-Iceland-Scotland ridge, the Greenland and North-West European shelf (fig. 1.3.3.).

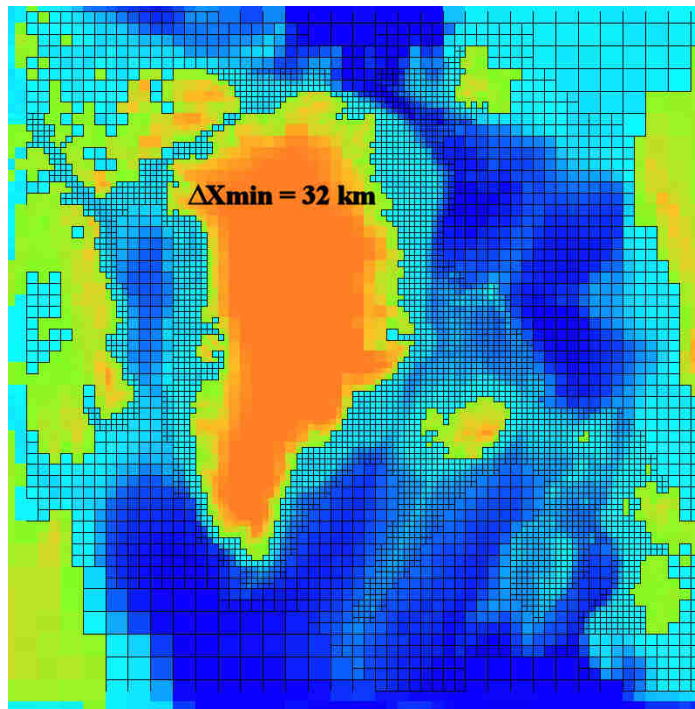


**Fig. 1.3.3.:** The computational mesh after the second step of horizontal mesh refinement.

The refinement level 3 ( $\Delta x = 16$  km) is applied along the Greenland-Iceland-Scotland ridge and to the Davis Strait (fig. 1.3.4.).

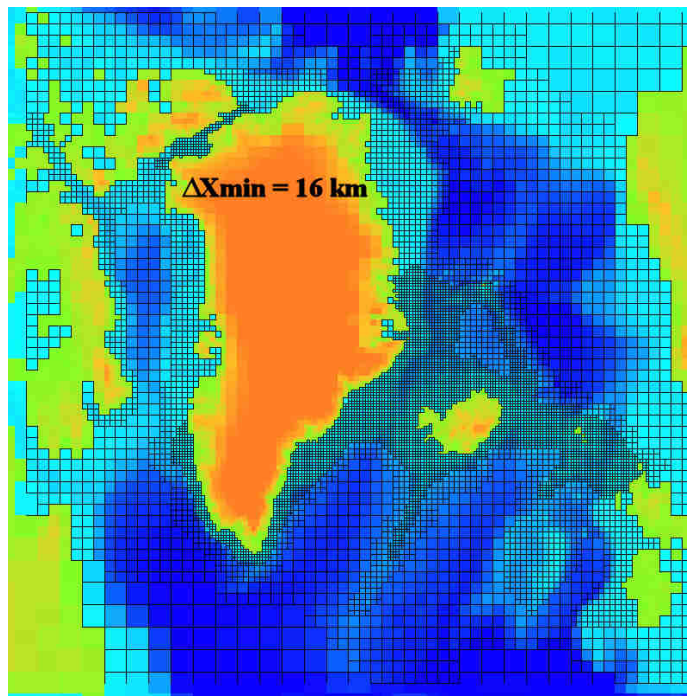


**Fig. 1.3.4.:** The computational mesh after the third step of horizontal mesh refinement.



The refinement level 4 ( $\Delta x = 8$  km) is applied along the Greenland-Iceland-Scotland ridge, to the Davis Strait and along the steepest slopes of the Iceland Sea (fig. 1.3.5.).

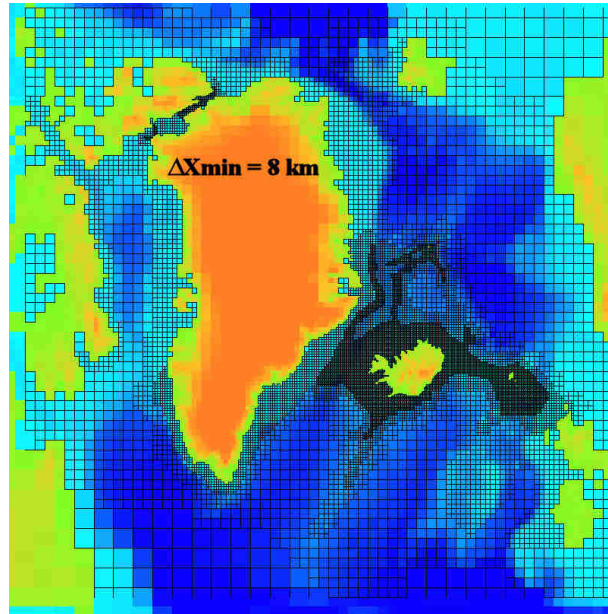


**Fig. 1.3.5.:** The computational mesh after the fourth step of horizontal mesh refinement.

The refinement levels 5, 6 and 7 ( $\Delta x = 4$ , 2 and 1 km) are applied to the coastal waters around Iceland (fig. 1.3.6., 1.3.7. and 1.3.8.).

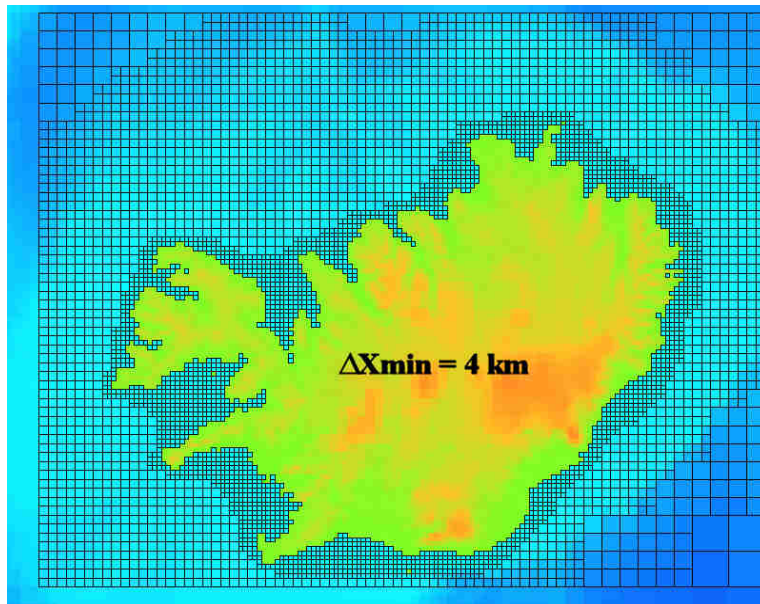


**Fig. 1.3.6.:** The computational mesh after the fifth step of horizontal mesh refinement.

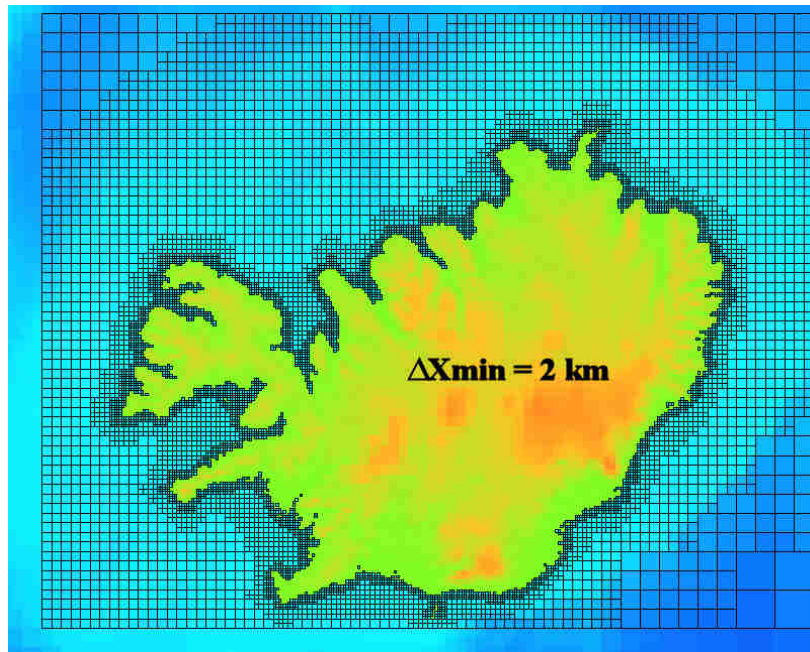


**Fig. 1.3.7.:** The computational mesh after the sixth step of horizontal mesh refinement.

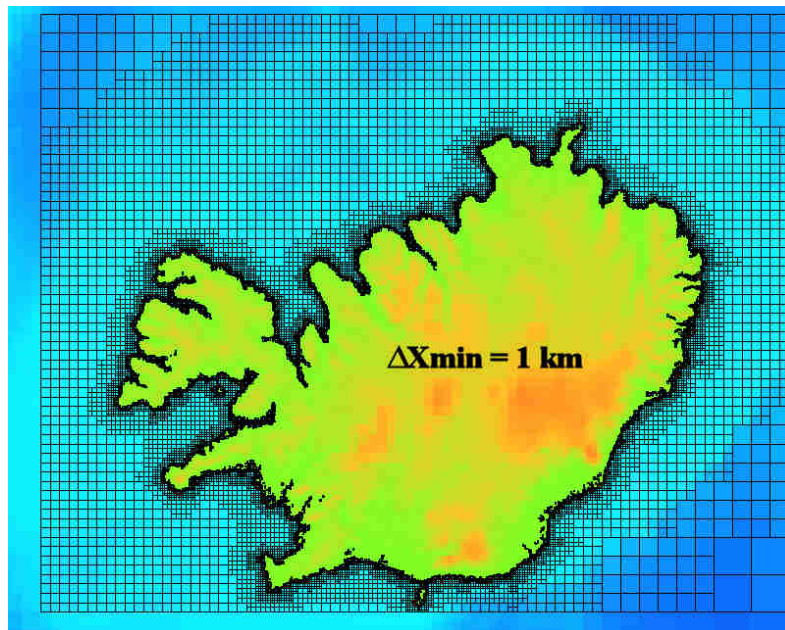


**Fig. 1.3.8.:** The computational mesh after the final seventh step of horizontal mesh refinement.

Vertically the adaptive mesh refinement is firstly applied to the near surface ocean of the entire model domain. Using six steps of mesh refinement the basic cell thickness  $\Delta z_0=160$  m is reduced to  $\Delta z=2.5$  m close to the sea surface (fig. 1.3.9.).

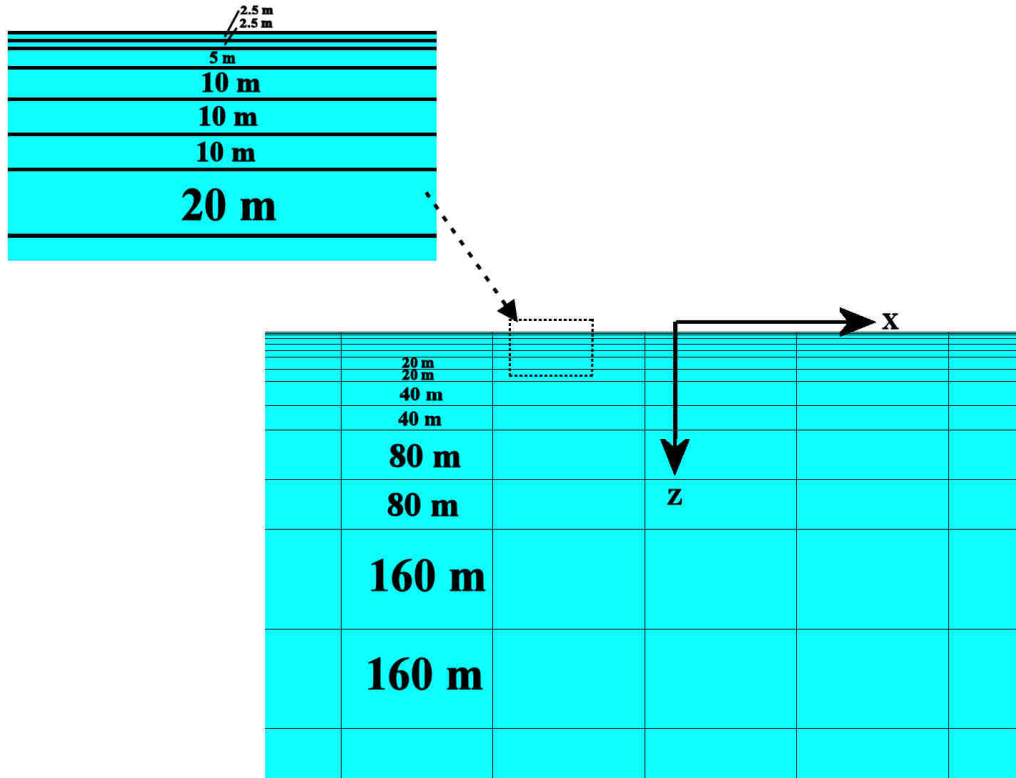


**Fig. 1.3.9.:** The computational mesh's vertical structure.

Additionally, depending on the horizontal level of refinement, a minimum level of vertical mesh refinement is set. Hence, grid cells with  $\Delta x=1$  km have a maximal thickness of  $\Delta z=10$  m (see table 1.3.1.). However, thereby the general structure with higher vertical resolution close to the sea surface and a reduced resolution for deeper waters is not altered. CODE does not use a vertical mesh refinement close to the sea bottom.



**Table 1.3.1.:** The minimum level of vertical mesh refinement as a function of horizontal mesh refinement.

level of horizontal mesh refinement	$\Delta x$ [km]	minimum level of vertical mesh refinement	$\Delta z_{MAX}$ [m]
0	128	0	160
1	64	0	160
2	32	0	160
3	16	0	160
4	8	1	80
5	4	2	40
6	2	3	20
7	1	4	10

### 1.3.2. Forcing data

The atmospheric forcing is taken from the NCEP/NCAR re-analysis data set (Kalnay et al. 1996). It consists of six-hourly fields of the following seven variables: precipitation rate, specific humidity (2 m), sea level pressure, air temperature (2 m), total cloud cover, zonal and meridional wind speed (10 m). This data is pre-processed by interpolating it onto the basic model grid ( $\Delta x_0 = 128$  km). Further interpolation, spatially onto the grid's higher resolving parts and temporally for each time step, is done during the simulation.

Around Iceland the freshwater release of numerous rivers is a further important process of forming the ocean upper layers stratification, with consequences to the coastal current field and to the ocean's primary production as well. To simulate this, the model uses estimates of the daily mean freshwater runoff along the Icelandic coast line. This data set is based on simulations of the hydrological model WaSiM (Schulla & Jasper 2007; Einarsson & Jónsson 2010) This way the model contains the discharge of 58 Icelandic rivers (fig. 1.3.10.).

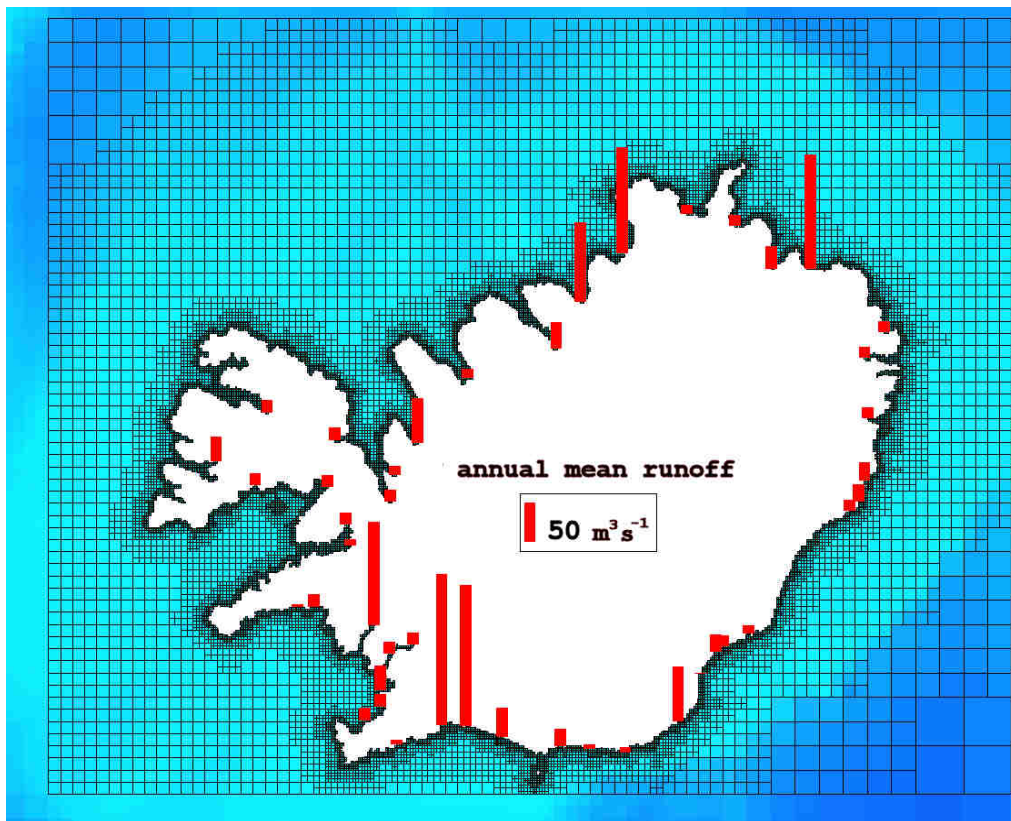


**Fig. 1.3.10.:** The location and mean discharge of rivers included within the simulation.

The simulated temperatures and salinities of the far field, i.e. the area south of 60°N, north of 70°N, west of 30°W and east of 5°W, are restored to the climatologic fields of the PHC (Polar Science Center Hydrographic Climatology) data set (Steele et al. 2001). The restoring consists of a 365-days Newtonian, scale selective scheme towards the 12 monthly fields of the PHC. The term “scale selective” means that differences between simulation and climatology are computed only up to the horizontal resolution of 16 km (refinement level 3). If the grid cell is smaller, the correction term of the surrounding 16 km cell (in the terminology of the tree-algorithm: the 16 km “ancestor” cell) is applied. This way, smaller-scale structures which cannot be resolved by the climatology are not damped by the restoring.

### 1.3.3. CTD data assimilation

We extracted 16,802 CTD profiles from the period 1992 to 2006 and from the area 60°N to 70°N, 30°W to 5°W by using the NISE (Nilsen et al. 2006) and the VEINS data set (ICES 2000) with some additional profiles from the ICES database ([www.ices.dk](http://www.ices.dk)). On average 93 profiles per simulated month were available (see figures 1.3.11. and 2.1 to 2.180). The profiles of each specific month were temporally shifted towards the 15<sup>th</sup> of the month by using the mean seasonal signal derived from the PHC climatology.

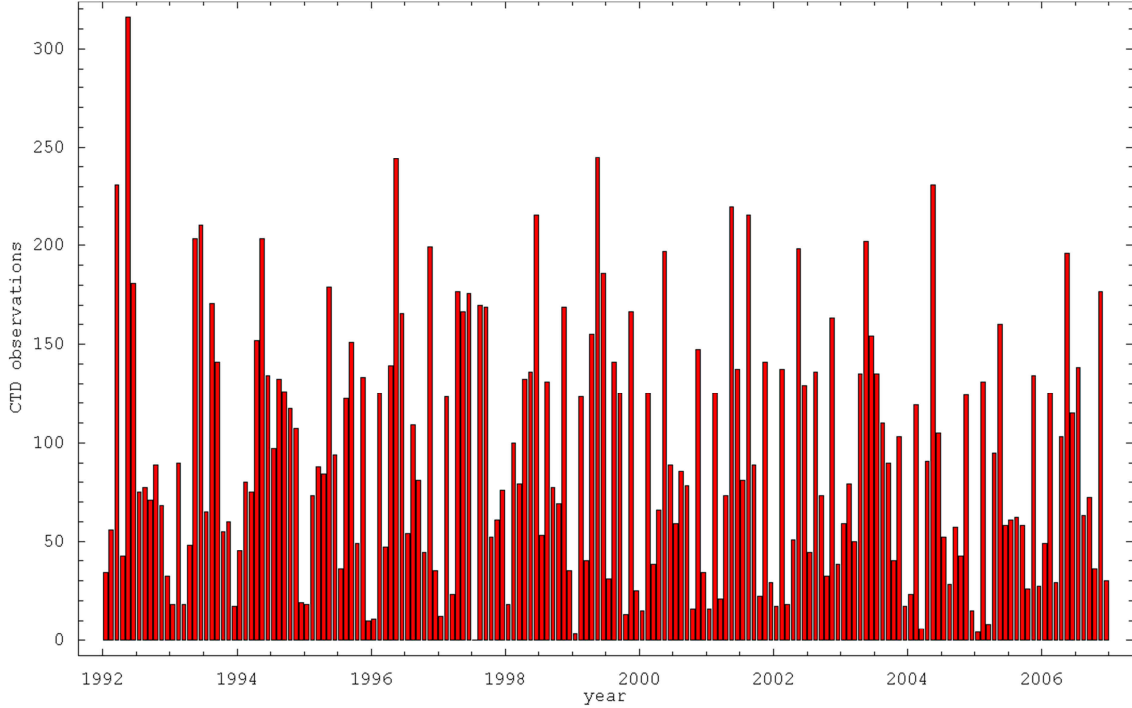


**Fig. 1.3.11.:** The number of assimilated CTD profiles per month. See figures 2.1. to 2.180. for spatial coverage.

The overall assimilation consists of an iterative process: First, the ocean model produces a free, prognostic solution. When having reached the 15<sup>th</sup> of each month the run is stopped and the simulation is compared with the CTD profiles. Assuming the CTD measurements to be true, profiles of the model temperature and salinity error are obtained. These profiles are horizontally interpolated in order to stretch out over all model grid cells. For each grid cell  $i$  the interpolated errors  $\Delta T_i$  and  $\Delta S_i$  are computed with:

$$\Delta T_i = \sum_{k=1}^{10} w_{i,k} A_{i,k} , \quad (90)$$

$$\Delta S_i = \sum_{k=1}^{10} w_{i,k} B_{i,k} , \quad (91)$$

where  $k$  is indexing the ten CTD profiles being spatially nearest to grid cell  $i$ .  $w_{i,k}$  denotes a spatial weighting being reciprocally proportional to the distance between the position of grid cell  $i$  ( $x_i, y_i$ ) and those of CTD profile  $k$  ( $x_k, y_k$ ):

$$w_{i,k} \sim \frac{1}{\sqrt{(x_i - x_k)^2 + (y_i - y_k)^2}}, \quad (91)$$

with

$$\sum_{k=1}^{10} w_{i,k} = 1. \quad (92)$$

The coefficients  $A_{i,k}$  (temperature) and  $B_{i,k}$  (salinity) contain the model error at the position of the CTD profile:  $\Delta T(x_k, y_k)$  and  $\Delta S(x_k, y_k)$  respectively, multiplied with an attenuation as this signal is propagated horizontally:

$$A_{i,k} = \Delta T(x_k, y_k) e^{-C_{i,k} ((x_i - x_k)^2 + (y_i - y_k)^2)} \quad (93)$$

$$B_{i,k} = \Delta S(x_k, y_k) e^{-D_{i,k} ((x_i - x_k)^2 + (y_i - y_k)^2)} \quad (94)$$

thereby the attenuation coefficients  $C_{i,k}$  and  $D_{i,k}$  are:

$$C_{i,k} = 0.75 \text{ K}^{-1} \text{ m}^{-2} \max(\Delta T(x_k, y_k), |T(x_i, y_i) - T(x_k, y_k)|, |T_{CTD} - T(x_i, y_i)|) \quad (95)$$

and

$$D_{i,k} = 5. \text{ psu}^{-1} \text{ m}^{-2} \max(\Delta S(x_k, y_k), |S(x_i, y_i) - S(x_k, y_k)|, |S_{CTD} - S(x_i, y_i)|). \quad (96)$$

Hence, the attenuation coefficients depend on the variance of the set: a) CTD value, b) model value at the position of the CTD, and c) model value of the considered grid cell. The physical meaning of this is that the CTD derived error has a greater significance if the CTD value and the considered model values stem from the same water mass. E.g. for the salinity field 20 km off-shore a salinity error of 15 psu detected close to a river mouth is less significant than an error in the range of 0.1 psu from 100 km off-shore.

After the errors  $\Delta T_i$  and  $\Delta S_i$  are computed for each grid cell  $i$  the model jumps one month back to the time  $t_0$  and repeats the simulation, but now introducing a set of correction terms. The errors  $\Delta T'_i$  and  $\Delta S'_i$  are linearly faded in during the first 15 days:

$$\Delta T'_i = \Delta T_i \min\left(1, \frac{t - t_0}{15 \text{ days}}\right) - (T_i^I - T_i^{\text{free}}), \quad (97)$$

$$\Delta S'_i = \Delta S_i \min\left(1, \frac{t - t_0}{15 \text{ days}}\right) - (S_i^I - S_i^{\text{free}}), \quad (98)$$

With  $T_i^I$ ,  $S_i^I$  being the temperature and salinity in grid cell  $i$  at the time  $t$  computed anew (first iteration) and  $T_i^{free}$ ,  $S_i^{free}$  the corresponding values of the first, free forecast.

At each time step for each grid cell the dominant fluxes within the equations of heat and salt conservation are determined. These dominant fluxes, i.e.  $x$ -directed,  $y$ -directed or  $z$ -directed advection, horizontal or vertical diffusion, or the surface flux, if the cell is located at the surface, are assumed to cause the errors  $\Delta T'_i$  and  $\Delta S'_i$  respectively. To compensate this, correction terms are used. I.e. the equation of heat conservation (15) becomes:

$$\begin{aligned} \frac{\partial T}{\partial t} = & -(u + \Delta u) \frac{\partial T}{\partial x} - (v + \Delta v) \frac{\partial T}{\partial y} - (w + \Delta w) \left( \frac{\partial T}{\partial z} + \Gamma \right) + \frac{\partial}{\partial x} \left( (K_{H,T} + \Delta K_{H,T}) \frac{\partial T}{\partial x} \right) + \\ & \frac{\partial}{\partial y} \left( (K_{H,T} + \Delta K_{H,T}) \frac{\partial T}{\partial y} \right) + \frac{\partial}{\partial z} \left( (K_{V,T} + \Delta K_{V,T}) \left( \frac{\partial T}{\partial z} + \Gamma \right) \right) + Q_T + \Delta Q_T + \Delta Q_T^{NUM} \quad . \end{aligned} \quad (99)$$

And equation (16) becomes:

$$\begin{aligned} \frac{\partial S}{\partial t} = & -(u + \Delta u) \frac{\partial S}{\partial x} - (v + \Delta v) \frac{\partial S}{\partial y} - (w + \Delta w) \frac{\partial S}{\partial z} + \frac{\partial}{\partial x} \left( (K_{H,S} + \Delta K_{H,S}) \frac{\partial S}{\partial x} \right) + \\ & \frac{\partial}{\partial y} \left( (K_{H,S} + \Delta K_{H,S}) \frac{\partial S}{\partial y} \right) + \frac{\partial}{\partial z} \left( (K_{V,S} + \Delta K_{V,S}) \frac{\partial S}{\partial z} \right) + Q_S + \Delta Q_S + \Delta Q_S^{NUM} \quad , \end{aligned} \quad (100)$$

whereas most of the correction terms:  $\Delta u$ ,  $\Delta v$ ,  $\Delta w$ ,  $\Delta K_{H,T}$ ,  $\Delta K_{V,T}$ ,  $\Delta K_{H,S}$ ,  $\Delta K_{V,S}$ ,  $\Delta Q_T^{NUM}$  and  $\Delta Q_S^{NUM}$  are zero except the surface flux corrections,  $\Delta Q_T$  and  $\Delta Q_S$ , if the grid cell is located at the sea surface, and those which are related to the dominant interior fluxes. (The numerical source terms,  $\Delta Q_T^{NUM}$  and  $\Delta Q_S^{NUM}$ , are activated within subsequent iterations.) E.g.: If  $x$ -directed advection is the dominant interior flux in eq. (15), it is

$$\Delta u_T = \alpha_T \frac{\Delta t}{24 \text{ h}} s_T \text{ m s}^{-1}, \quad (101)$$

with  $s_T$  being 1 or -1 depending on the sign of  $\Delta T'$ ,  $u$  and  $\partial T / \partial x$  and always chosen in the way to reduce the error  $\Delta T'$ , whereas

$$\alpha_T = \max \left( 1, \frac{|\Delta T'|}{1. \text{ K}} \right) \quad (102)$$

controls the magnitude of the error term.

If  $x$ -directed advection is dominant in eq. (16) it follows:

$$\Delta u_S = \alpha_S \frac{\Delta t}{24 \text{ h}} s_S \text{ m s}^{-1}, \quad (103)$$

with

$$\alpha_s = \max \left( 1, \frac{|\Delta S'|}{0.1 \text{ psu}} \right). \quad (104)$$

To keep the simulation of advection consistent a sole correction  $\Delta u$  is used in equations (99) and (100), this is obtained by:

$$\Delta u = \begin{cases} \frac{1}{2} (\Delta u_T + \Delta u_S) & \text{if } \Delta u_T \Delta u_S > 0 \\ \Delta u_T + \Delta u_S & \text{if } \Delta u_T \Delta u_S = 0 \\ 0 & \text{if } \Delta u_T \Delta u_S < 0 \end{cases} \quad (105)$$

$\Delta u_T \Delta u_S > 0$  means that the  $x$ -directed advection is the dominant heat and salt flux and assumed to be the source both for the temperature and the salinity error. In this case  $\Delta u$  will be the mean of both velocities. If  $\Delta u_T \Delta u_S = 0$  then the  $x$ -directed advection is not dominant in at least one of the equations (99) and (100). Hence, if one equation demands a  $\Delta u \neq 0$  the impact on the other equation is assumed to be rather small and tolerable. Finally, if  $\Delta u_T \Delta u_S < 0$  both equations demand for a  $\Delta u \neq 0$  but with different signs (different flow directions), the case becomes unsolvable and  $\Delta u$  is set to zero.

The  $y$ -directed advection is treated analogously. The correction term for vertical advection is computed with

$$\Delta w_T = \alpha_T \frac{\Delta t}{24 \text{ h}} s_T \text{ cm s}^{-1}, \quad (106)$$

and

$$\Delta w_S = \alpha_S \frac{\Delta t}{24 \text{ h}} s_S \text{ cm s}^{-1}, \quad (107)$$

whereas the sole correction  $\Delta w$  is determined analogously to equation (105). The correction terms regarding horizontal diffusion are:

$$\Delta K_{H,T} = \alpha_T 0.1 \frac{\Delta x^2}{\Delta t} s_T, \quad (108)$$

and

$$\Delta K_{H,S} = \alpha_S 0.1 \frac{\Delta x^2}{\Delta t} s_S, \quad (109)$$

for the vertical diffusion:

$$\Delta K_{V,T} = \alpha_T 0.1 \frac{\Delta z^2}{\Delta t} s_T, \quad (110)$$

and

$$\Delta K_{V,S} = \alpha_S 0.1 \frac{\Delta z^2}{\Delta t} s_S. \quad (111)$$

If the grid cell is located at the sea surface, the surface flux corrections,  $\Delta Q_T$  and  $\Delta Q_S$ , are computed with:

$$\Delta Q_T = \alpha_T \frac{1 \text{ K}}{24 \text{ h}}, \quad (112)$$

and

$$\Delta Q_S = \alpha_S \frac{0.1 \text{ psu}}{24 \text{ h}}. \quad (113)$$

This way, the model re-simulates the last 30 days. When having reached again the 15th of the month the run is stopped again. Again the deviations between model and CTD data are determined. This time, the errors  $\Delta T^I$  and  $\Delta S^I$  are computed, i.e. the errors of the first iteration. These are added to the errors of the free forecast,  $\Delta T^{free}$  and  $\Delta S^{free}$ . The model jumps back in time by one week, to the time  $t = t_I$ , and starts the second iteration. Now, the updated errors are:

$$\Delta T' = \Delta T^{free} \min\left(1, \frac{t - t_0}{15 \text{ days}}\right) + \Delta T^I \min\left(1, \frac{t - t_1}{2 \text{ days}}\right) - (T^{II} - T^{free}), \quad (114)$$

and

$$\Delta S' = \Delta S^{free} \min\left(1, \frac{t - t_0}{15 \text{ days}}\right) + \Delta S^I \min\left(1, \frac{t - t_1}{2 \text{ days}}\right) - (S^{II} - S^{free}), \quad (115)$$

with  $T^{free}$ ,  $S^{free}$  being the simulated temperature and salinities of the free forecast, and  $T^{II}$ ,  $S^{II}$  those of the current, second iteration.

Hence, at the third, final iteration, after jumping back in time by 5 days towards  $t = t_2$ , the errors are:

$$\Delta T' = \Delta T^{free} \min\left(1, \frac{t - t_0}{15 \text{ days}}\right) + \Delta T^I \min\left(1, \frac{t - t_1}{2 \text{ days}}\right) + \Delta T^{II} \min\left(1, \frac{t - t_2}{2 \text{ days}}\right) - (T^{III} - T^{free}), \quad (116)$$

and

$$\Delta S' = \Delta S^{free} \min\left(1, \frac{t - t_0}{15 \text{ days}}\right) + \Delta S^I \min\left(1, \frac{t - t_1}{2 \text{ days}}\right) + \Delta S^{II} \min\left(1, \frac{t - t_2}{2 \text{ days}}\right) - (S^{III} - S^{free}). \quad (117)$$

Within the second and third iteration the “numerical source terms”  $\Delta Q_T^{NUM}$ ,  $\Delta Q_S^{NUM}$  of equation (99) and (100) are activated. We call these terms “numerical” because they cannot be linked to a specific physical process but compensate model errors which probably are of

numerical origin, e.g. imprecise initial or boundary data. The terms have the form of a Newtonian relaxation towards the fields  $T(t=t_a)-\Delta T$  and  $S(t=t_a)-\Delta S$ . I.e. the simulated temperature and salinity fields at  $t=t_a$ , the time of the comparison with observations (15<sup>th</sup> of the month), corrected by the errors,  $\Delta T$  and  $\Delta S$ , which are determined by the comparison, analysis and interpolation.

Within the second iteration it is:

$$\Delta Q_T^{NUM} = \frac{T(t=t_a) - \Delta T - T^{II}}{3 \text{ days}} \quad (118)$$

and

$$\Delta Q_S^{NUM} = \frac{S(t=t_a) - \Delta S - S^{II}}{3 \text{ days}} . \quad (119)$$

Within the third iteration:

$$\Delta Q_T^{NUM} = \frac{T(t=t_a) - \Delta T - T^{III}}{1.5 \text{ days}} \quad (120)$$

and

$$\Delta Q_S^{NUM} = \frac{S(t=t_a) - \Delta S - S^{III}}{1.5 \text{ days}} . \quad (121)$$

Figure 1.3.12. shows the iterative convergence of the simulated fields towards the observations. Note that the data assimilation technique described here does not lead to the identity of simulated and observed station data but that it will remain a small difference (see chapter 3).



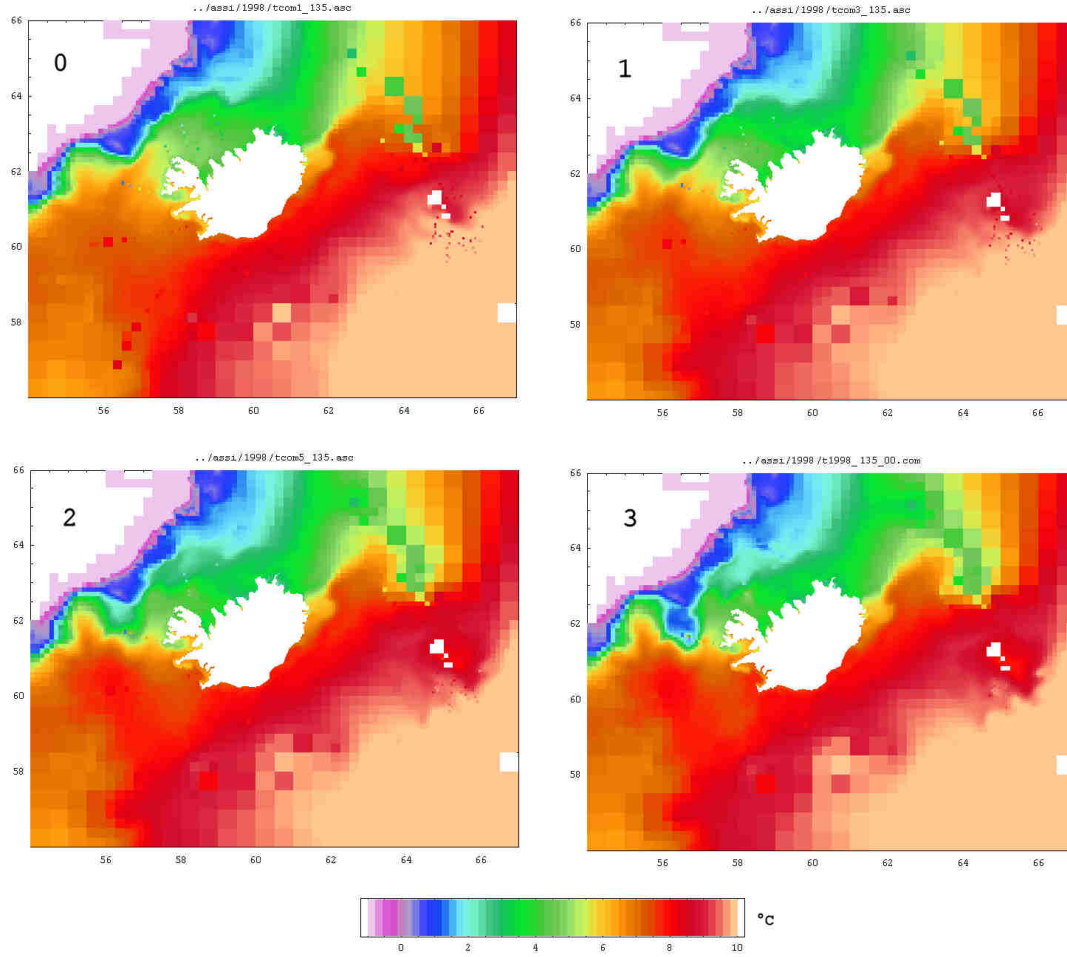


Fig. 1.3.12.: Simulated and observed SST of 15.05.98, model output with overlaid CTD values. The images show the free forecast (0), the first (1), second (2) and third iteration (3).

#### 1.3.4. Output data

During the simulation three-hourly means of the following 12 variables, describing the physical ocean state, are computed and stored on the hard disk: the velocity field ( $u, v, w$ ), the sea surface elevation ( $\zeta$ ), the temperature ( $T$ ) and salinity ( $S$ ) field, the horizontal and vertical exchange coefficients ( $A_H, A_V$ ), the sea ice drift ( $u_i, v_i$ ), the sea ice thickness ( $h_i$ ) and coverage ( $A_i$ ). The averaging period of three hours was chosen to resolve tidal dynamics. Additionally, in order to obtain deeper insights into the near-surface thermodynamics, the three-hourly means of following variables are stored: sea surface freshwater flux (precipitation – evaporation,  $P-E$ ), short-wave radiative heat flux ( $Q_{SW}$ ), long-wave radiative heat flux ( $Q_{LW}$ ), latent heat flux ( $Q_{LAT}$ ) and sensible heat flux ( $Q_{SENS}$ ).

## 2. Results

We confine the presentation of the model output to charts of monthly mean temperature, salinity and flow at the depth of 50 m. A depth, where we find the maximum of interior, oceanic variability, which is not just reflecting the variations of atmospheric forcing.

In general, the model shows realistic structures. Though there seems to be a tendency to over-estimate the salinity of the East Greenland Current (EGC) at the depth of 50 m. This becomes clearly perceptible when CTD profiles from the Polar Waters of the EGC were assimilated into the model (e.g. fig. 2.69) leading to unrealistic structures of local, negative salinity anomalies west of Iceland. However, when concentrating on Icelandic waters, the comparison with the output of a former model run without data assimilation (Logemann et al. 2010) shows a clear improvement towards realism. E.g.: Whereas the former version had the tendency to under-estimate the strength of the North Icelandic Irminger Current (NIIC), the current of warm Atlantic Water onto the north Icelandic shelf, this problem, obviously linked to the simulation of the density field, was solved immediately as soon as the CTD data assimilation had been activated. Temporal anomalies, like the NIIC collapse during spring 1995 or the NIIC maximum during July 2003 are also precisely reproduced.

The simulated flow fields show a surprising strong, eastward current along the south coast. During some months this current even forms the dominant structure of the circulation of Icelandic waters. Little is known about the circulation south-east of Iceland, though fishermen reported a strong eastward current from that region. Hence, the examination of this model result remains a field of future oceanographic research.

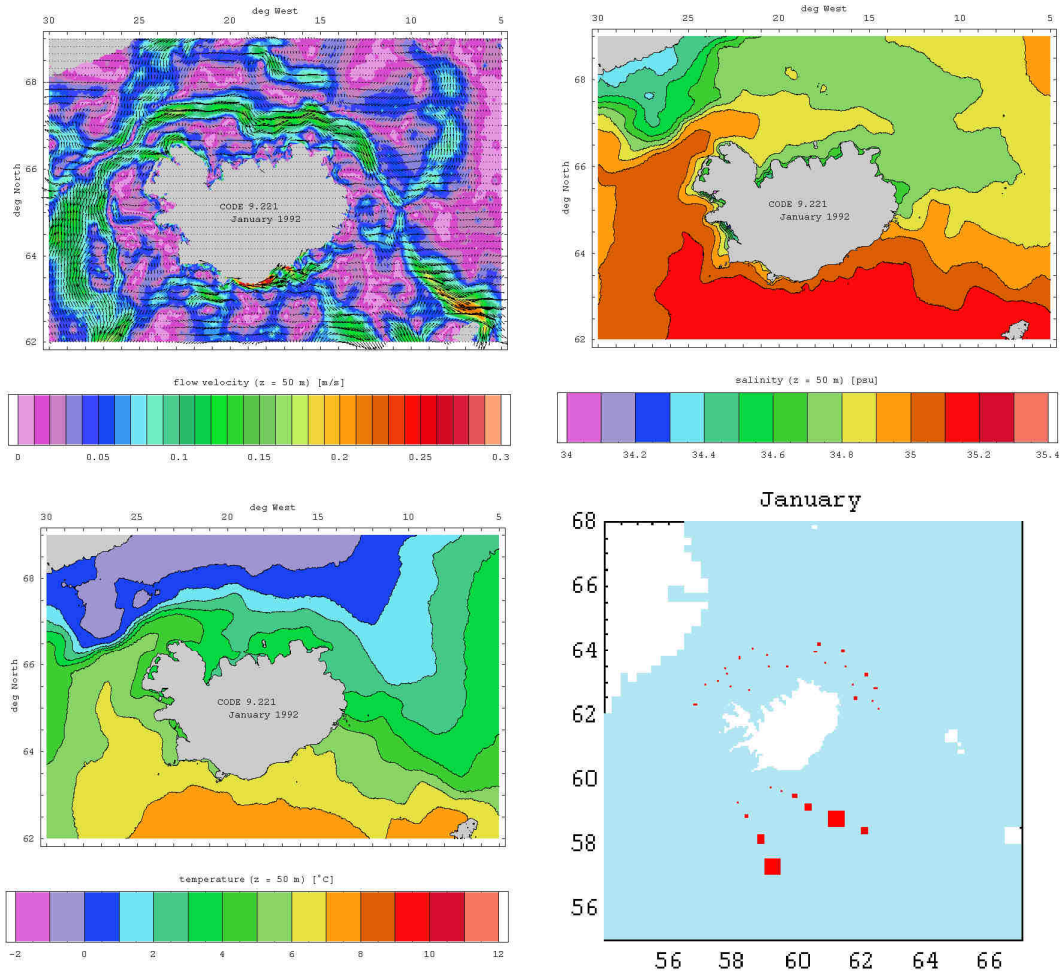


Fig. 2.1.: Monthly mean flow, salinity and temperature fields at 50 m depth and location of used CTD profiles – January 1992. The lower right image shows the model coordinate system with grid cells marked red when containing at least one CTD profile.

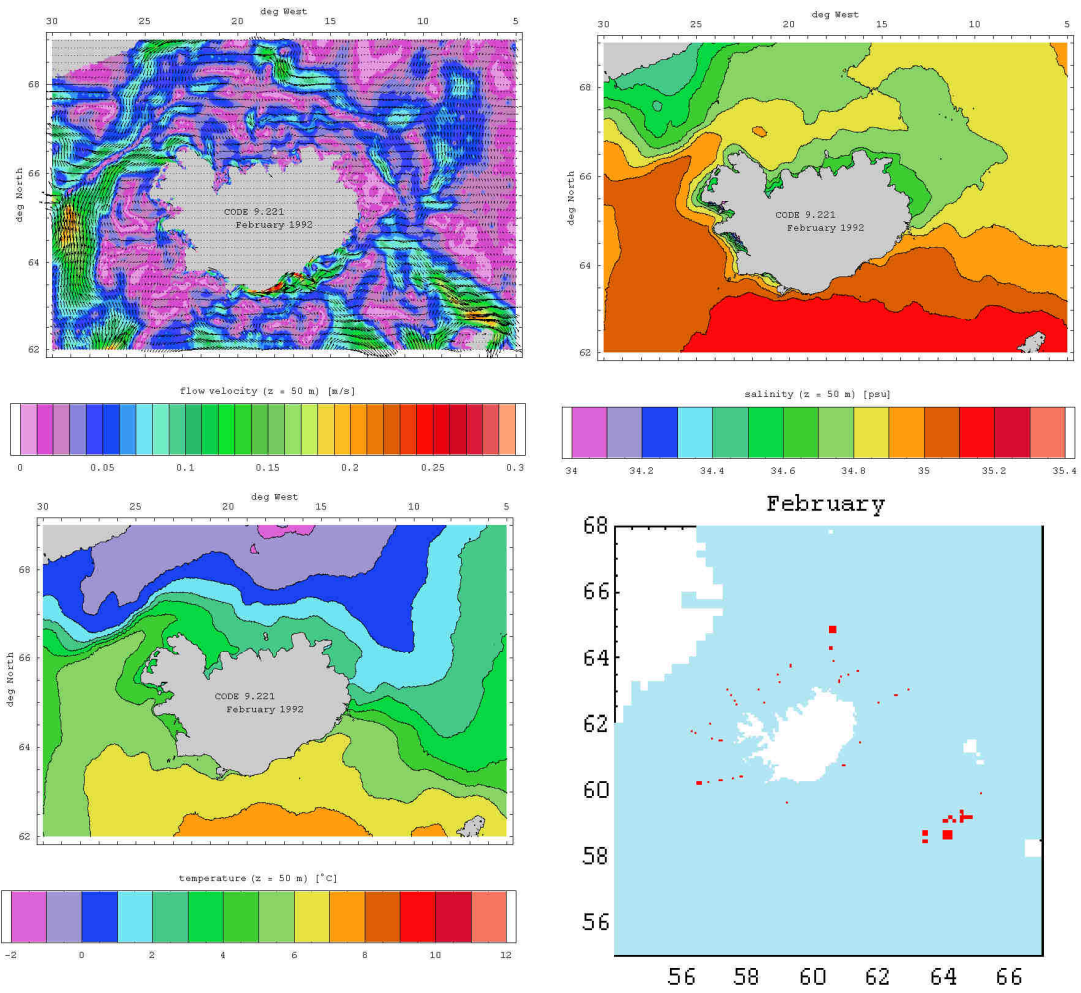


Fig. 2.2.: Monthly mean flow, salinity and temperature fields at 50 m depth and location of used CTD profiles – February 1992.

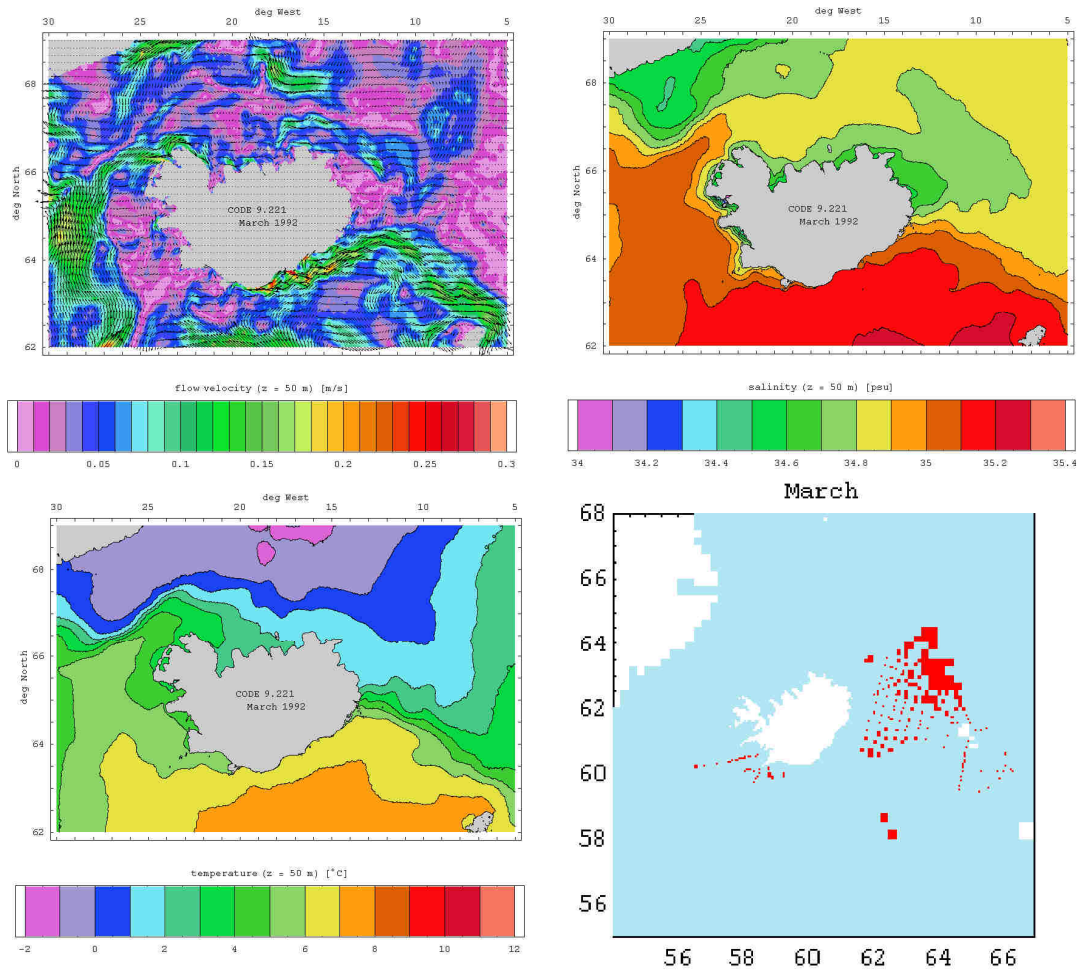


Fig. 2.3.: Monthly mean flow, salinity and temperature fields at 50 m depth and location of used CTD profiles – March 1992.

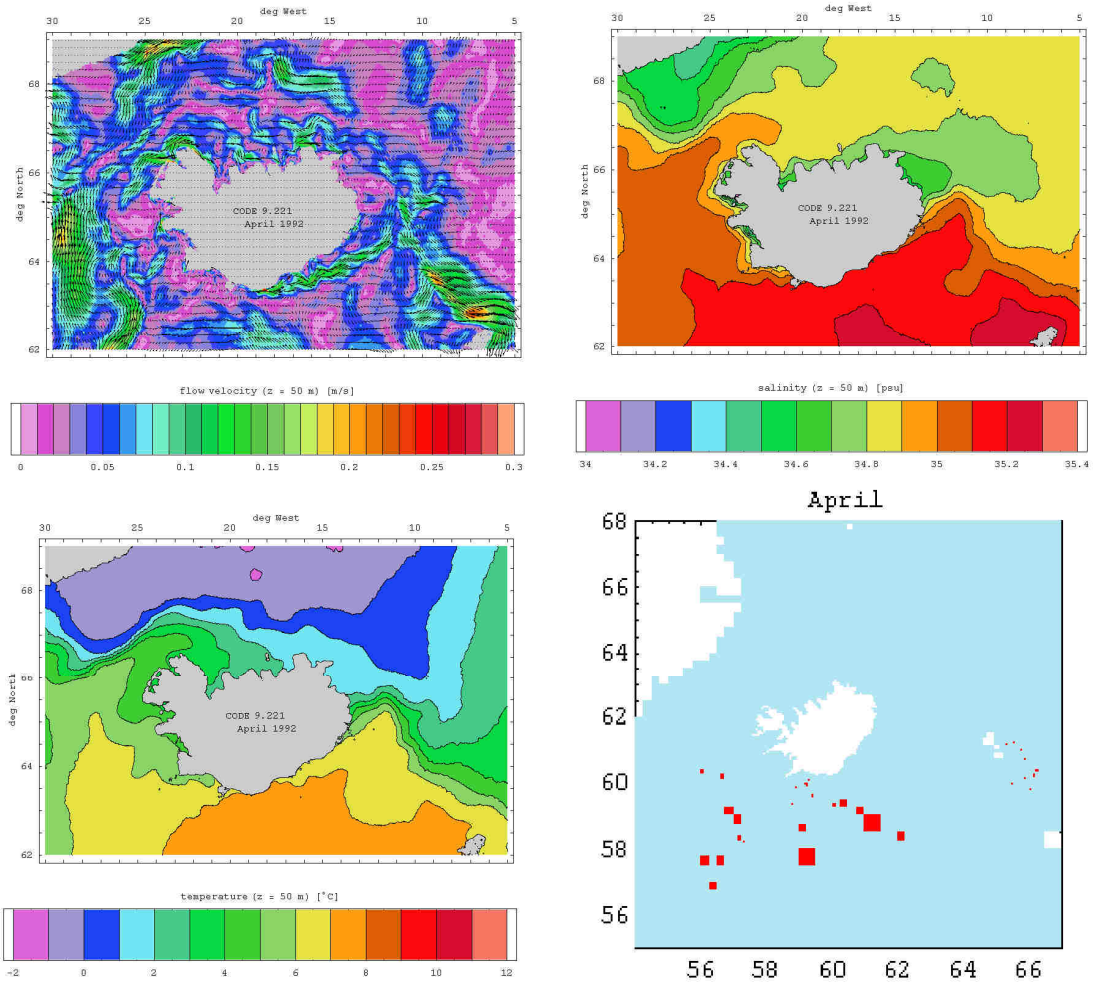


Fig. 2.4.: Monthly mean flow, salinity and temperature fields at 50 m depth and location of used CTD profiles – April 1992.



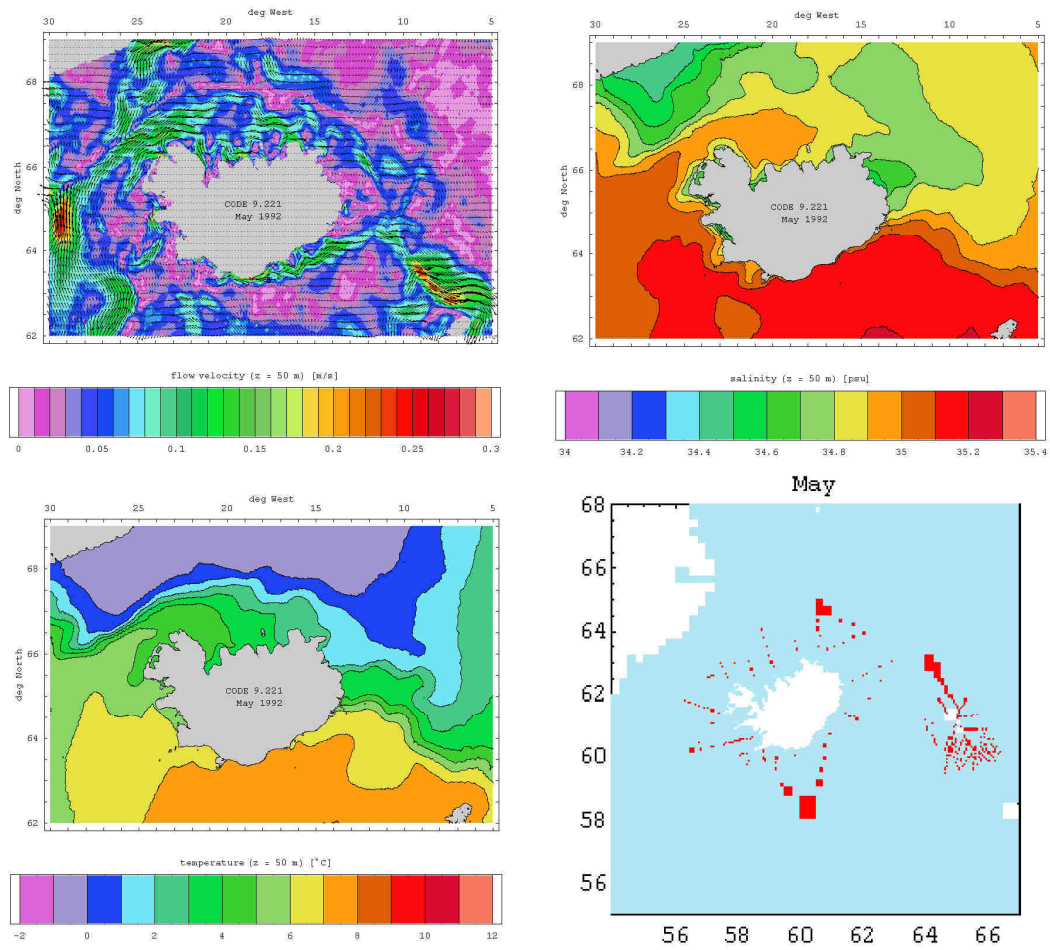


Fig. 2.5.: Monthly mean flow, salinity and temperature fields at 50 m depth and location of used CTD profiles – May 1992.

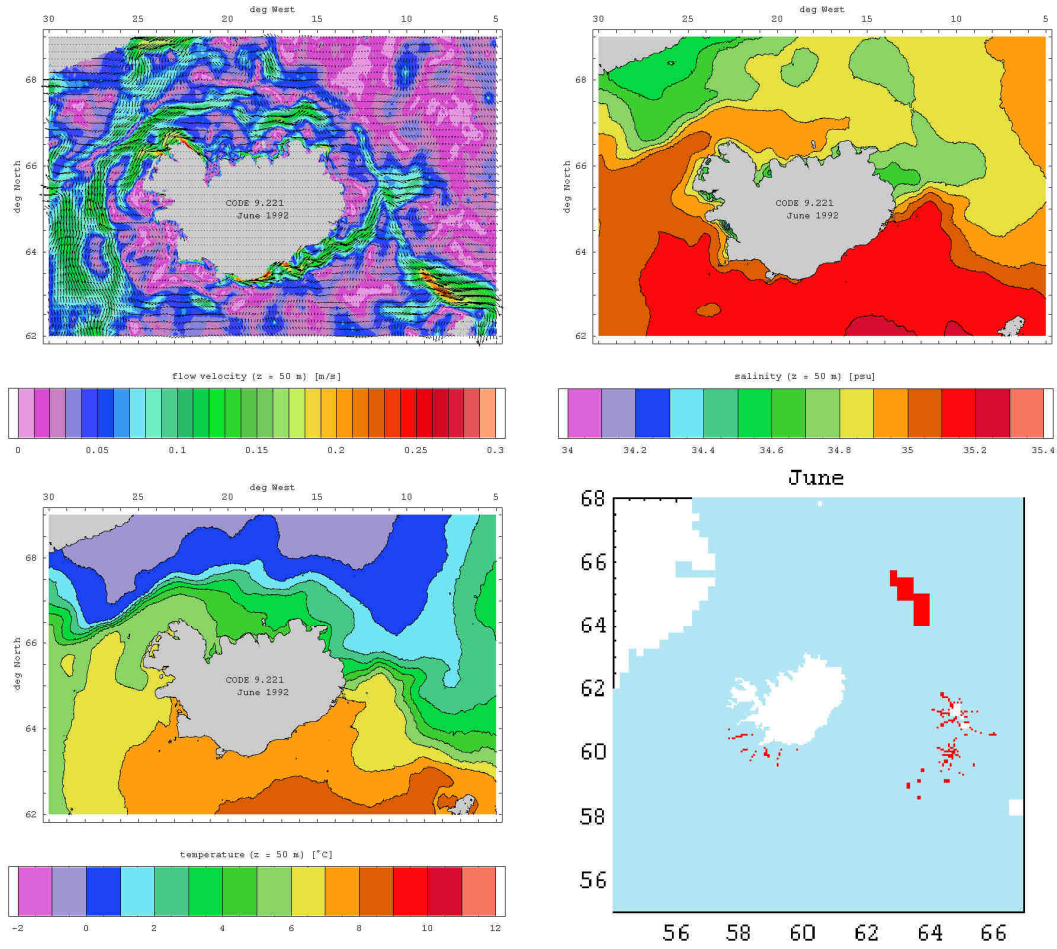


Fig. 2.6.: Monthly mean flow, salinity and temperature fields at 50 m depth and location of used CTD profiles – June 1992.



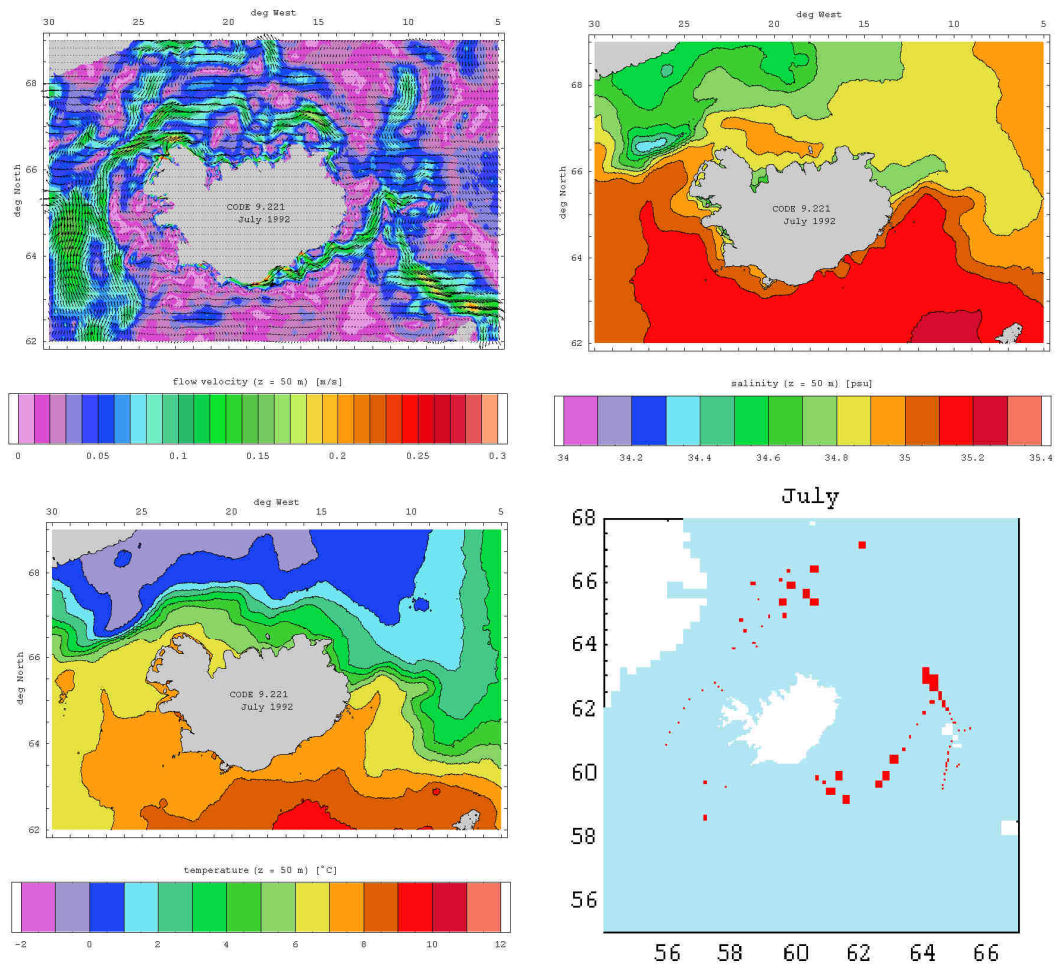


Fig. 2.7.: Monthly mean flow, salinity and temperature fields at 50 m depth and location of used CTD profiles – July 1992.

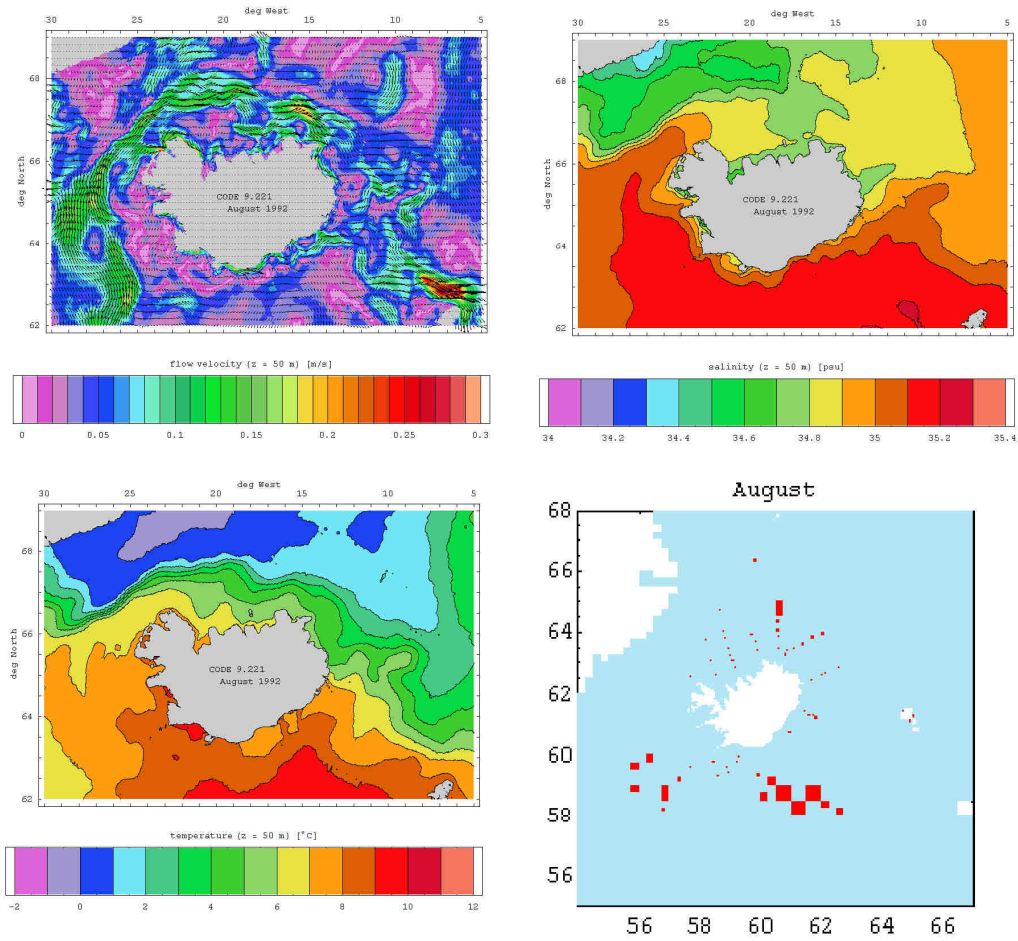


Fig. 2.8.: Monthly mean flow, salinity and temperature fields at 50 m depth and location of used CTD profiles – August 1992.

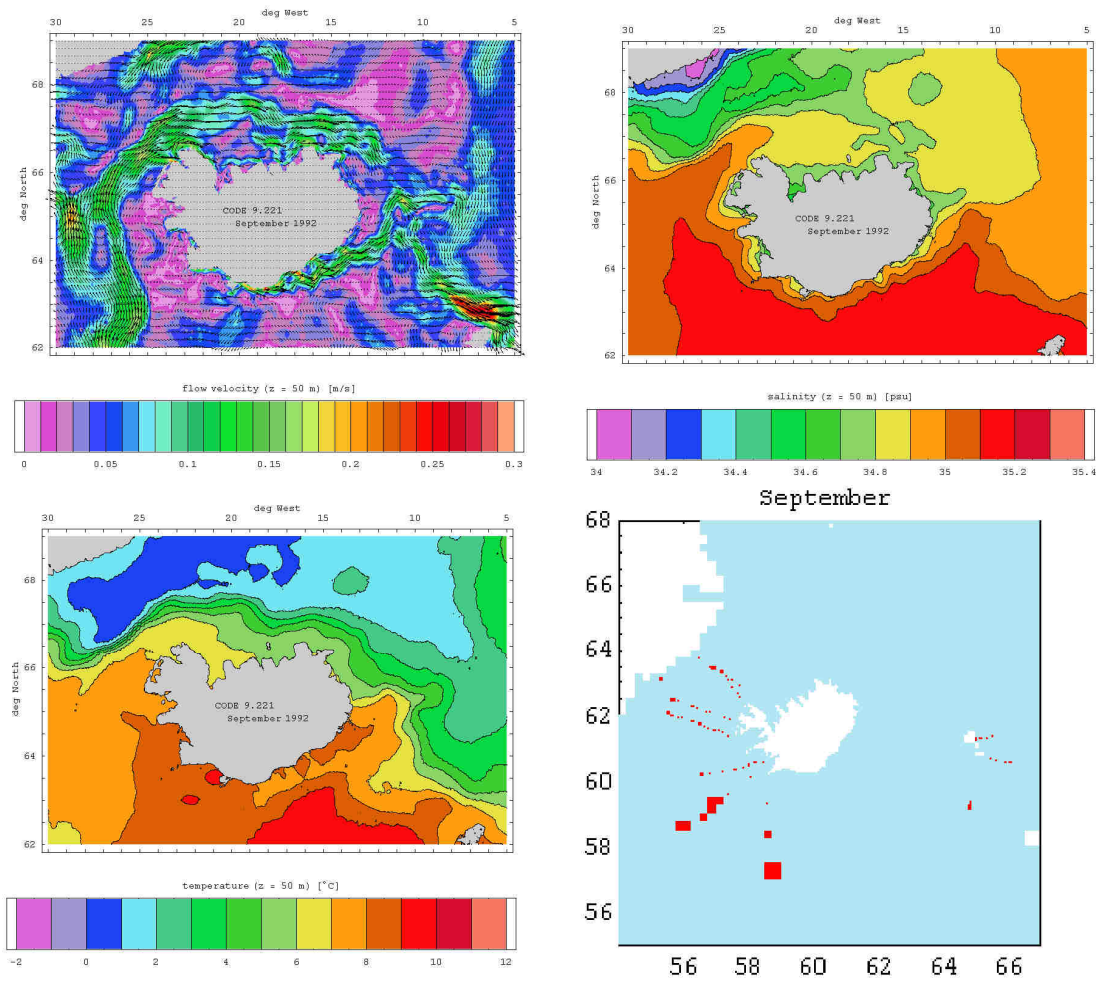


Fig. 2.9.: Monthly mean flow, salinity and temperature fields at 50 m depth and location of used CTD profiles – September 1992.

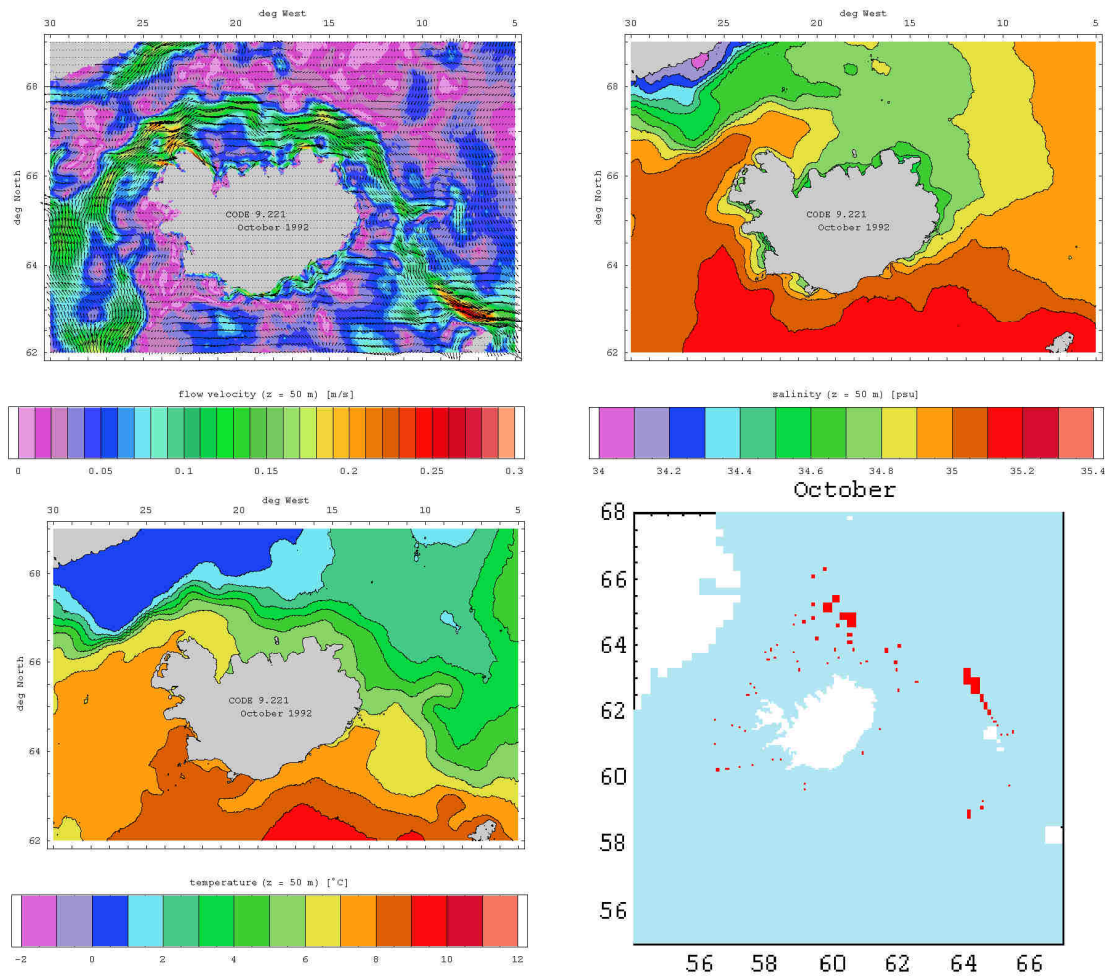


Fig. 2.10.: Monthly mean flow, salinity and temperature fields at 50 m depth and location of used CTD profiles – October 1992.

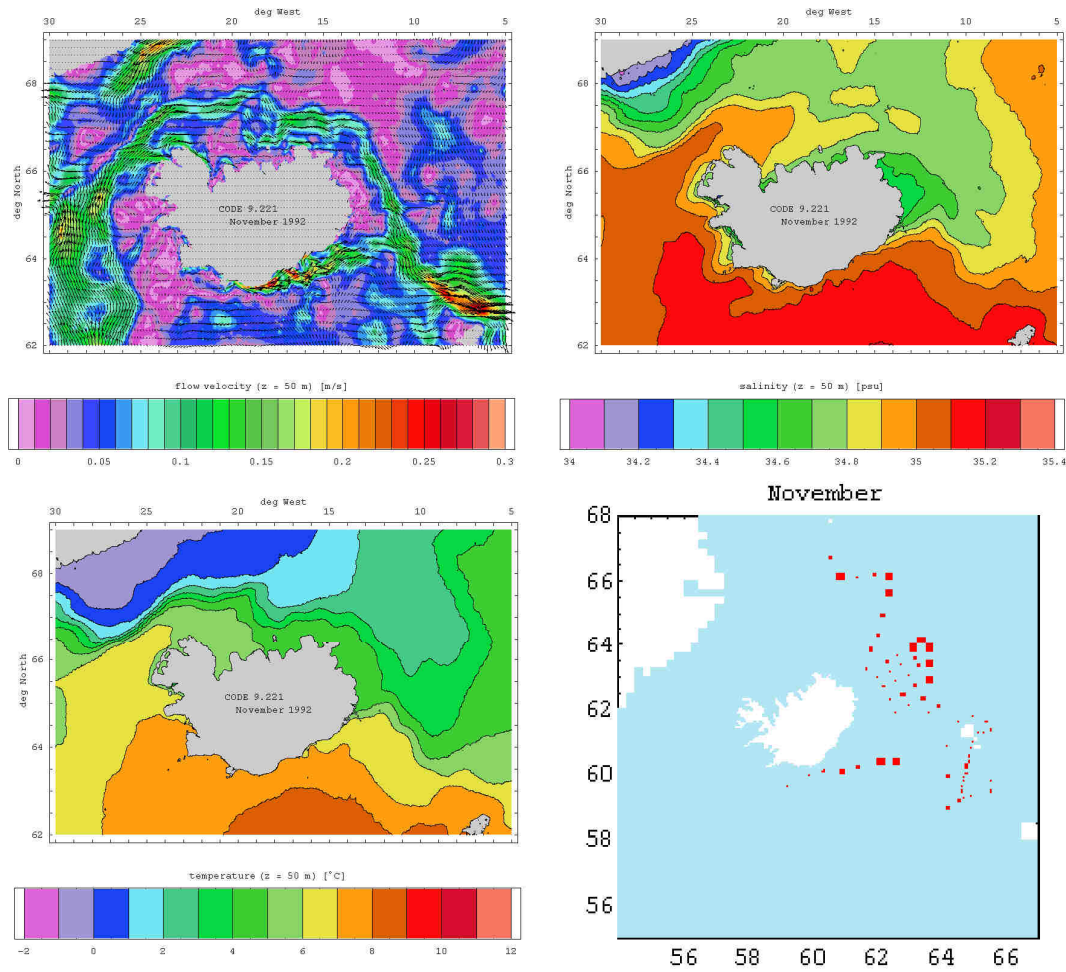


Fig. 2.11.: Monthly mean flow, salinity and temperature fields at 50 m depth and location of used CTD profiles – November 1992.



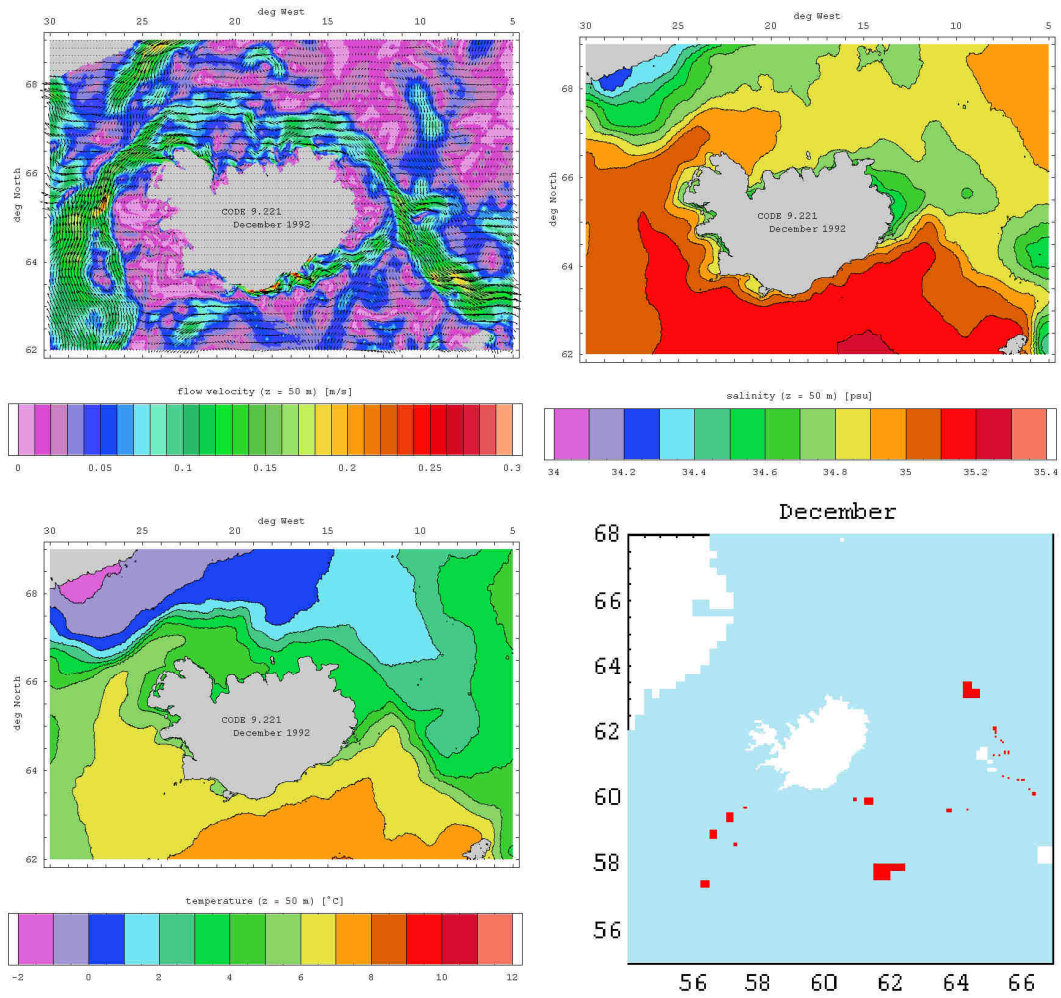


Fig. 2.12.: Monthly mean flow, salinity and temperature fields at 50 m depth and location of used CTD profiles – December 1992.

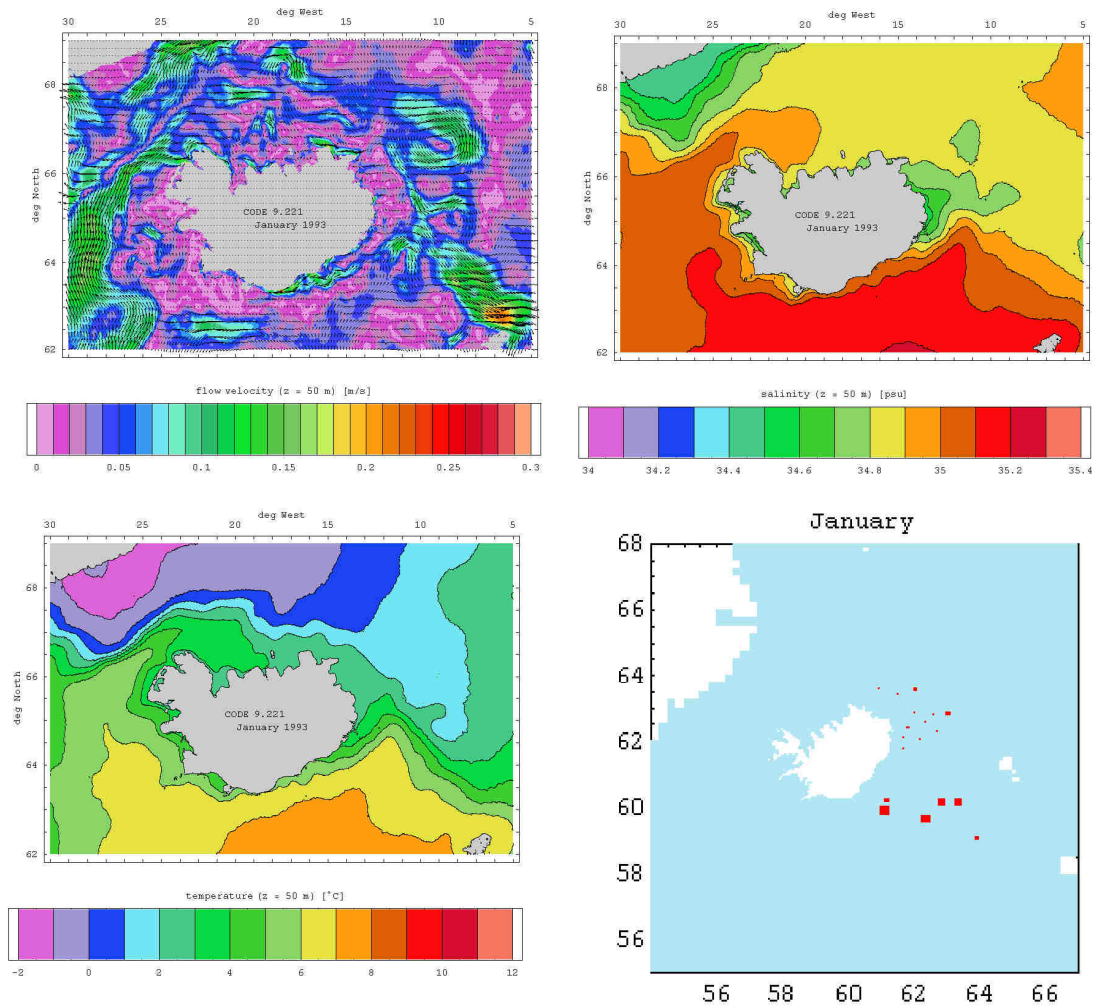


Fig. 2.13.: Monthly mean flow, salinity and temperature fields at 50 m depth and location of used CTD profiles – January 1993.

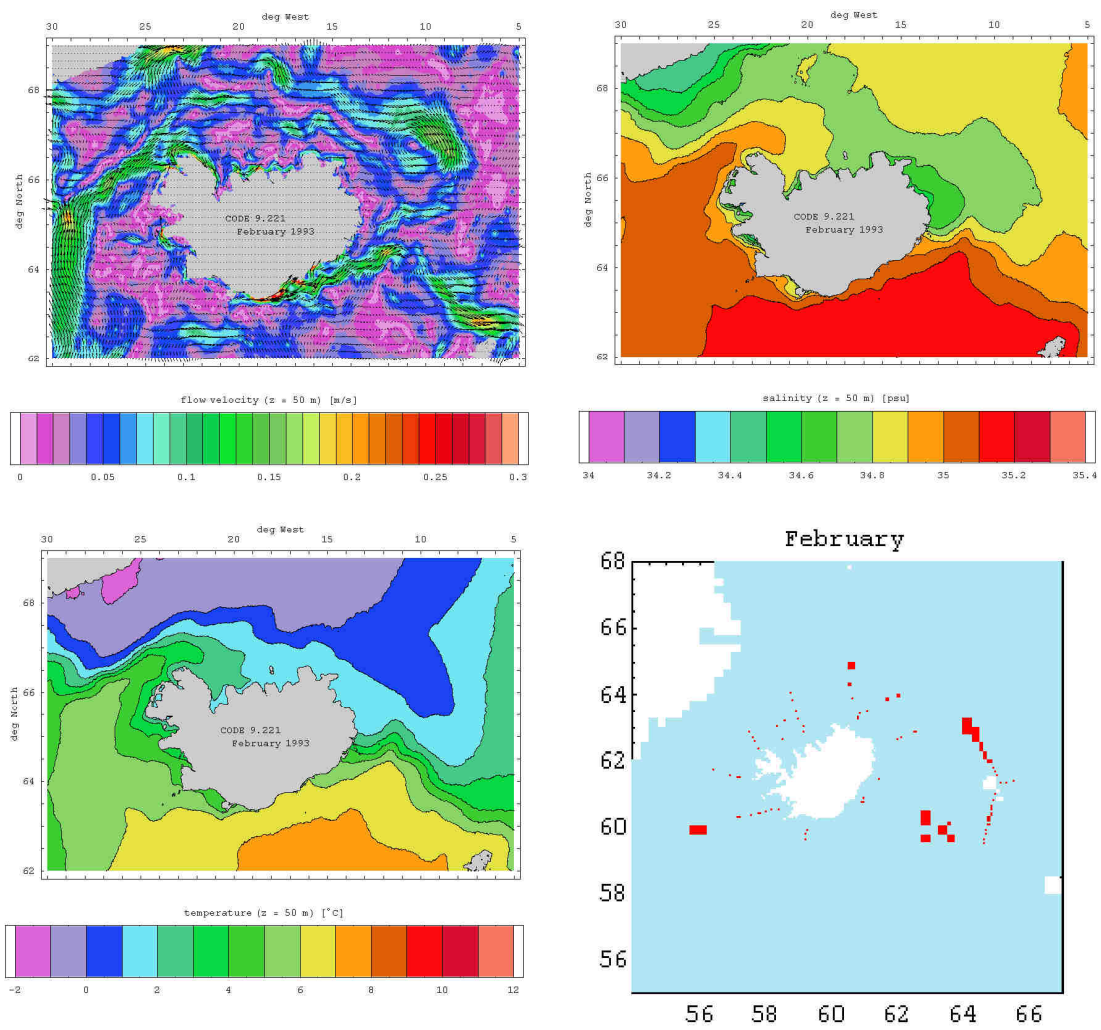


Fig. 2.14.: Monthly mean flow, salinity and temperature fields at 50 m depth and location of used CTD profiles – February 1993.



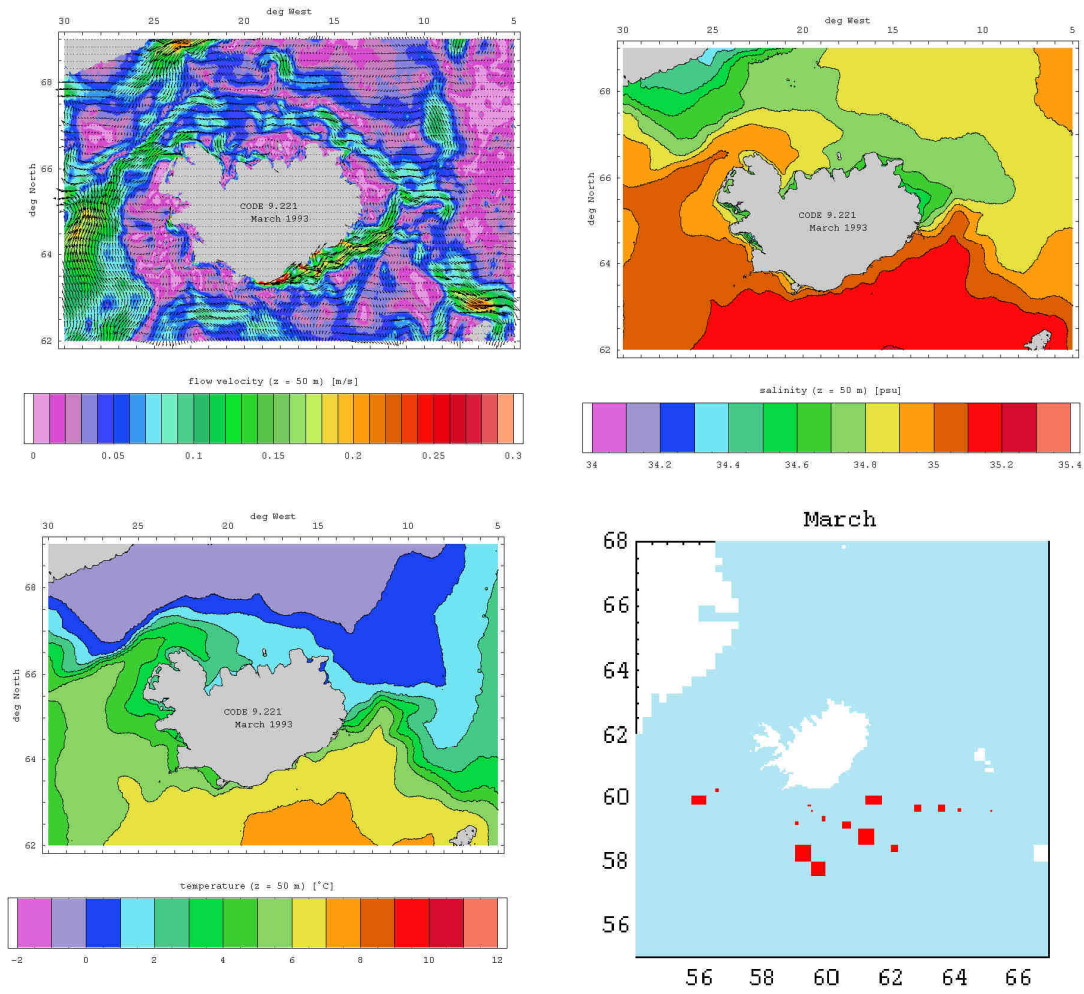


Fig. 2.15.: Monthly mean flow, salinity and temperature fields at 50 m depth and location of used CTD profiles – March 1993.

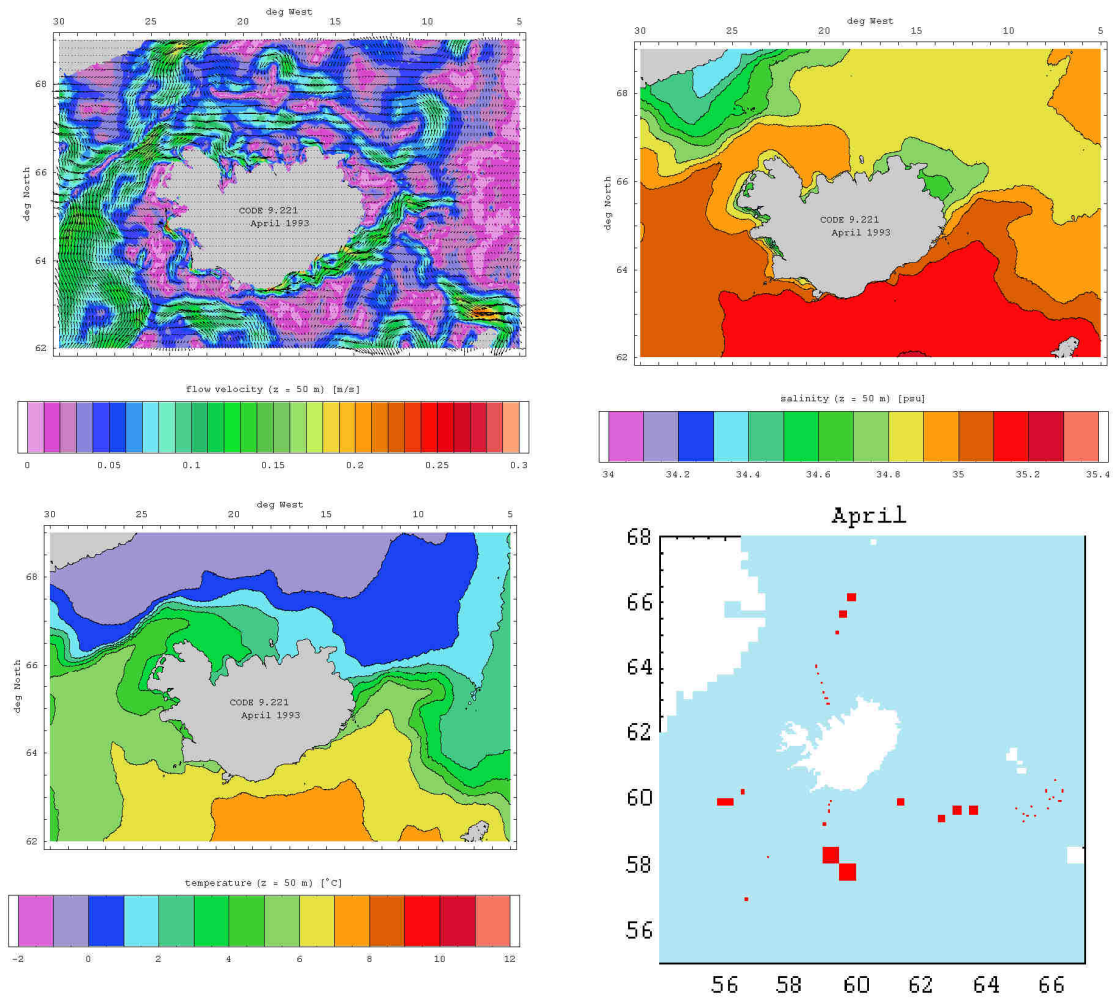


Fig. 2.16.: Monthly mean flow, salinity and temperature fields at 50 m depth and location of used CTD profiles – April 1993.

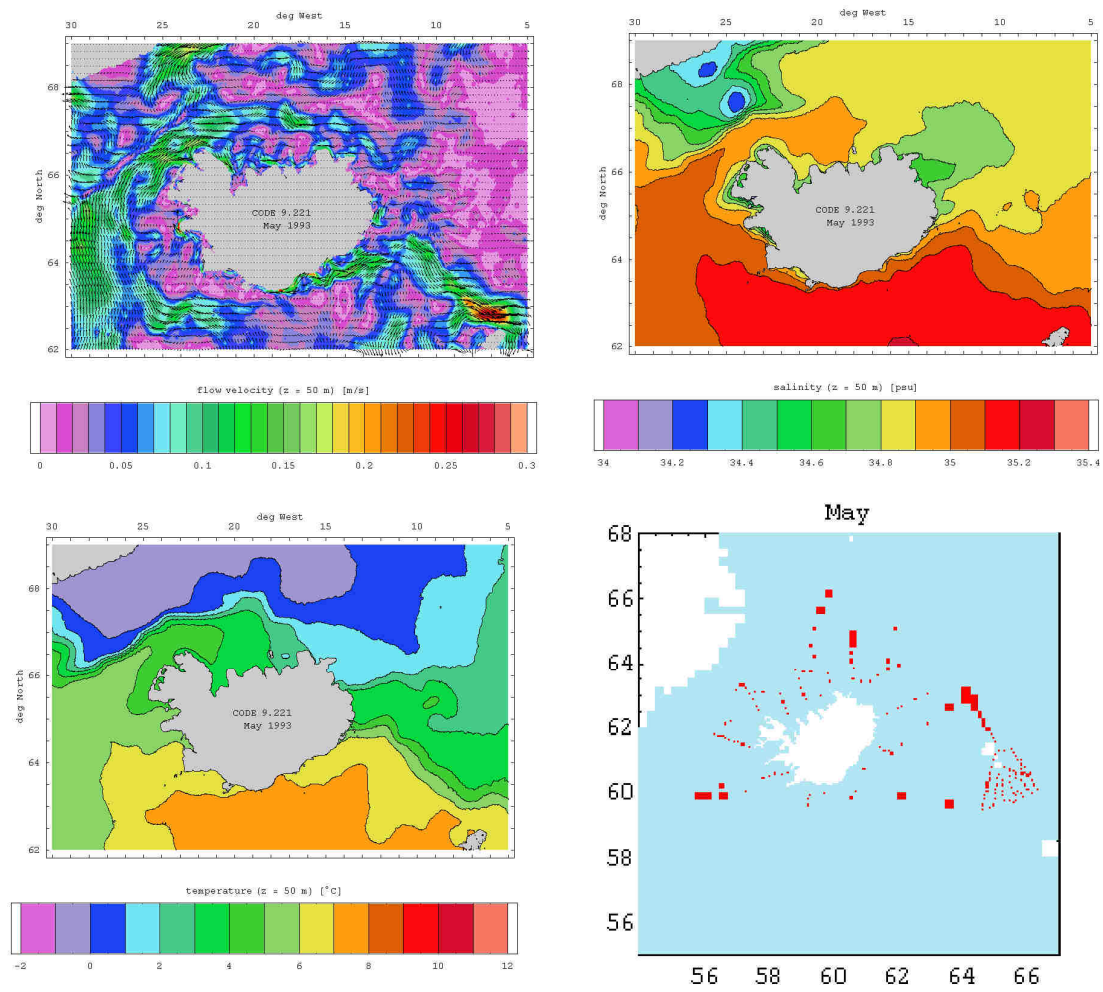


Fig. 2.17.: Monthly mean flow, salinity and temperature fields at 50 m depth and location of used CTD profiles – April 1993.

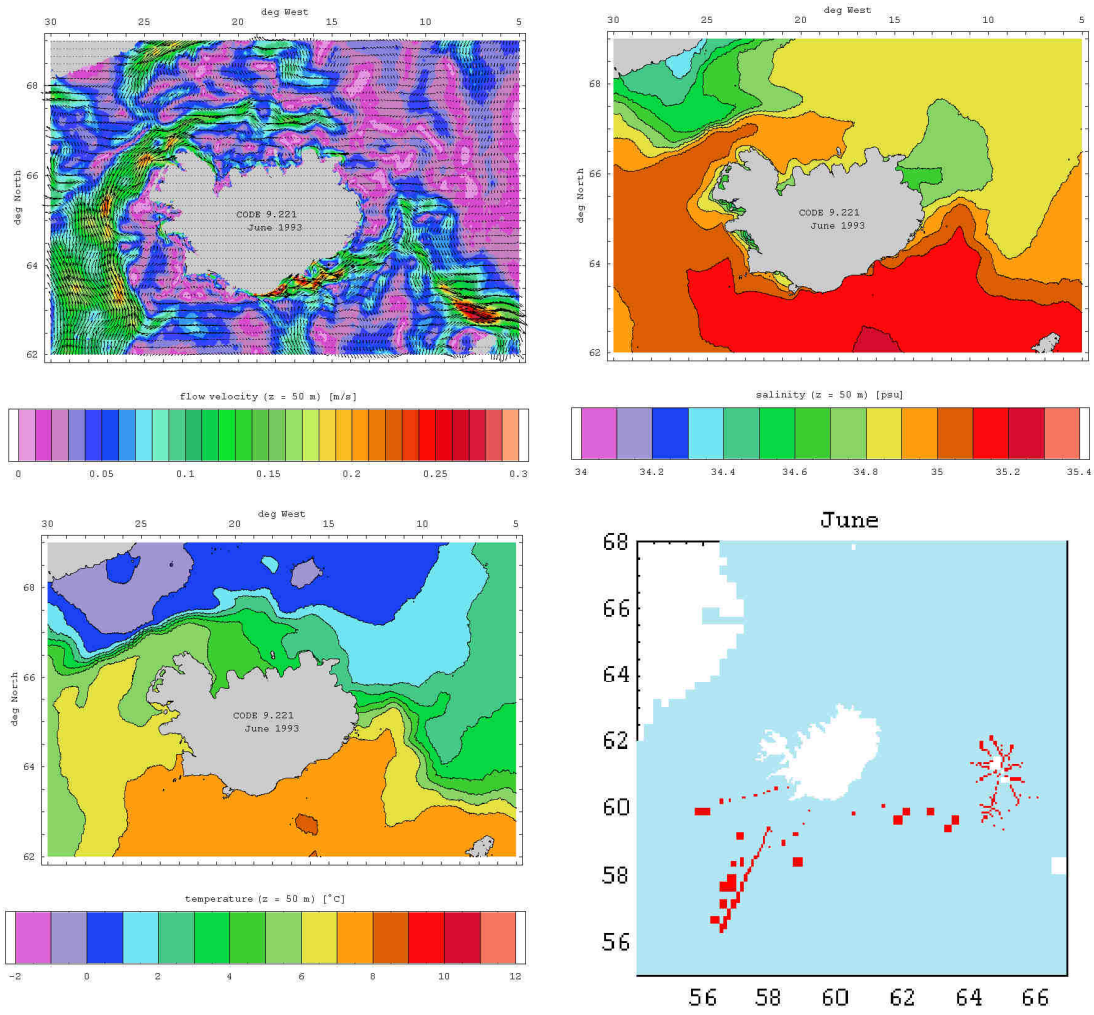


Fig. 2.18.: Monthly mean flow, salinity and temperature fields at 50 m depth and location of used CTD profiles – June 1993.

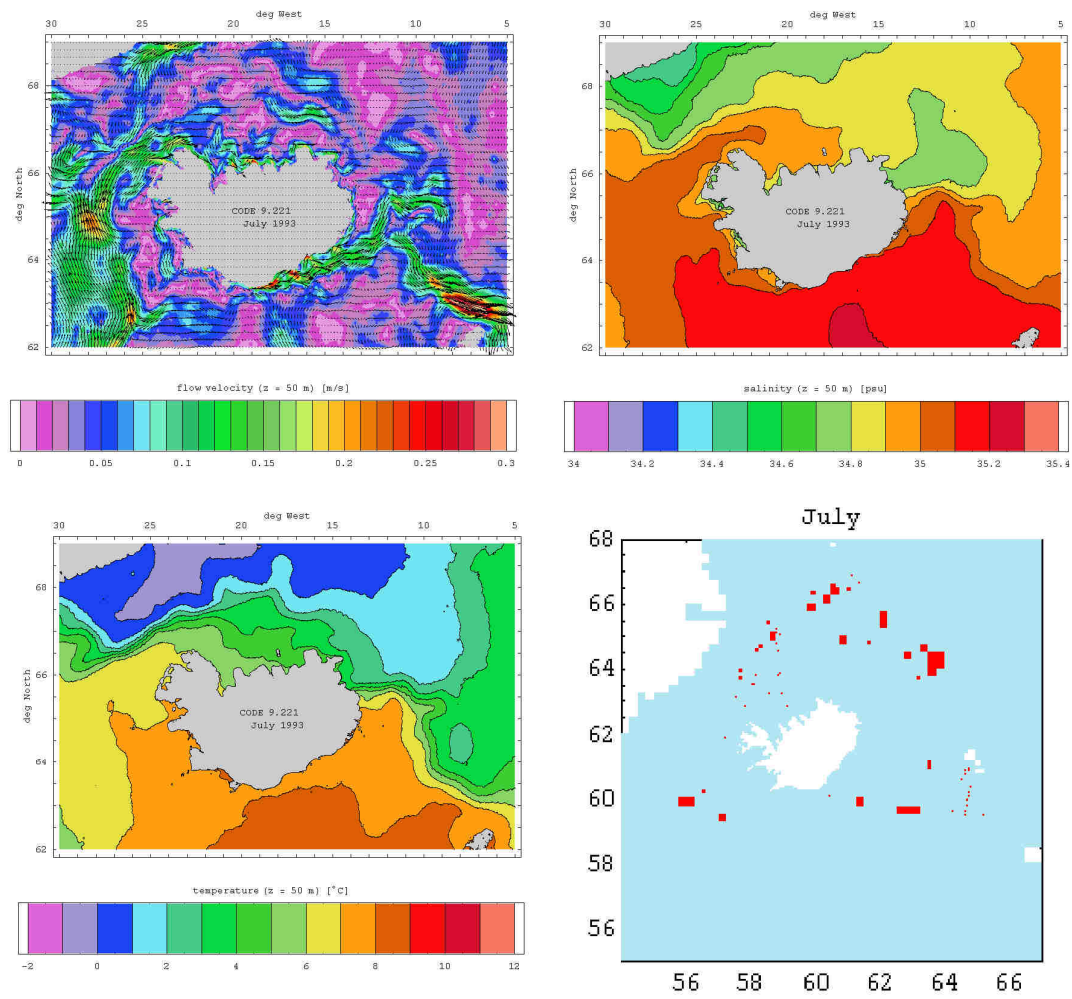


Fig. 2.19.: Monthly mean flow, salinity and temperature fields at 50 m depth and location of used CTD profiles – July 1993.



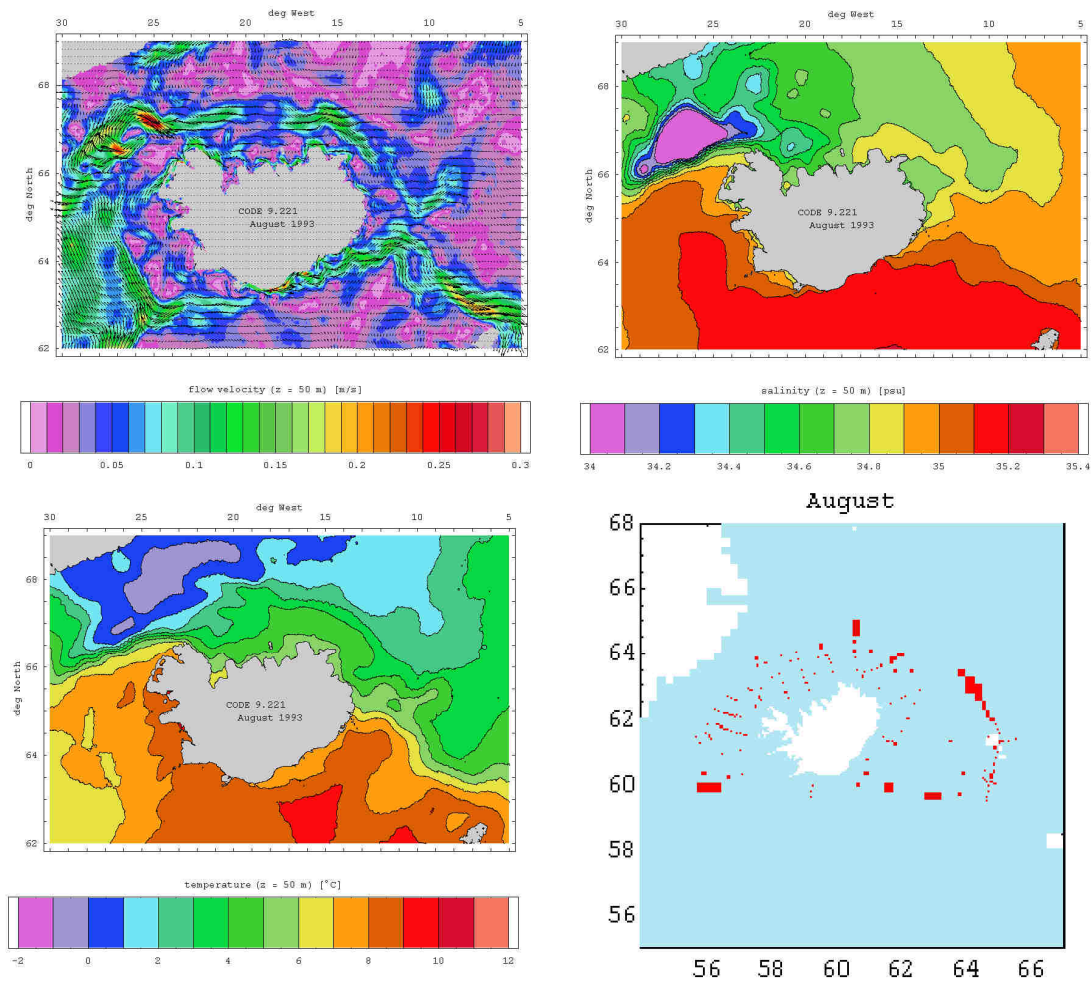


Fig. 2.20.: Monthly mean flow, salinity and temperature fields at 50 m depth and location of used CTD profiles – August 1993.

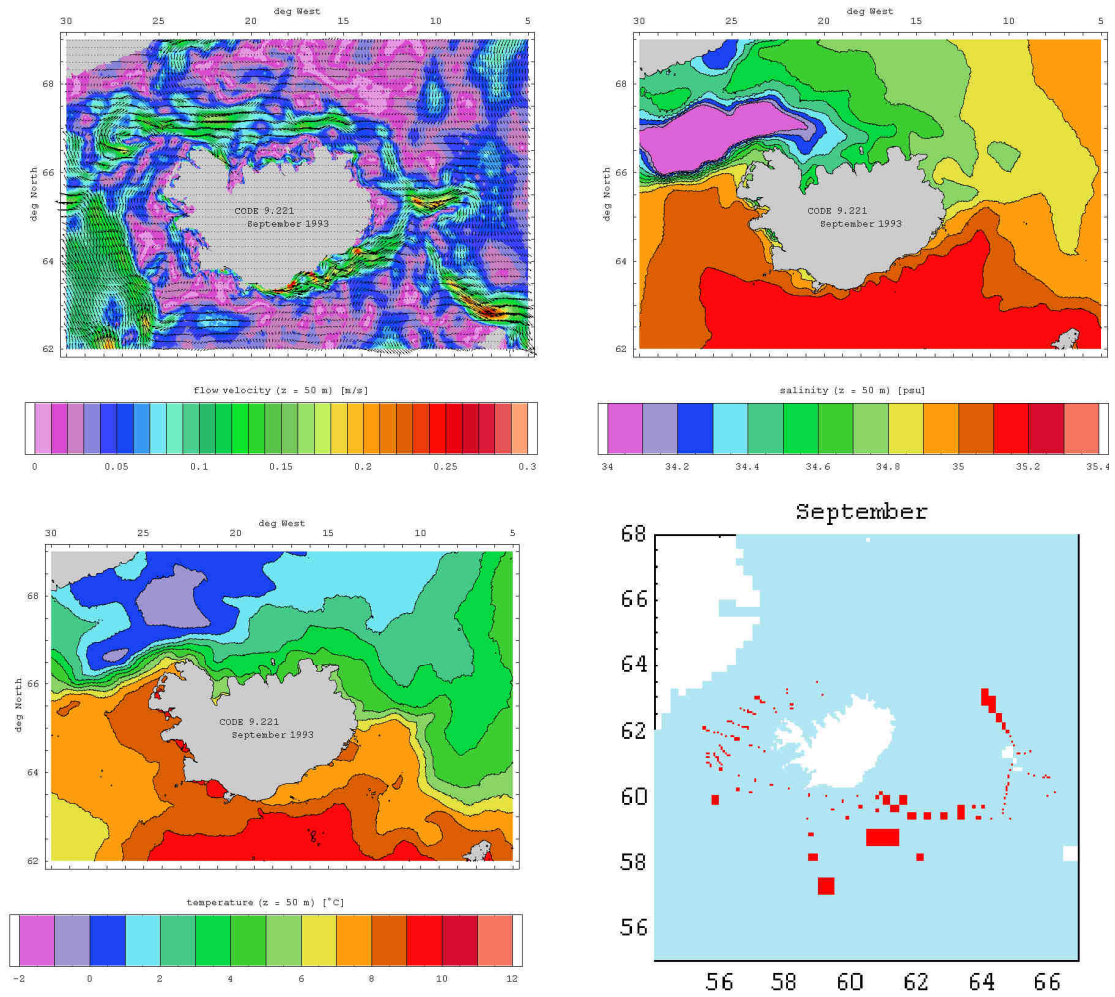


Fig. 2.21.: Monthly mean flow, salinity and temperature fields at 50 m depth and location of used CTD profiles – September 1993.

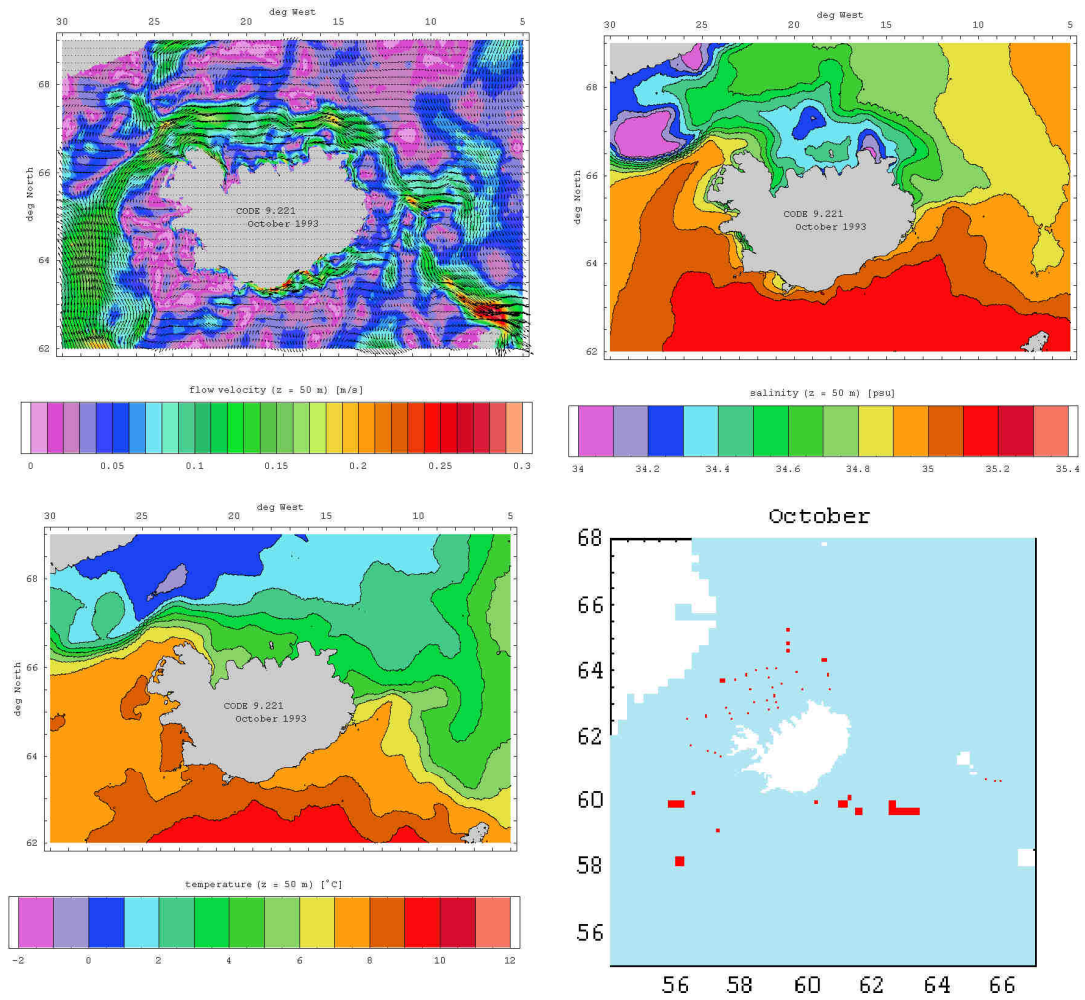


Fig. 2.22.: Monthly mean flow, salinity and temperature fields at 50 m depth and location of used CTD profiles – October 1993.



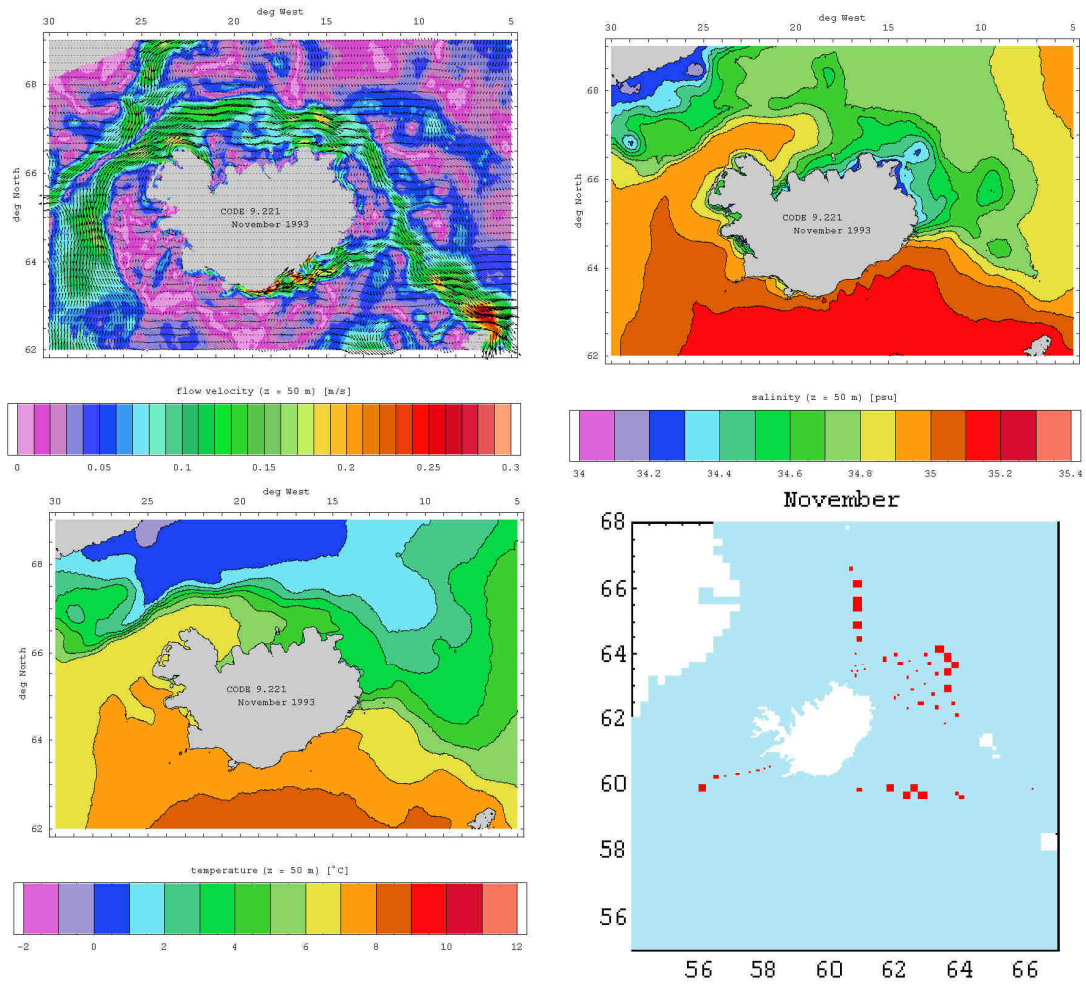


Fig. 2.23.: Monthly mean flow, salinity and temperature fields at 50 m depth and location of used CTD profiles – November 1993.

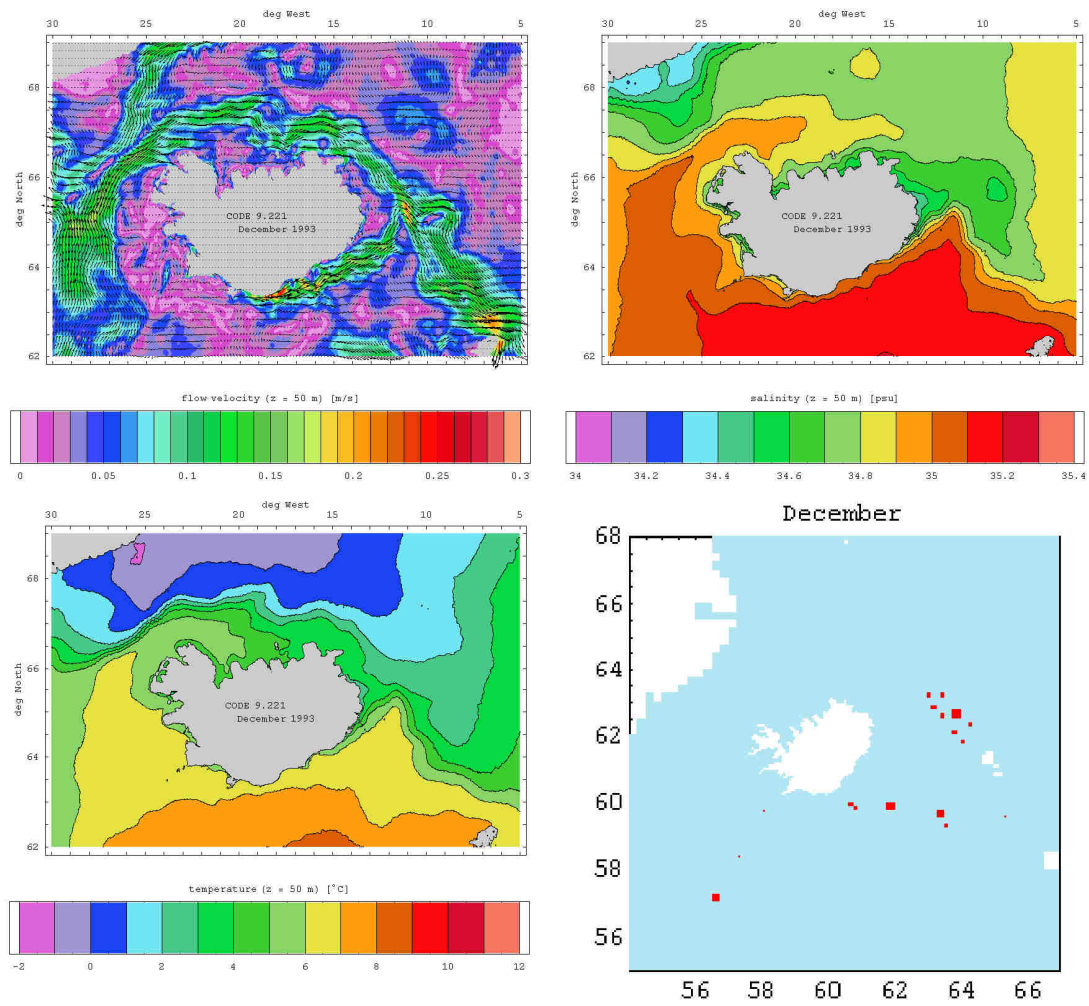


Fig. 2.24.: Monthly mean flow, salinity and temperature fields at 50 m depth and location of used CTD profiles – December 1993.

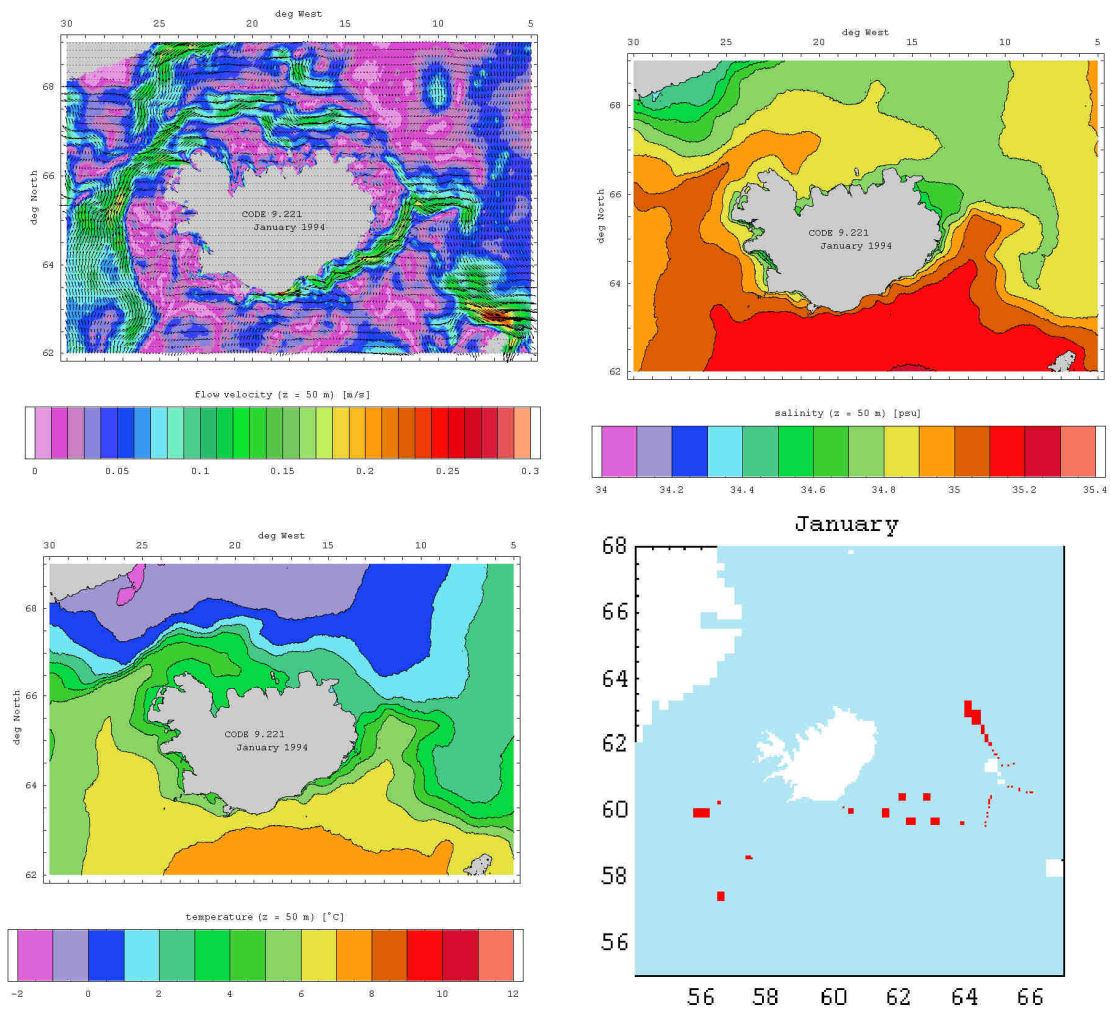


Fig. 2.25.: Monthly mean flow, salinity and temperature fields at 50 m depth and location of used CTD profiles – January 1994.

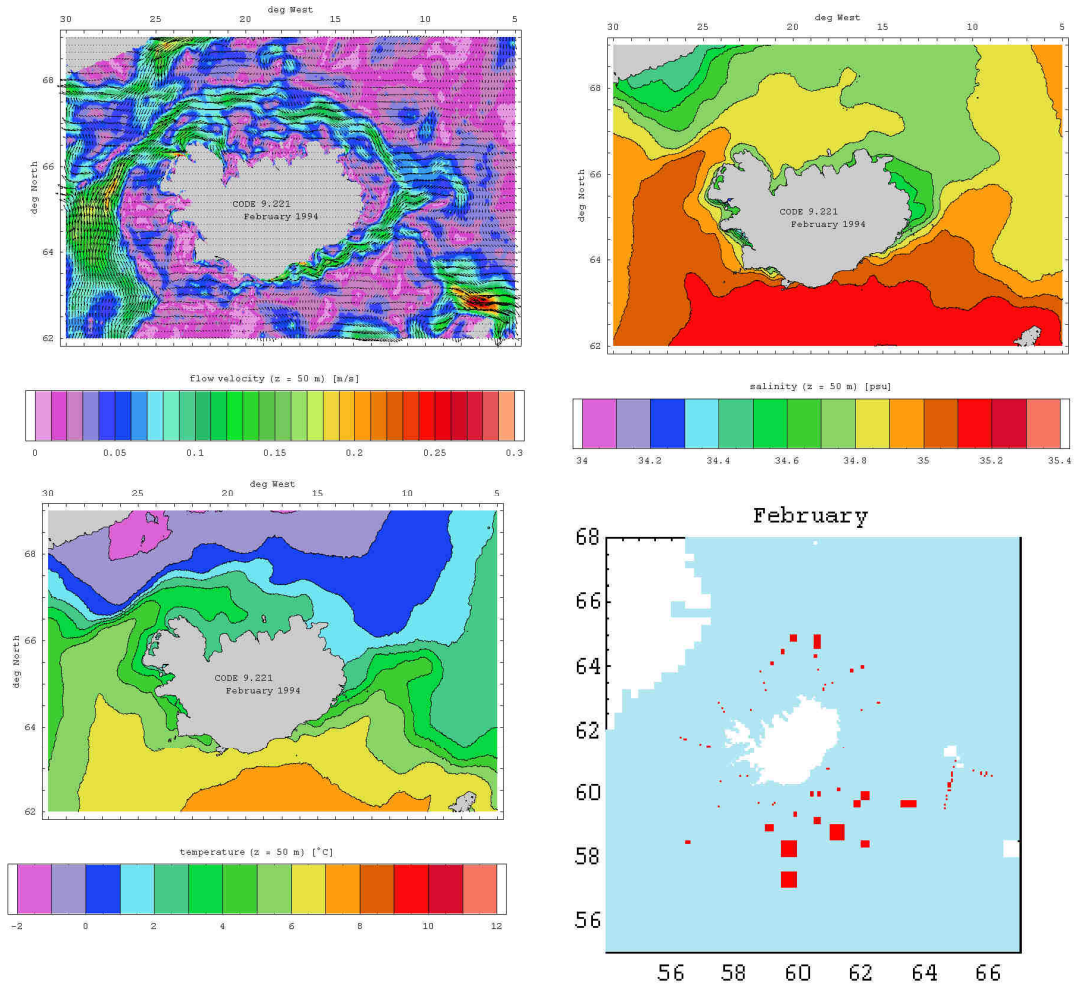


Fig. 2.26.: Monthly mean flow, salinity and temperature fields at 50 m depth and location of used CTD profiles – February 1994.

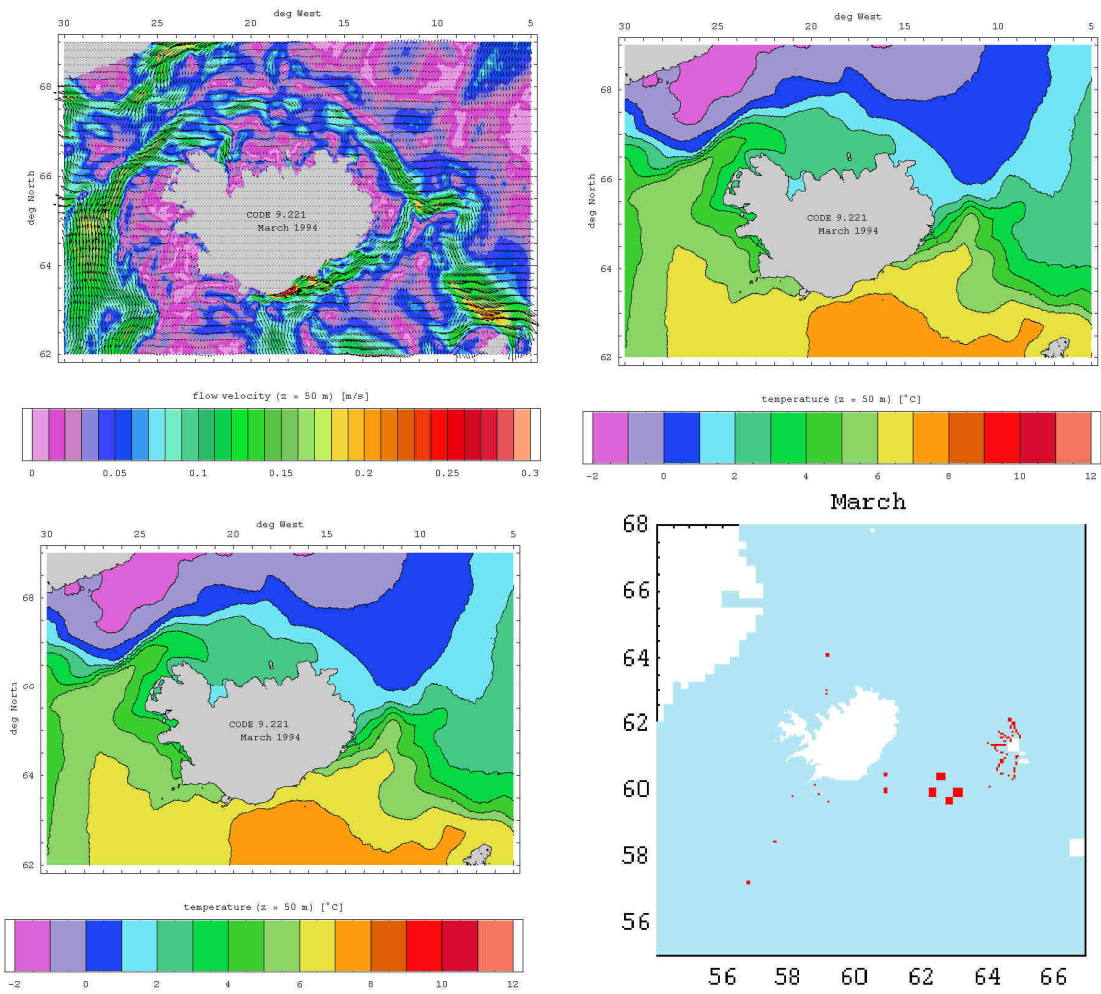


Fig. 2.27.: Monthly mean flow, salinity and temperature fields at 50 m depth and location of used CTD profiles – March 1994.



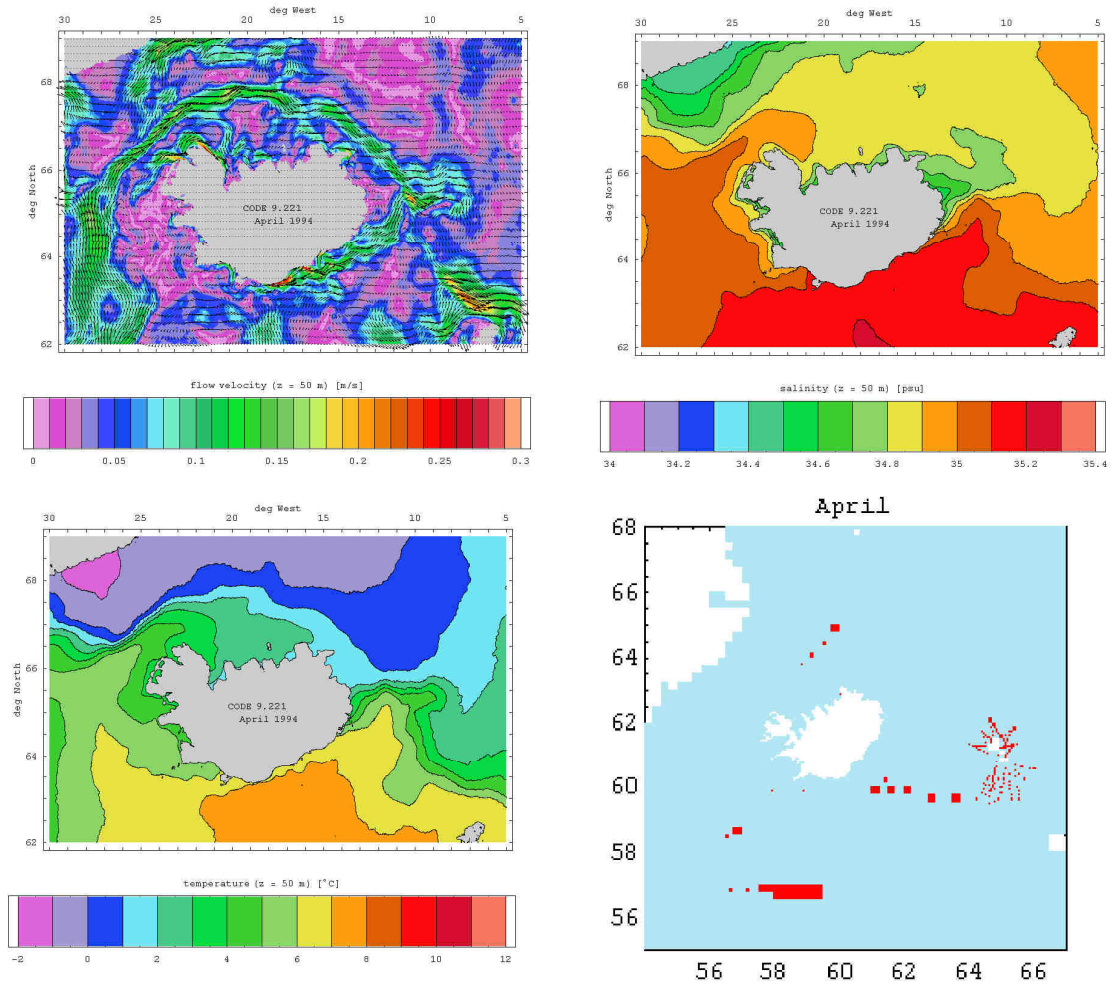


Fig. 2.28.: Monthly mean flow, salinity and temperature fields at 50 m depth and location of used CTD profiles – April 1994.

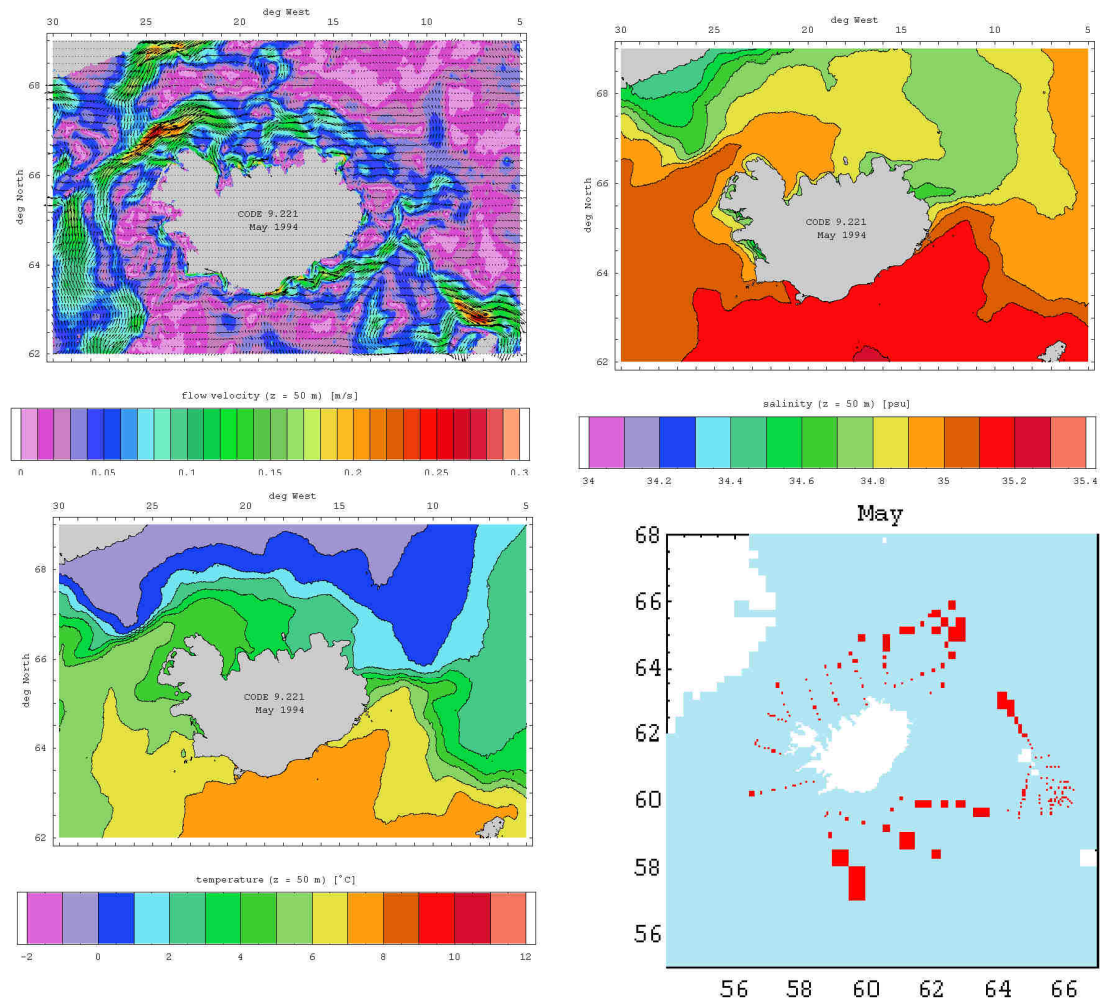


Fig. 2.29.: Monthly mean flow, salinity and temperature fields at 50 m depth and location of used CTD profiles – May 1994.

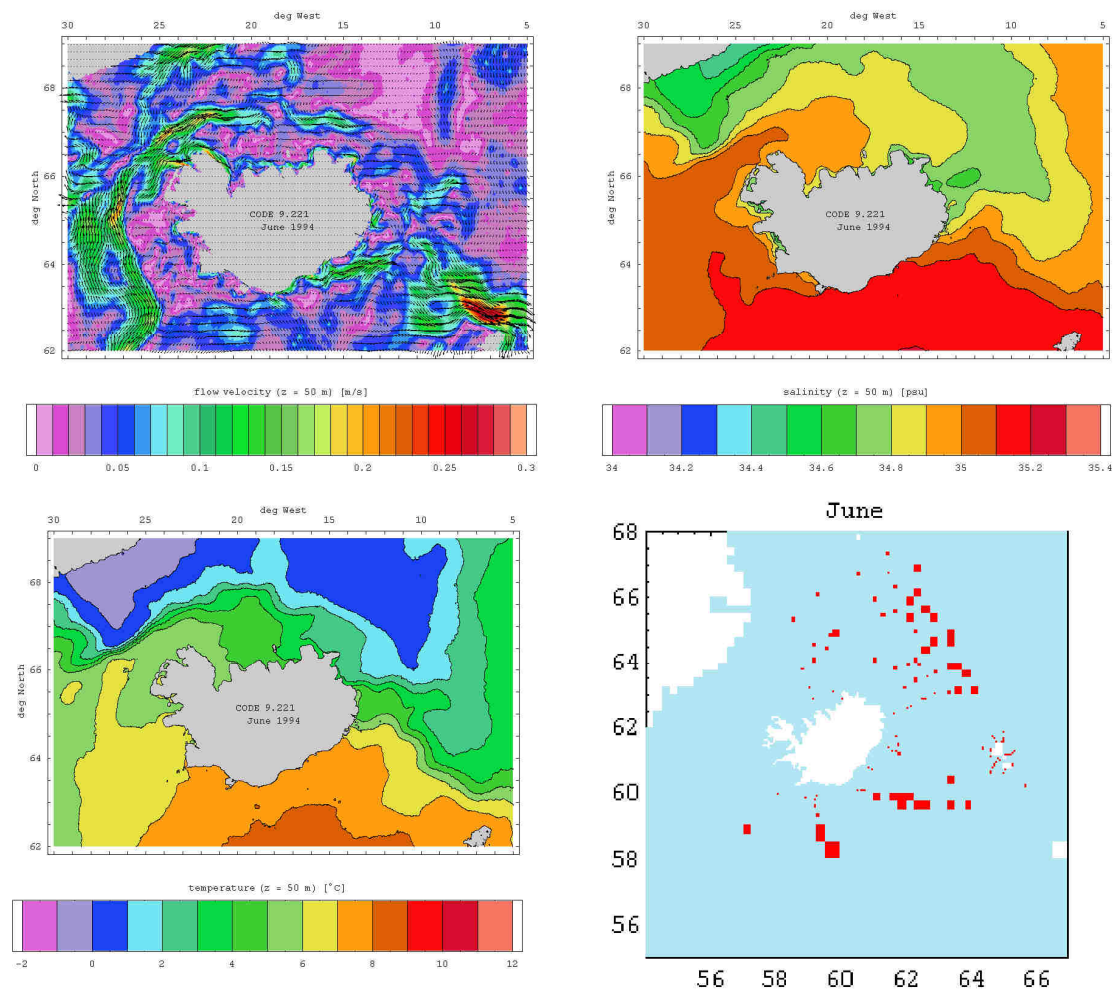


Fig. 2.30.: Monthly mean flow, salinity and temperature fields at 50 m depth and location of used CTD profiles – June 1994.



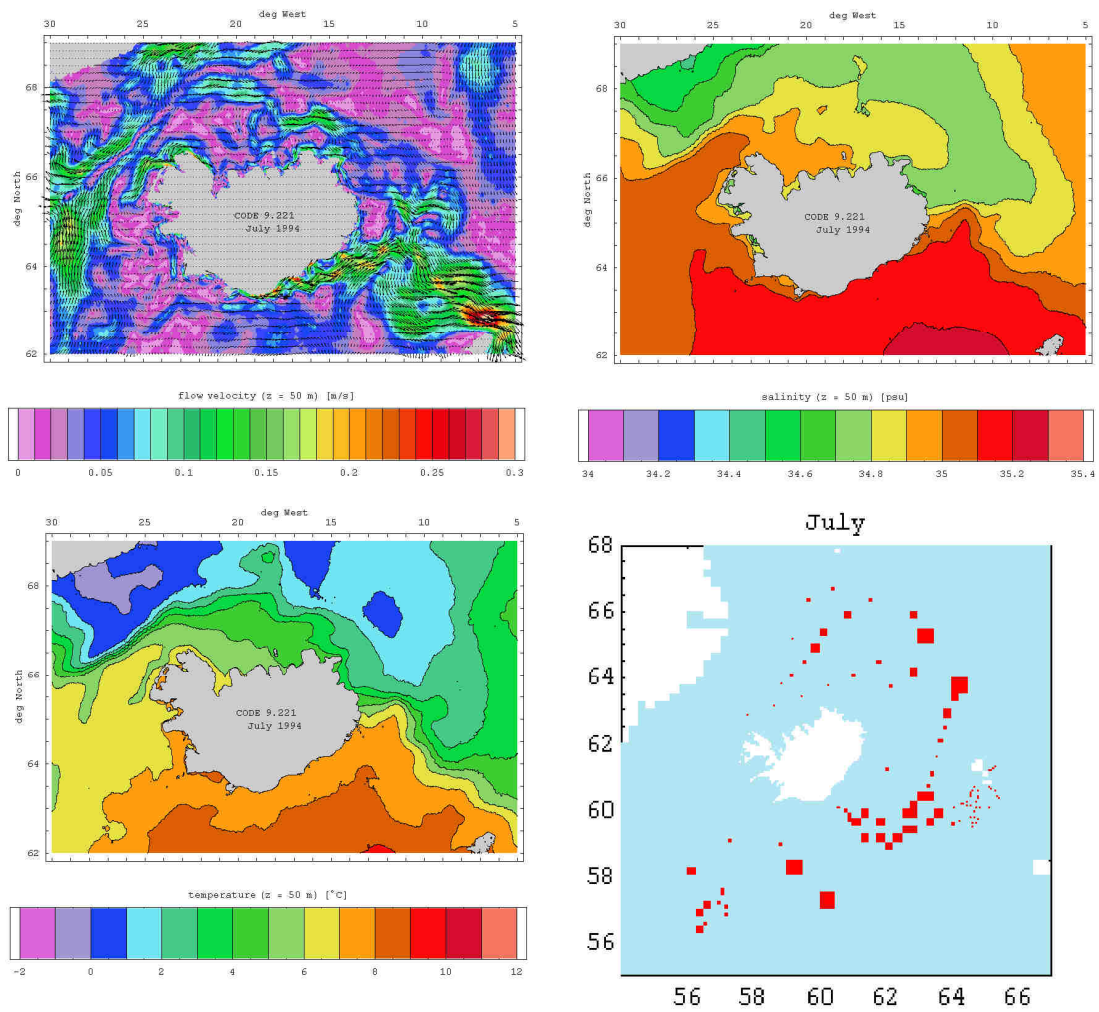


Fig. 2.31.: Monthly mean flow, salinity and temperature fields at 50 m depth and location of used CTD profiles – July 1994.

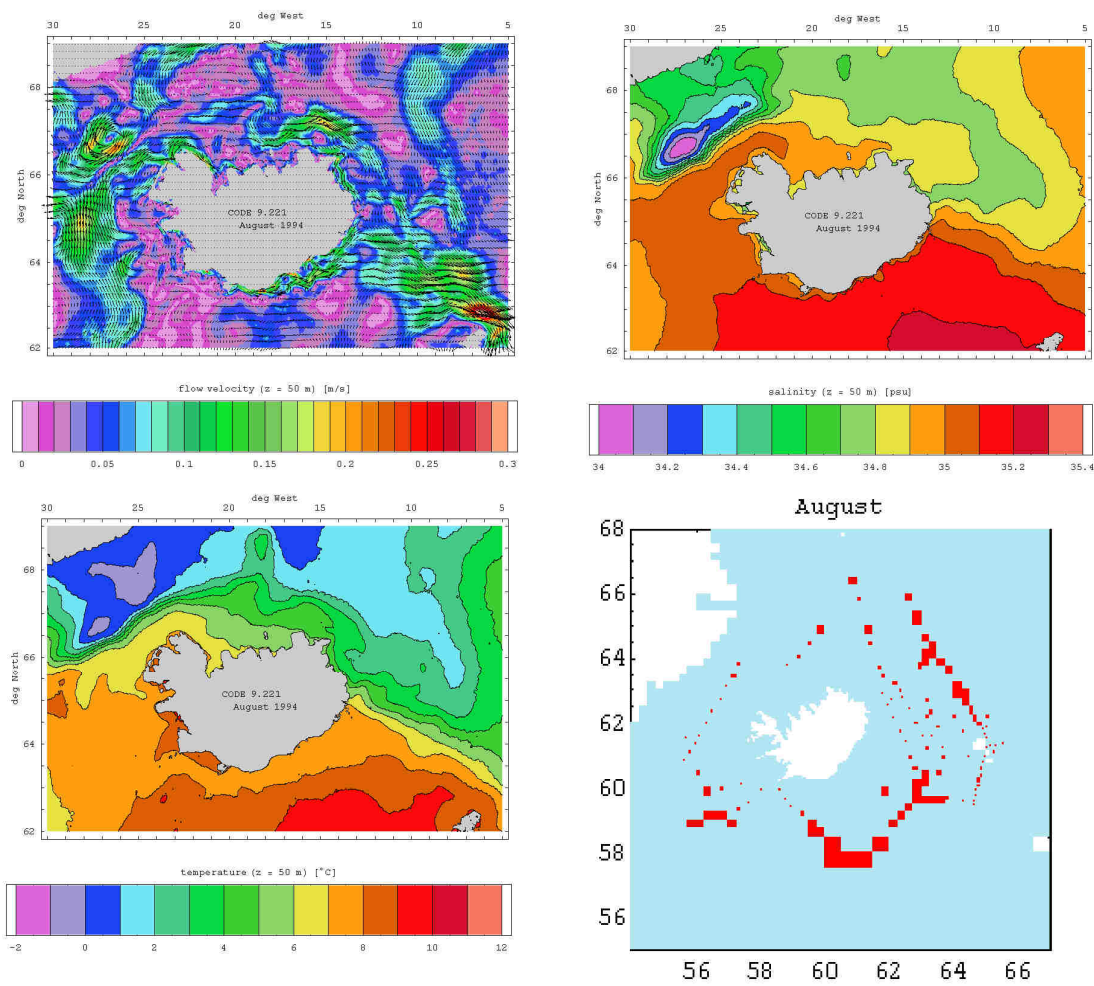


Fig. 2.32.: Monthly mean flow, salinity and temperature fields at 50 m depth and location of used CTD profiles – August 1994.

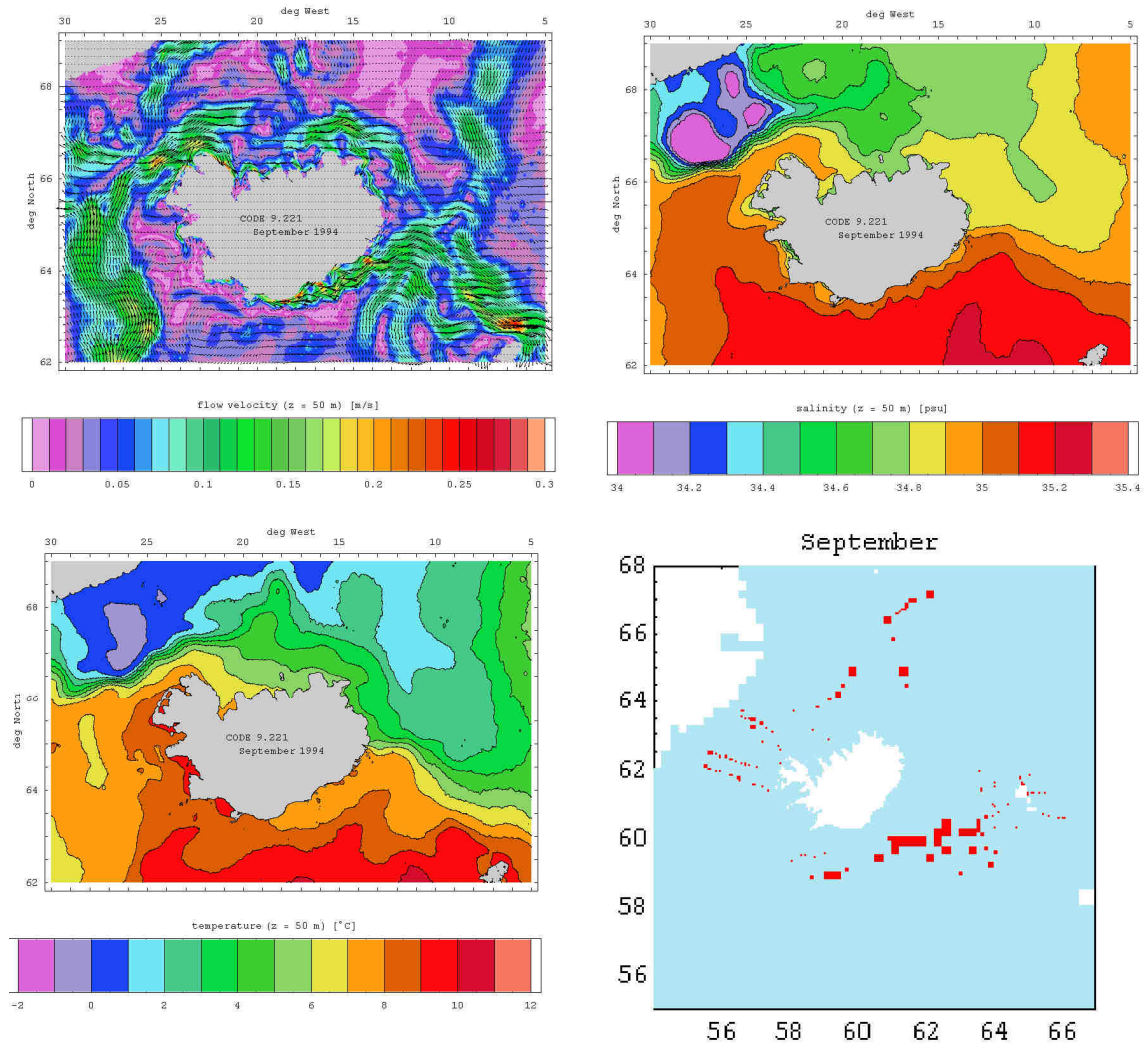


Fig. 2.33.: Monthly mean flow, salinity and temperature fields at 50 m depth and location of used CTD profiles – September 1994.

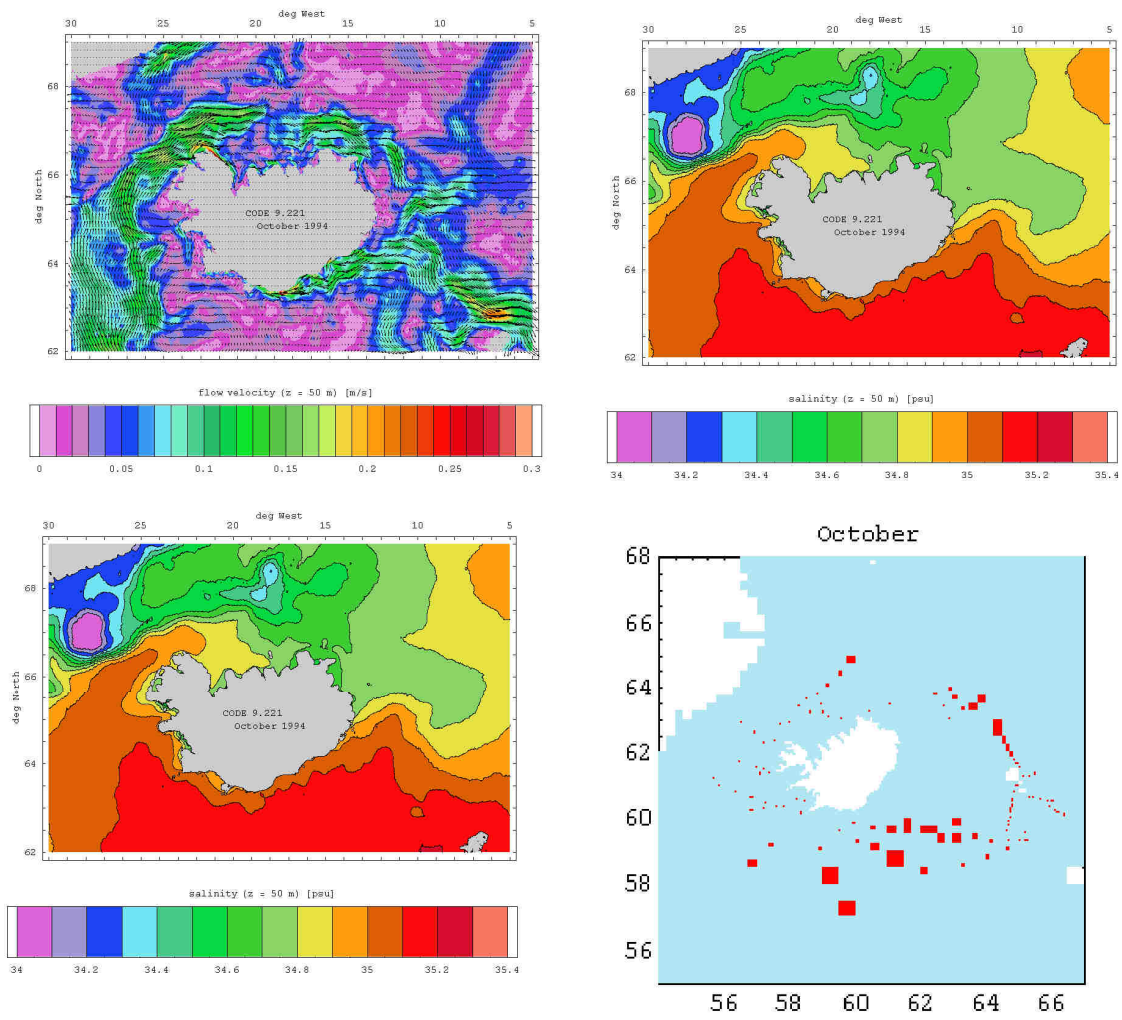


Fig. 2.34.: Monthly mean flow, salinity and temperature fields at 50 m depth and location of used CTD profiles – October 1994.



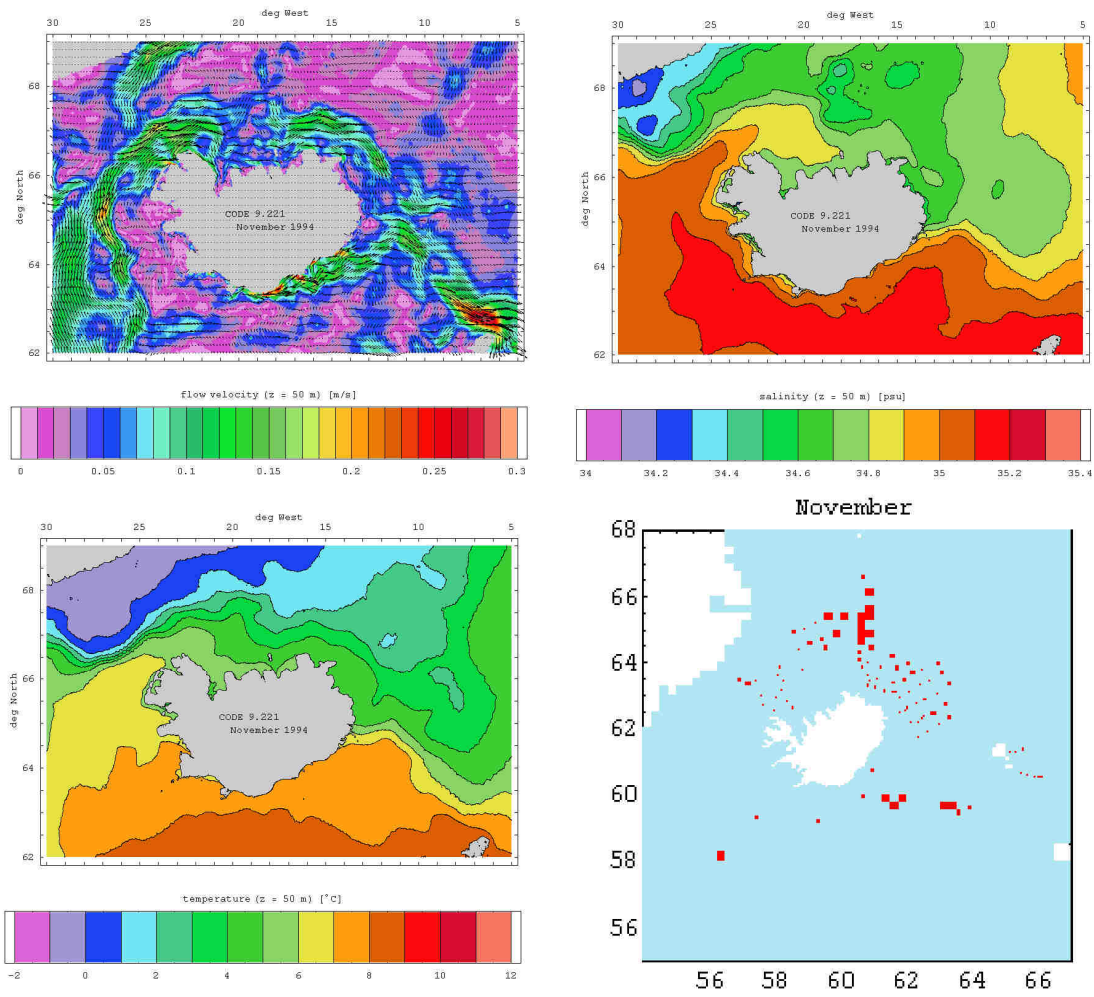


Fig. 2.35.: Monthly mean flow, salinity and temperature fields at 50 m depth and location of used CTD profiles – November 1994.

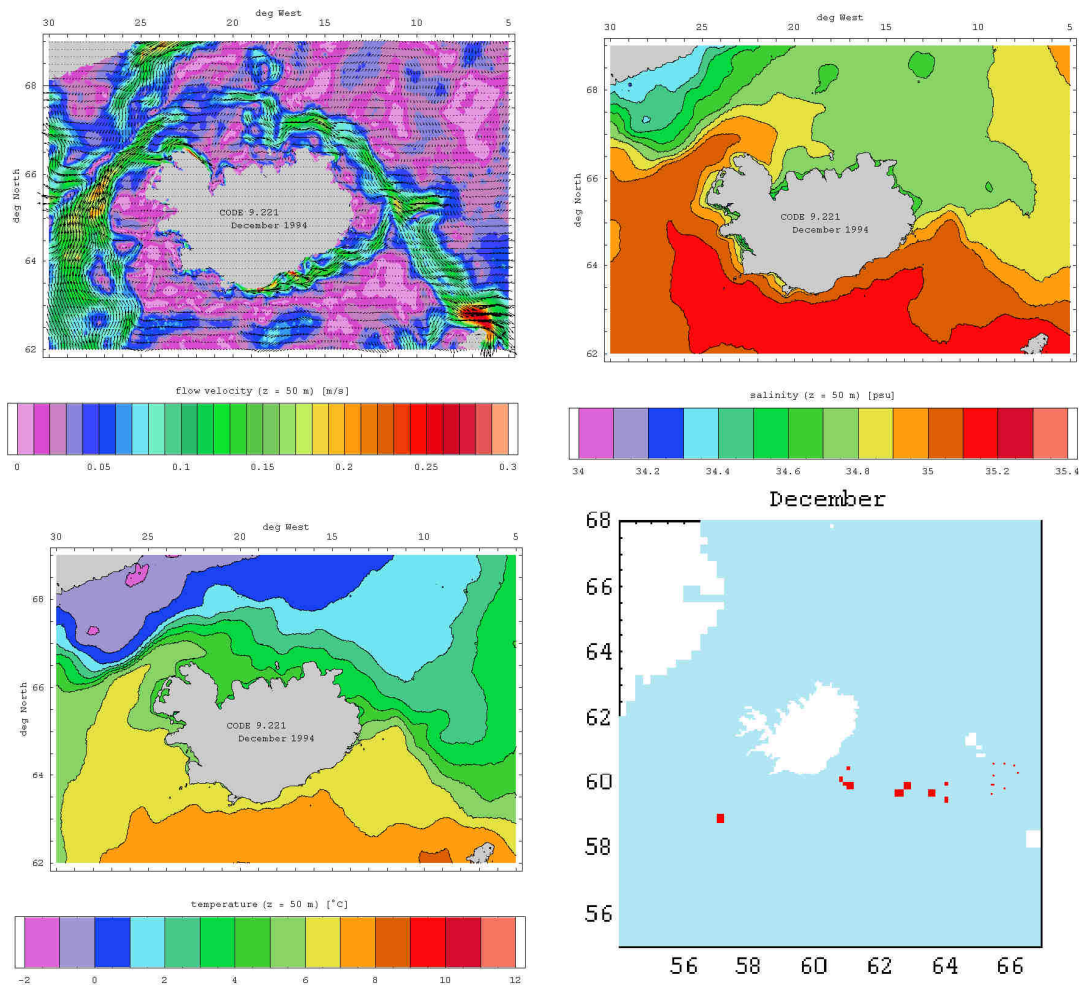


Fig. 2.36.: Monthly mean flow, salinity and temperature fields at 50 m depth and location of used CTD profiles – December 1994.

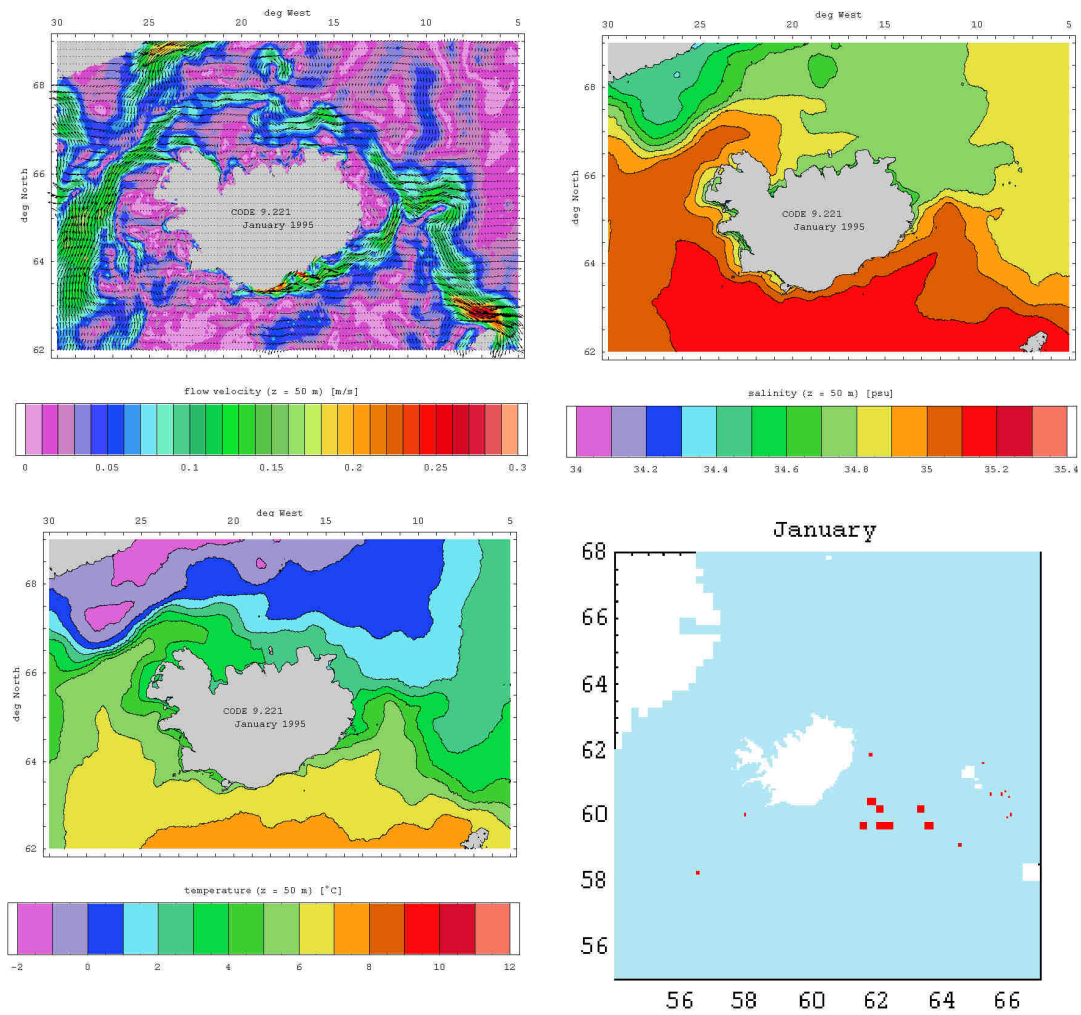


Fig. 2.37.: Monthly mean flow, salinity and temperature fields at 50 m depth and location of used CTD profiles – January 1995.



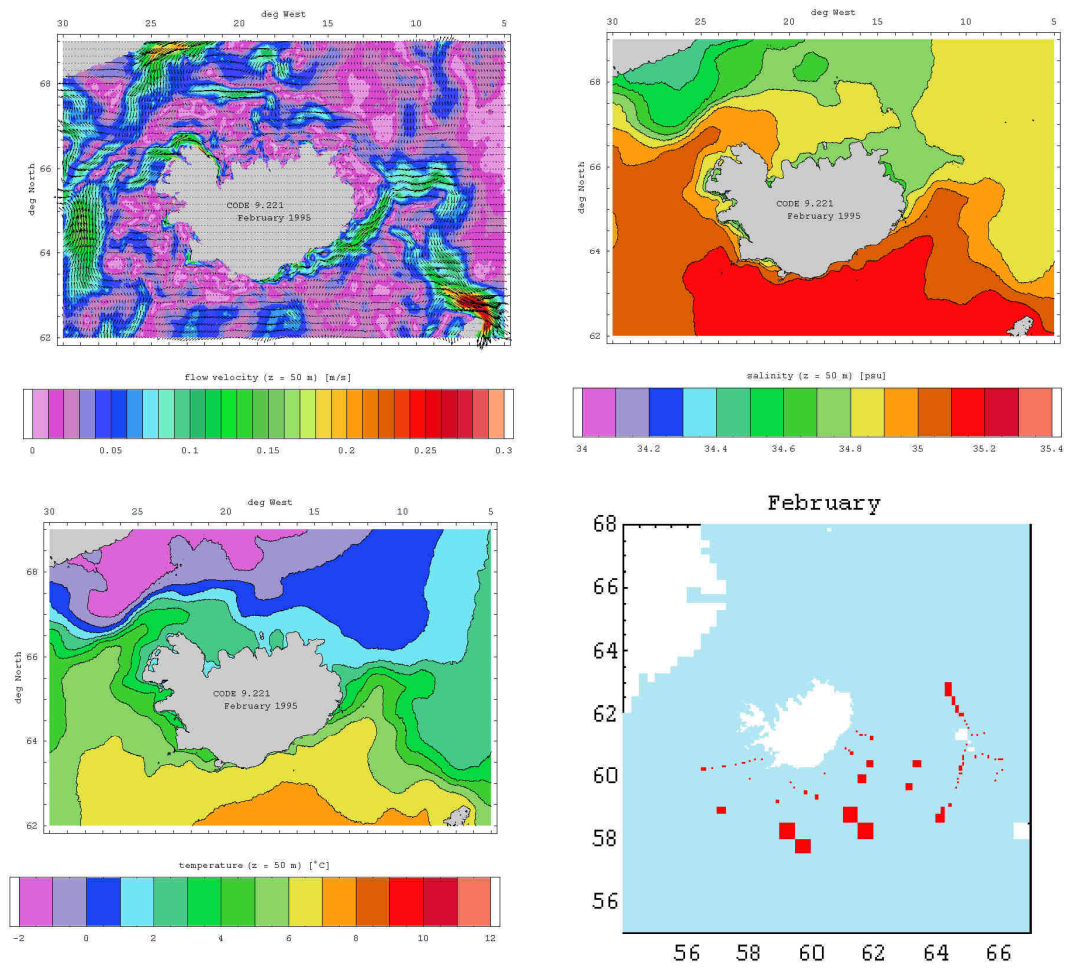


Fig. 2.38.: Monthly mean flow, salinity and temperature fields at 50 m depth and location of used CTD profiles – February 1995.

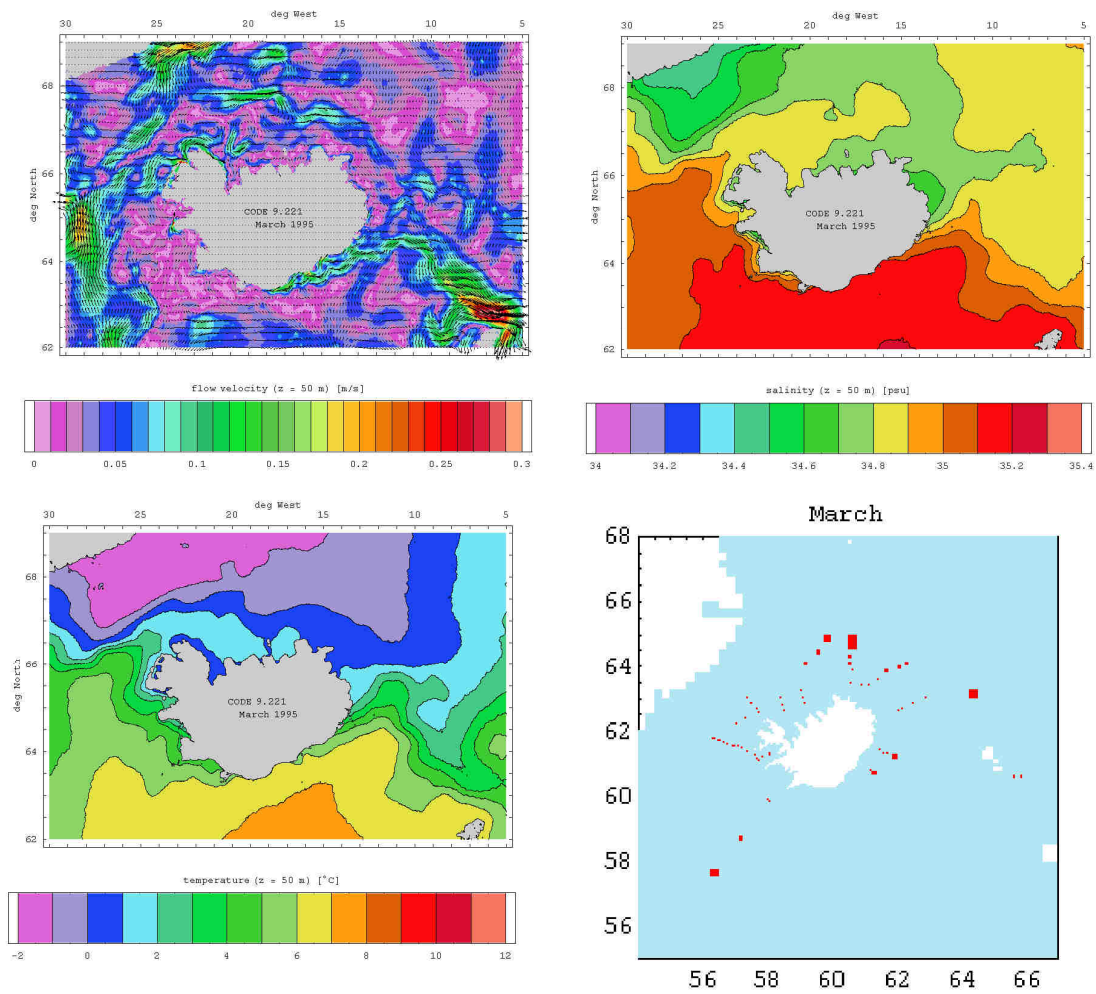


Fig. 2.39.: Monthly mean flow, salinity and temperature fields at 50 m depth and location of used CTD profiles – March 1995.

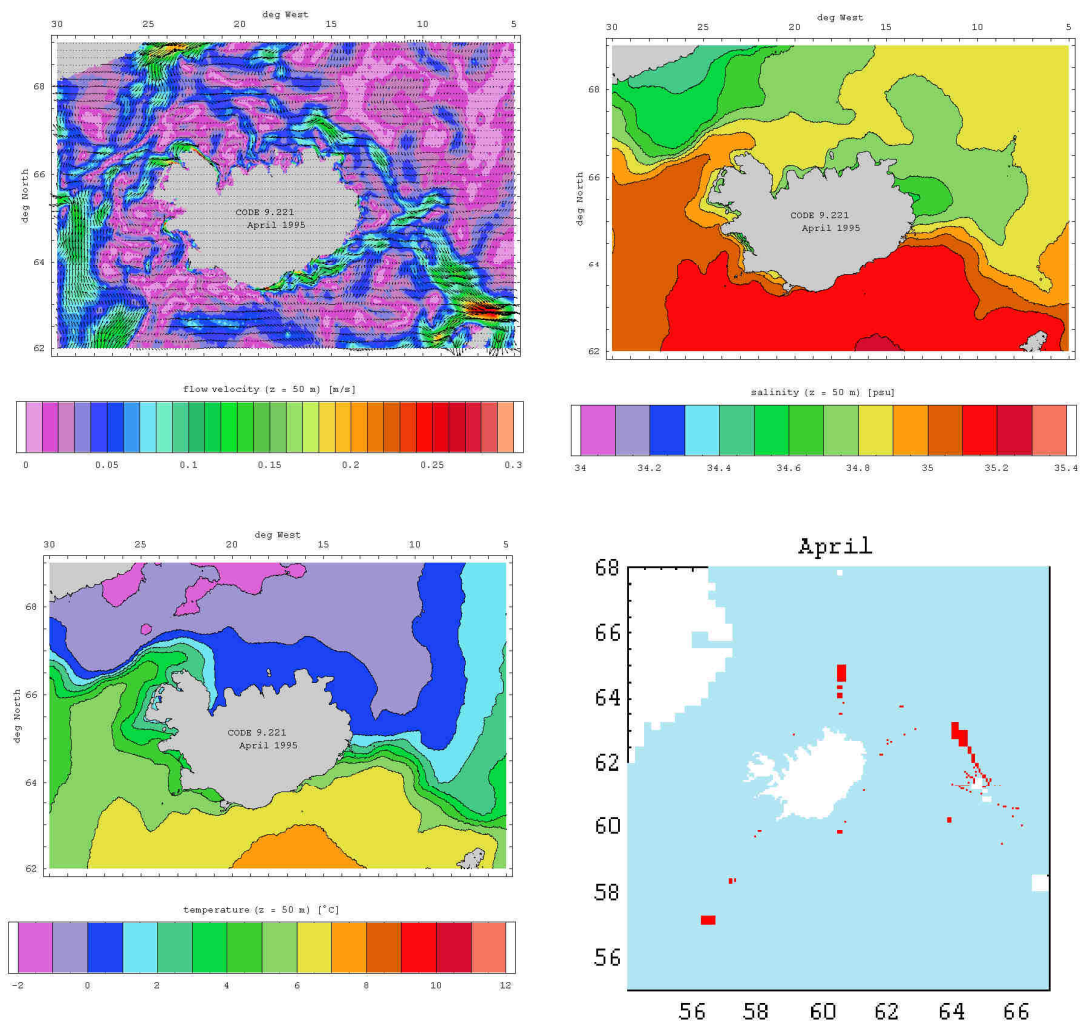


Fig. 2.40.: Monthly mean flow, salinity and temperature fields at 50 m depth and location of used CTD profiles – April 1995.

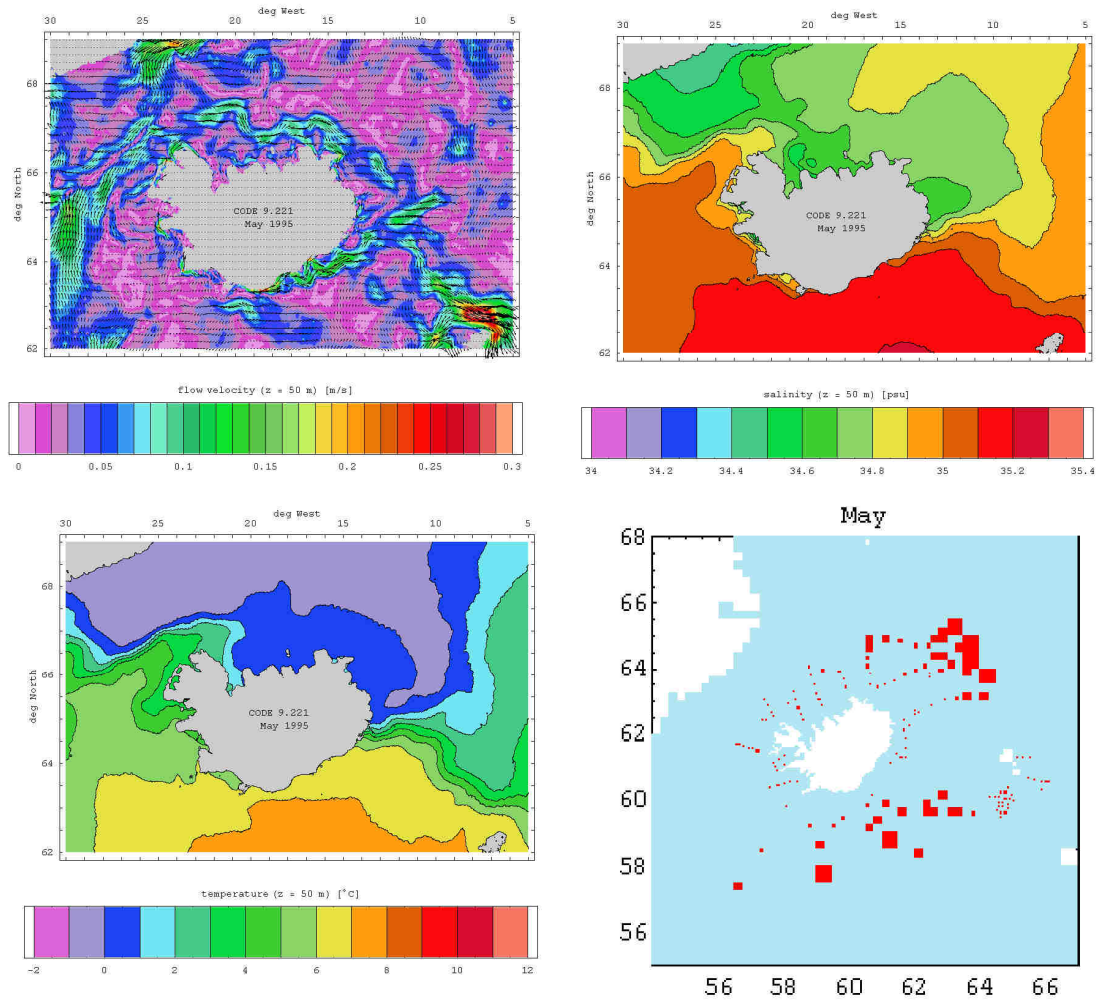


Fig. 2.41.: Monthly mean flow, salinity and temperature fields at 50 m depth and location of used CTD profiles – May 1995.

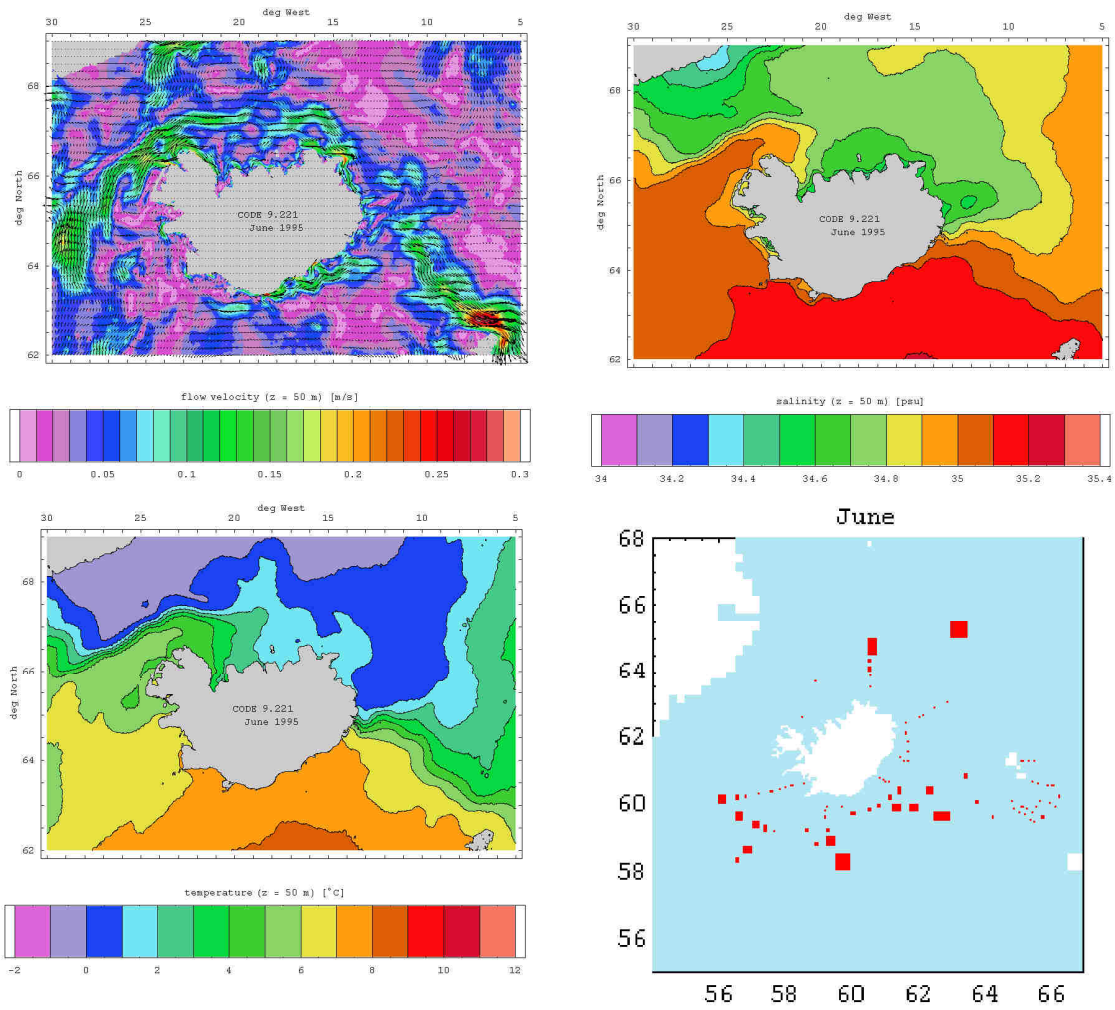


Fig. 2.42.: Monthly mean flow, salinity and temperature fields at 50 m depth and location of used CTD profiles – June 1995.



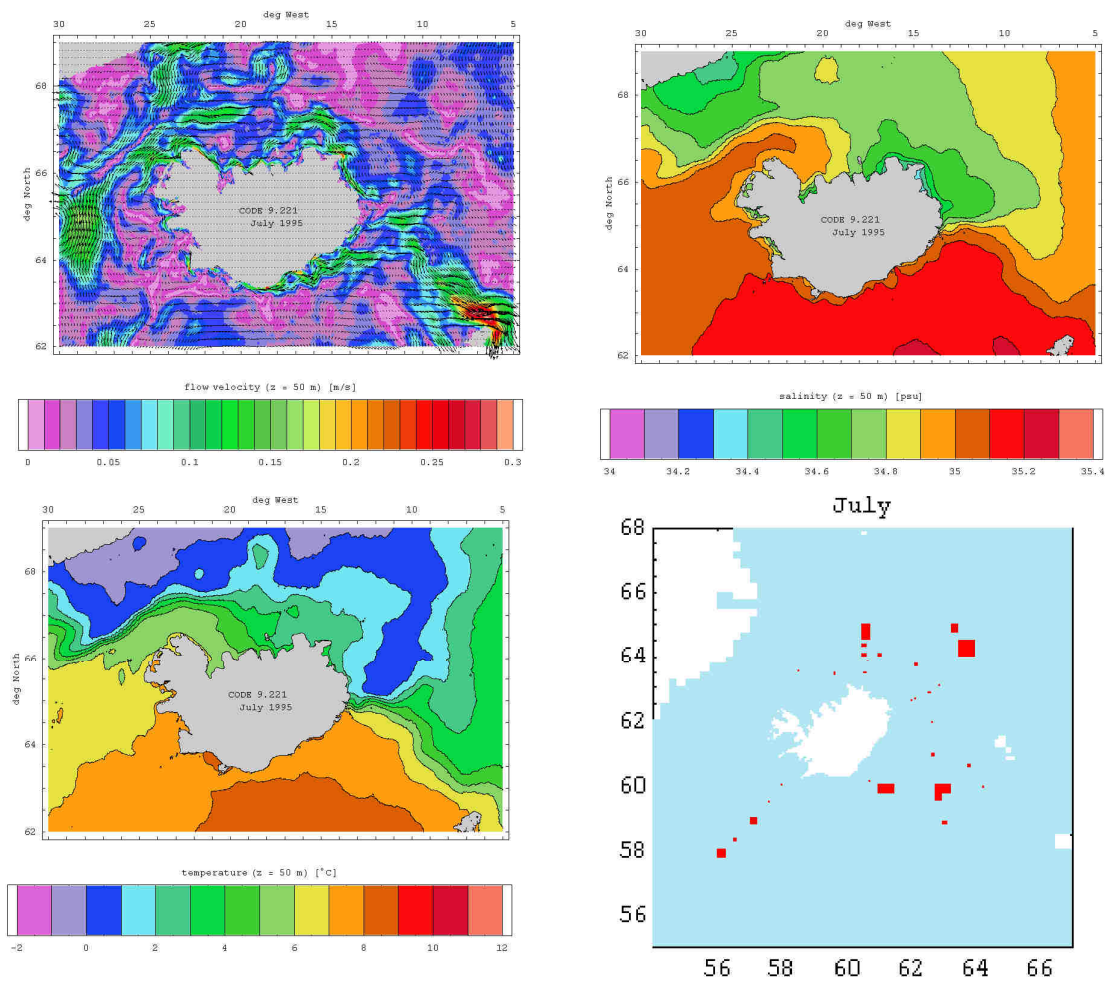


Fig. 2.43.: Monthly mean flow, salinity and temperature fields at 50 m depth and location of used CTD profiles – July 1995.

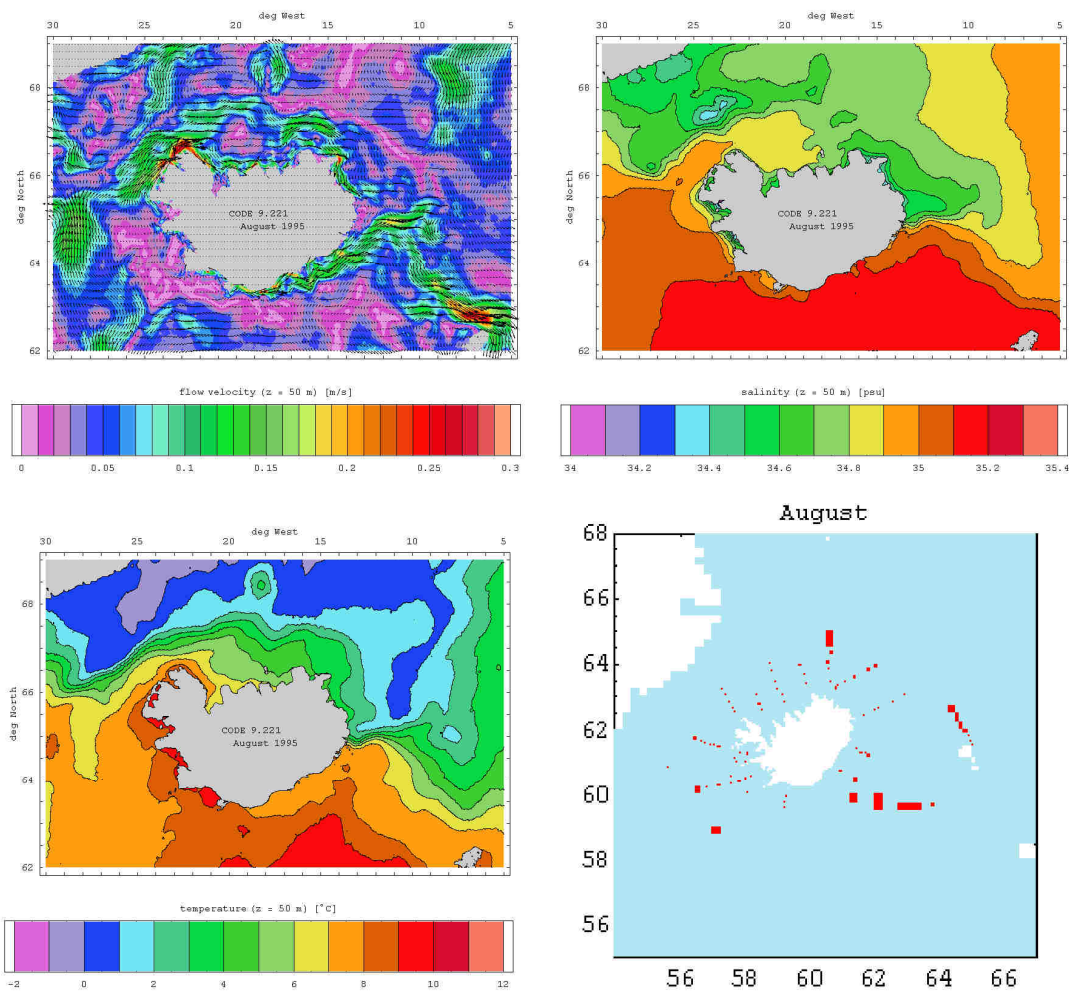


Fig. 2.44.: Monthly mean flow, salinity and temperature fields at 50 m depth and location of used CTD profiles – August 1995.



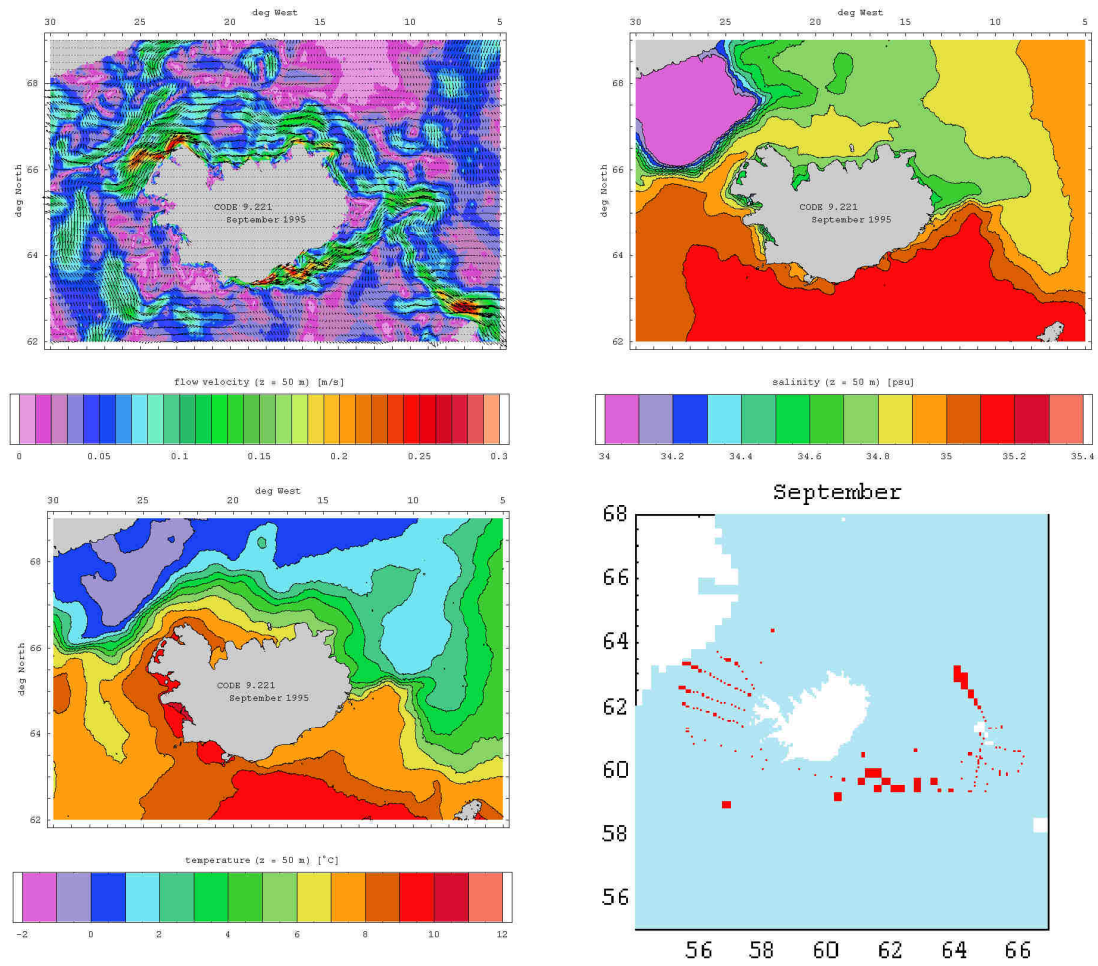


Fig. 2.45.: Monthly mean flow, salinity and temperature fields at 50 m depth and location of used CTD profiles – September 1995.

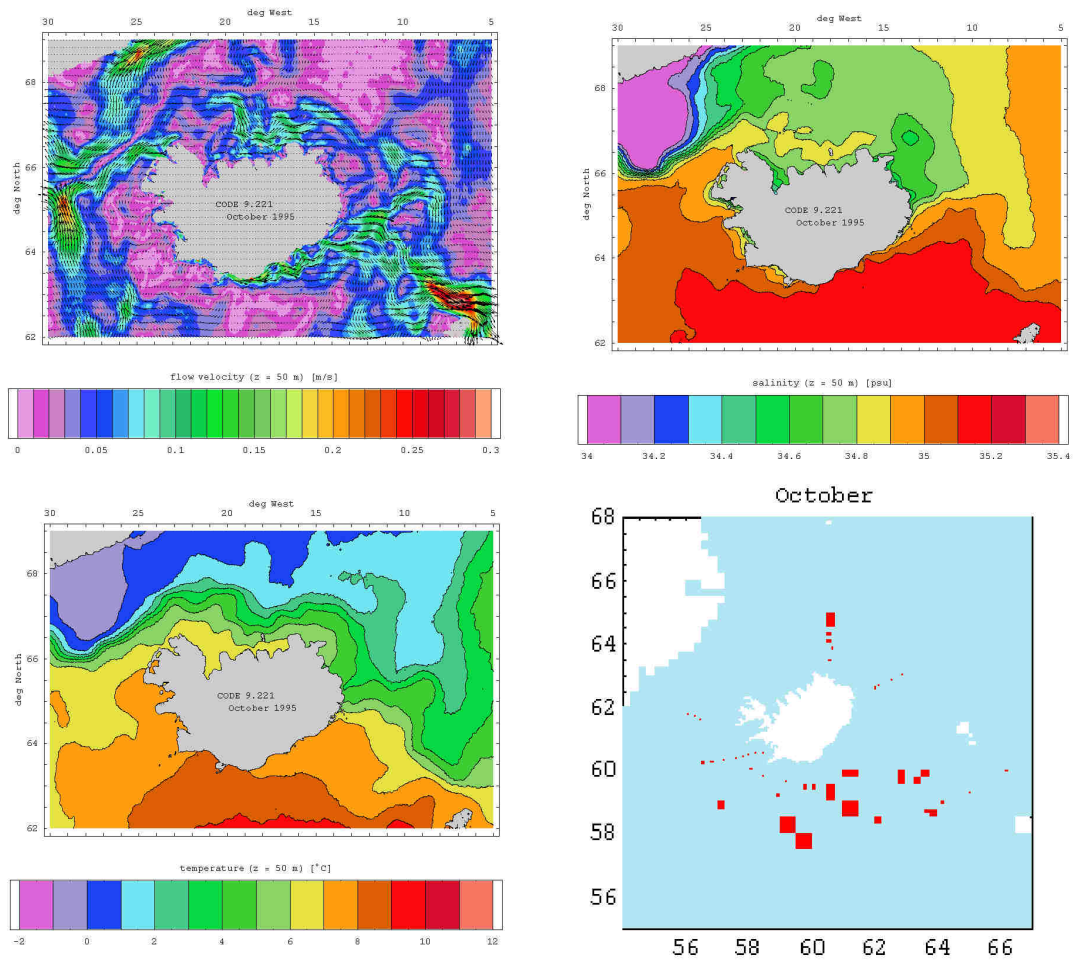


Fig. 2.46.: Monthly mean flow, salinity and temperature fields at 50 m depth and location of used CTD profiles – October 1995.

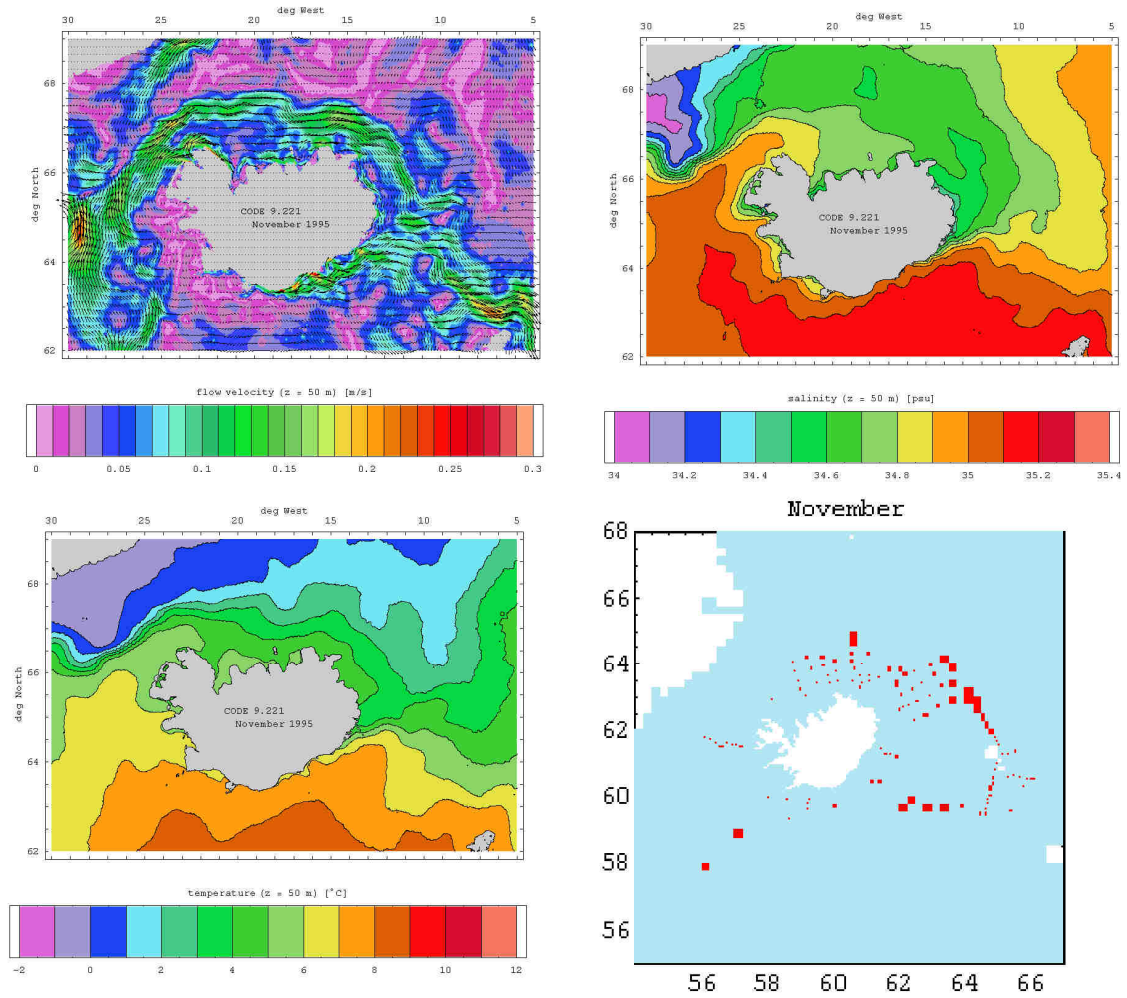


Fig. 2.47.: Monthly mean flow, salinity and temperature fields at 50 m depth and location of used CTD profiles – November 1995.

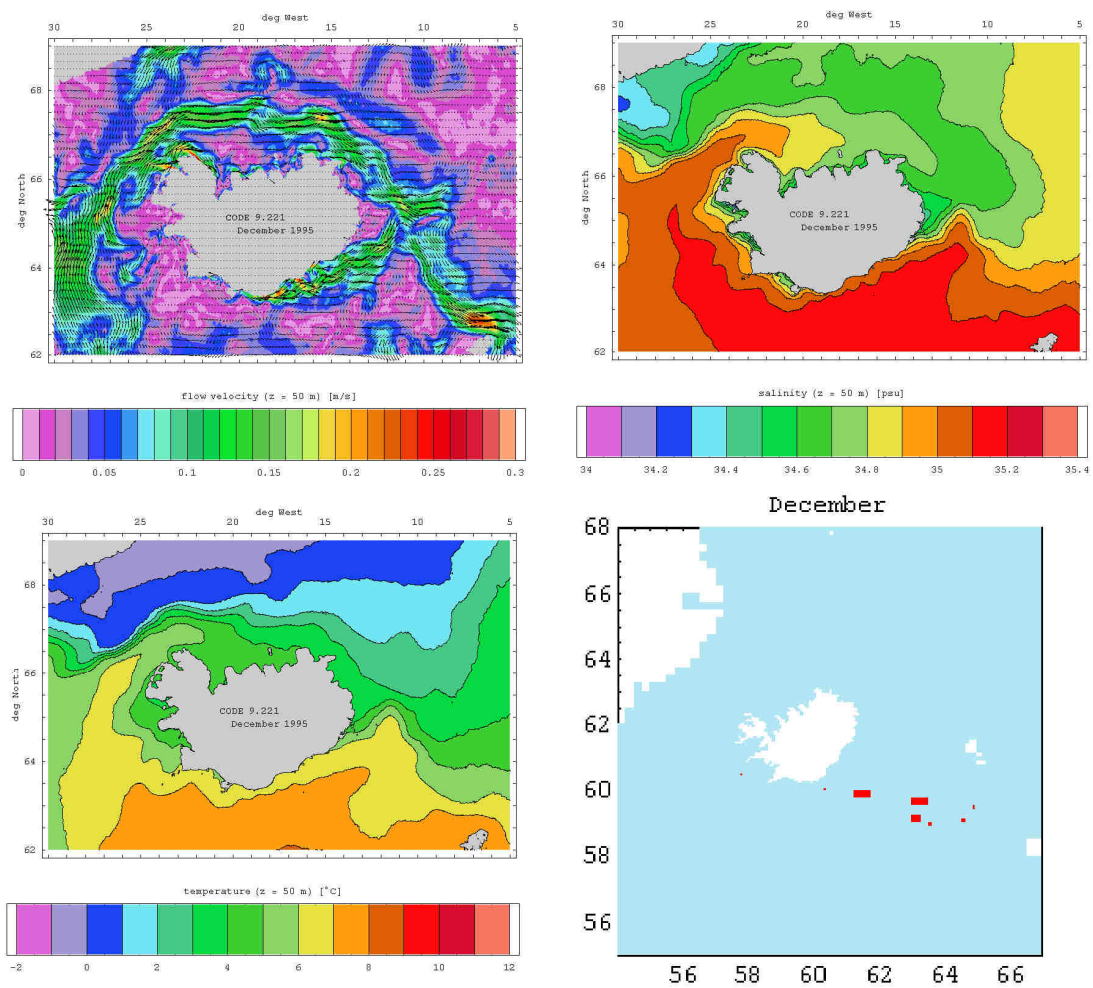


Fig. 2.48.: Monthly mean flow, salinity and temperature fields at 50 m depth and location of used CTD profiles – December 1995.

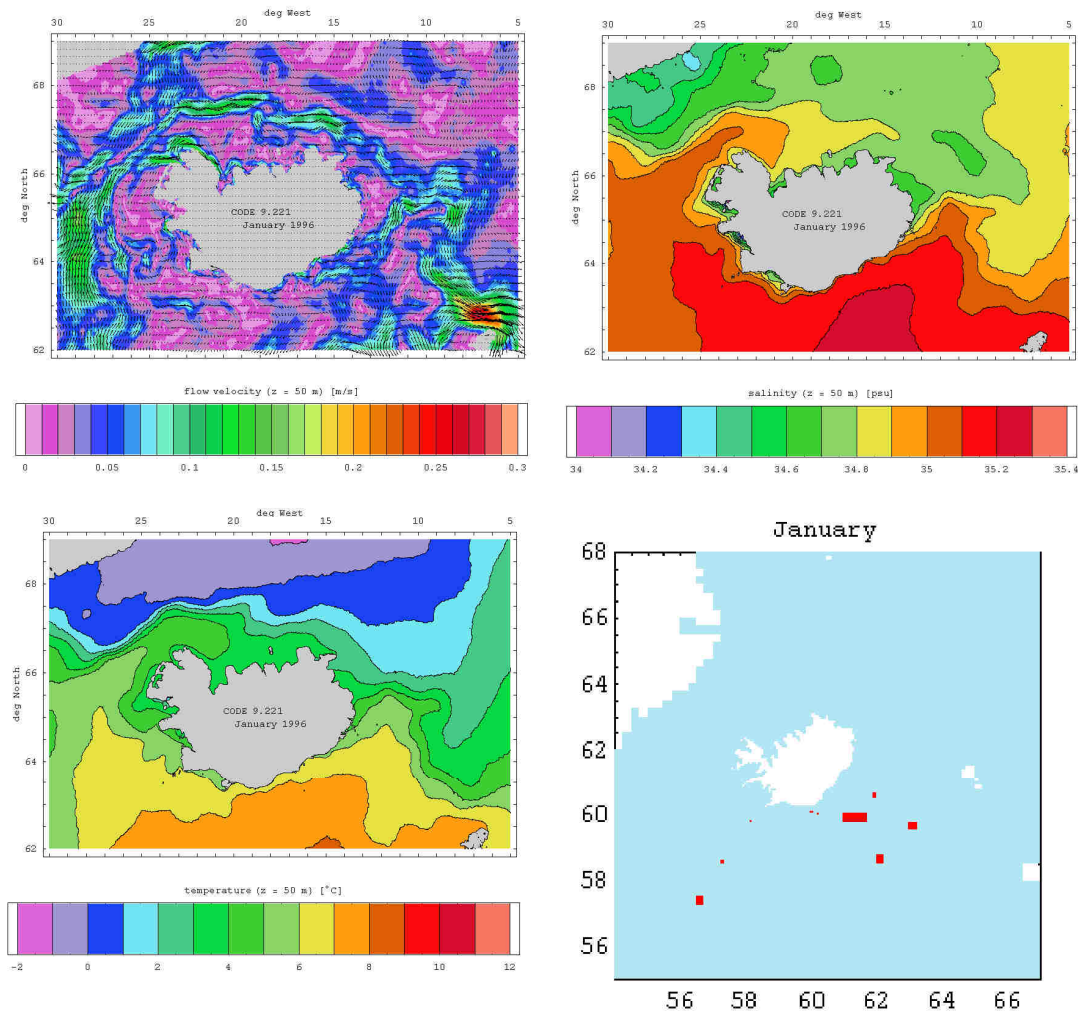


Fig. 2.49.: Monthly mean flow, salinity and temperature fields at 50 m depth and location of used CTD profiles – January 1996.



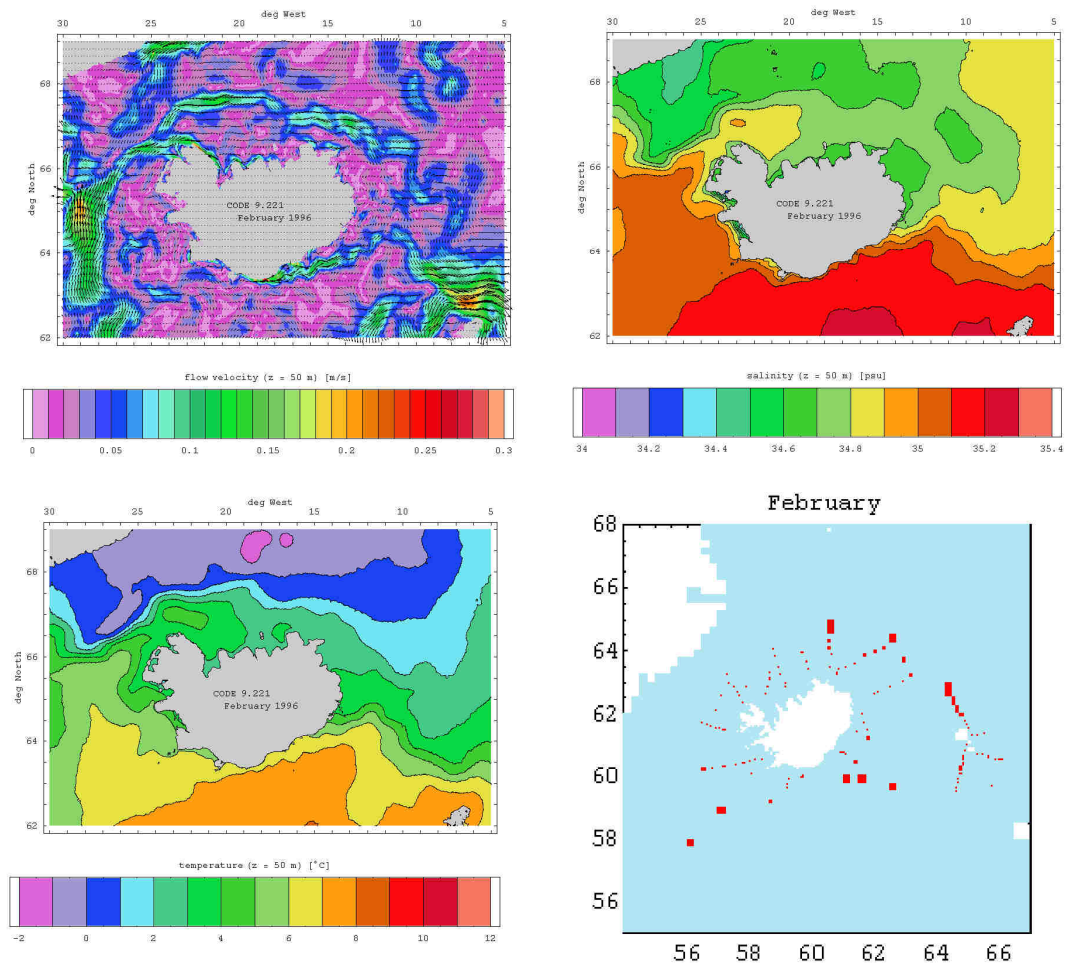


Fig. 2.50.: Monthly mean flow, salinity and temperature fields at 50 m depth and location of used CTD profiles – February 1996.

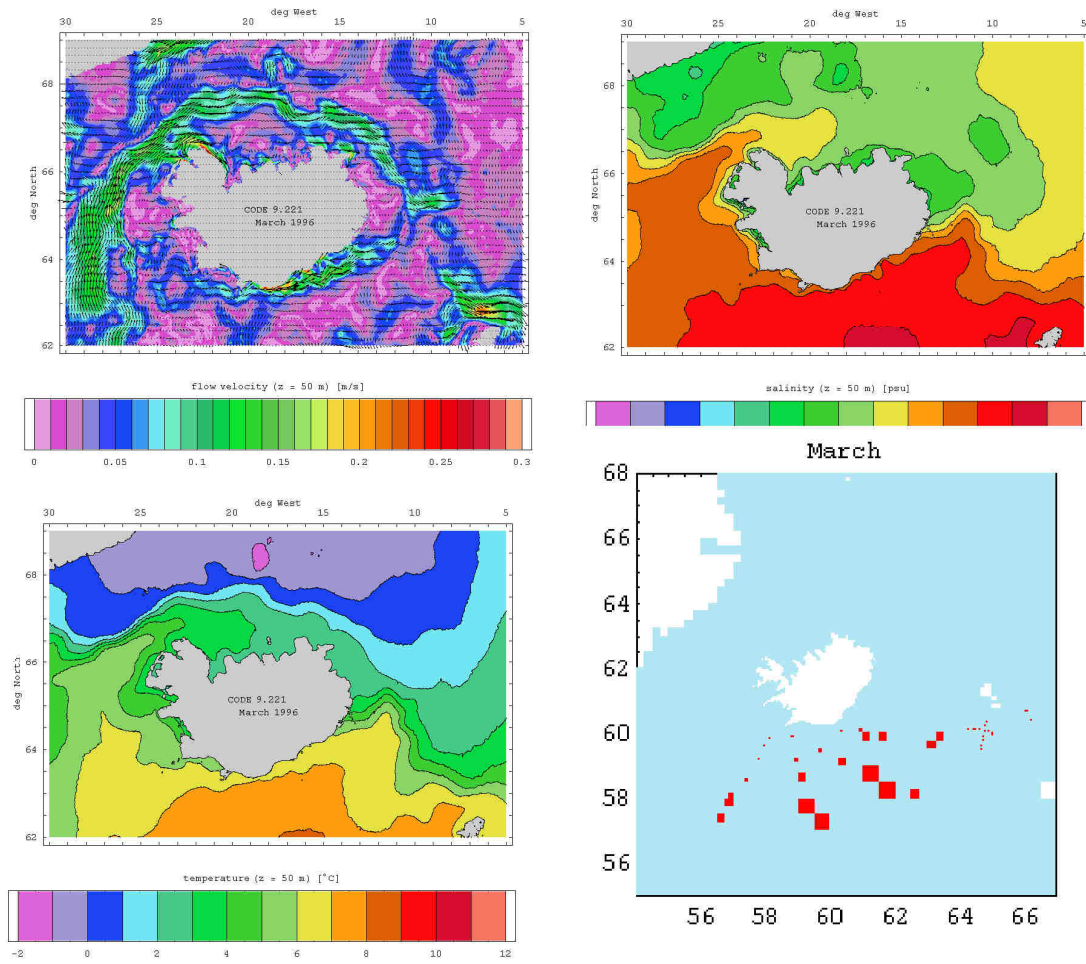


Fig. 2.51.: Monthly mean flow, salinity and temperature fields at 50 m depth and location of used CTD profiles – March 1996.



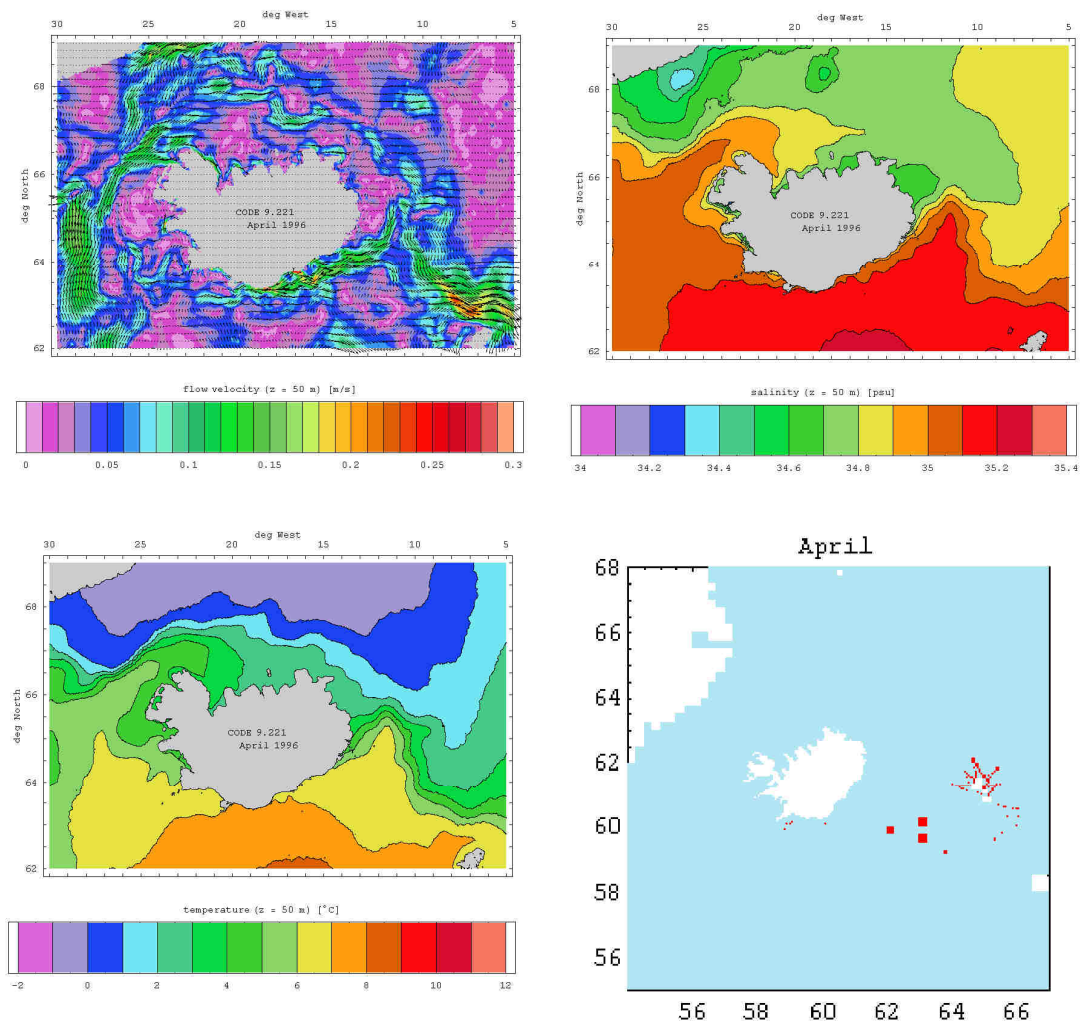


Fig. 2.52.: Monthly mean flow, salinity and temperature fields at 50 m depth and location of used CTD profiles – April 1996.

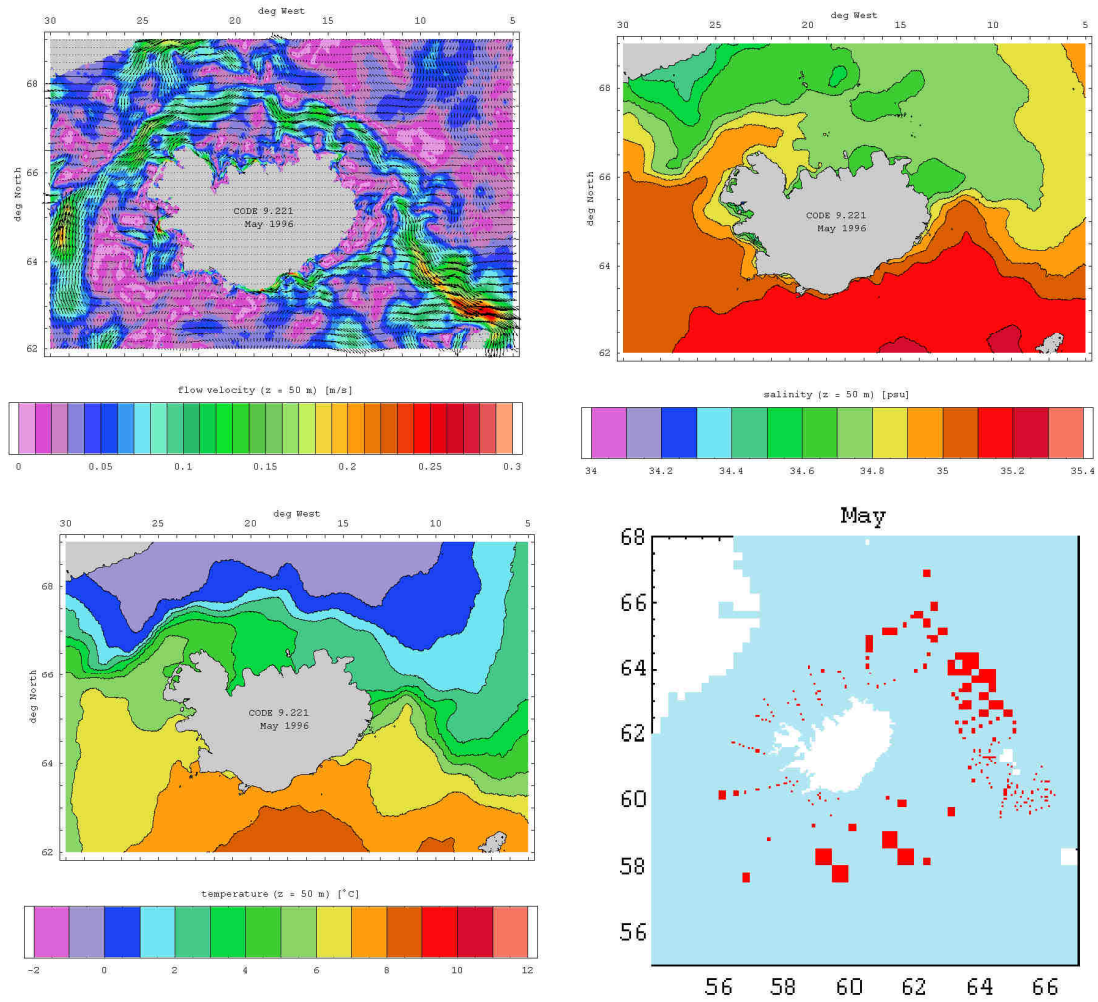


Fig. 2.53.: Monthly mean flow, salinity and temperature fields at 50 m depth and location of used CTD profiles – May 1996.

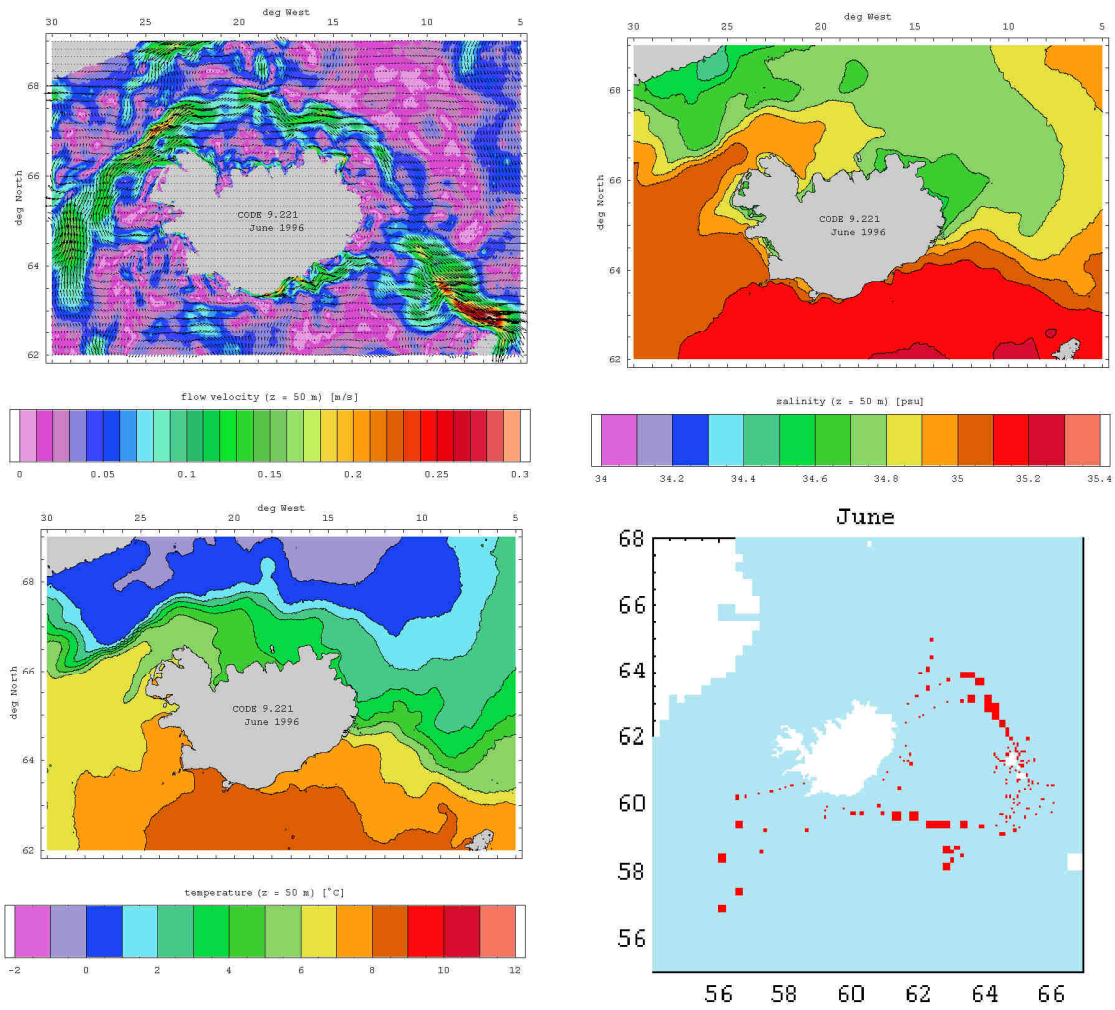


Fig. 2.54.: Monthly mean flow, salinity and temperature fields at 50 m depth and location of used CTD profiles – June 1996.

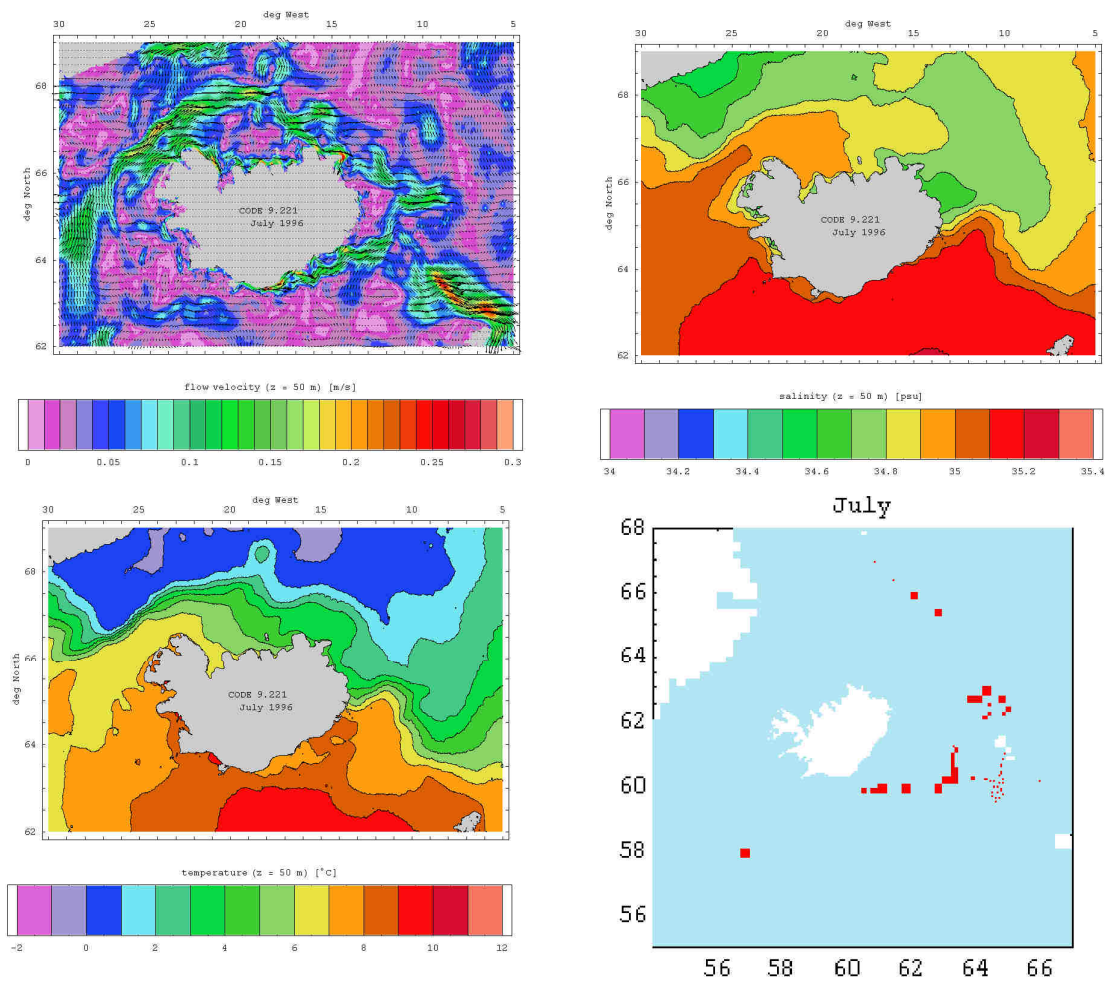


Fig. 2.55.: Monthly mean flow, salinity and temperature fields at 50 m depth and location of used CTD profiles – July 1996.

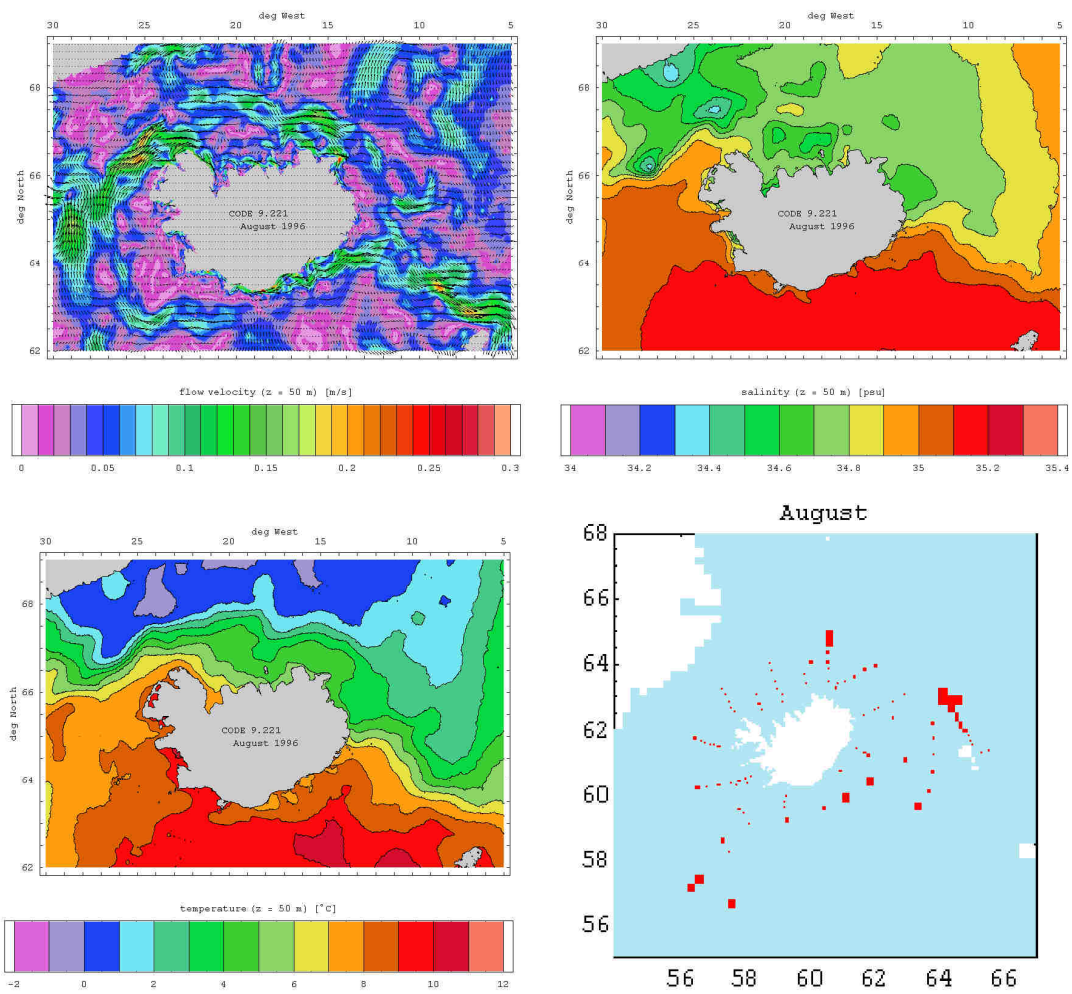


Fig. 2.56.: Monthly mean flow, salinity and temperature fields at 50 m depth and location of used CTD profiles – August 1996.



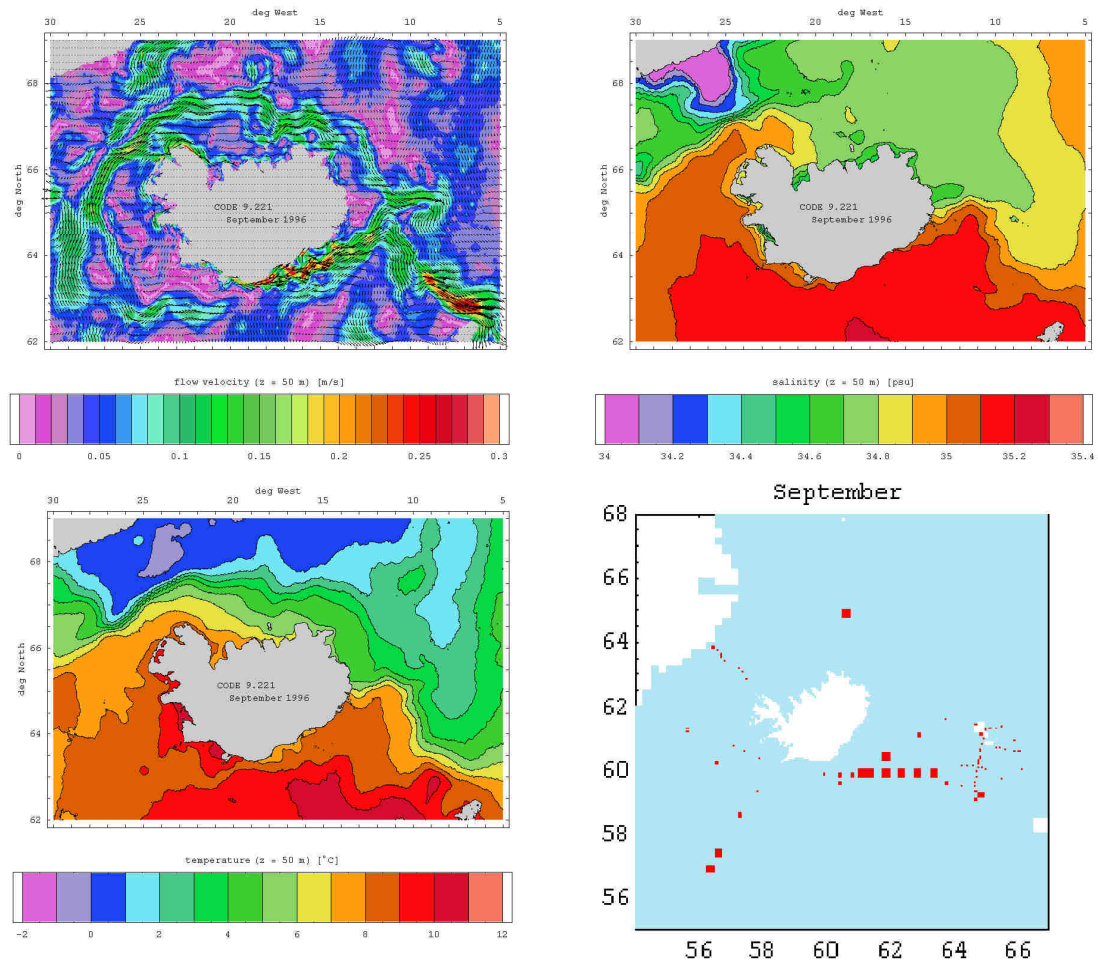


Fig. 2.57.: Monthly mean flow, salinity and temperature fields at 50 m depth and location of used CTD profiles – September 1996.

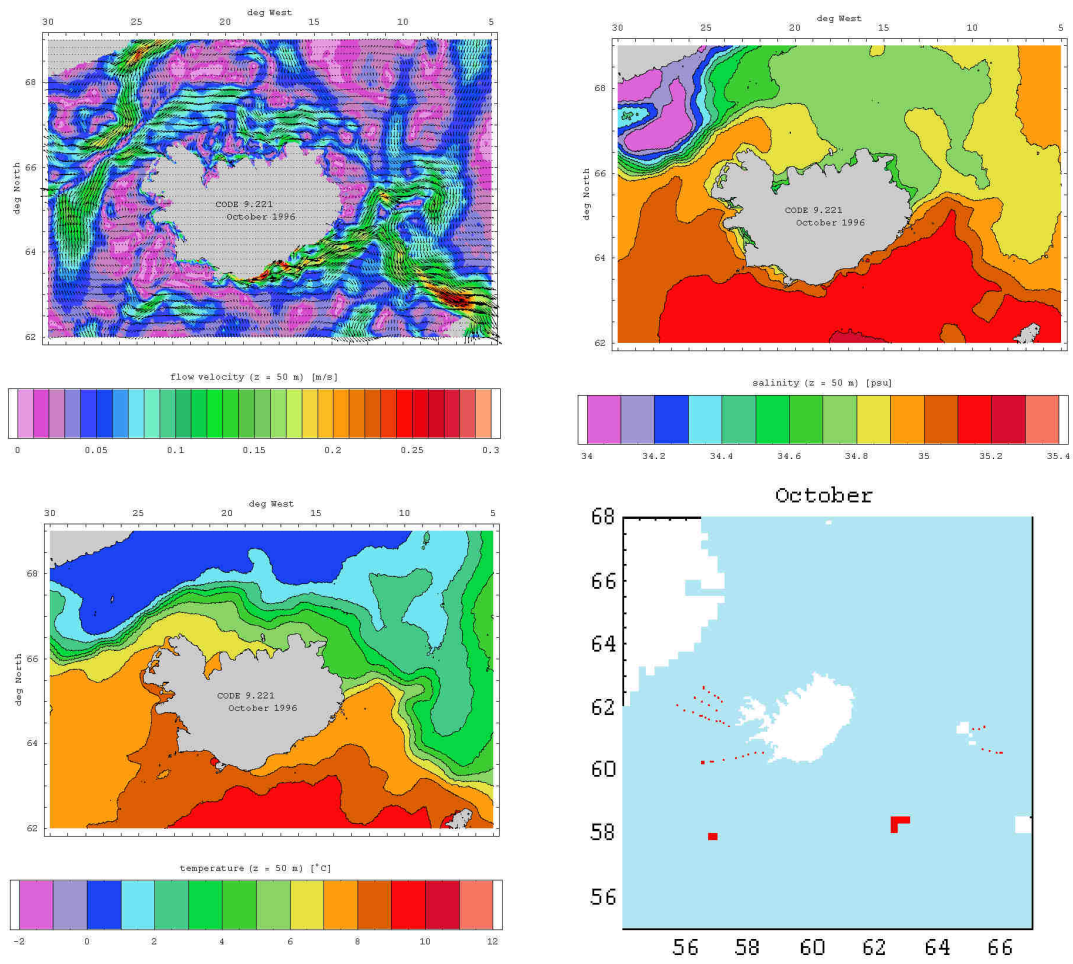


Fig. 2.58.: Monthly mean flow, salinity and temperature fields at 50 m depth and location of used CTD profiles – October 1996.



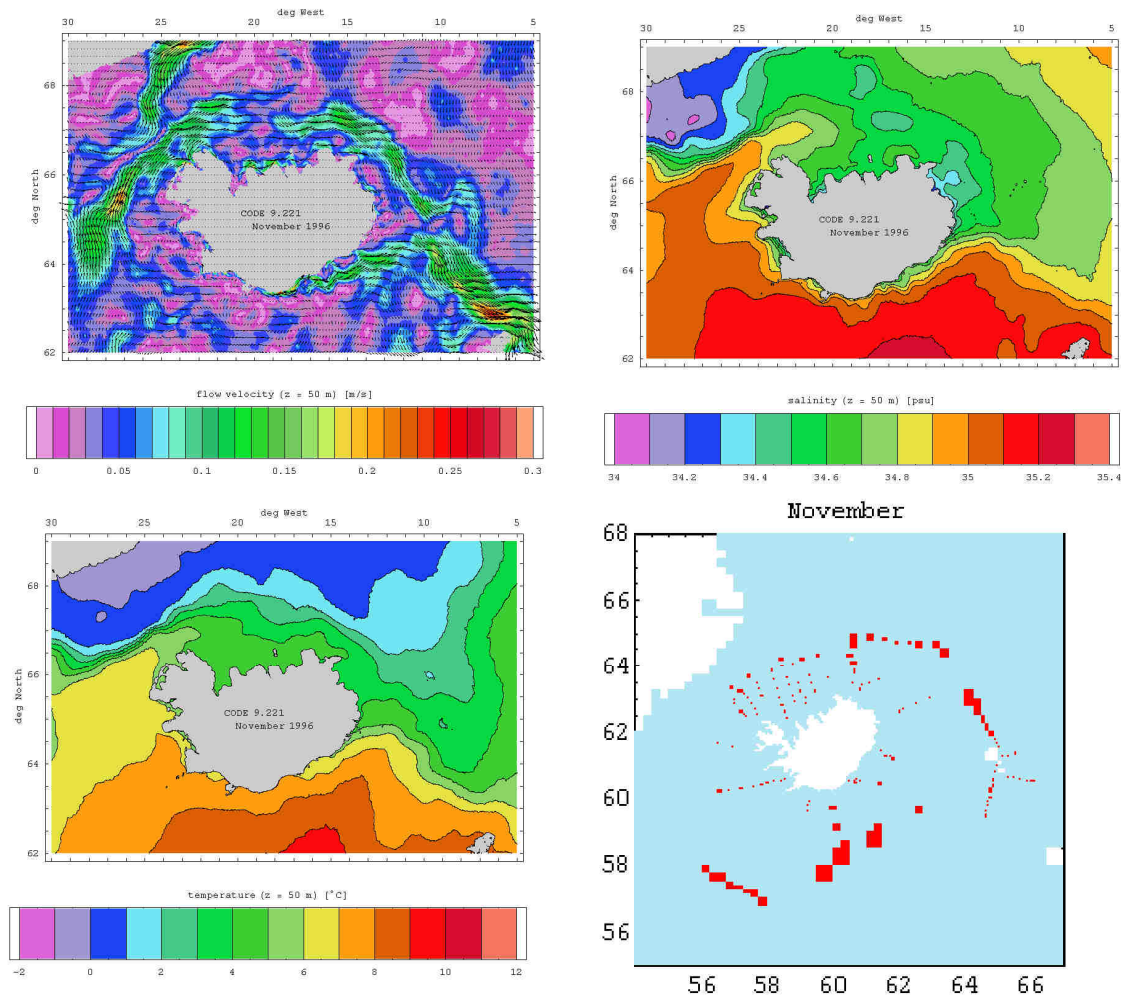


Fig. 2.59.: Monthly mean flow, salinity and temperature fields at 50 m depth and location of used CTD profiles – November 1996.

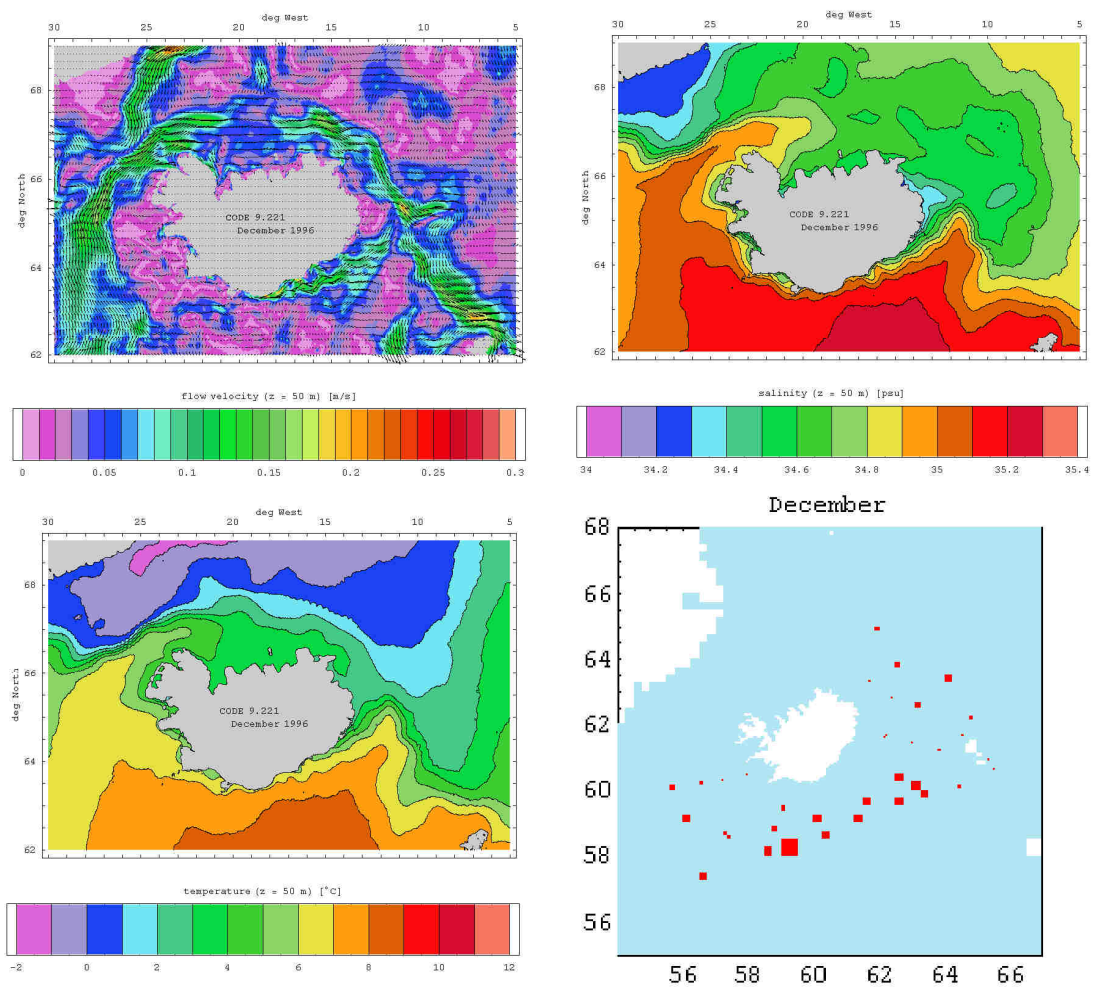


Fig. 2.60.: Monthly mean flow, salinity and temperature fields at 50 m depth and location of used CTD profiles – December 1996.

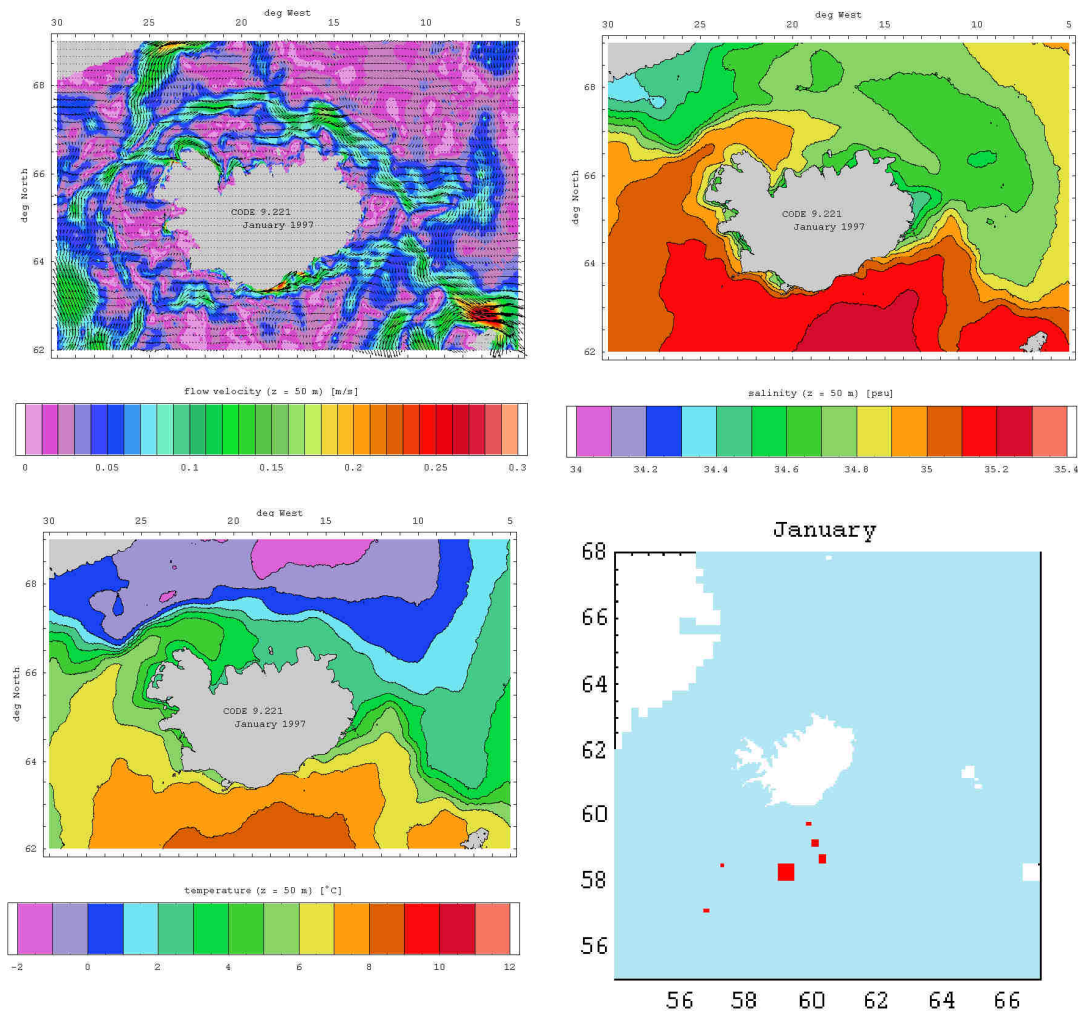


Fig. 2.61.: Monthly mean flow, salinity and temperature fields at 50 m depth and location of used CTD profiles – January 1997.

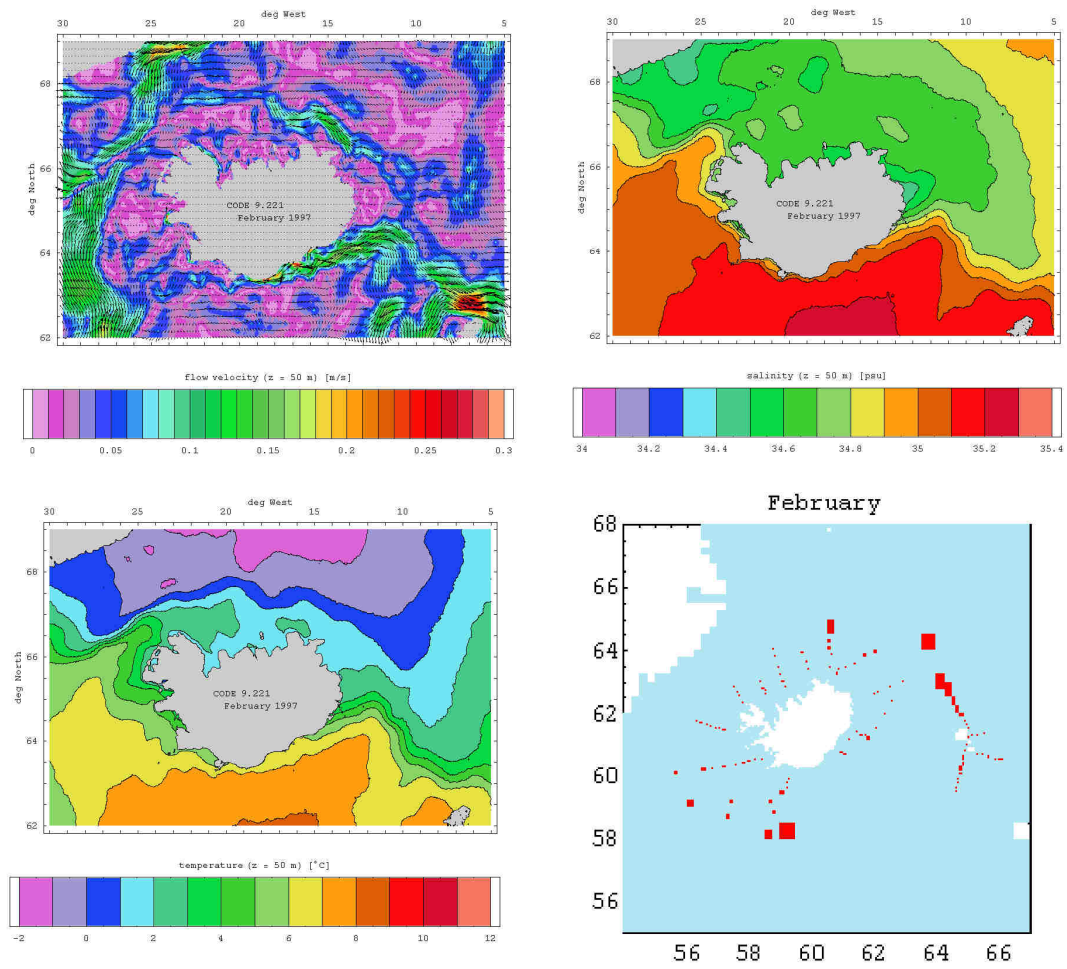


Fig. 2.62.: Monthly mean flow, salinity and temperature fields at 50 m depth and location of used CTD profiles – February 1997.

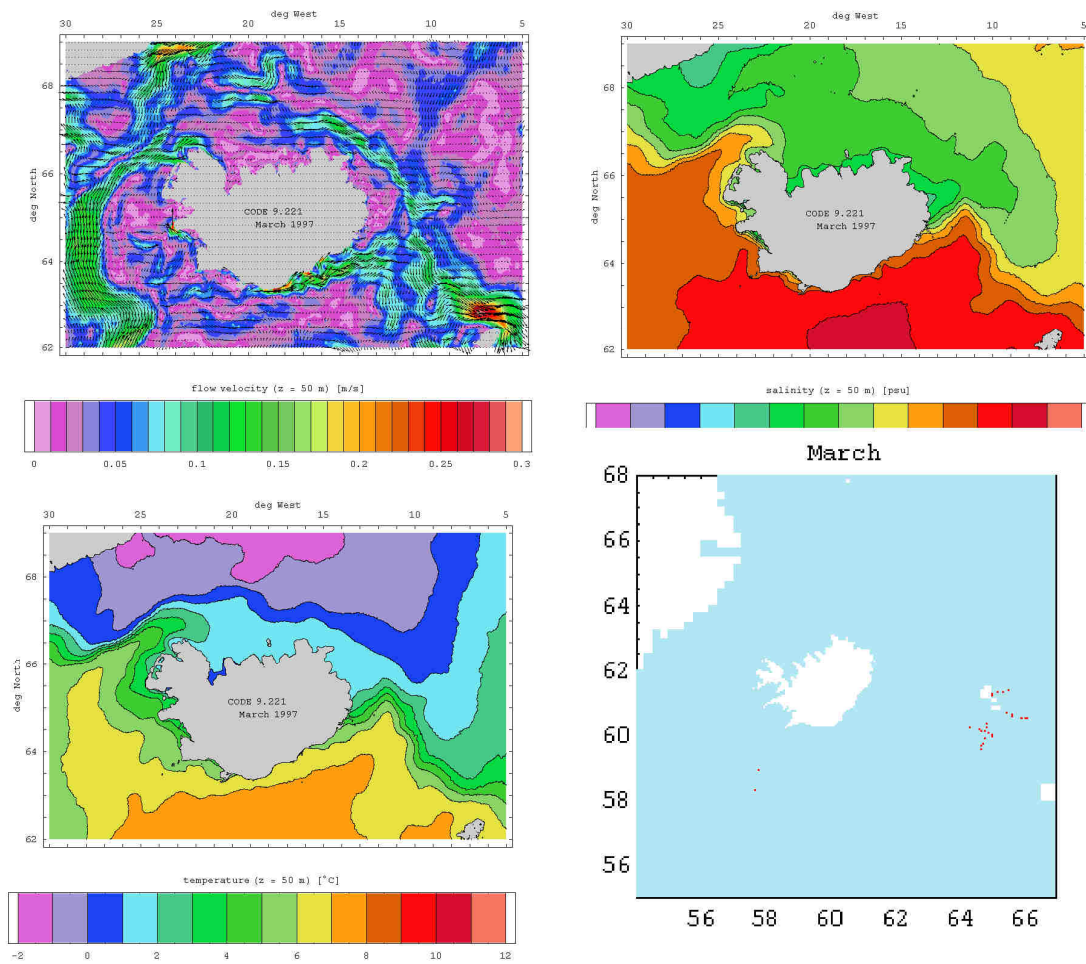


Fig. 2.63.: Monthly mean flow, salinity and temperature fields at 50 m depth and location of used CTD profiles – March 1997.



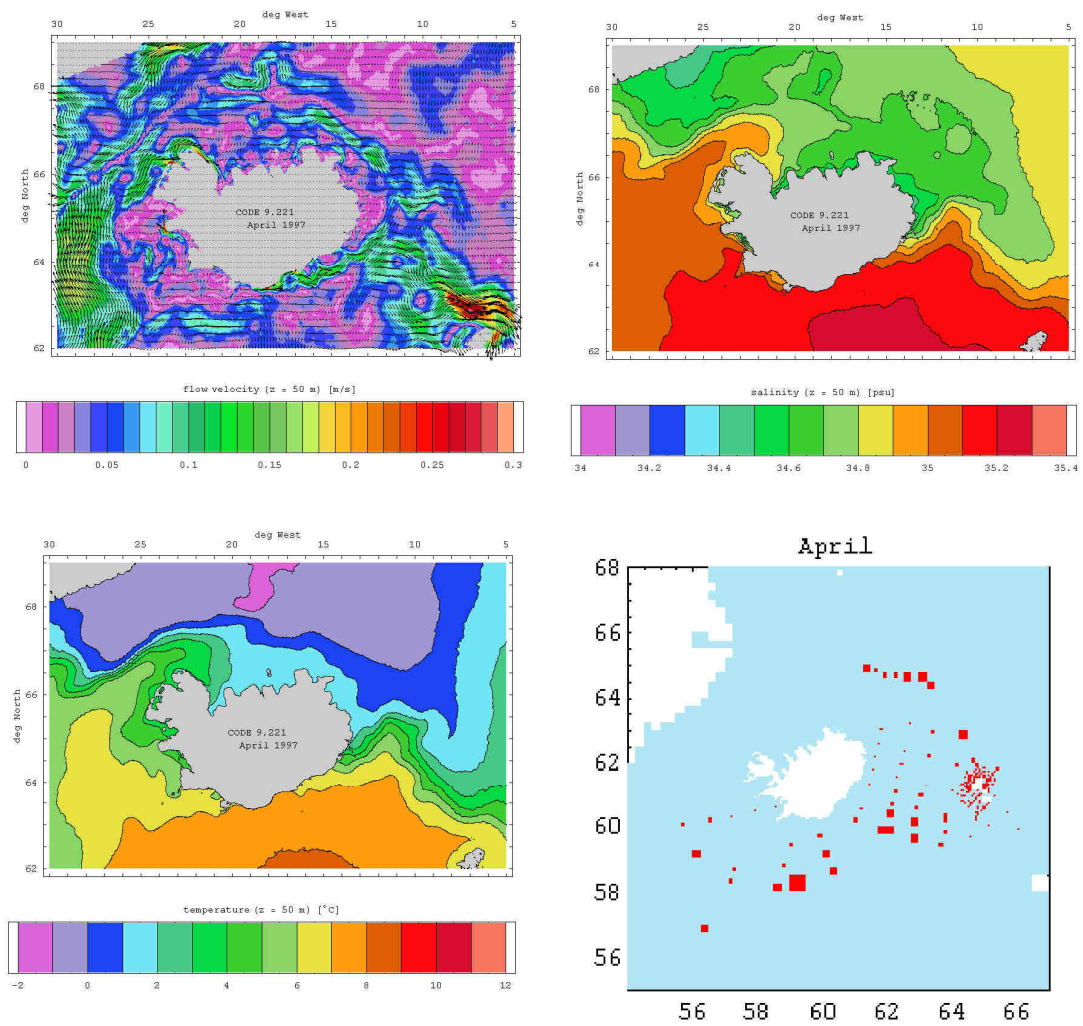


Fig. 2.64.: Monthly mean flow, salinity and temperature fields at 50 m depth and location of used CTD profiles – April 1997.



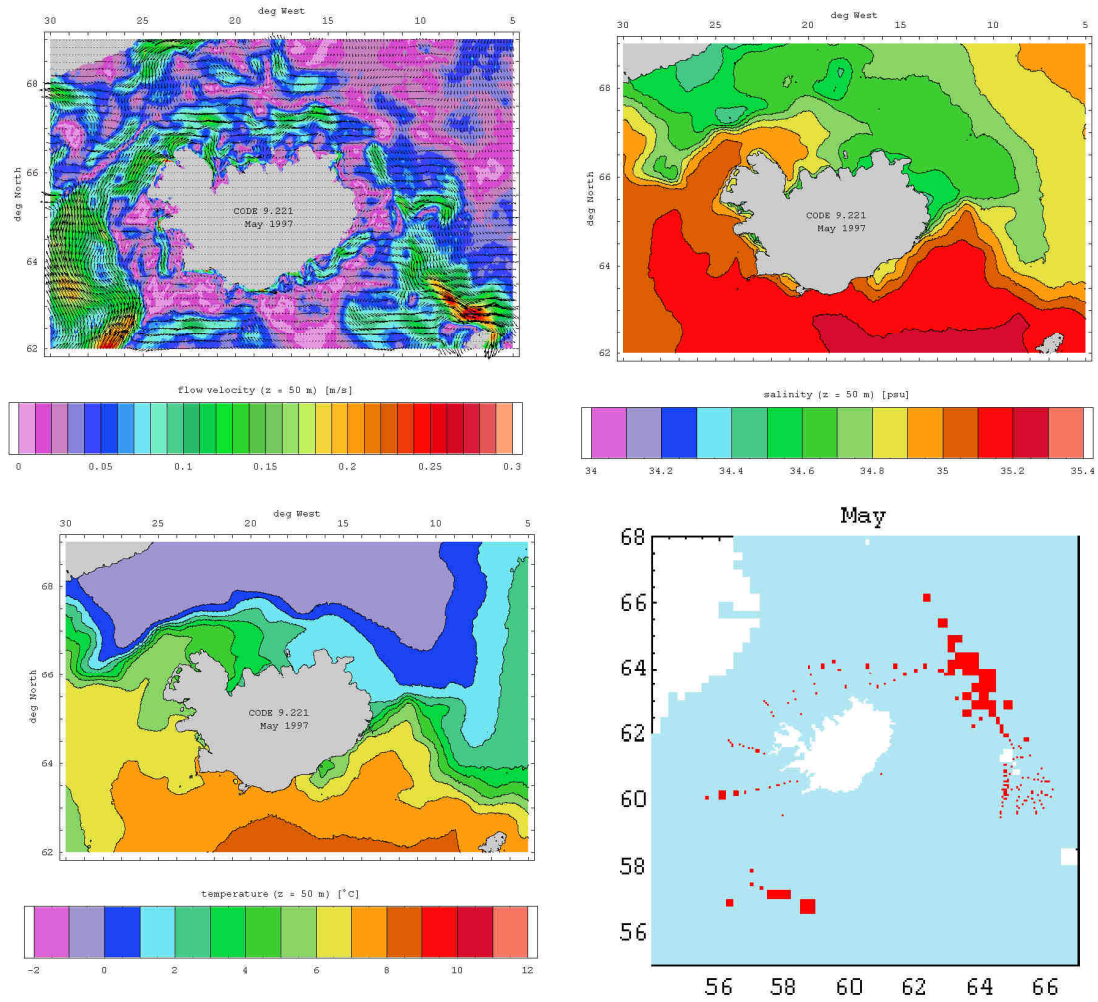


Fig. 2.65.: Monthly mean flow, salinity and temperature fields at 50 m depth and location of used CTD profiles – May 1997.

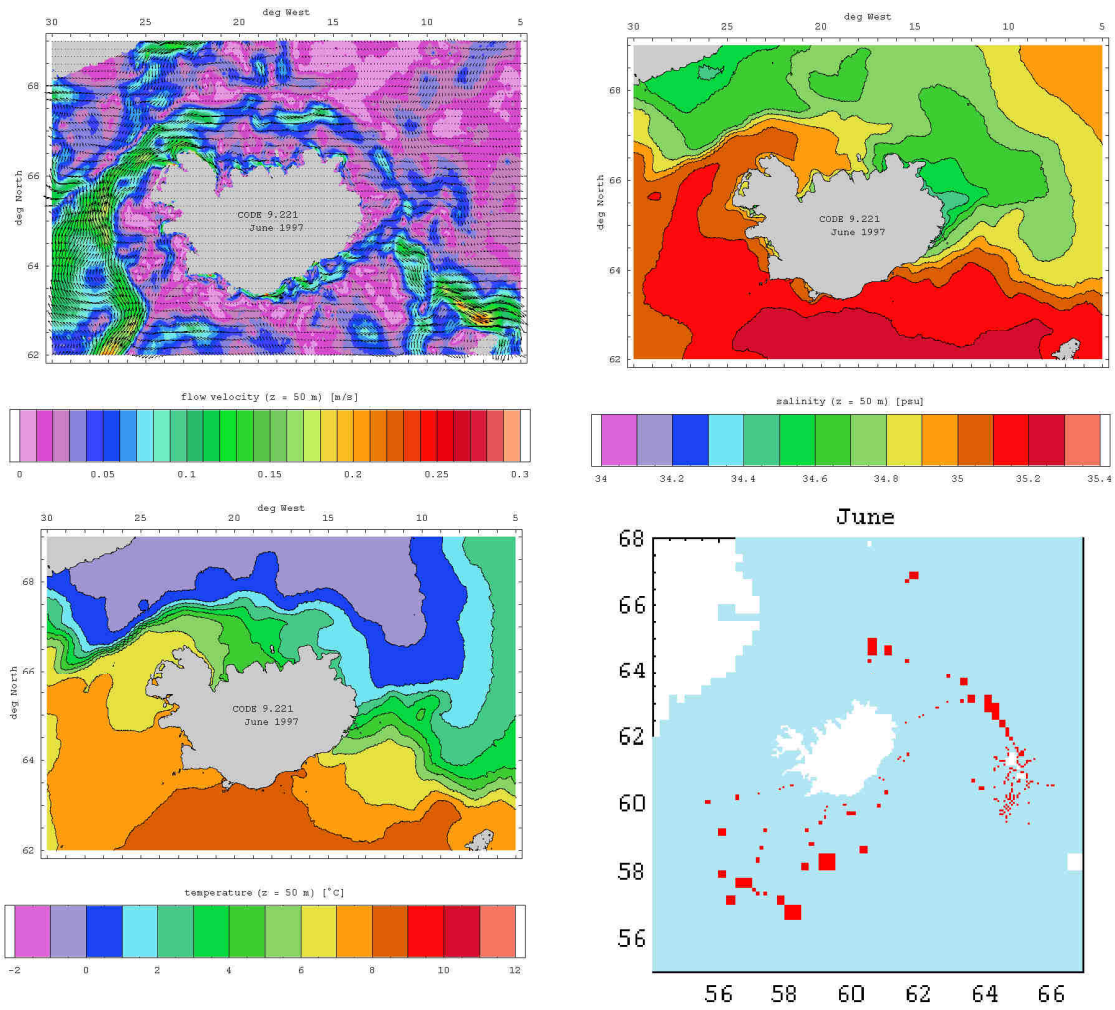


Fig. 2.66.: Monthly mean flow, salinity and temperature fields at 50 m depth and location of used CTD profiles – June 1997.

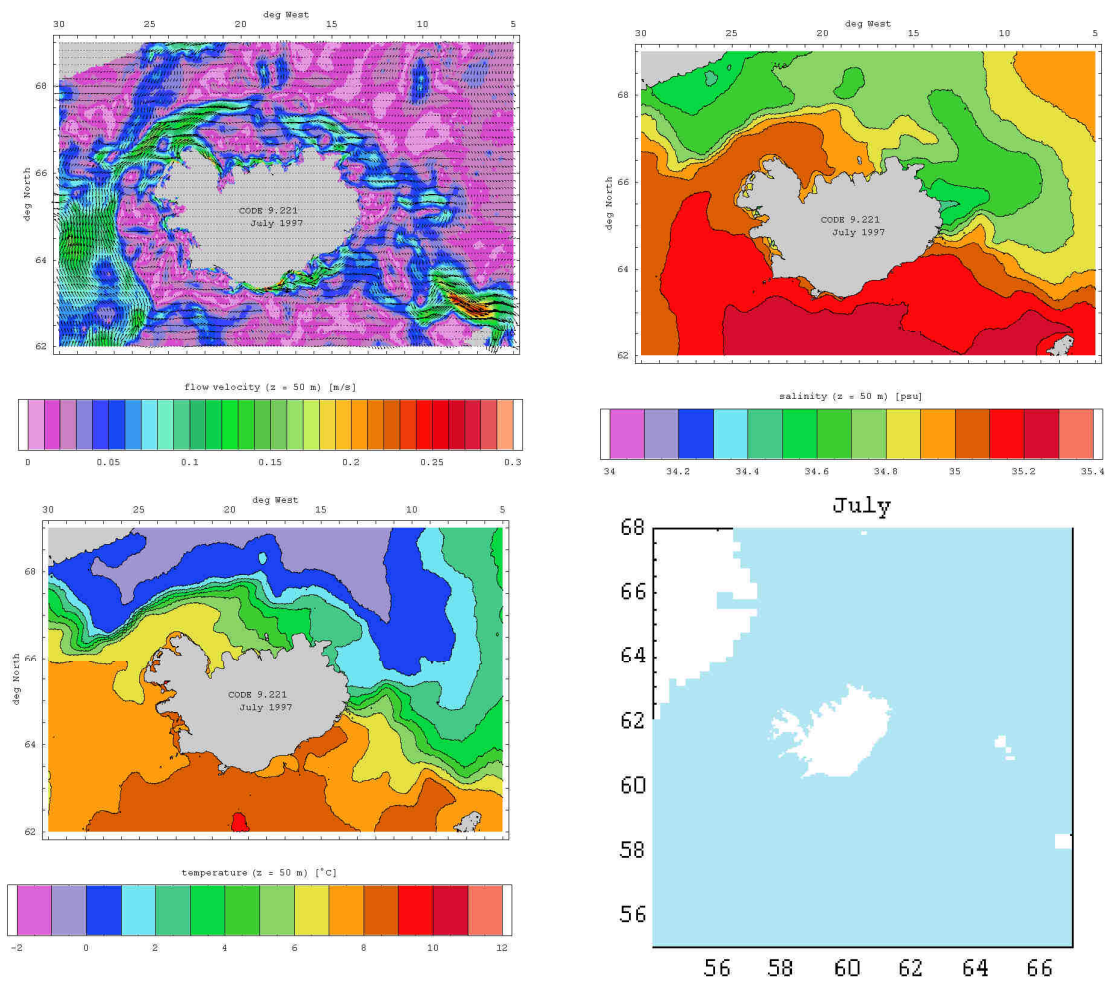


Fig. 2.67.: Monthly mean flow, salinity and temperature fields at 50 m depth and location of used CTD profiles – July 1997.

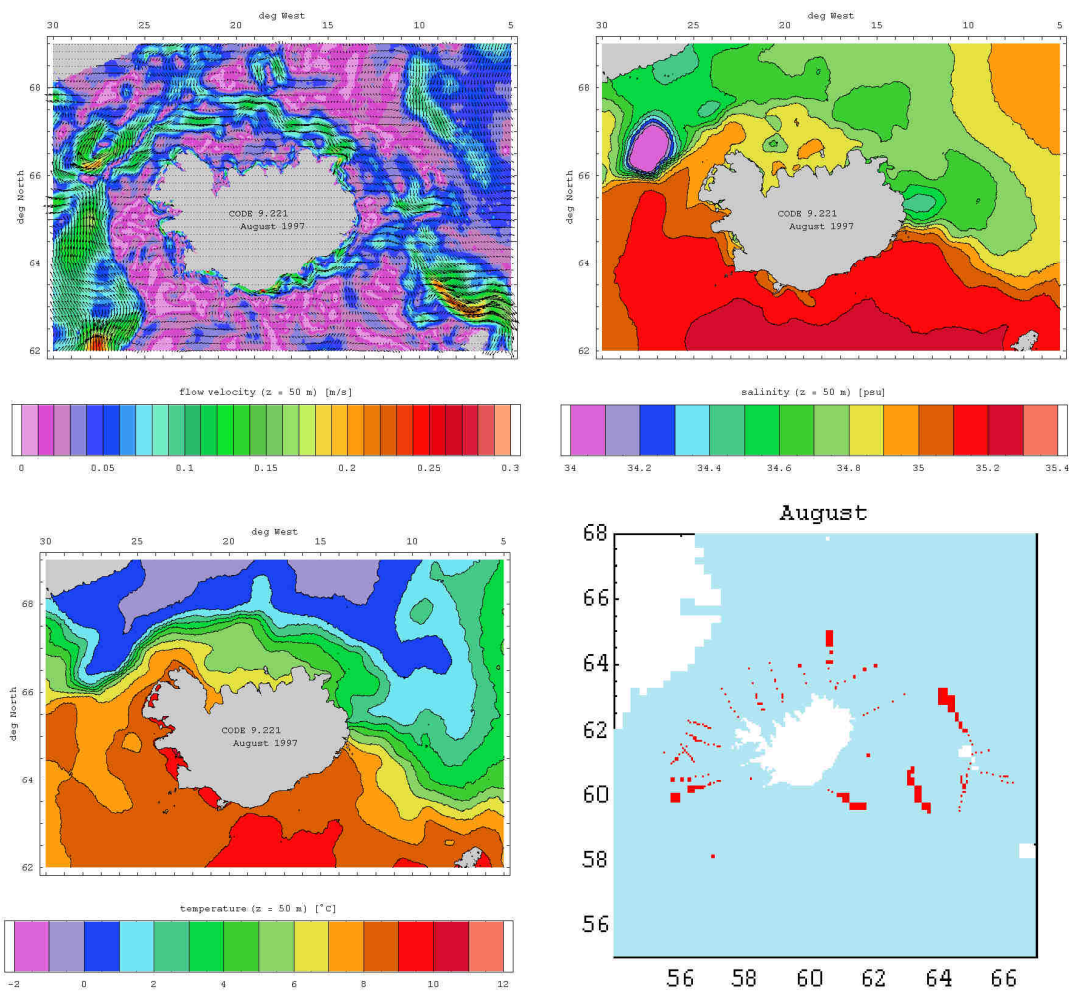


Fig. 2.68.: Monthly mean flow, salinity and temperature fields at 50 m depth and location of used CTD profiles – August 1997.

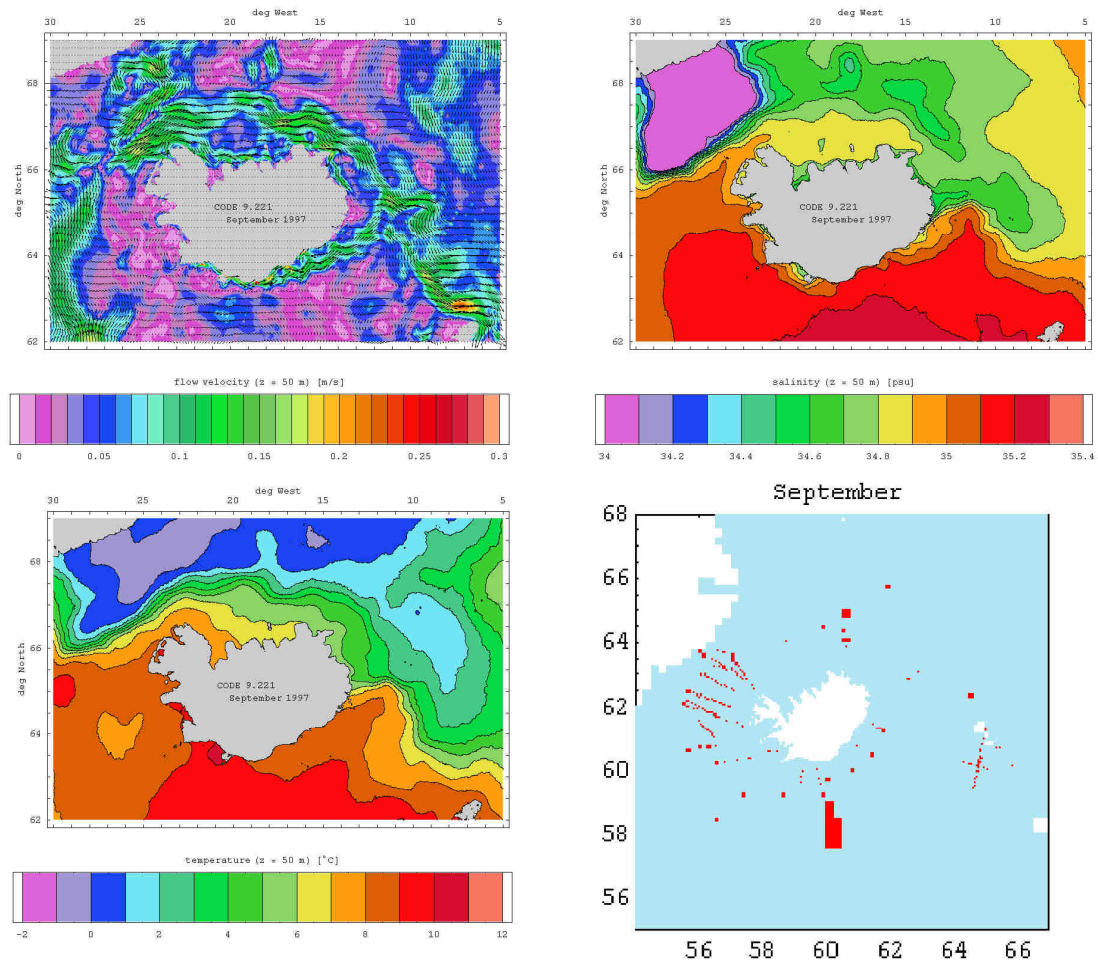


Fig. 2.69.: Monthly mean flow, salinity and temperature fields at 50 m depth and location of used CTD profiles – September 1997.



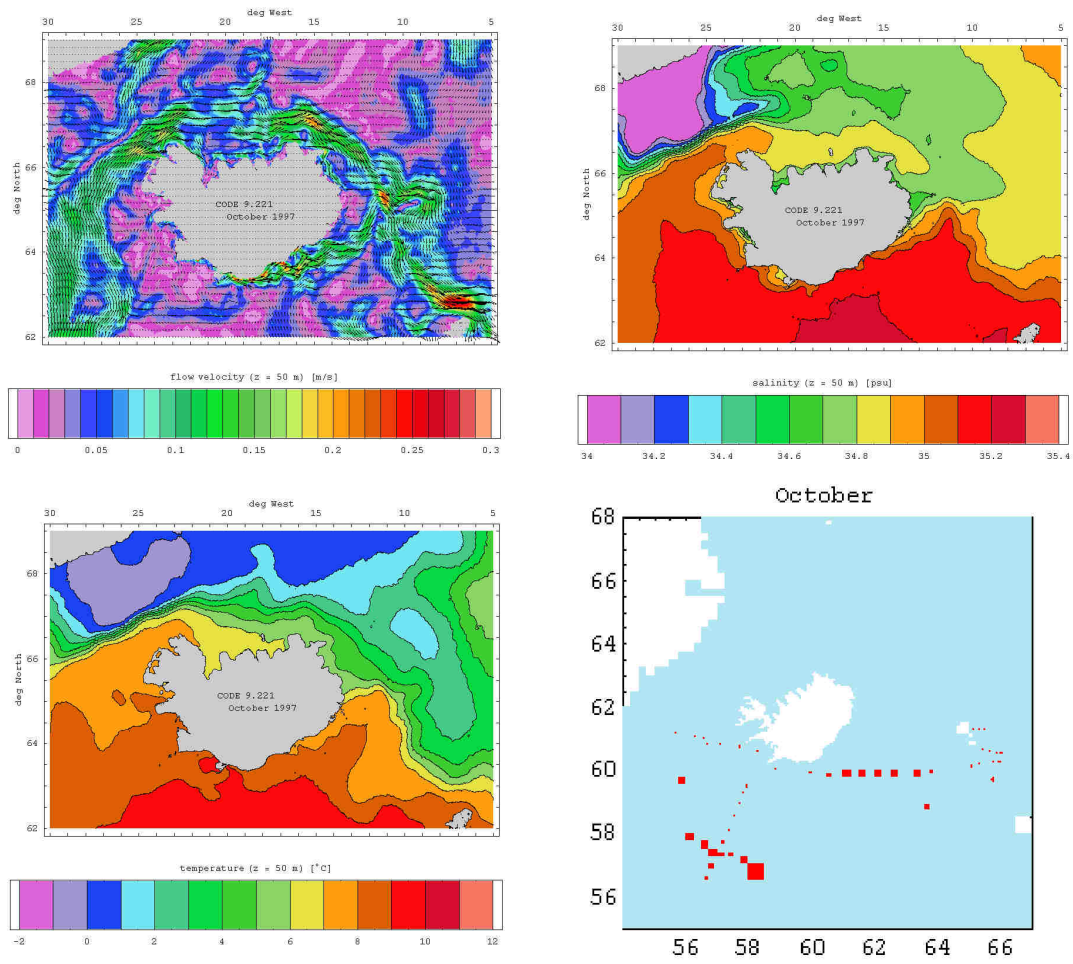


Fig. 2.70.: Monthly mean flow, salinity and temperature fields at 50 m depth and location of used CTD profiles – October 1997.



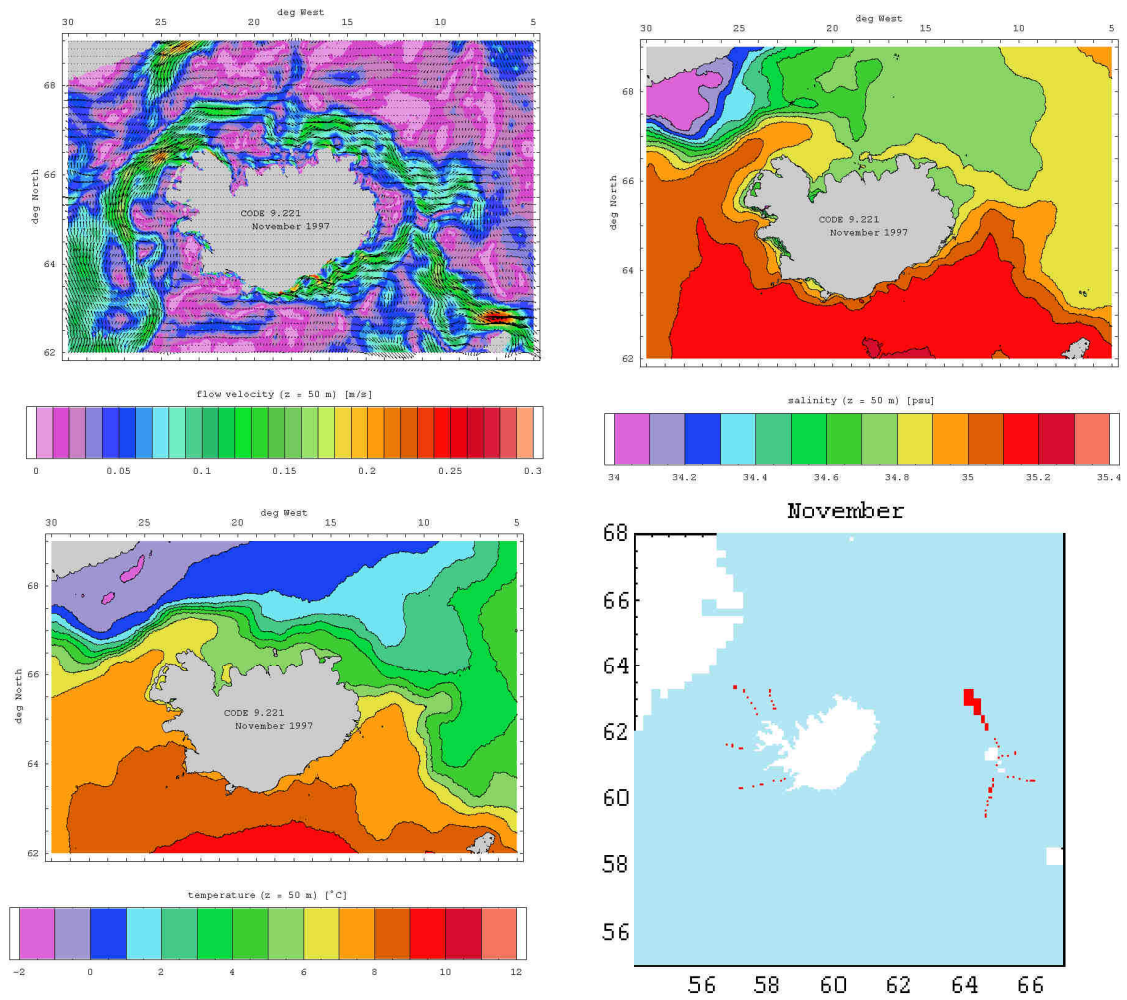


Fig. 2.71.: Monthly mean flow, salinity and temperature fields at 50 m depth and location of used CTD profiles – November 1997.

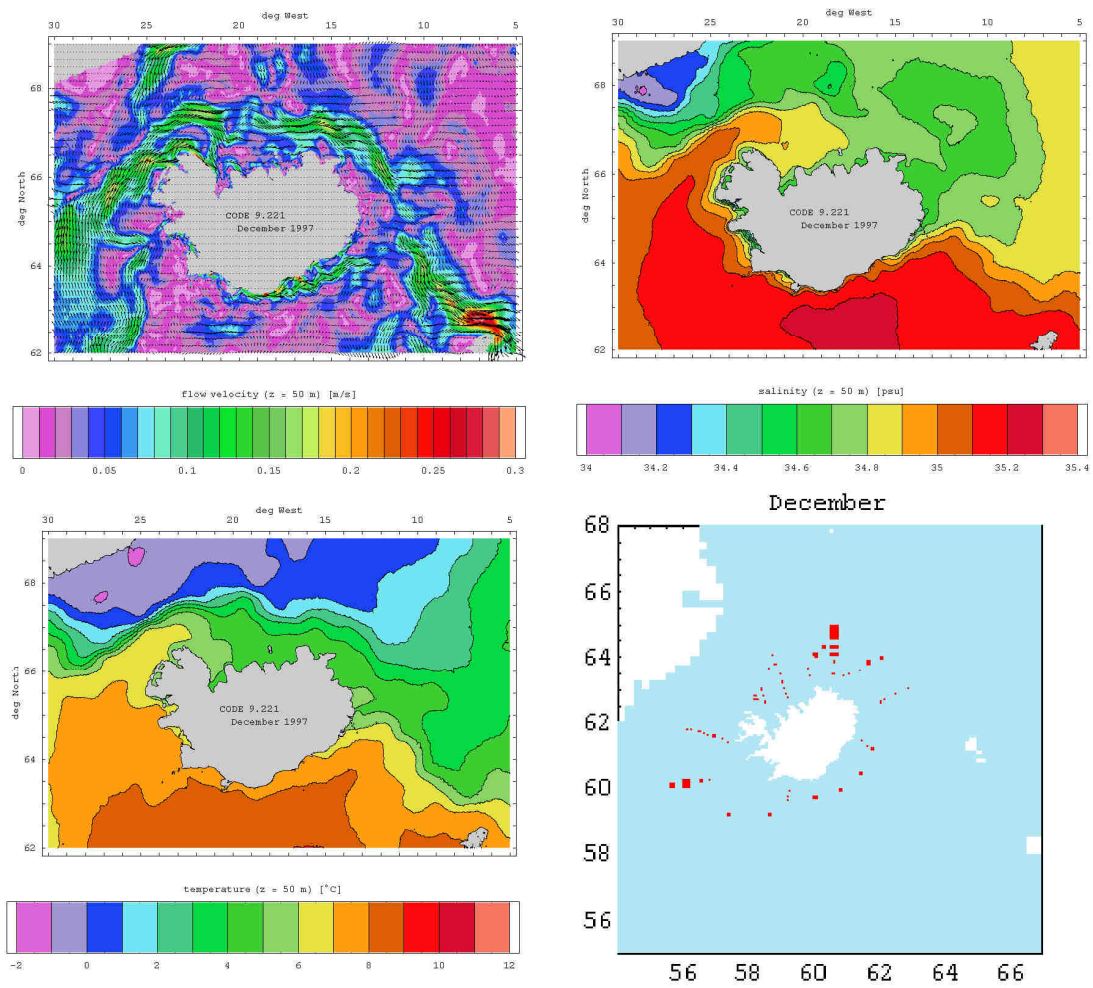


Fig. 2.72.: Monthly mean flow, salinity and temperature fields at 50 m depth and location of used CTD profiles – December 1997.

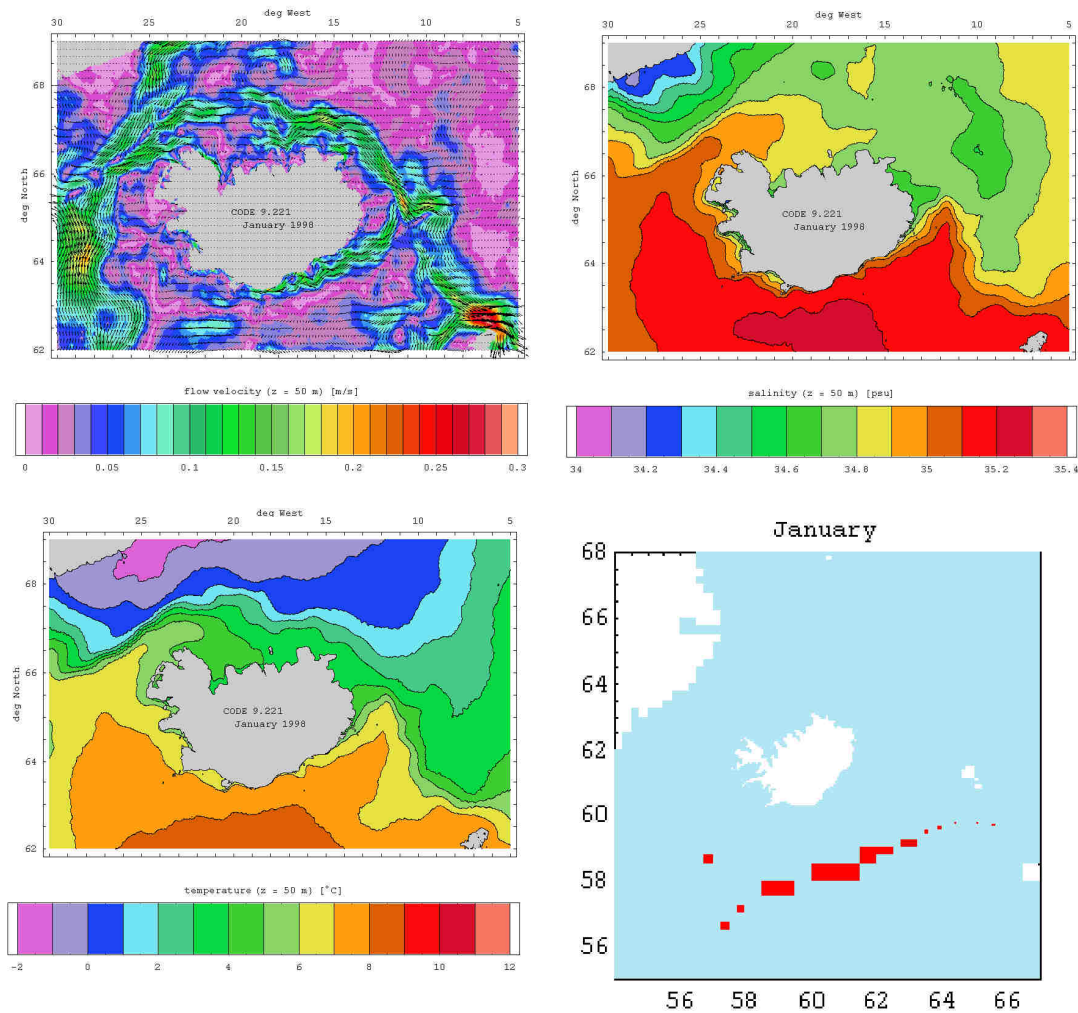


Fig. 2.73.: Monthly mean flow, salinity and temperature fields at 50 m depth and location of used CTD profiles – January 1998.

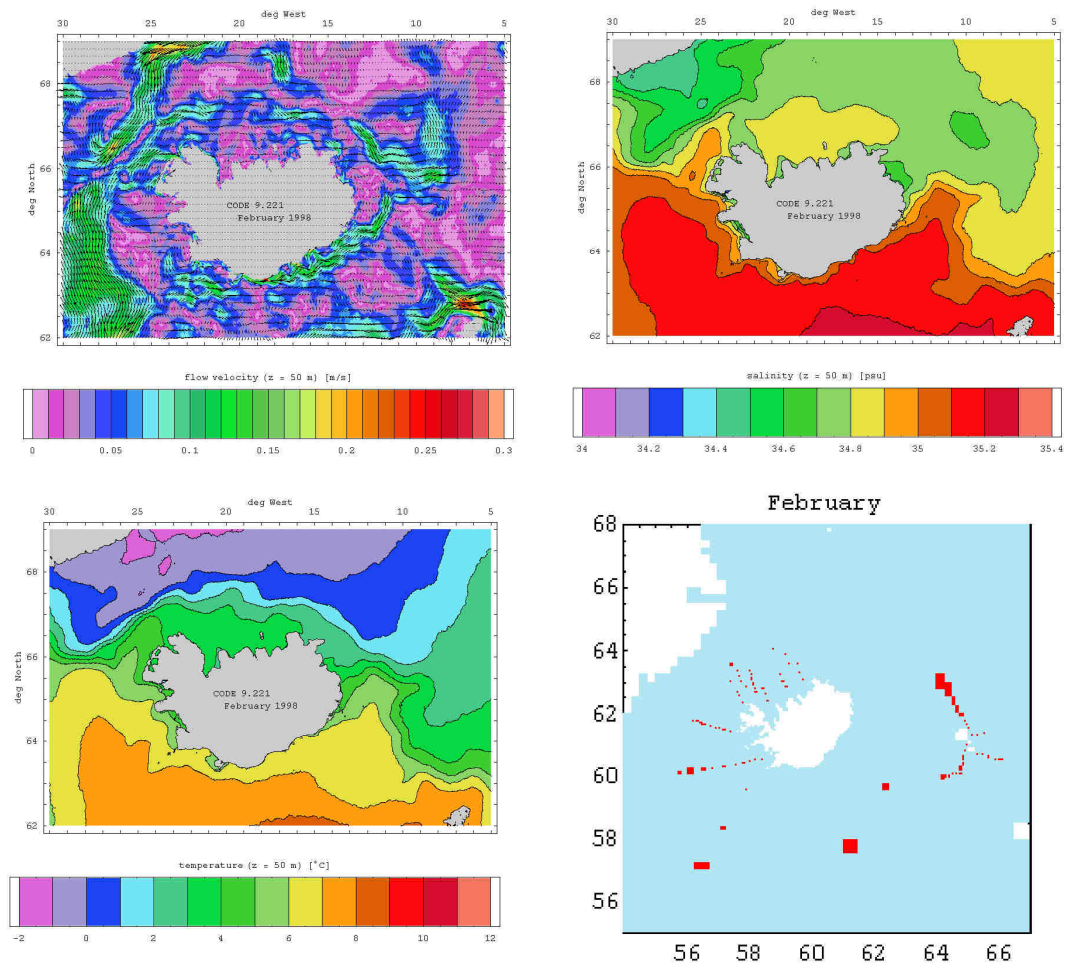


Fig. 2.74.: Monthly mean flow, salinity and temperature fields at 50 m depth and location of used CTD profiles – February 1998.

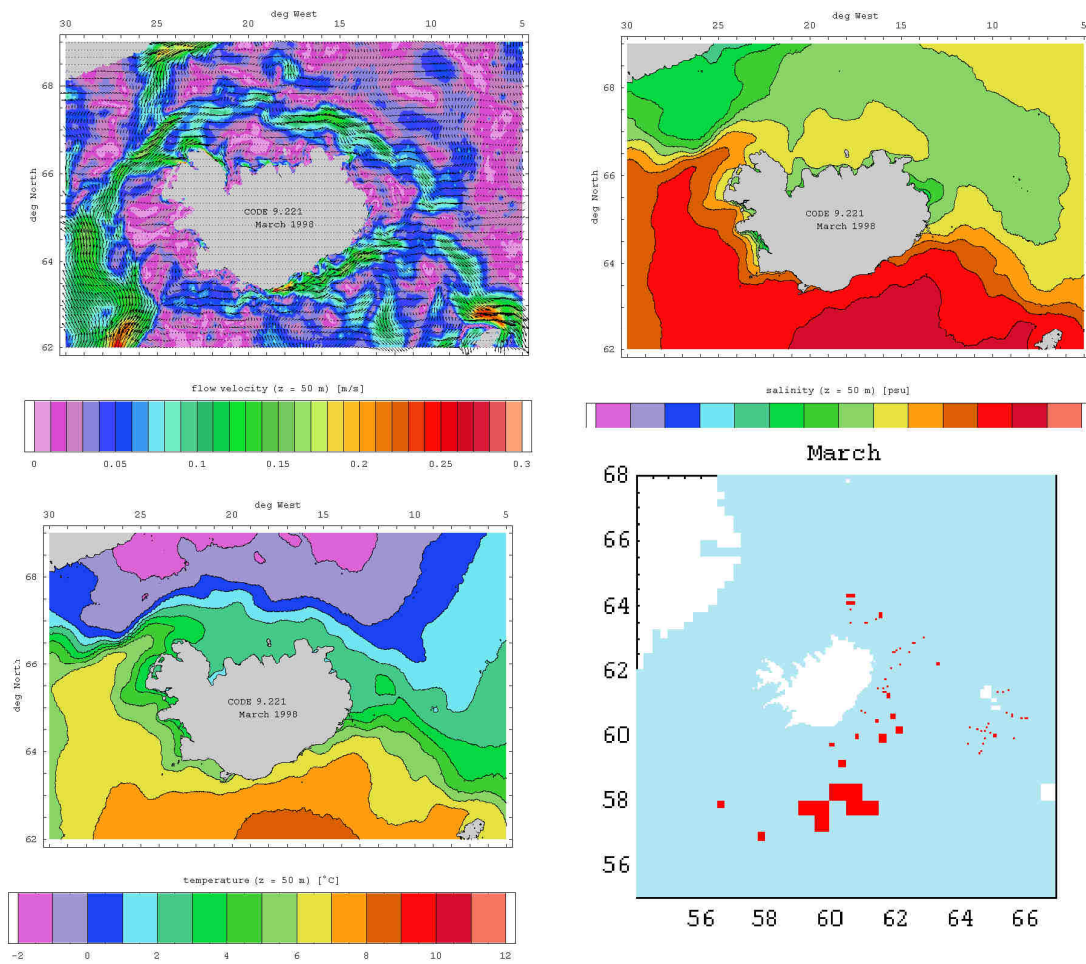


Fig. 2.75.: Monthly mean flow, salinity and temperature fields at 50 m depth and location of used CTD profiles – March 1998.



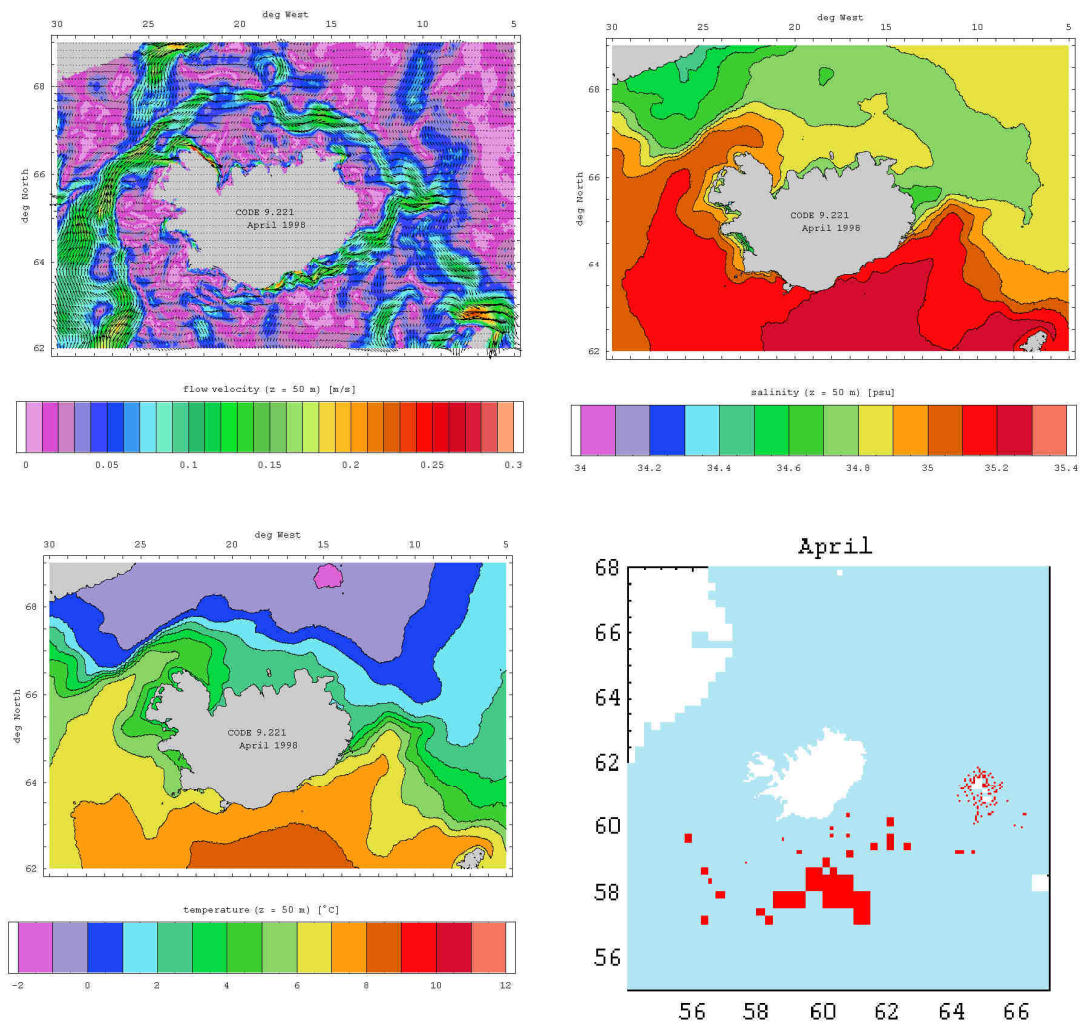


Fig. 2.76.: Monthly mean flow, salinity and temperature fields at 50 m depth and location of used CTD profiles – April 1998.



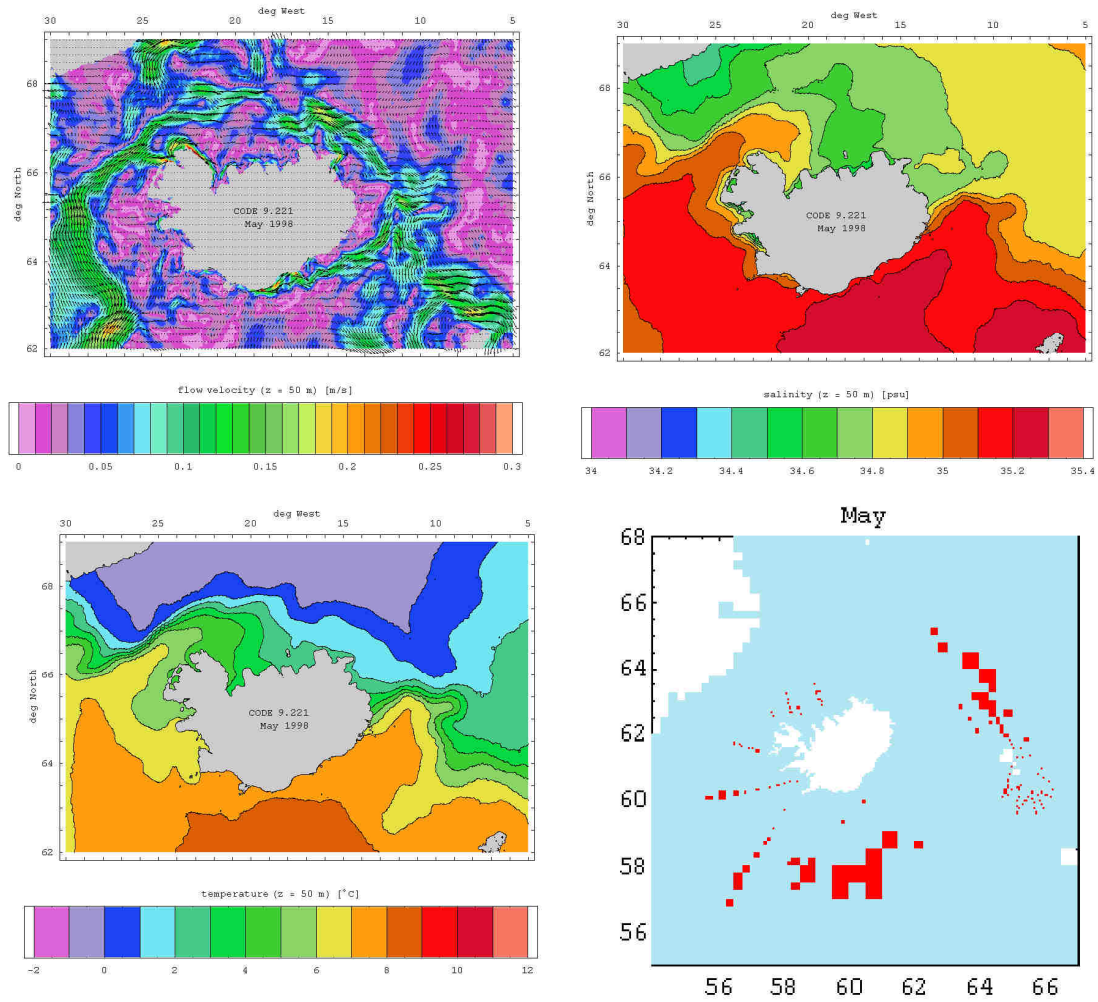


Fig. 2.77.: Monthly mean flow, salinity and temperature fields at 50 m depth and location of used CTD profiles – May 1998.

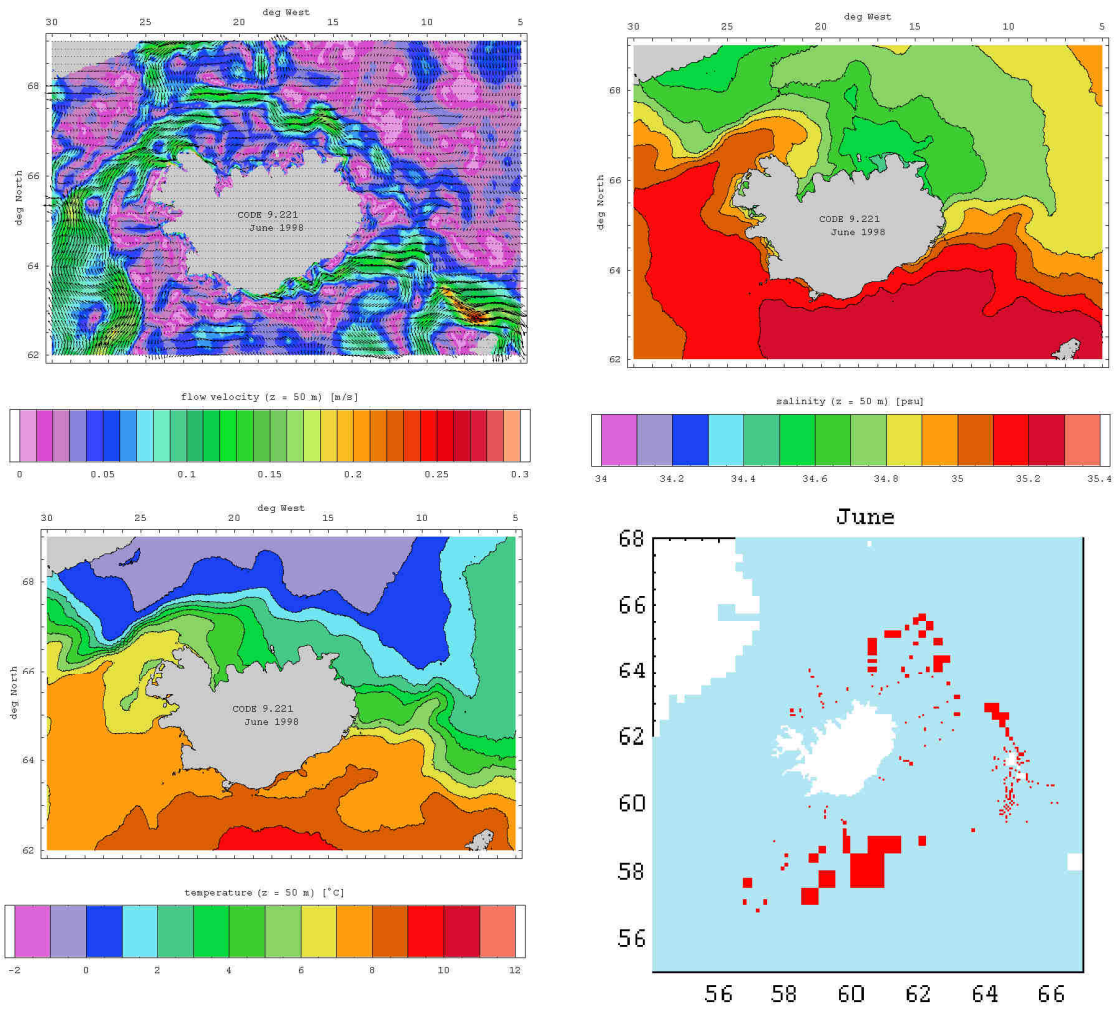


Fig. 2.78.: Monthly mean flow, salinity and temperature fields at 50 m depth and location of used CTD profiles – June 1998.

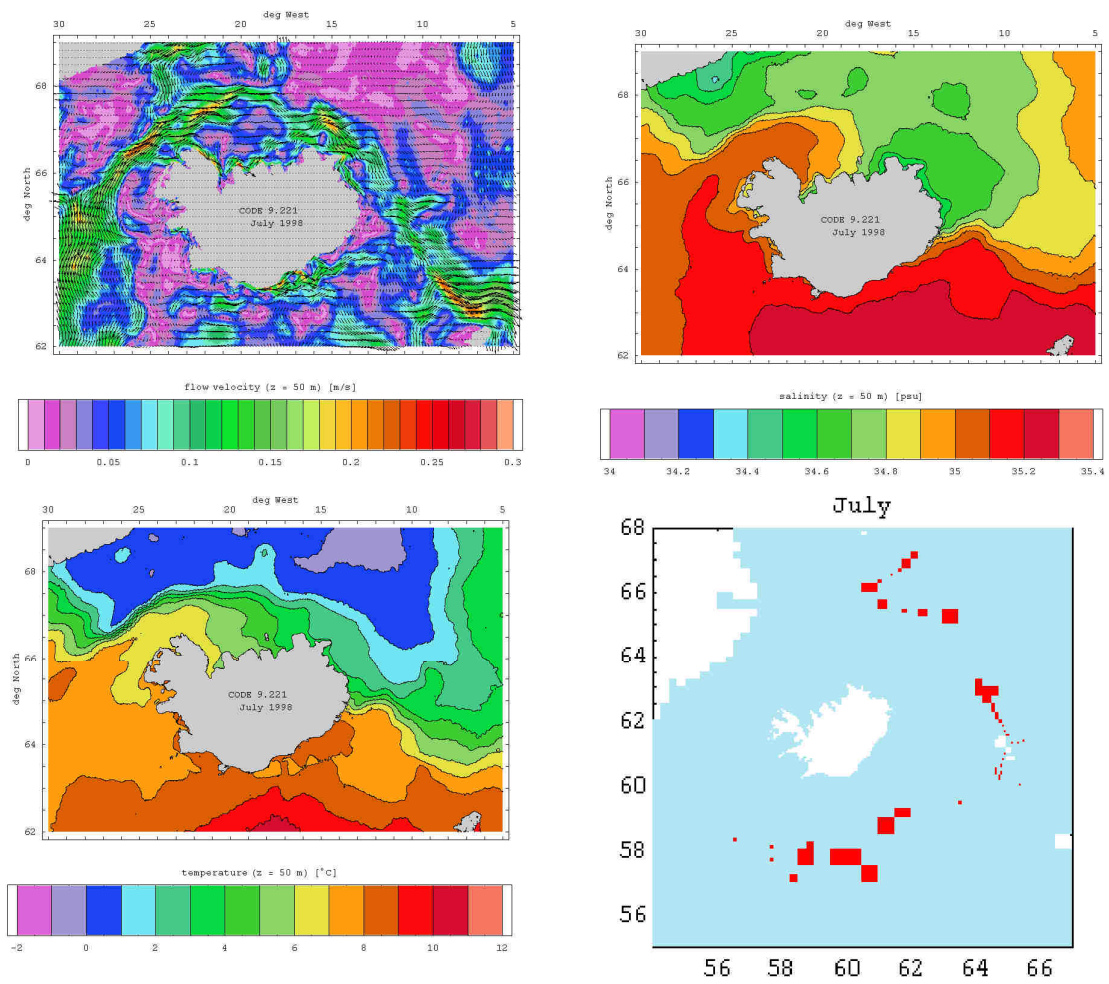


Fig. 2.79.: Monthly mean flow, salinity and temperature fields at 50 m depth and location of used CTD profiles – July 1998.

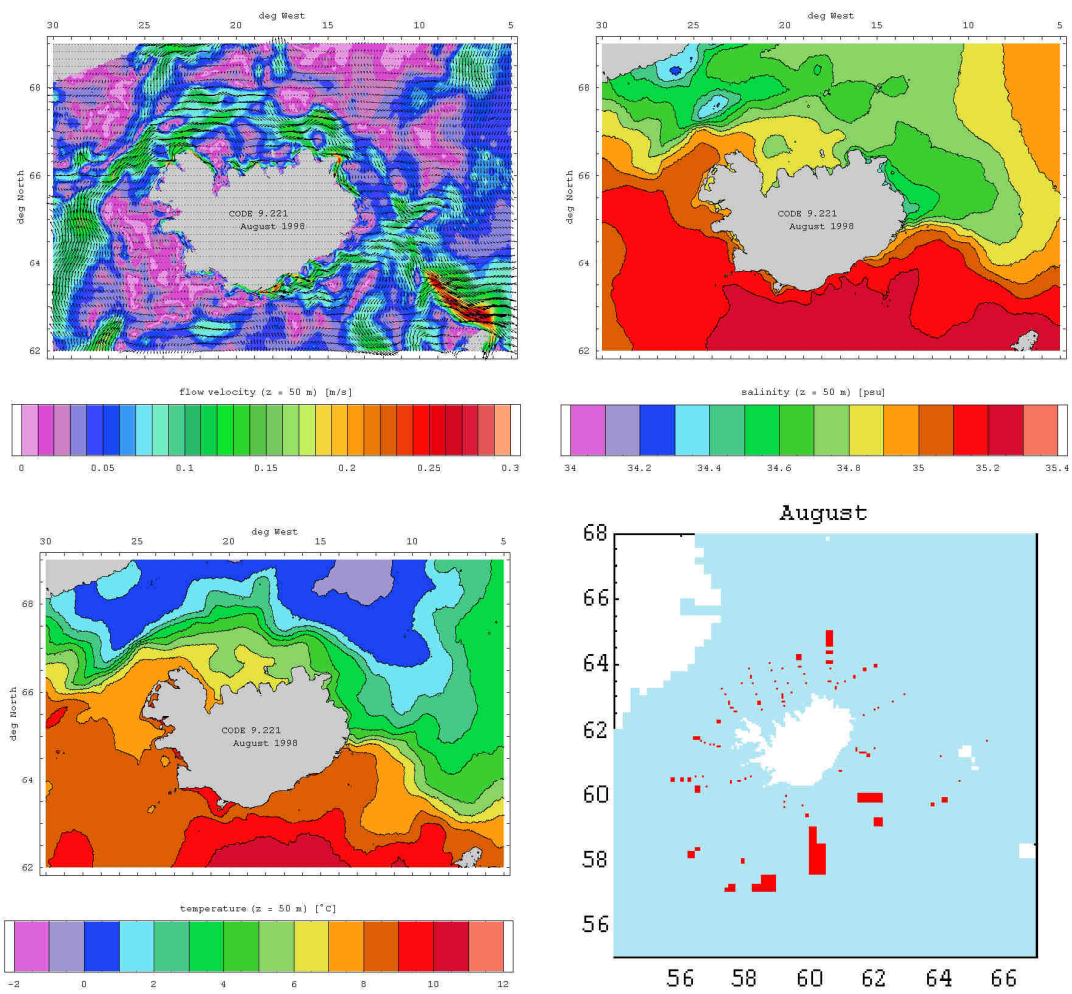


Fig. 2.80.: Monthly mean flow, salinity and temperature fields at 50 m depth and location of used CTD profiles – August 1998.

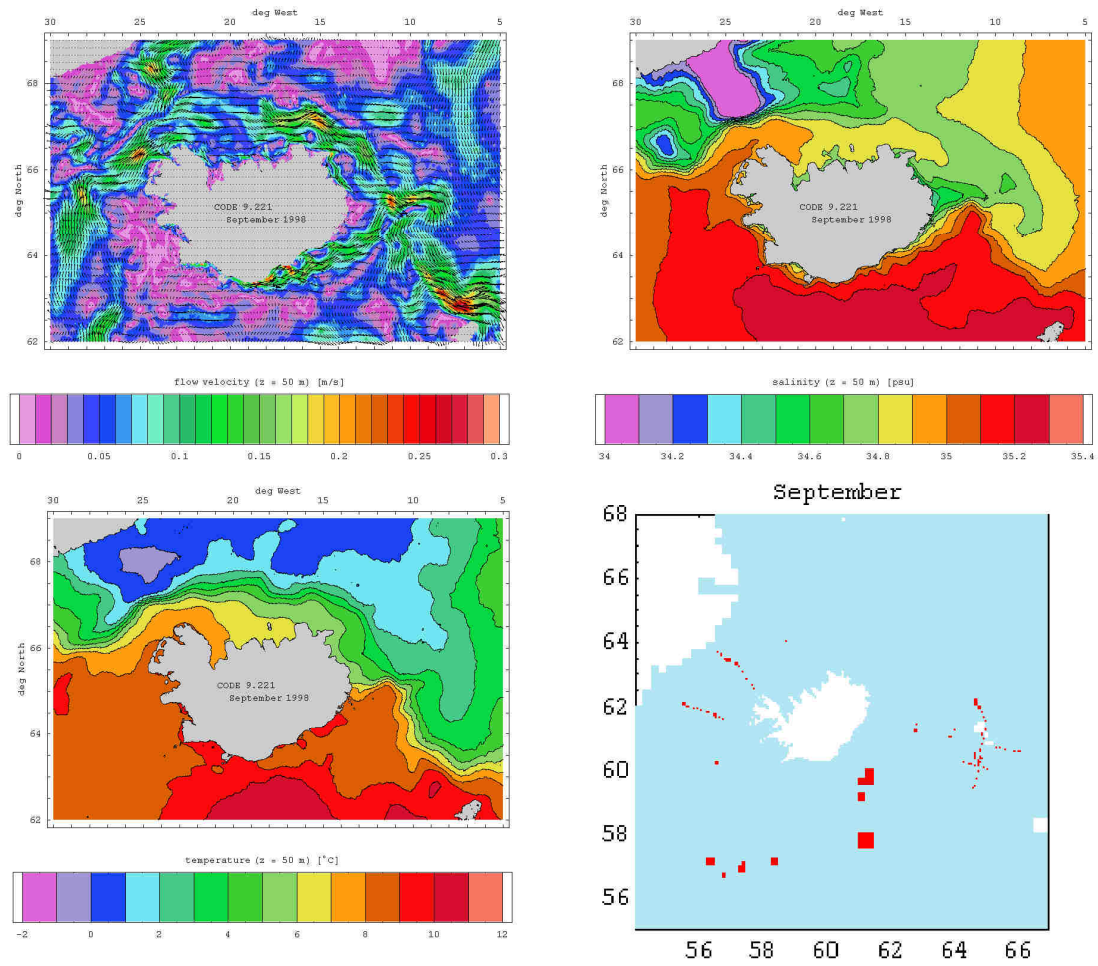


Fig. 2.81.: Monthly mean flow, salinity and temperature fields at 50 m depth and location of used CTD profiles – September 1998.



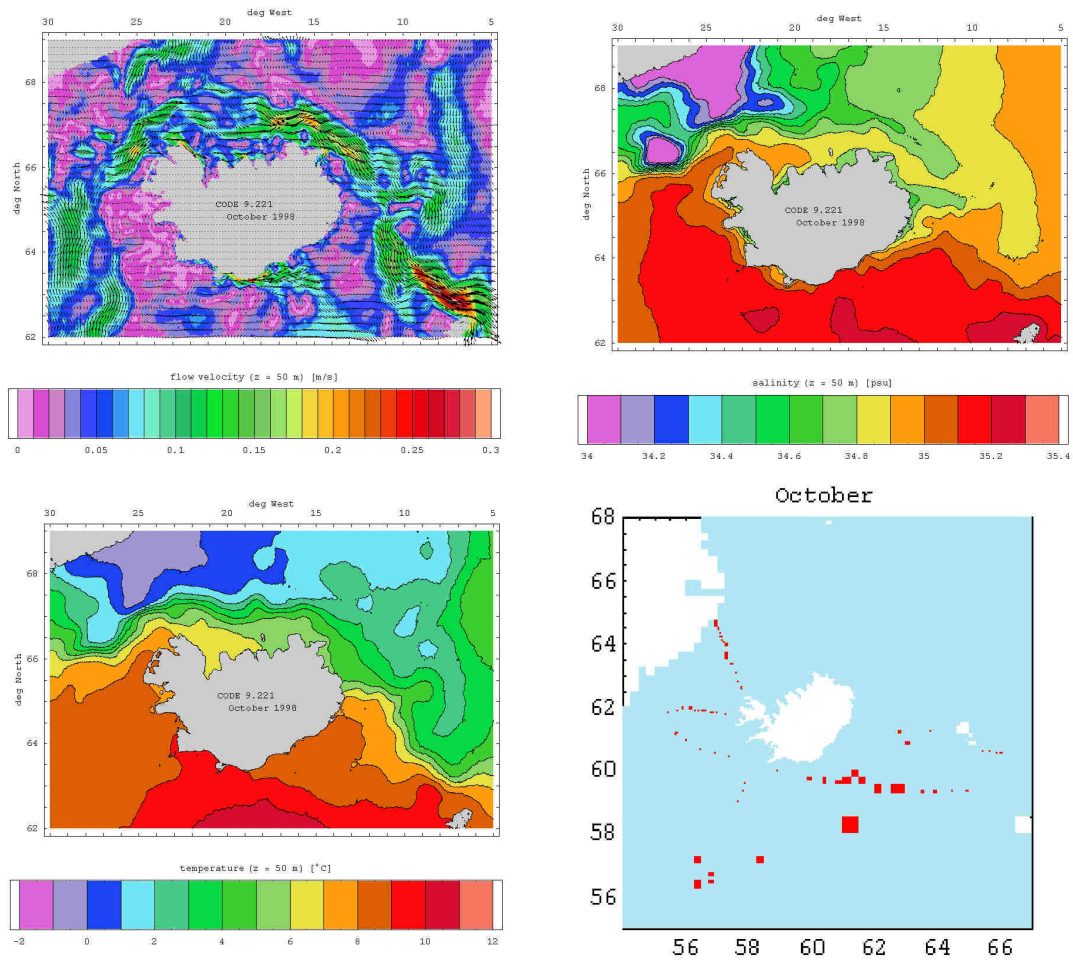


Fig. 2.82.: Monthly mean flow, salinity and temperature fields at 50 m depth and location of used CTD profiles – October 1998.



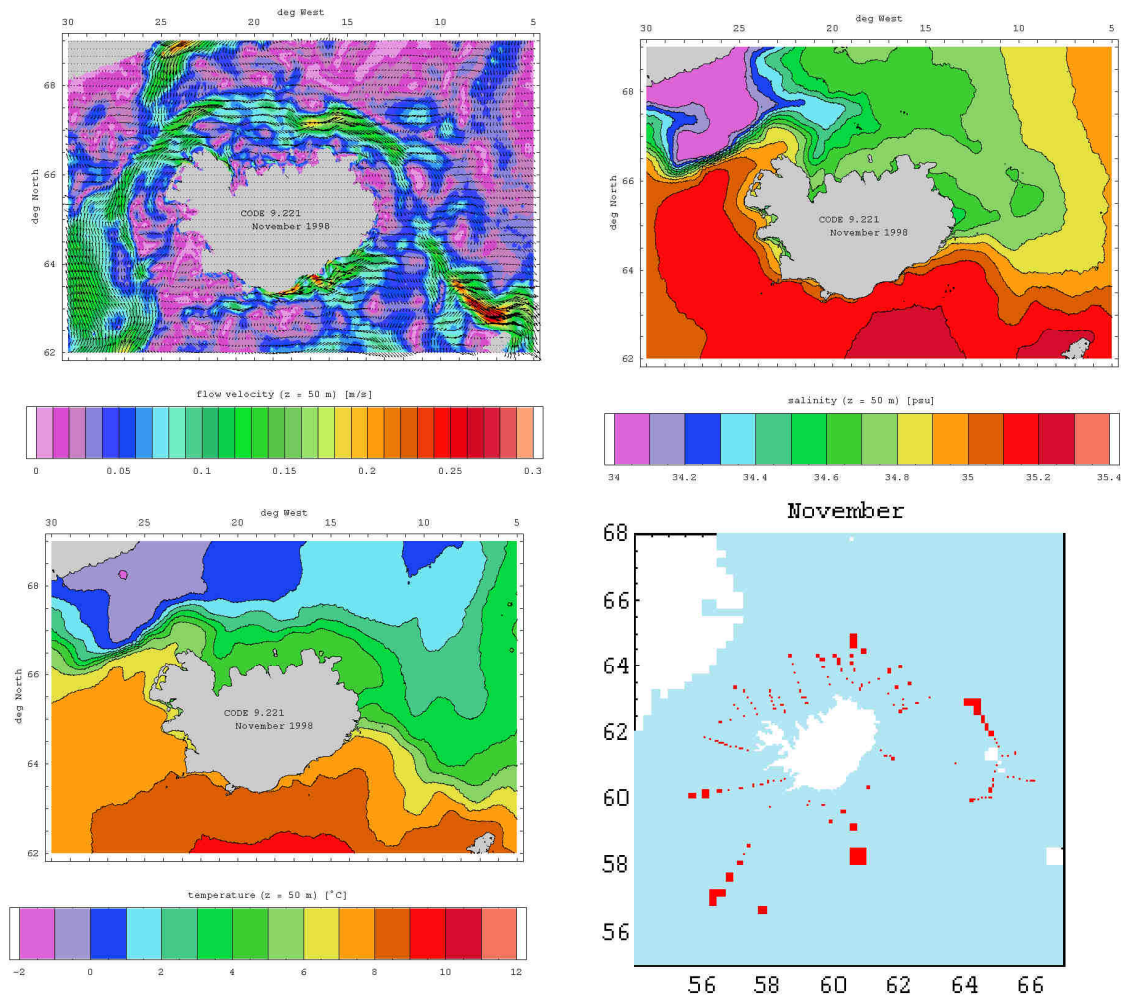


Fig. 2.83.: Monthly mean flow, salinity and temperature fields at 50 m depth and location of used CTD profiles – November 1998.

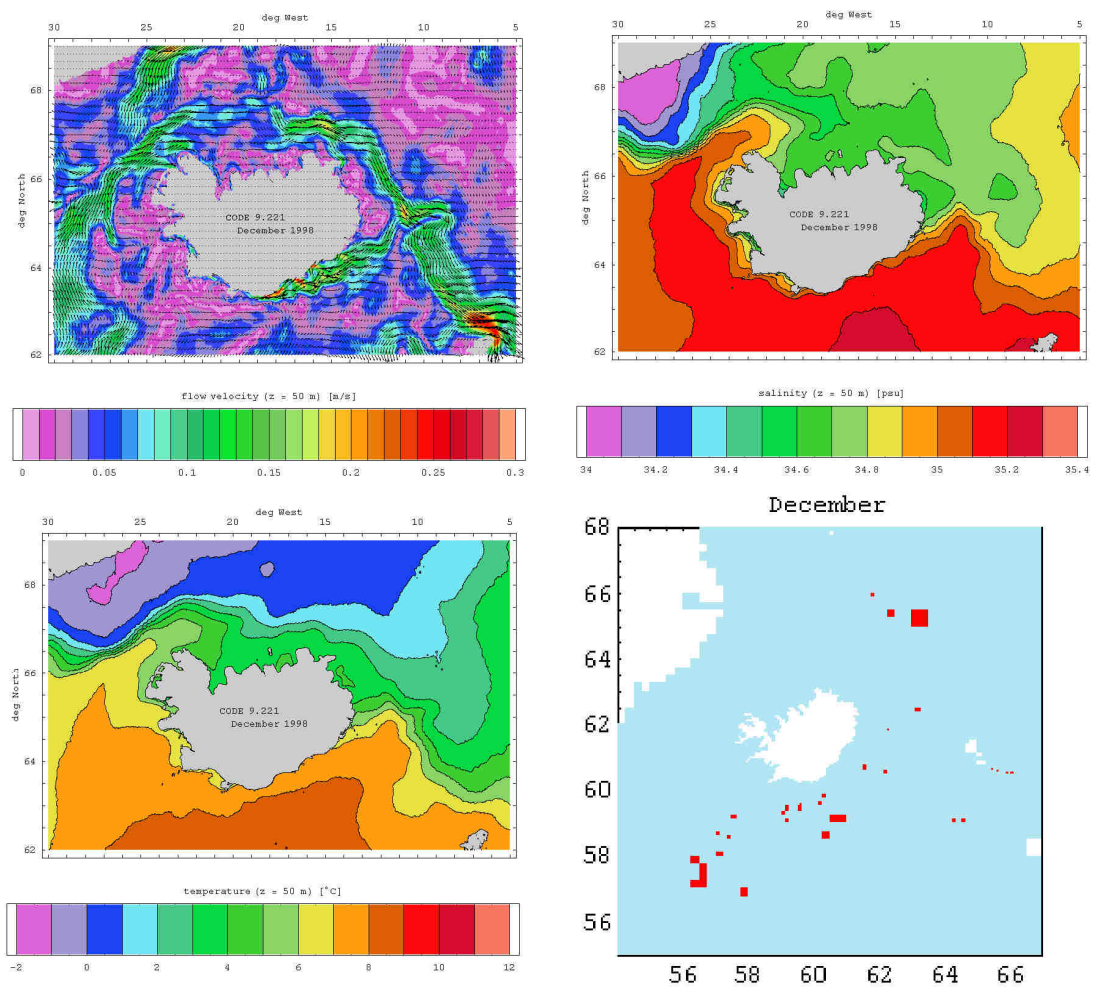


Fig. 2.84.: Monthly mean flow, salinity and temperature fields at 50 m depth and location of used CTD profiles – December 1998.

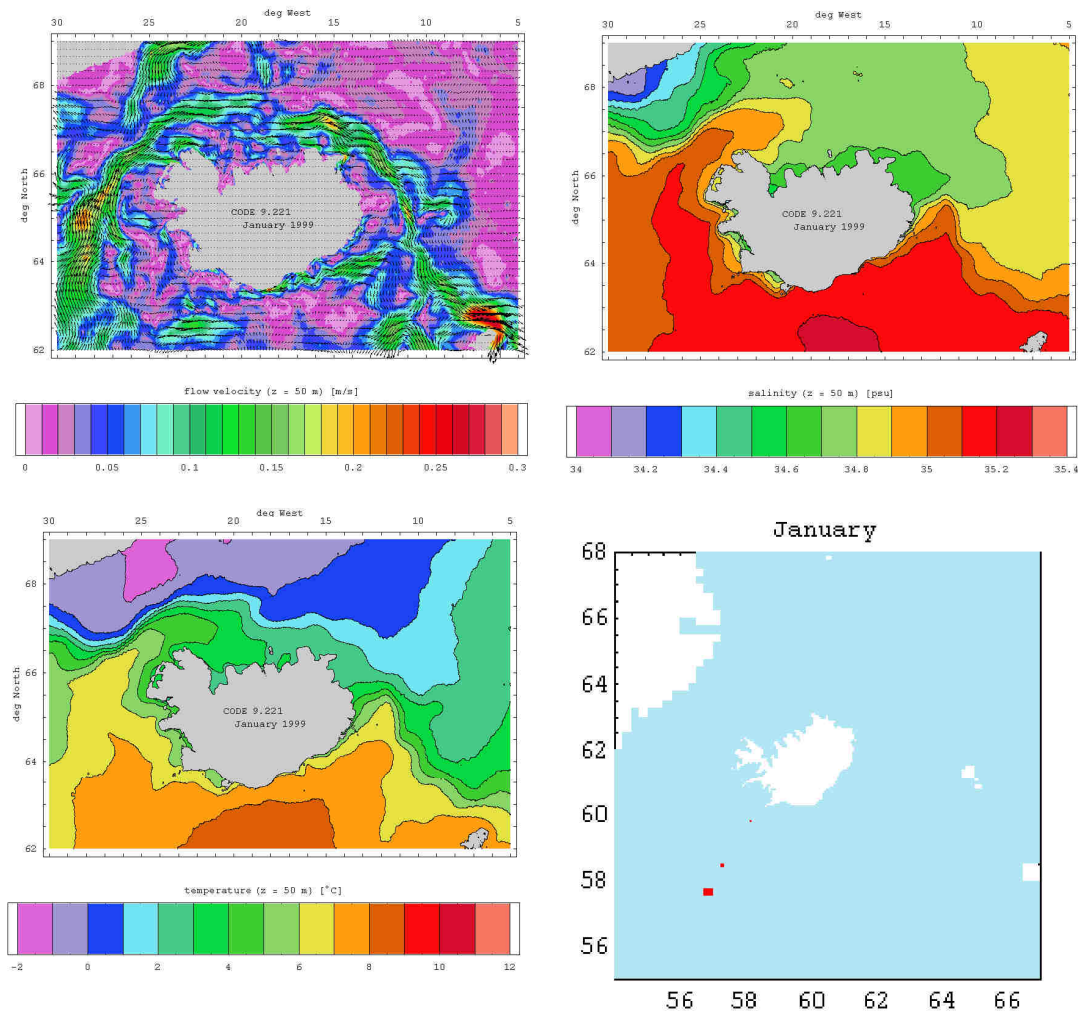


Fig. 2.85.: Monthly mean flow, salinity and temperature fields at 50 m depth and location of used CTD profiles – January 1999.

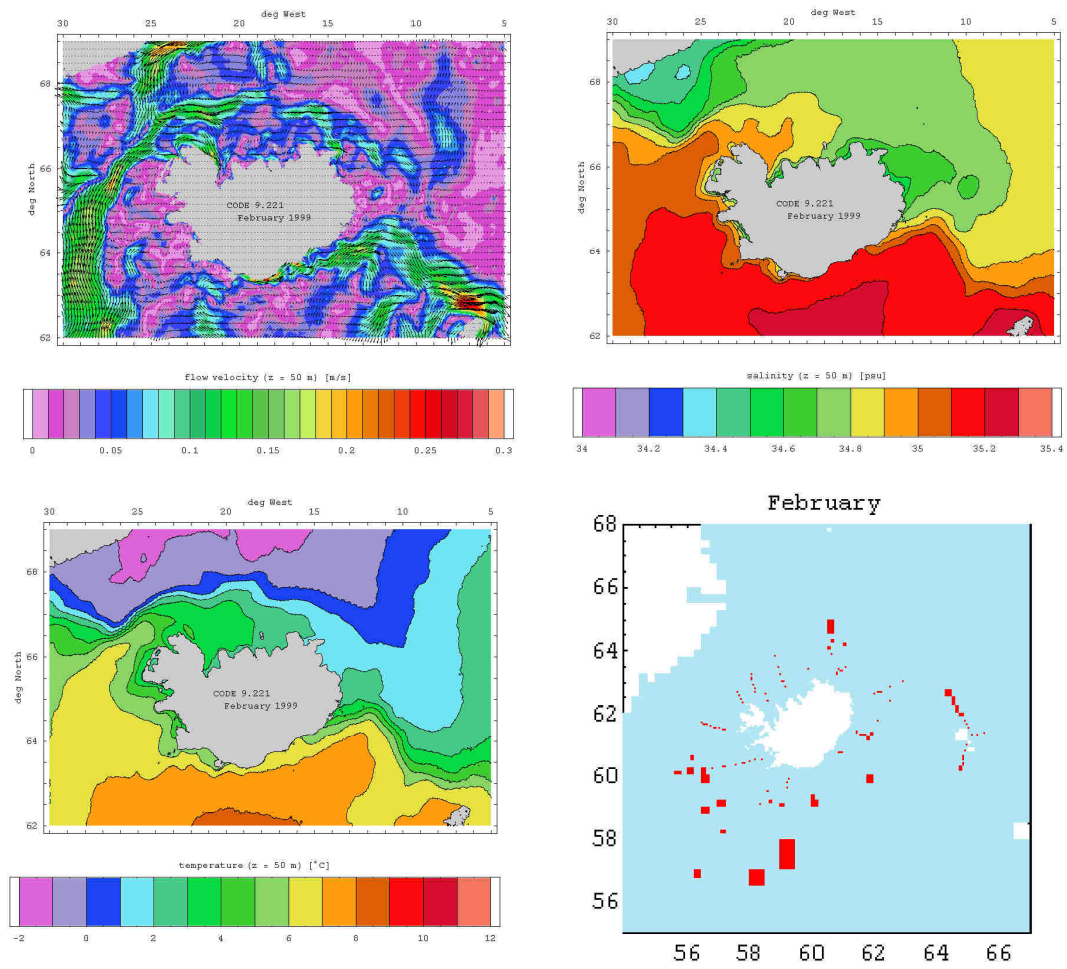


Fig. 2.86.: Monthly mean flow, salinity and temperature fields at 50 m depth and location of used CTD profiles – February 1999.

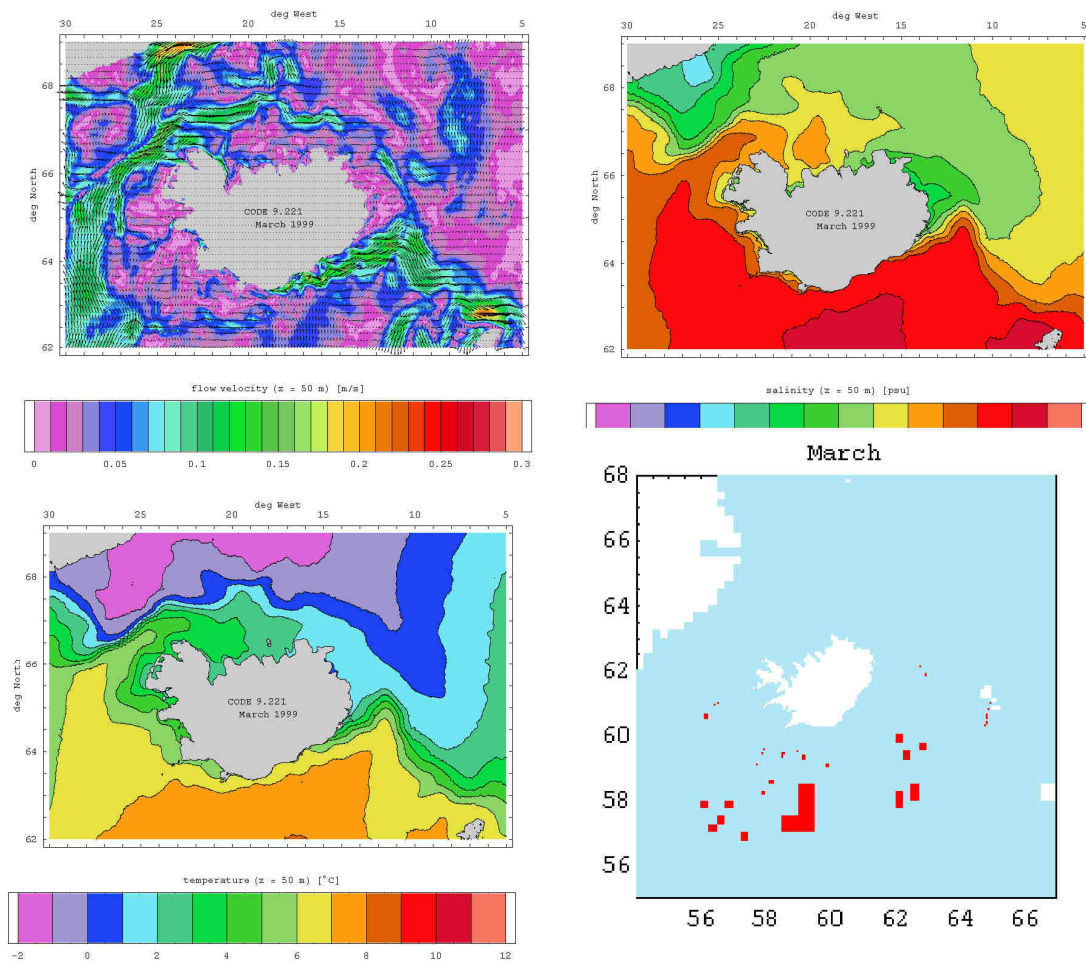


Fig. 2.87.: Monthly mean flow, salinity and temperature fields at 50 m depth and location of used CTD profiles – March 1999.



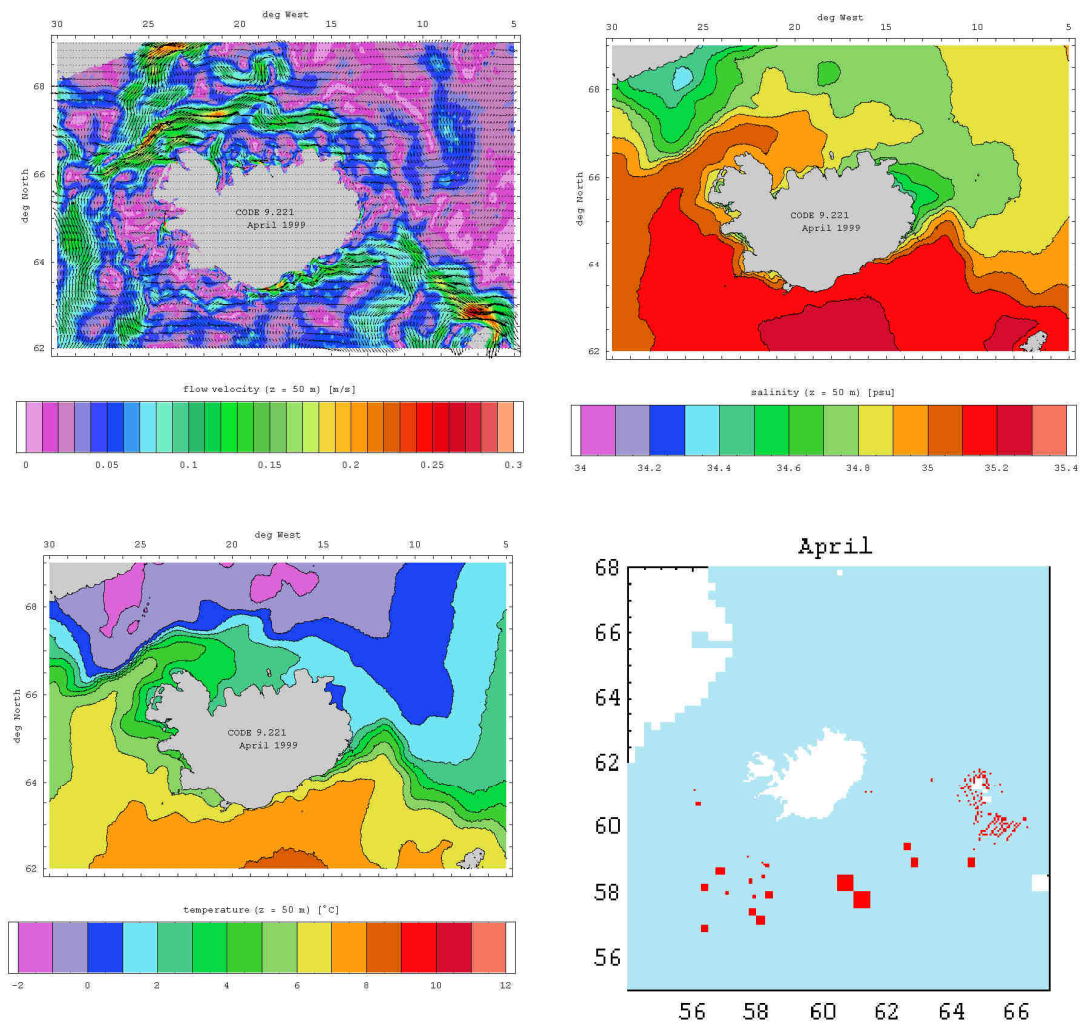


Fig. 2.88.: Monthly mean flow, salinity and temperature fields at 50 m depth and location of used CTD profiles – April 1999.



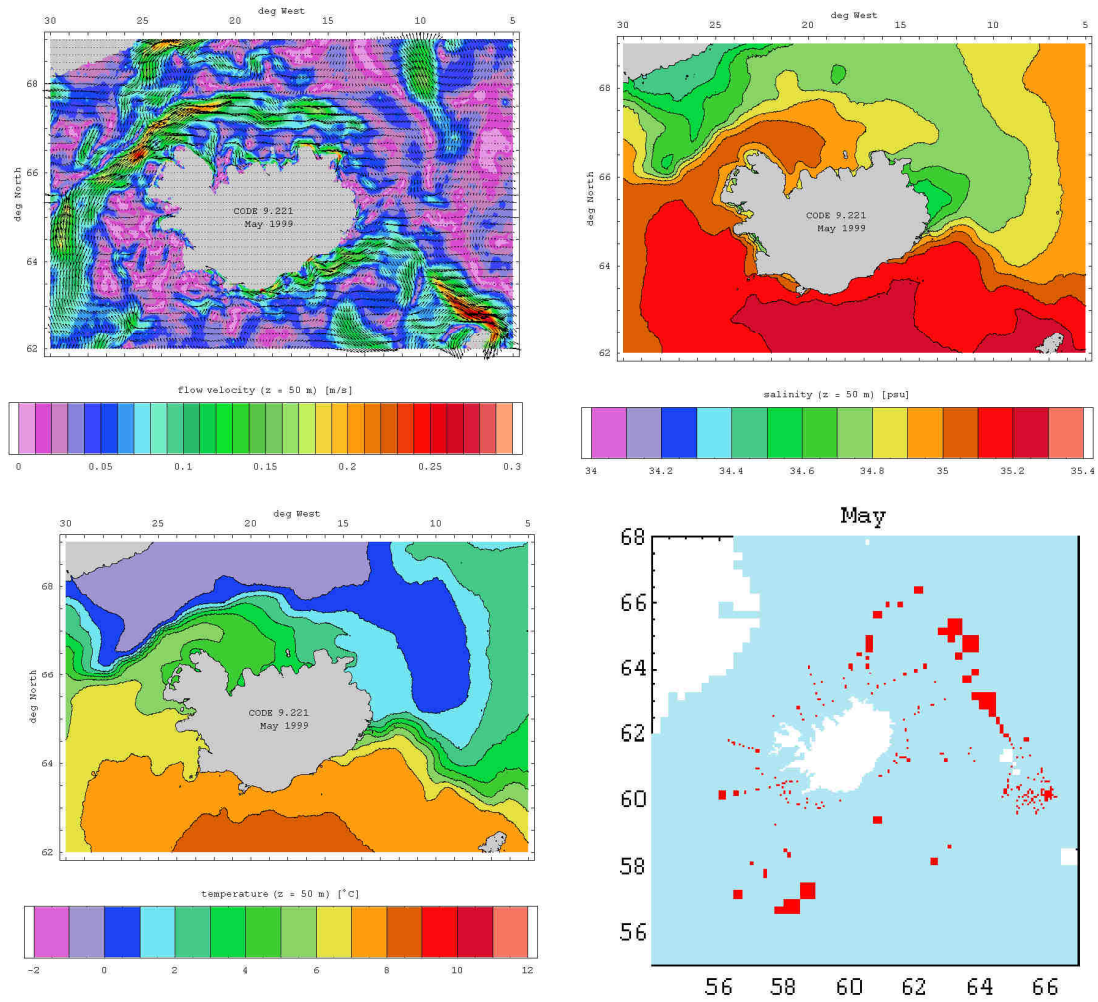


Fig. 2.89.: Monthly mean flow, salinity and temperature fields at 50 m depth and location of used CTD profiles – May 1999.

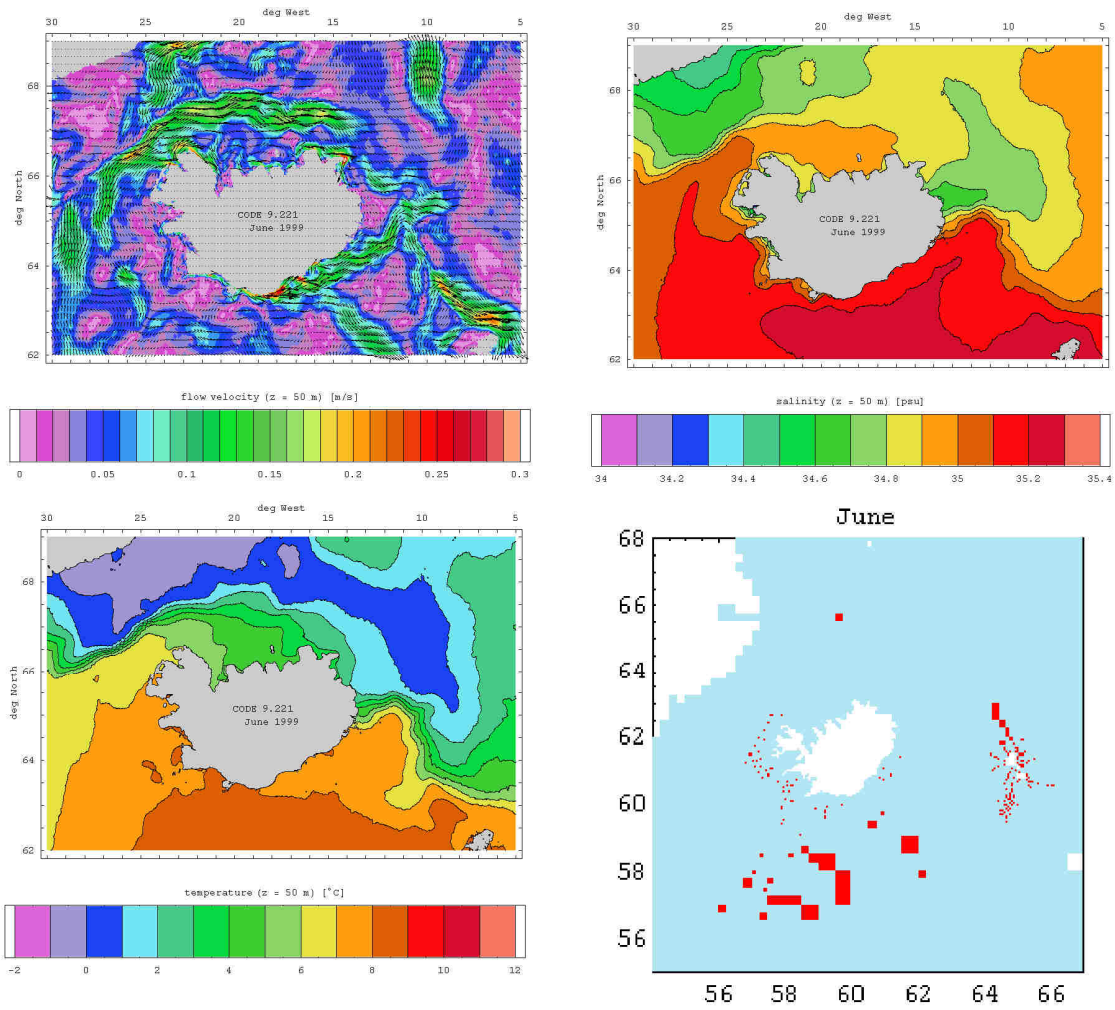


Fig. 2.90.: Monthly mean flow, salinity and temperature fields at 50 m depth and location of used CTD profiles – June 1999.

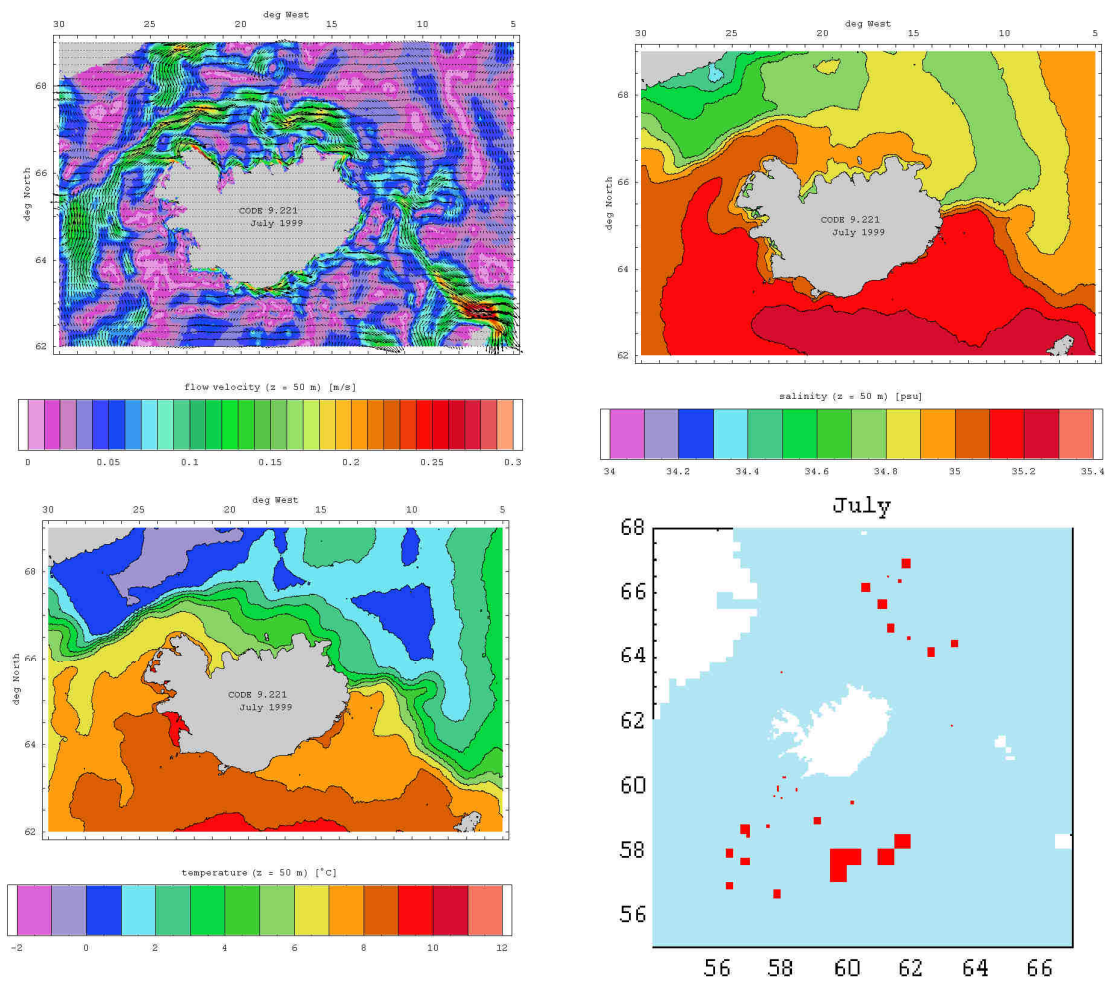


Fig. 2.91.: Monthly mean flow, salinity and temperature fields at 50 m depth and location of used CTD profiles – July 1999.

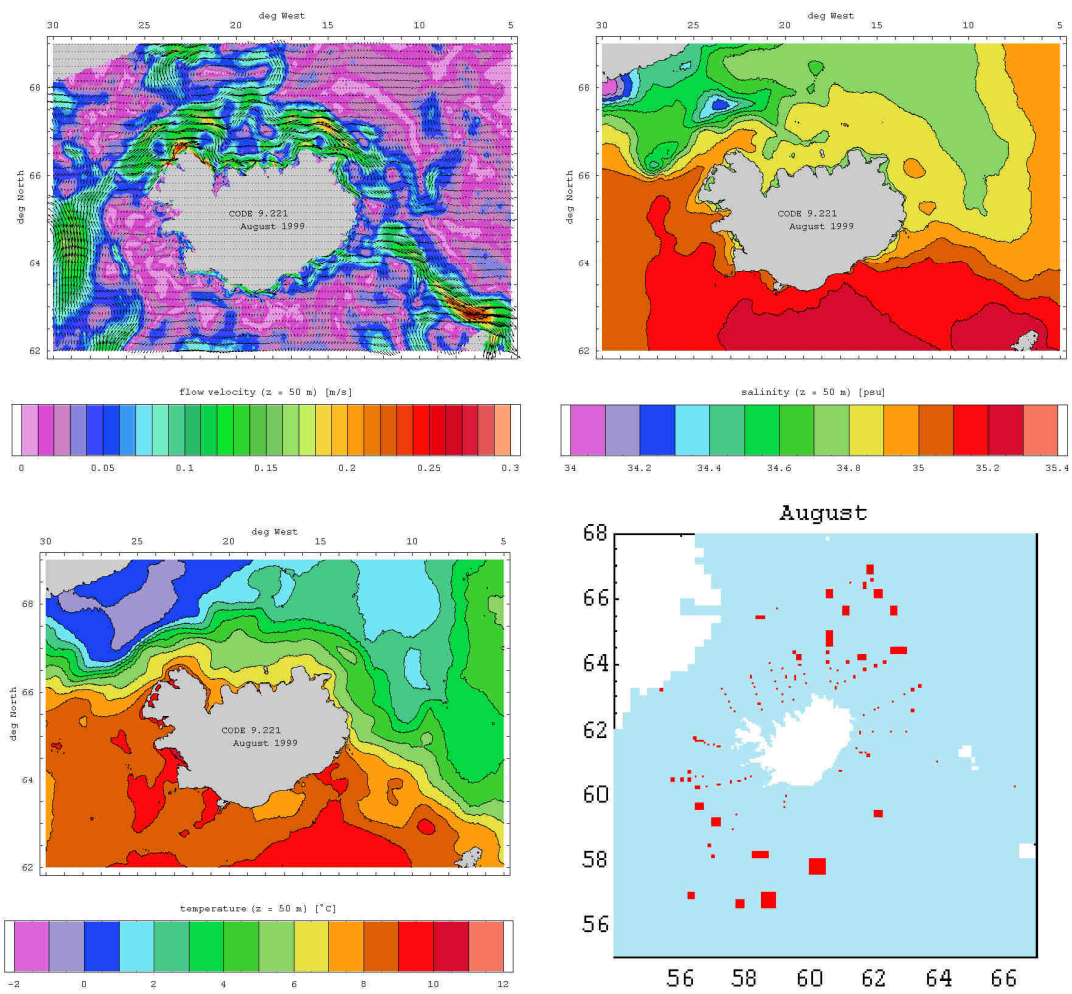


Fig. 2.92.: Monthly mean flow, salinity and temperature fields at 50 m depth and location of used CTD profiles – August 1999.

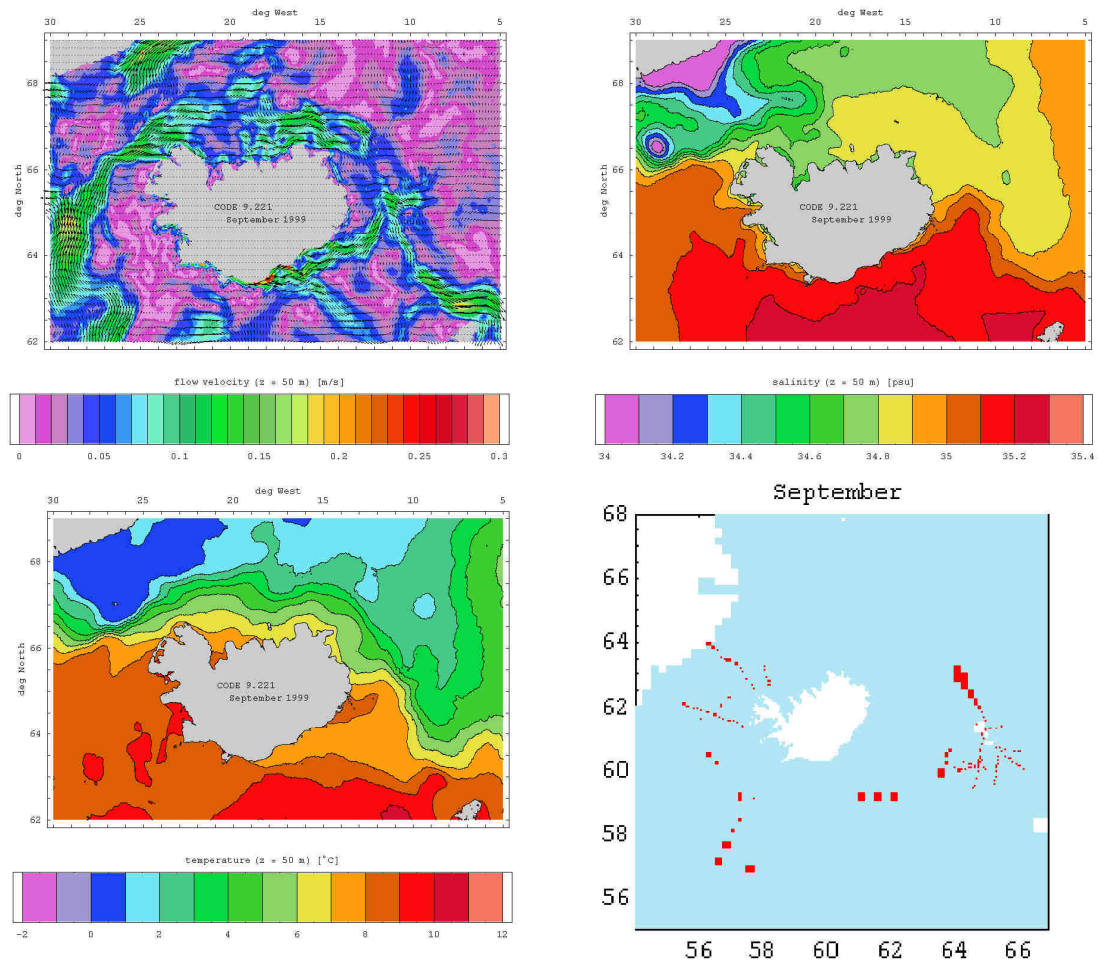


Fig. 2.93.: Monthly mean flow, salinity and temperature fields at 50 m depth and location of used CTD profiles – September 1999.



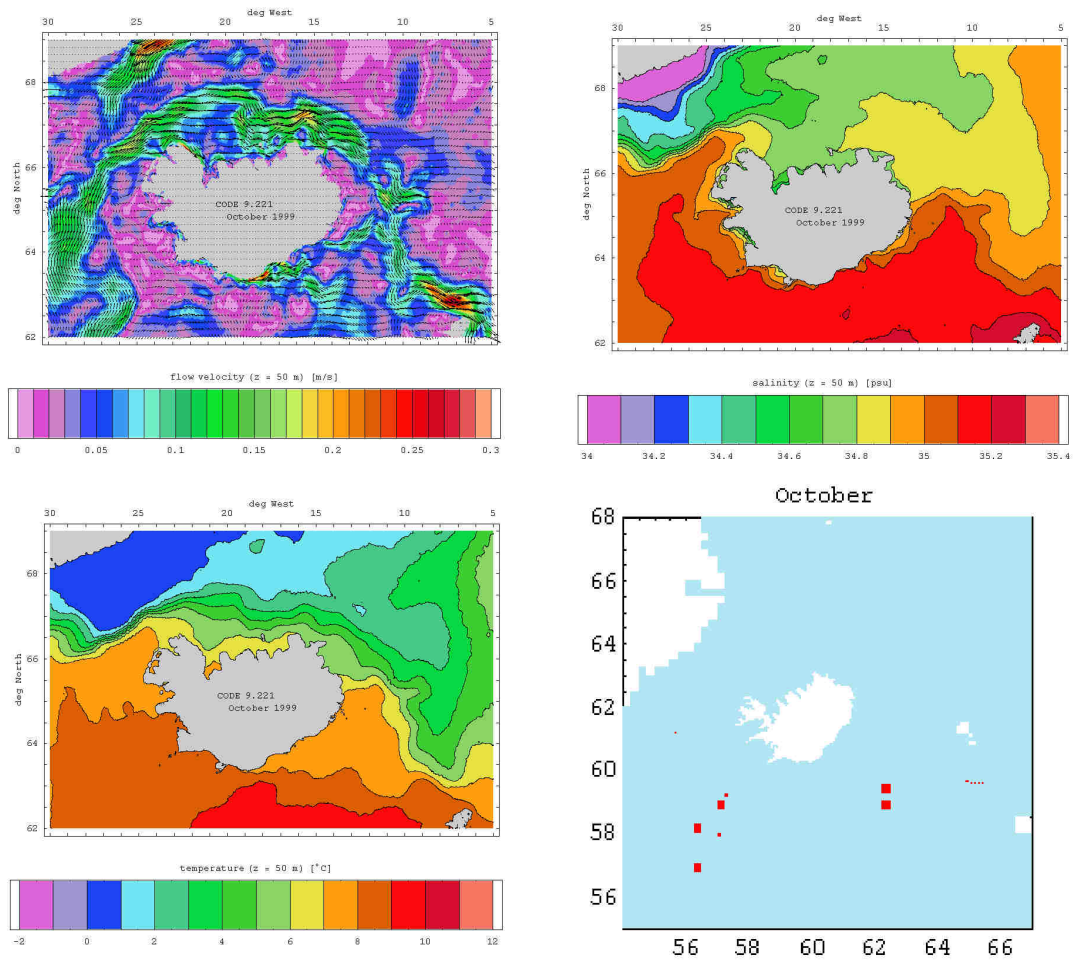


Fig. 2.94.: Monthly mean flow, salinity and temperature fields at 50 m depth and location of used CTD profiles – October 1999.



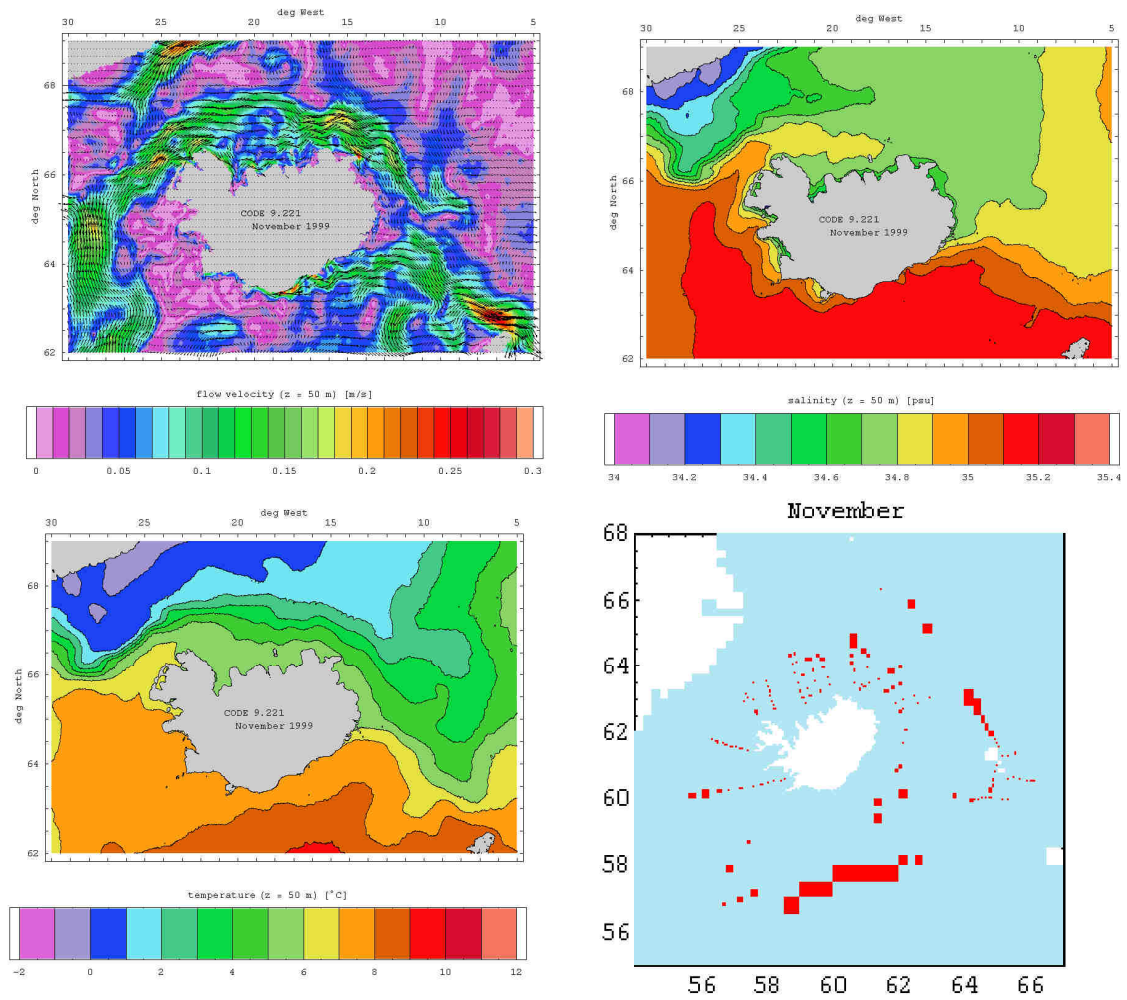


Fig. 2.95.: Monthly mean flow, salinity and temperature fields at 50 m depth and location of used CTD profiles – November 1999.

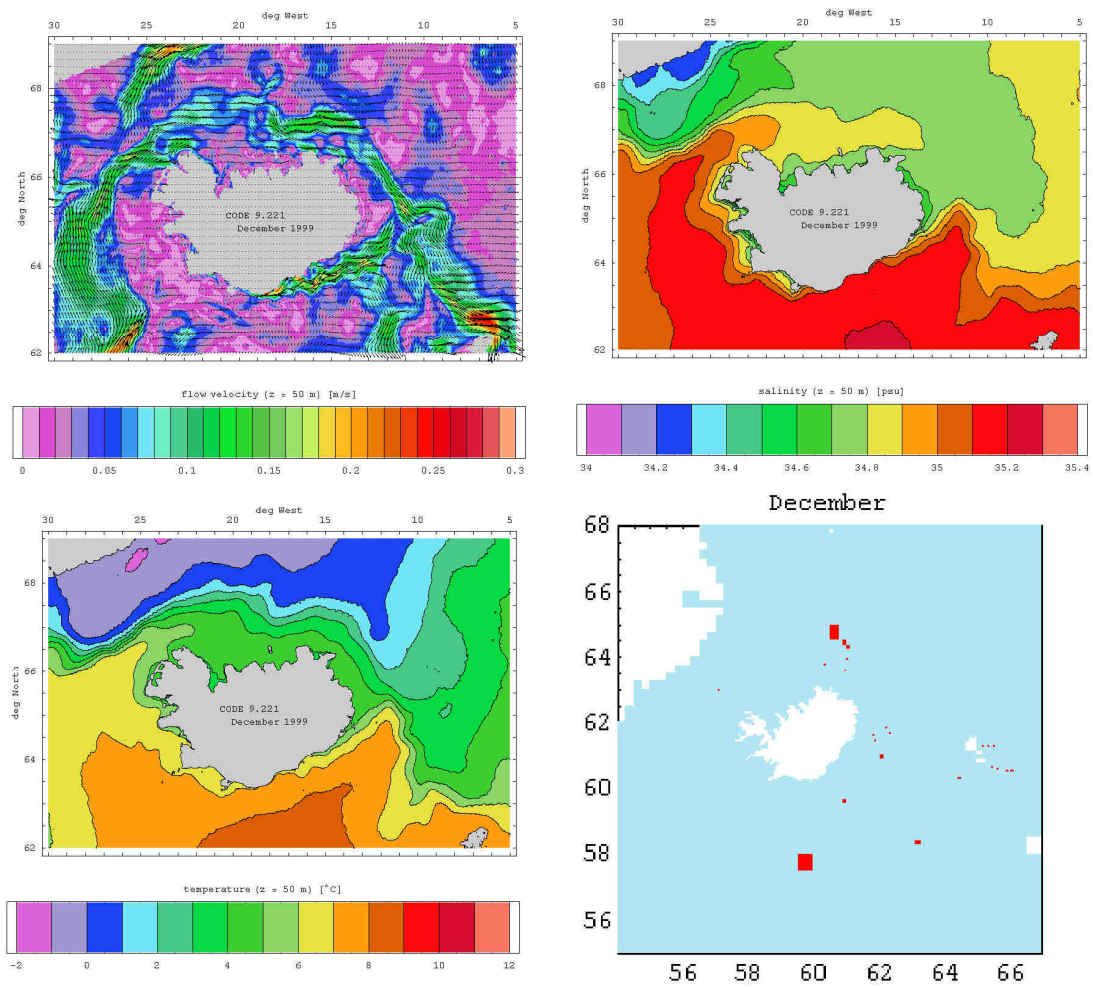


Fig. 2.96.: Monthly mean flow, salinity and temperature fields at 50 m depth and location of used CTD profiles – December 1999.

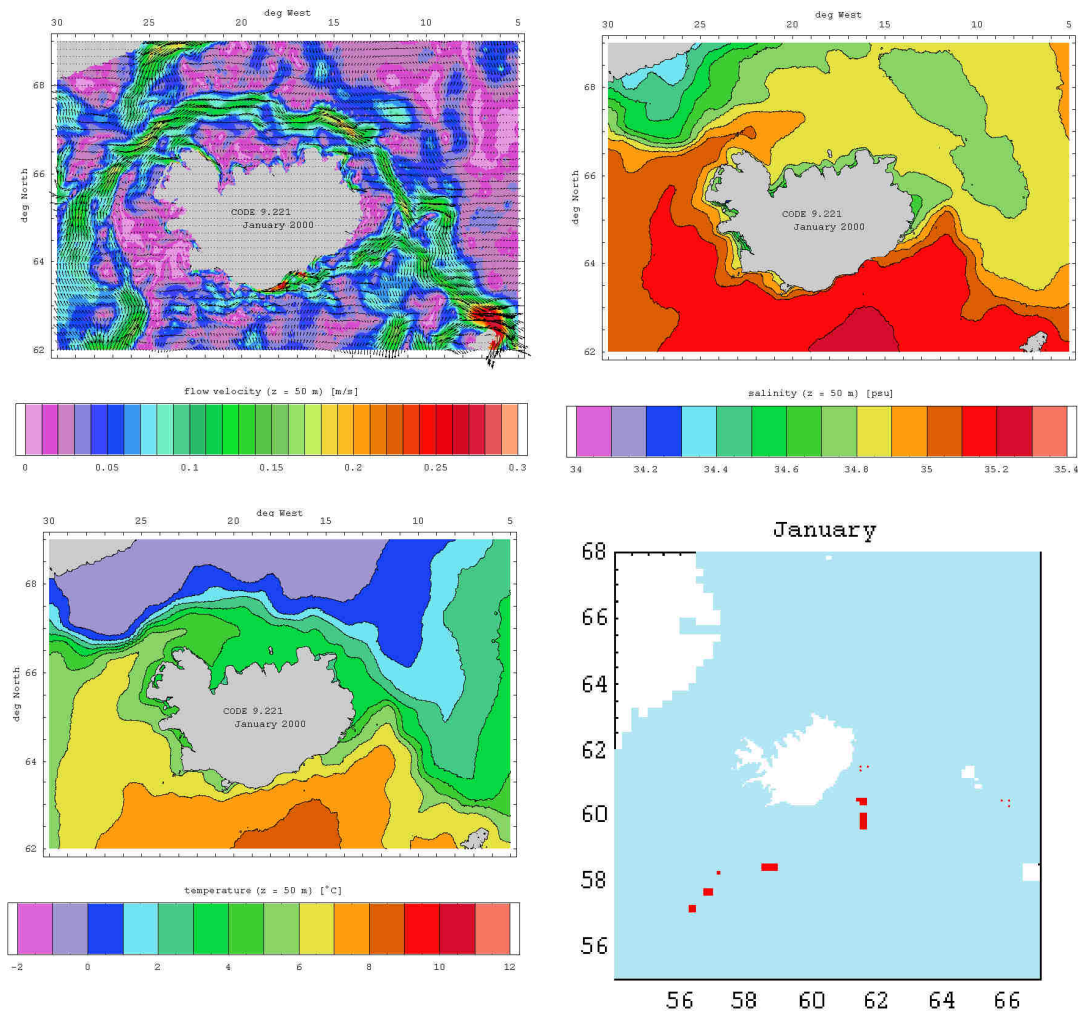


Fig. 2.97.: Monthly mean flow, salinity and temperature fields at 50 m depth and location of used CTD profiles – January 2000.

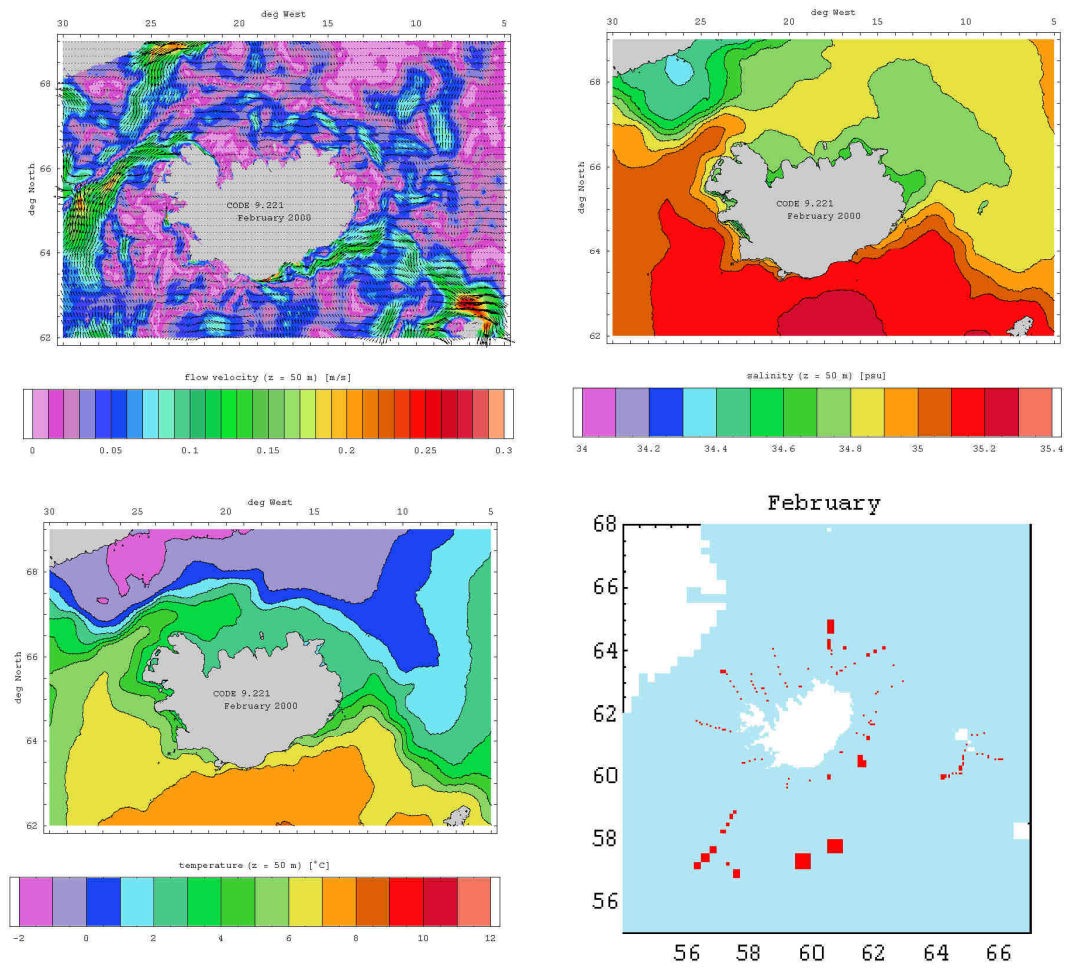


Fig. 2.98.: Monthly mean flow, salinity and temperature fields at 50 m depth and location of used CTD profiles – February 2000.

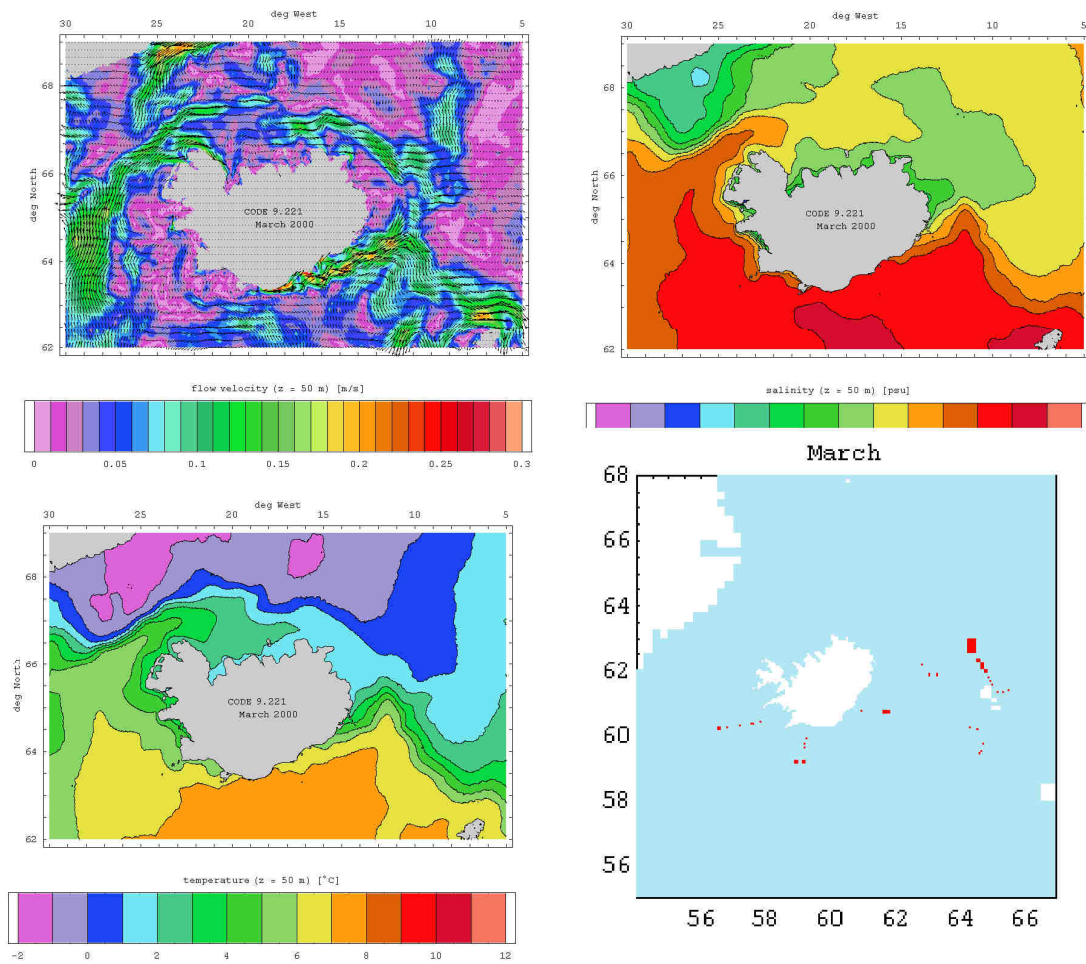


Fig. 2.99.: Monthly mean flow, salinity and temperature fields at 50 m depth and location of used CTD profiles – March 2000.



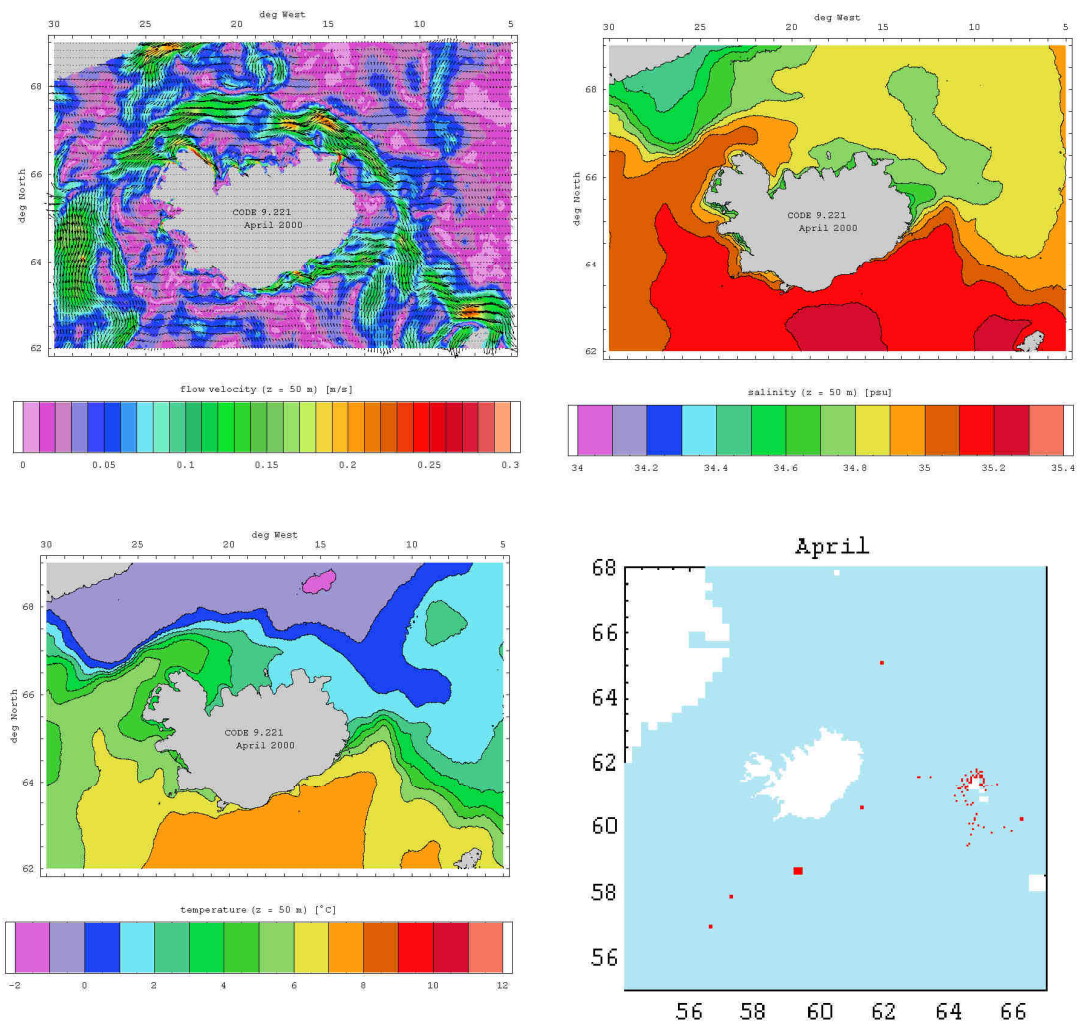


Fig. 2.100.: Monthly mean flow, salinity and temperature fields at 50 m depth and location of used CTD profiles – April 2000.



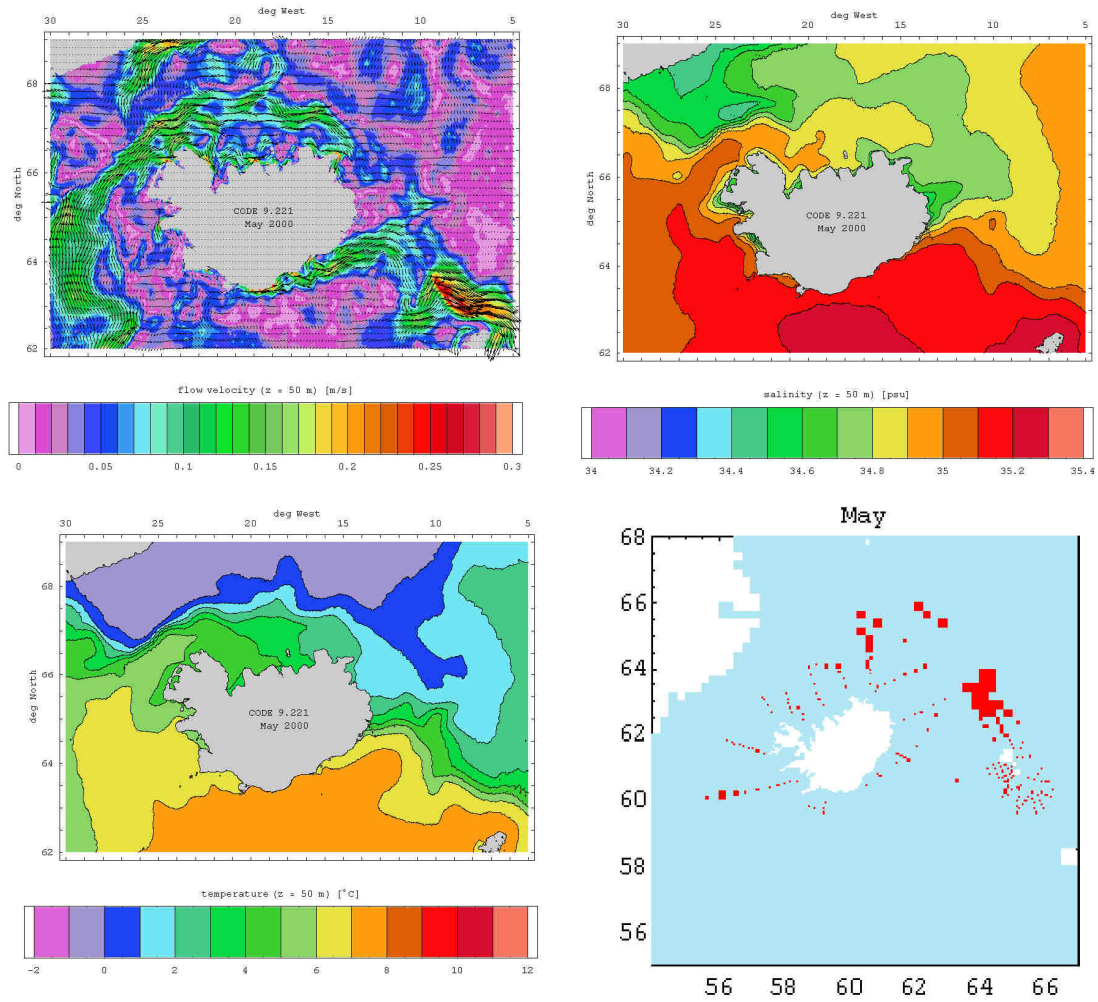


Fig. 2.101.: Monthly mean flow, salinity and temperature fields at 50 m depth and location of used CTD profiles – May 2000.

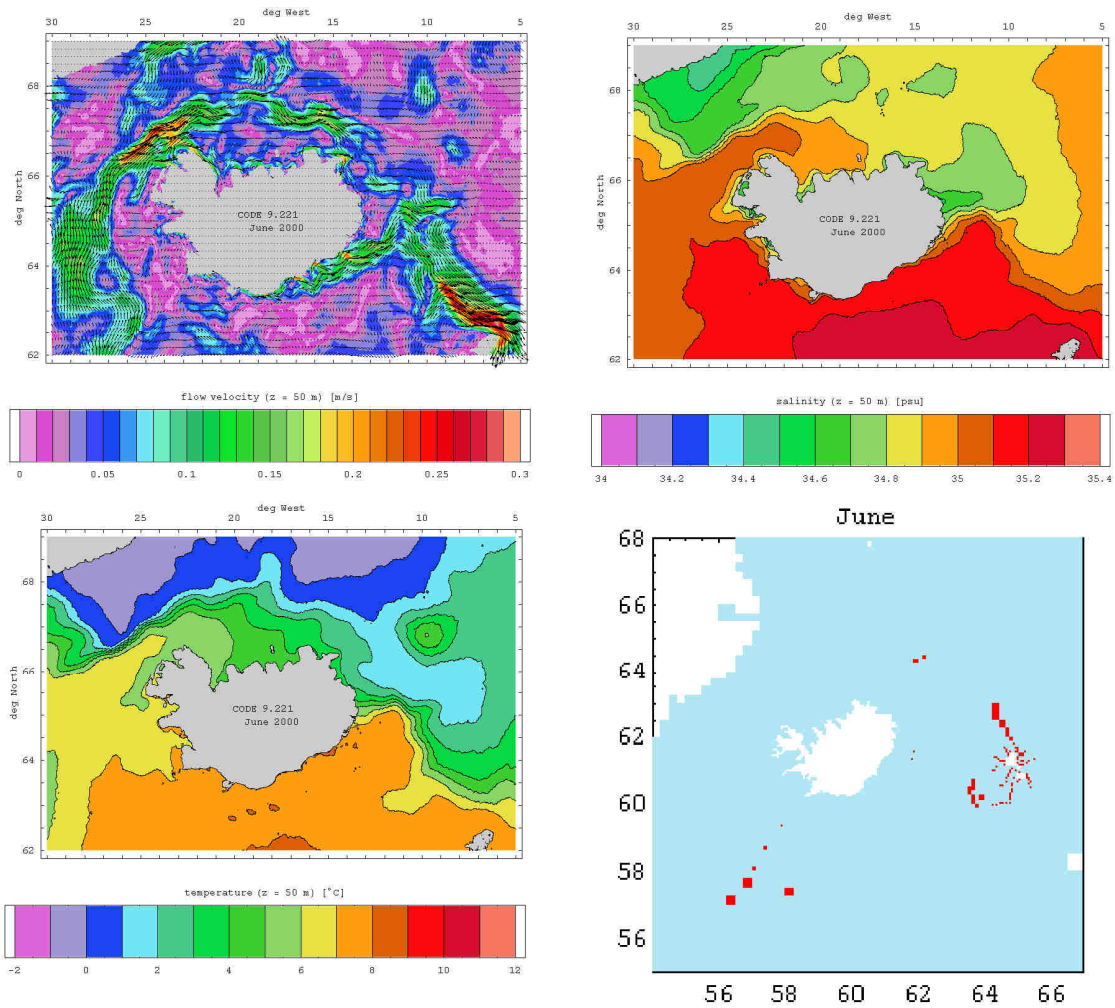


Fig. 2.102.: Monthly mean flow, salinity and temperature fields at 50 m depth and location of used CTD profiles – June 2000.

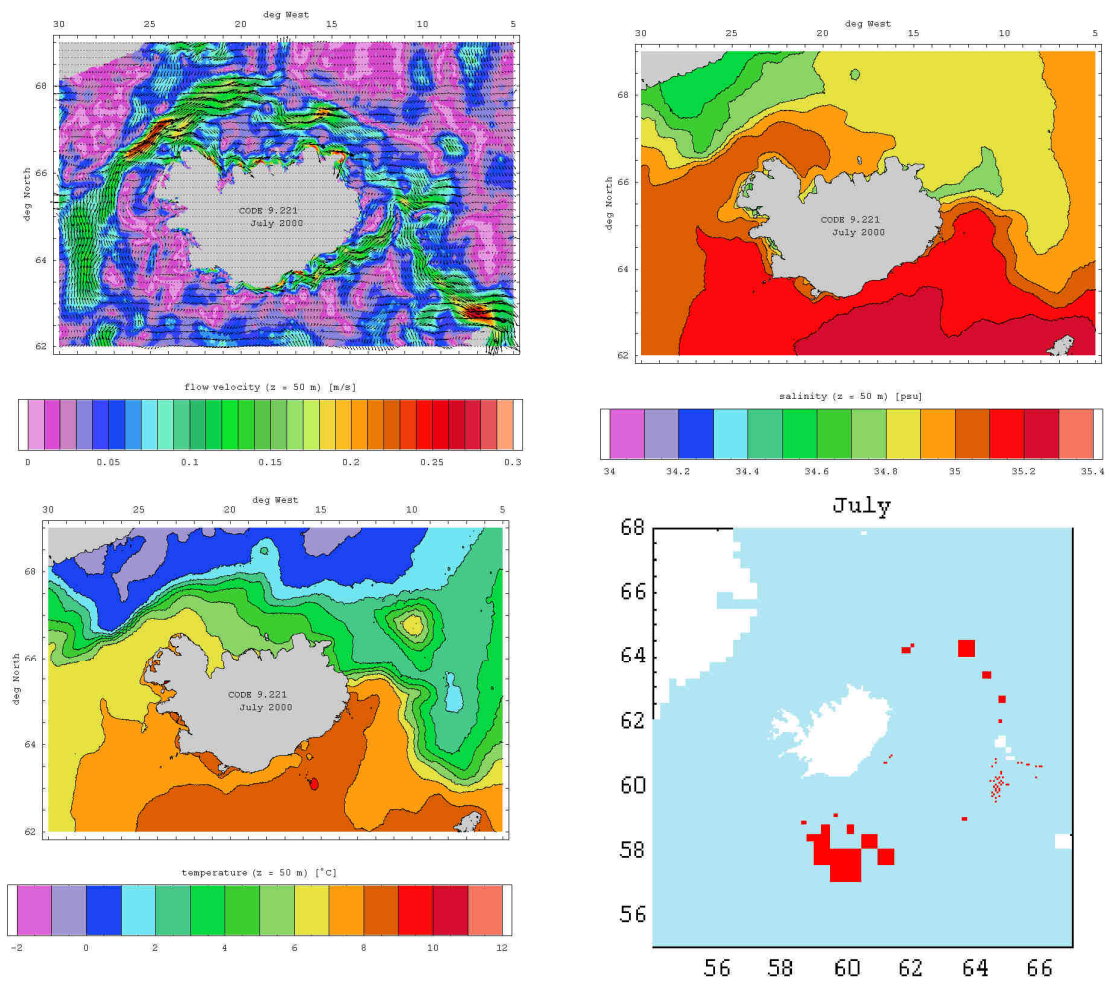


Fig. 2.103.: Monthly mean flow, salinity and temperature fields at 50 m depth and location of used CTD profiles – July 2000.

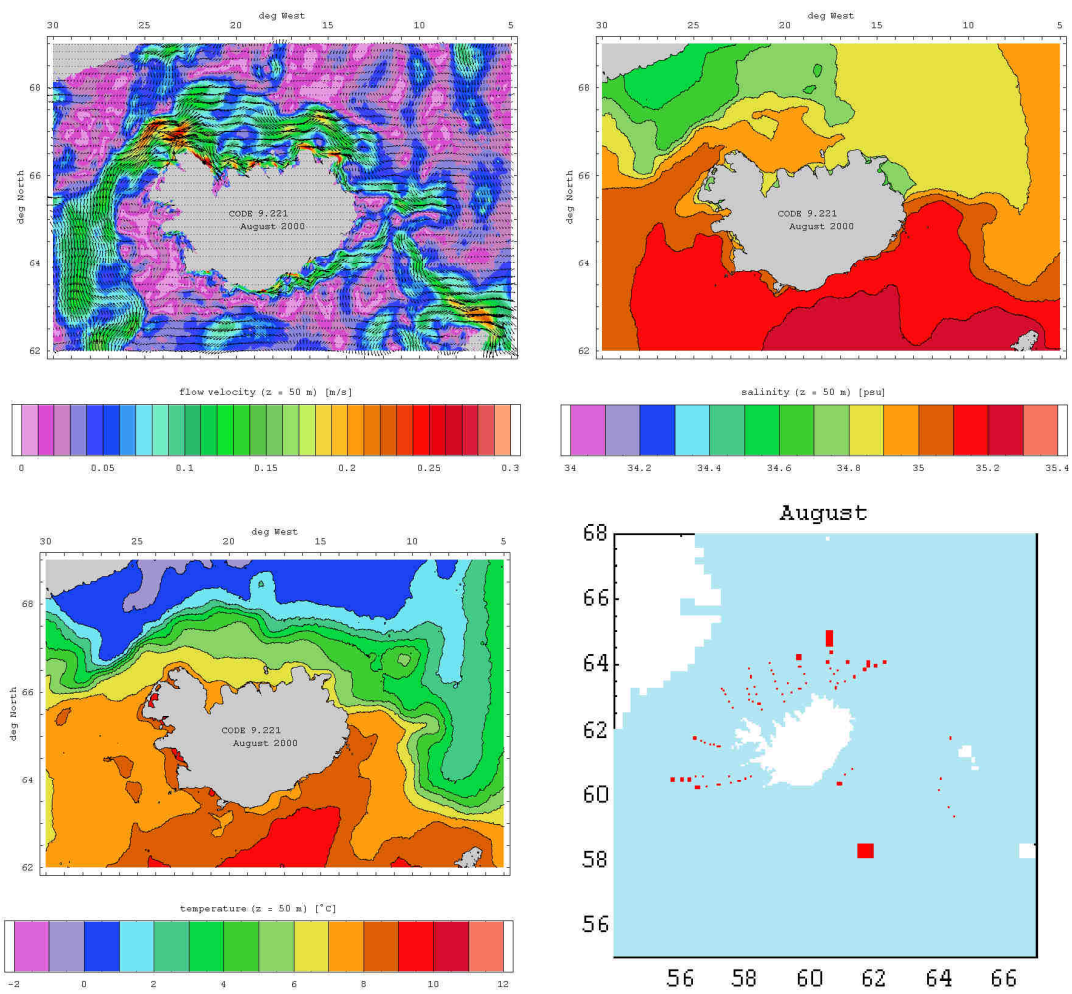


Fig. 2.104.: Monthly mean flow, salinity and temperature fields at 50 m depth and location of used CTD profiles – August 2000.

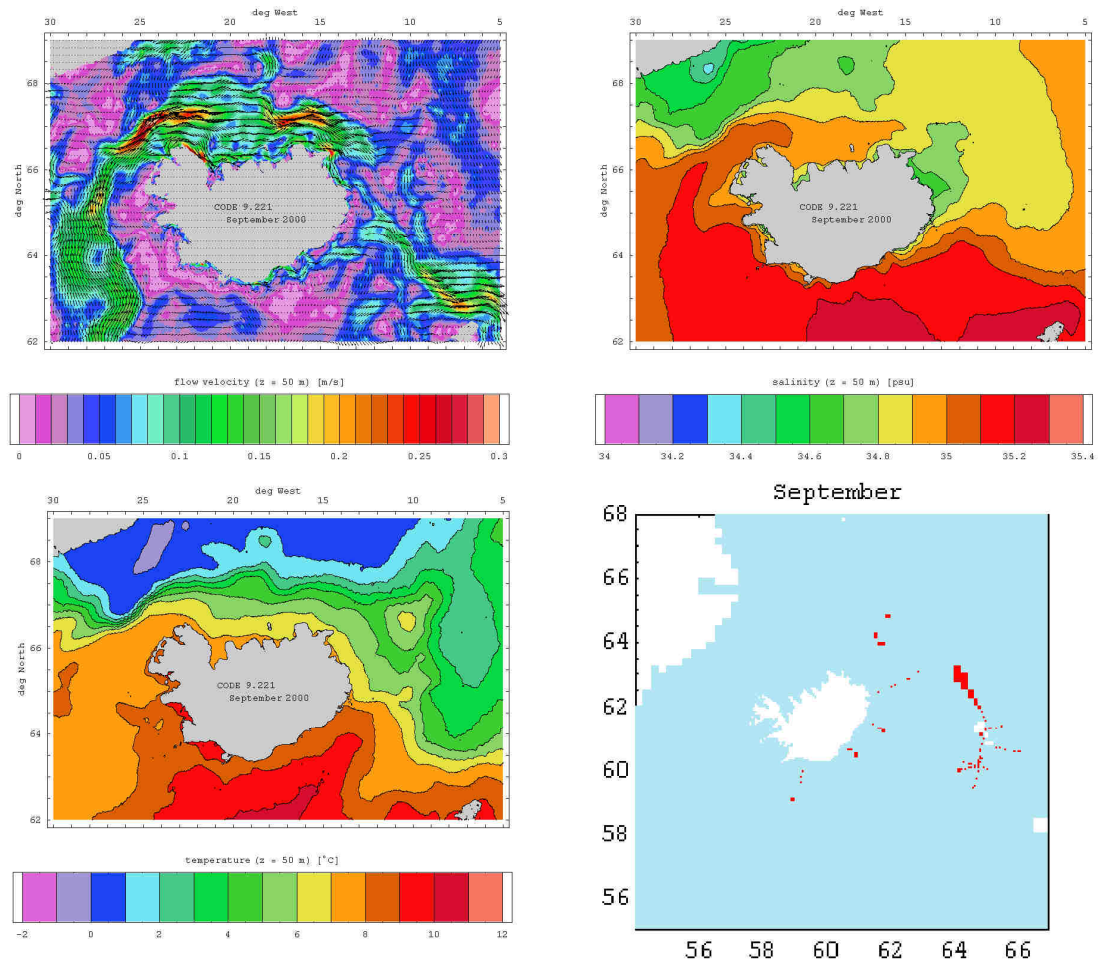


Fig. 2.105.: Monthly mean flow, salinity and temperature fields at 50 m depth and location of used CTD profiles – September 2000.



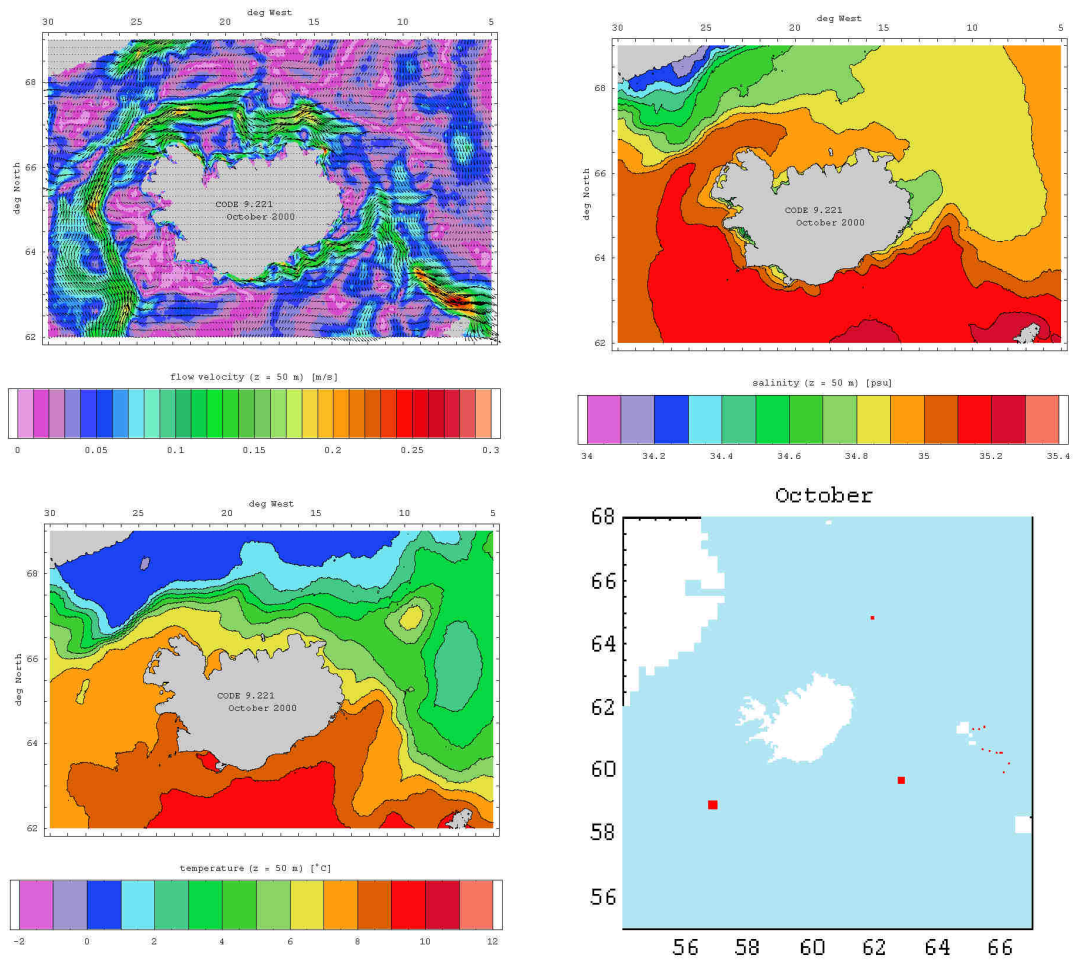


Fig. 2.106.: Monthly mean flow, salinity and temperature fields at 50 m depth and location of used CTD profiles – October 2000.



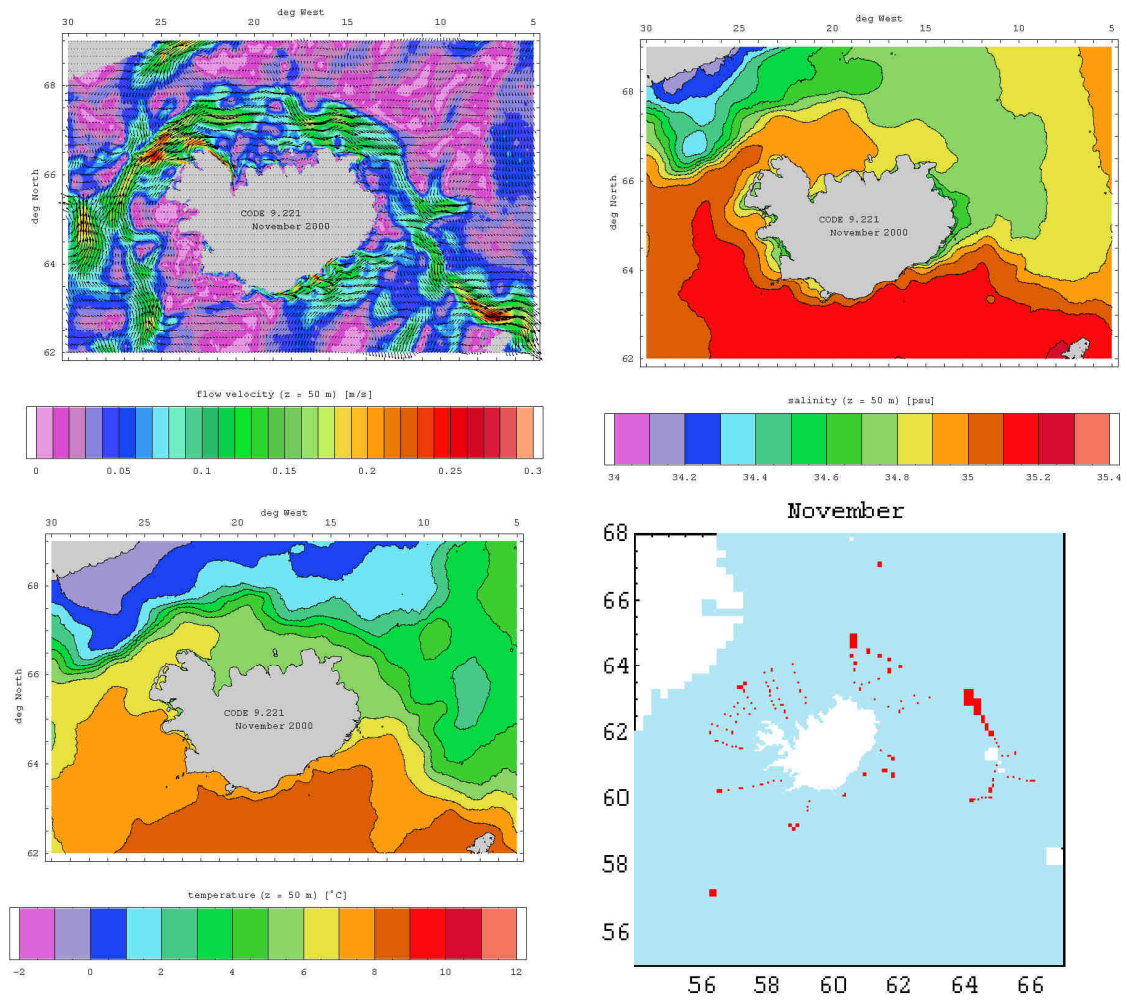


Fig. 2.107.: Monthly mean flow, salinity and temperature fields at 50 m depth and location of used CTD profiles – November 2000.

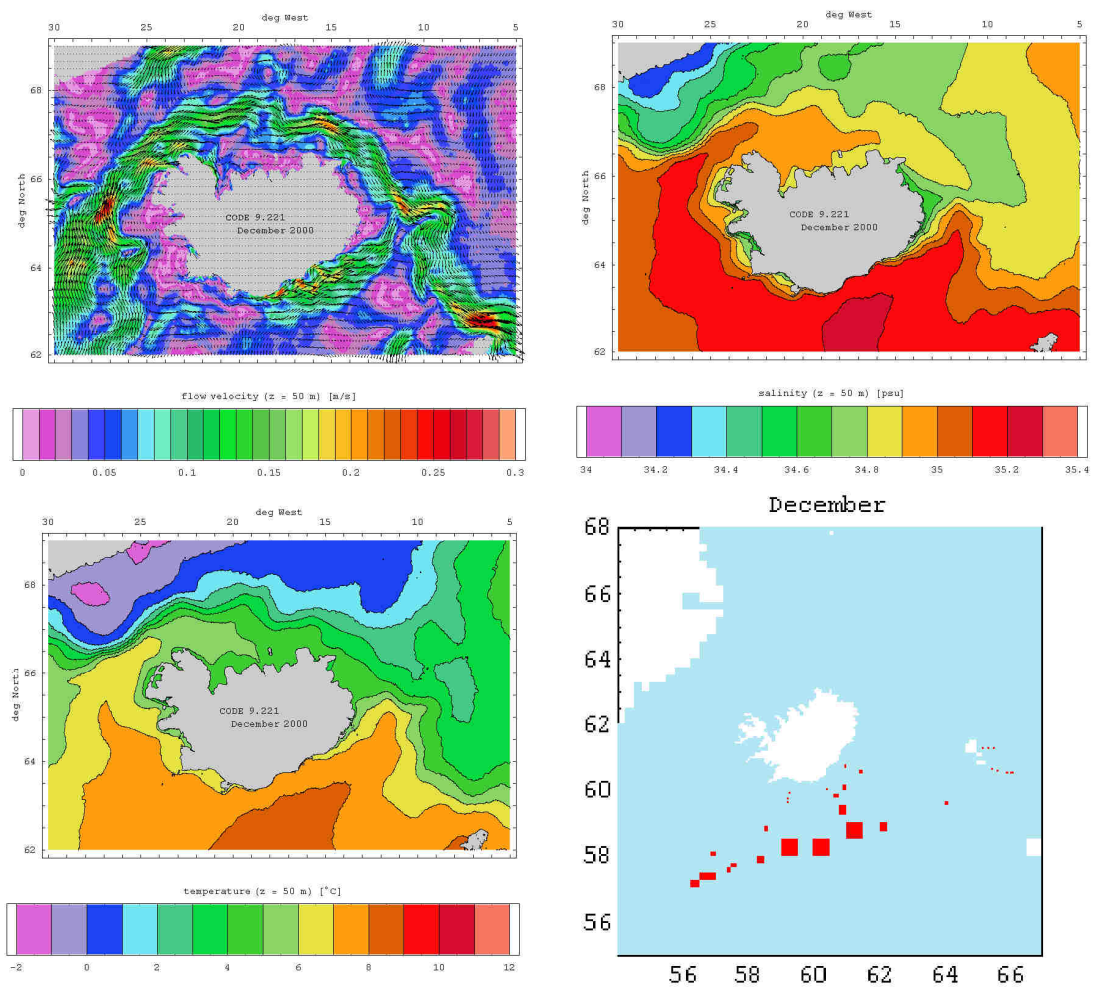


Fig. 2.108.: Monthly mean flow, salinity and temperature fields at 50 m depth and location of used CTD profiles – December 2000.

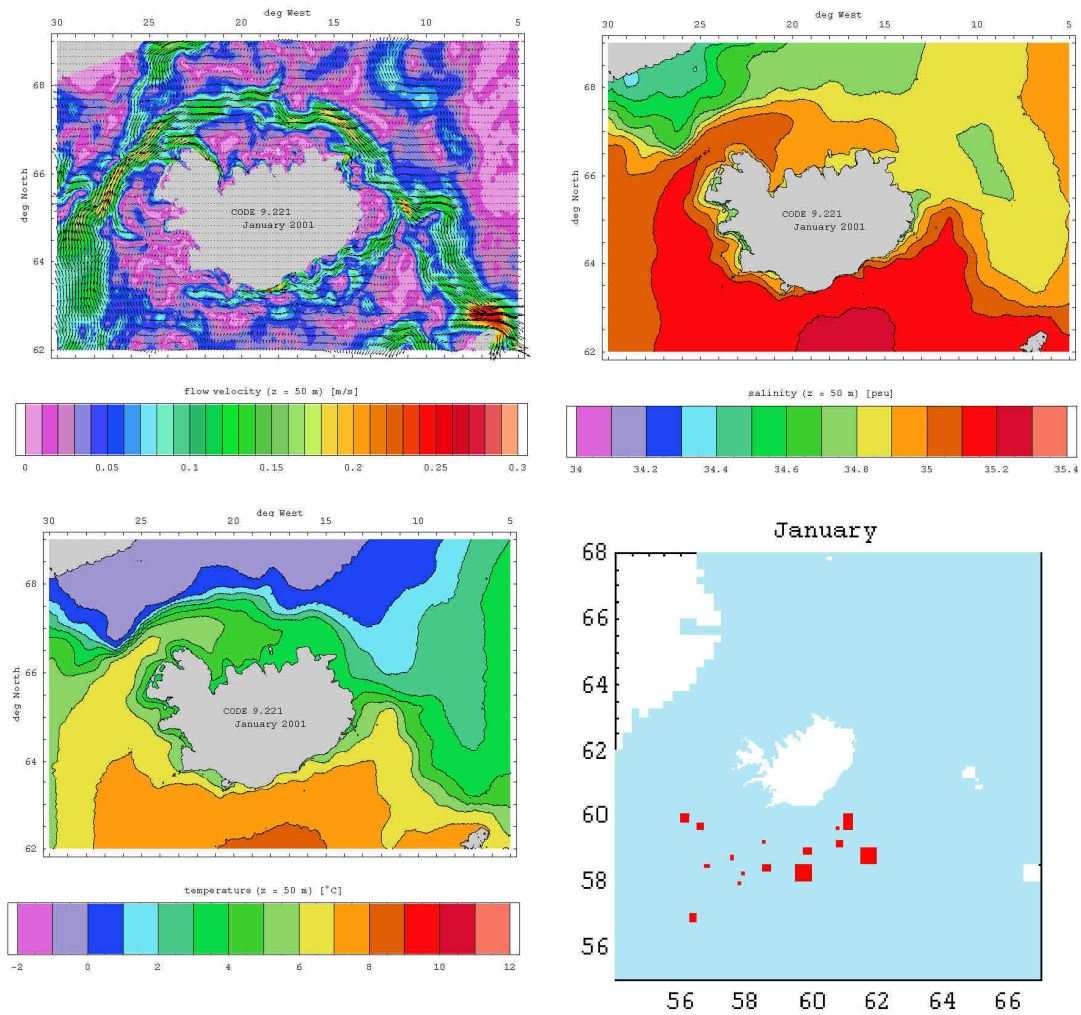


Fig. 2.109.: Monthly mean flow, salinity and temperature fields at 50 m depth and location of used CTD profiles – January 2001.

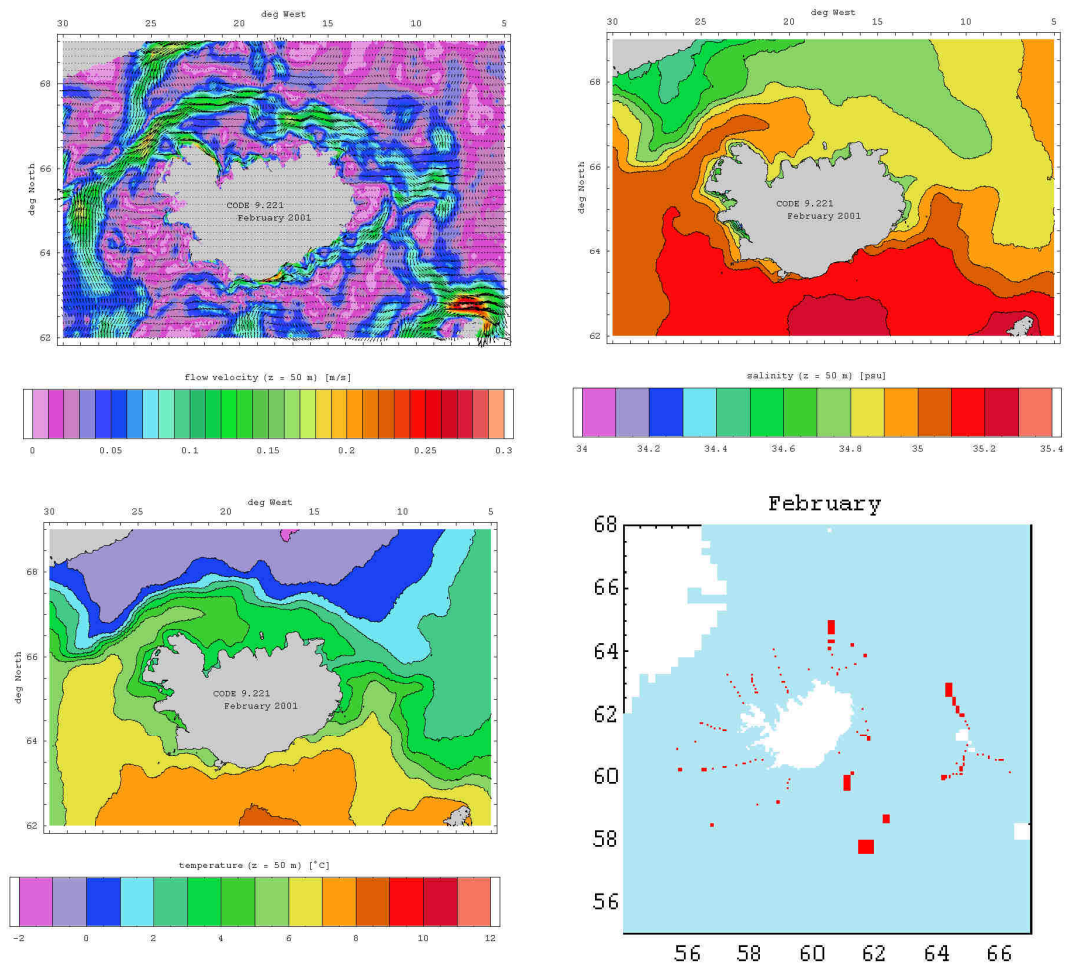


Fig. 2.110.: Monthly mean flow, salinity and temperature fields at 50 m depth and location of used CTD profiles – February 2001.

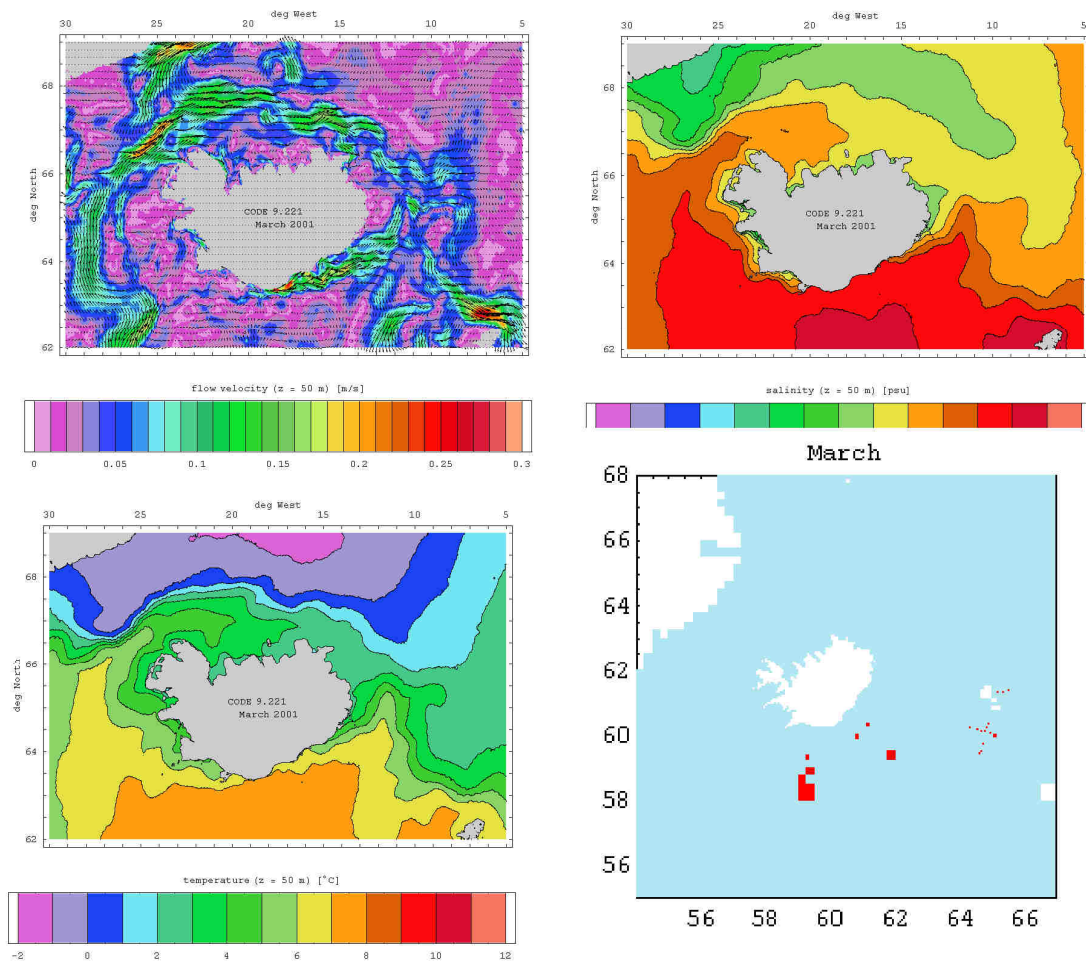


Fig. 2.111.: Monthly mean flow, salinity and temperature fields at 50 m depth and location of used CTD profiles – March 2001.



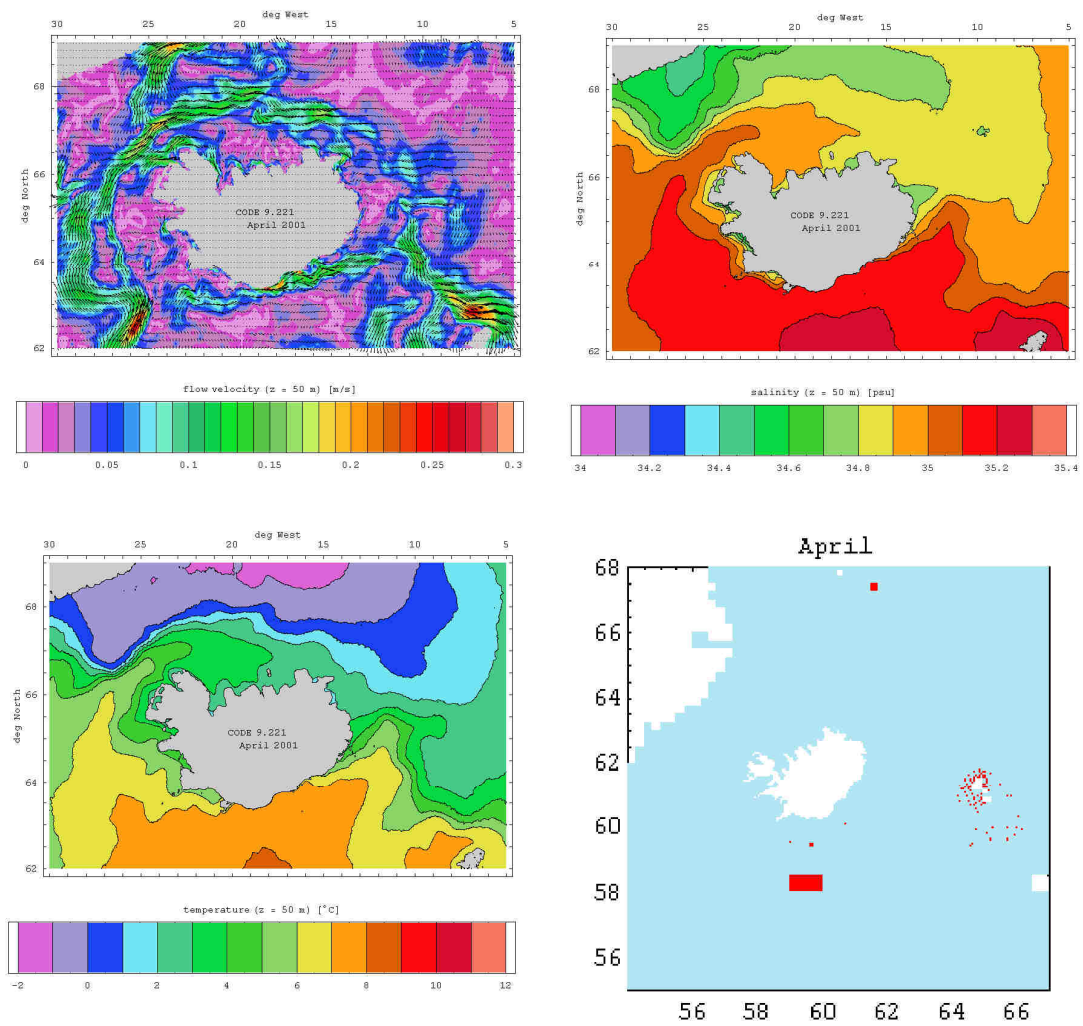


Fig. 2.112.: Monthly mean flow, salinity and temperature fields at 50 m depth and location of used CTD profiles – April 2001.



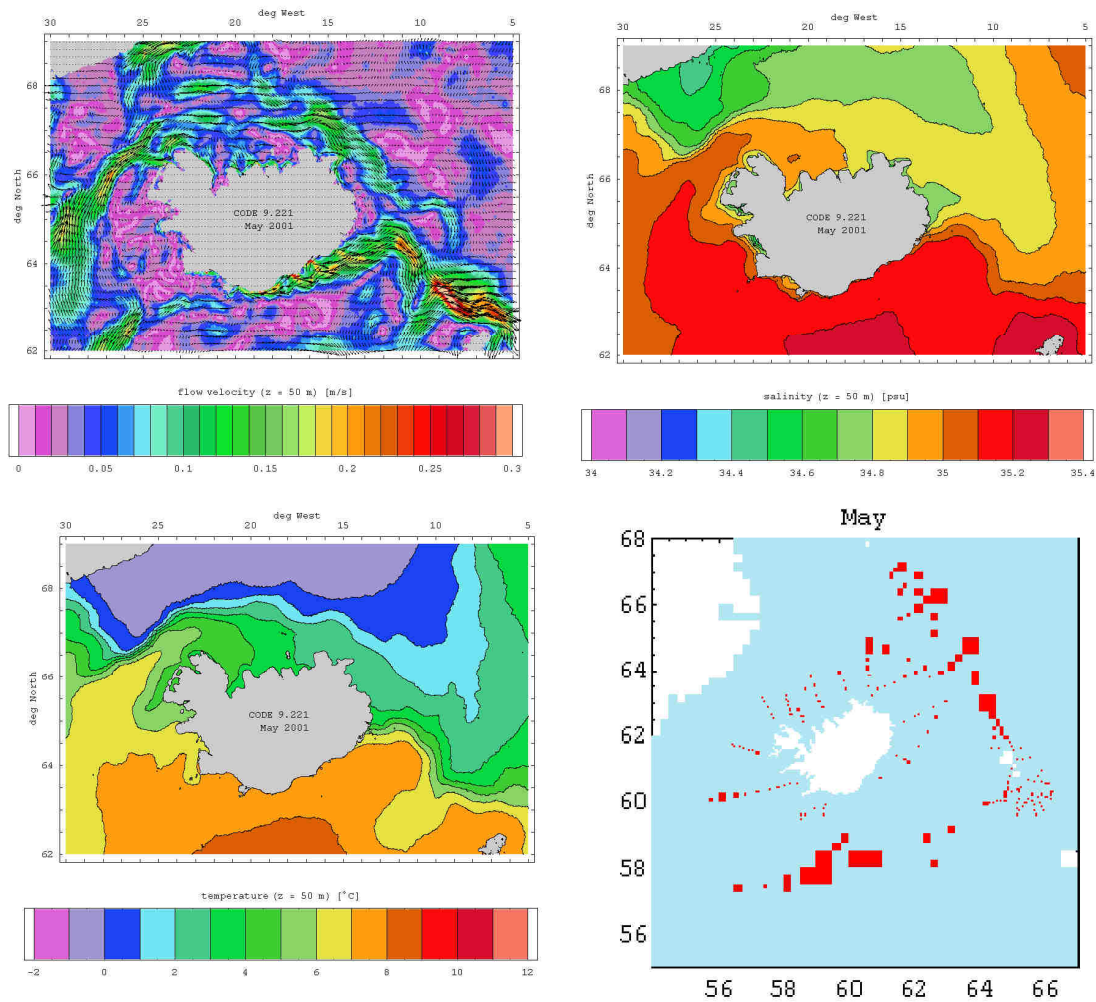


Fig. 2.113.: Monthly mean flow, salinity and temperature fields at 50 m depth and location of used CTD profiles –May 2001.

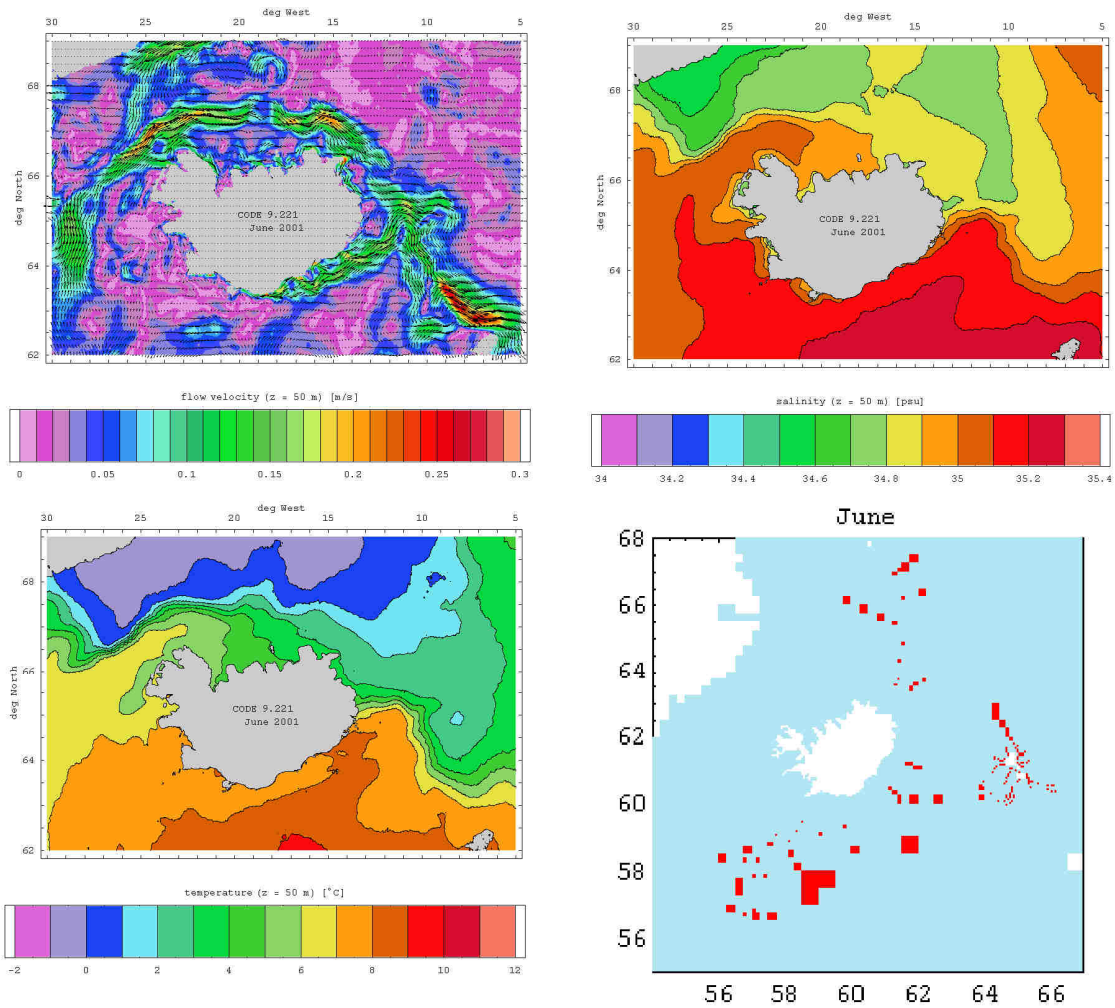


Fig. 2.114.: Monthly mean flow, salinity and temperature fields at 50 m depth and location of used CTD profiles – June 2001.

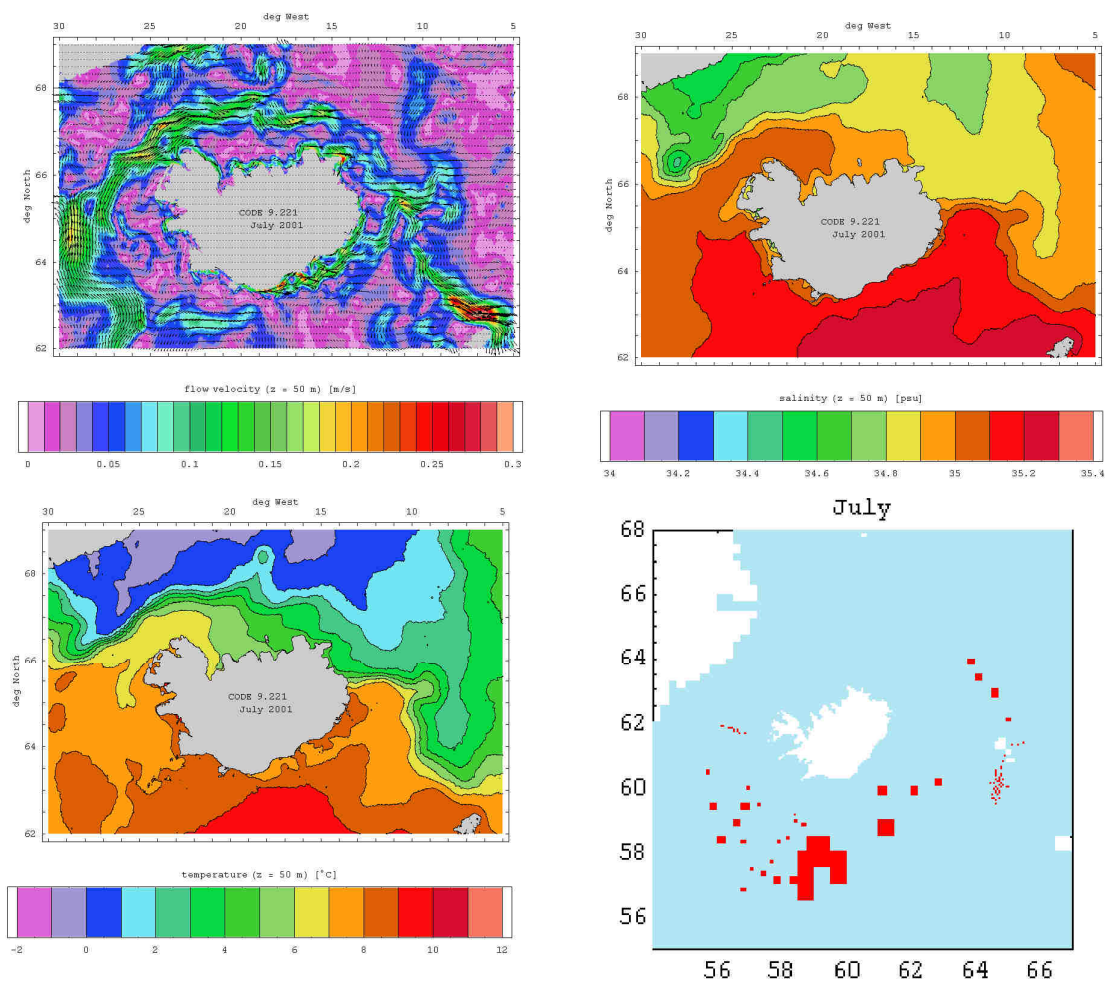


Fig. 2.115.: Monthly mean flow, salinity and temperature fields at 50 m depth and location of used CTD profiles – July 2001.

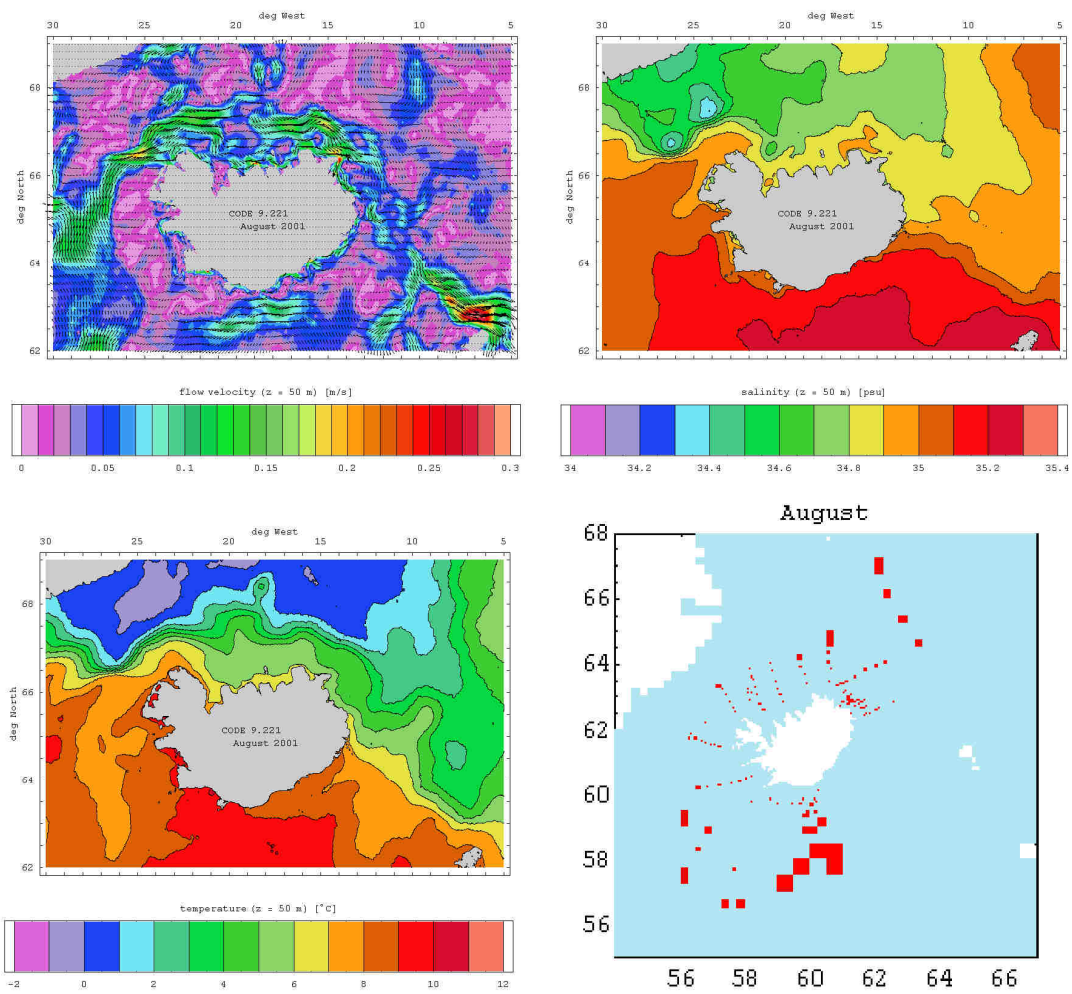


Fig. 2.116.: Monthly mean flow, salinity and temperature fields at 50 m depth and location of used CTD profiles – August 2001.

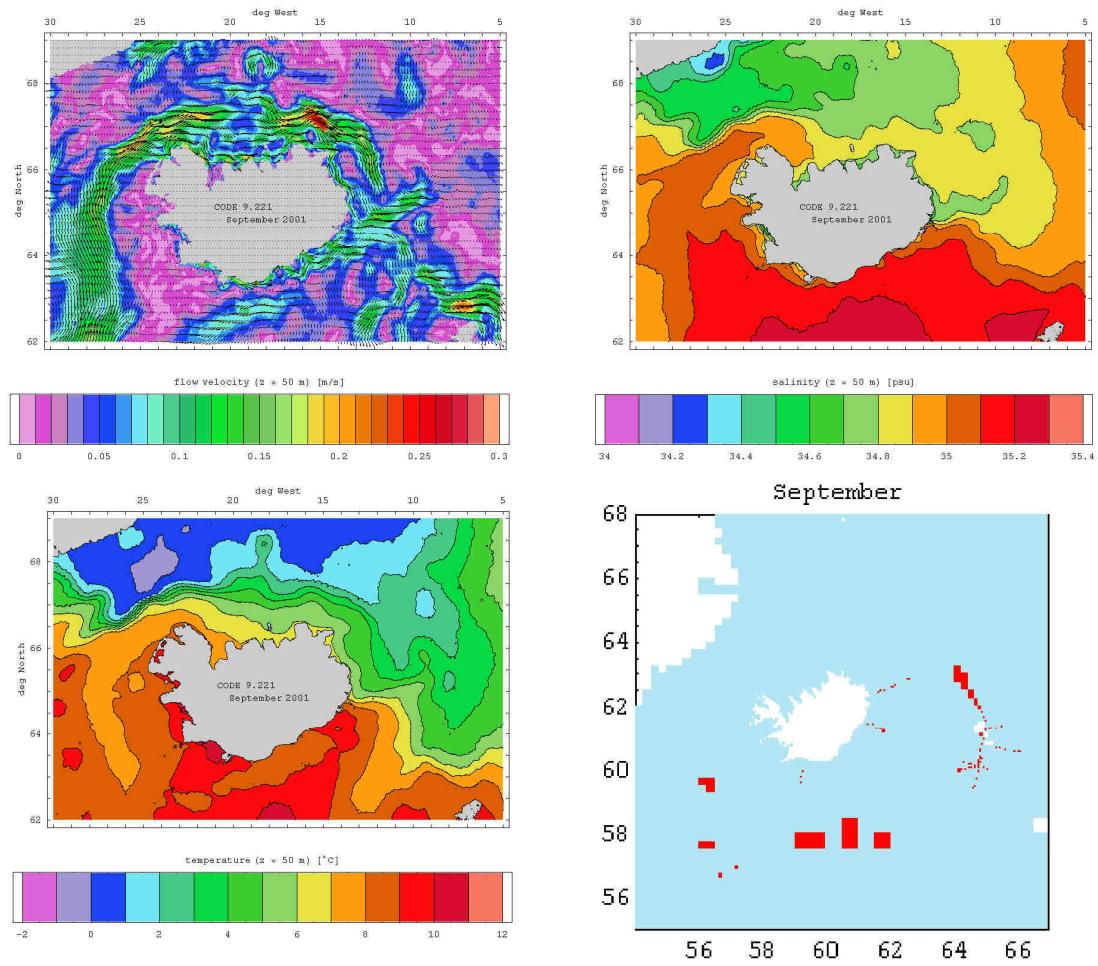


Fig. 2.117.: Monthly mean flow, salinity and temperature fields at 50 m depth and location of used CTD profiles – September 2001.



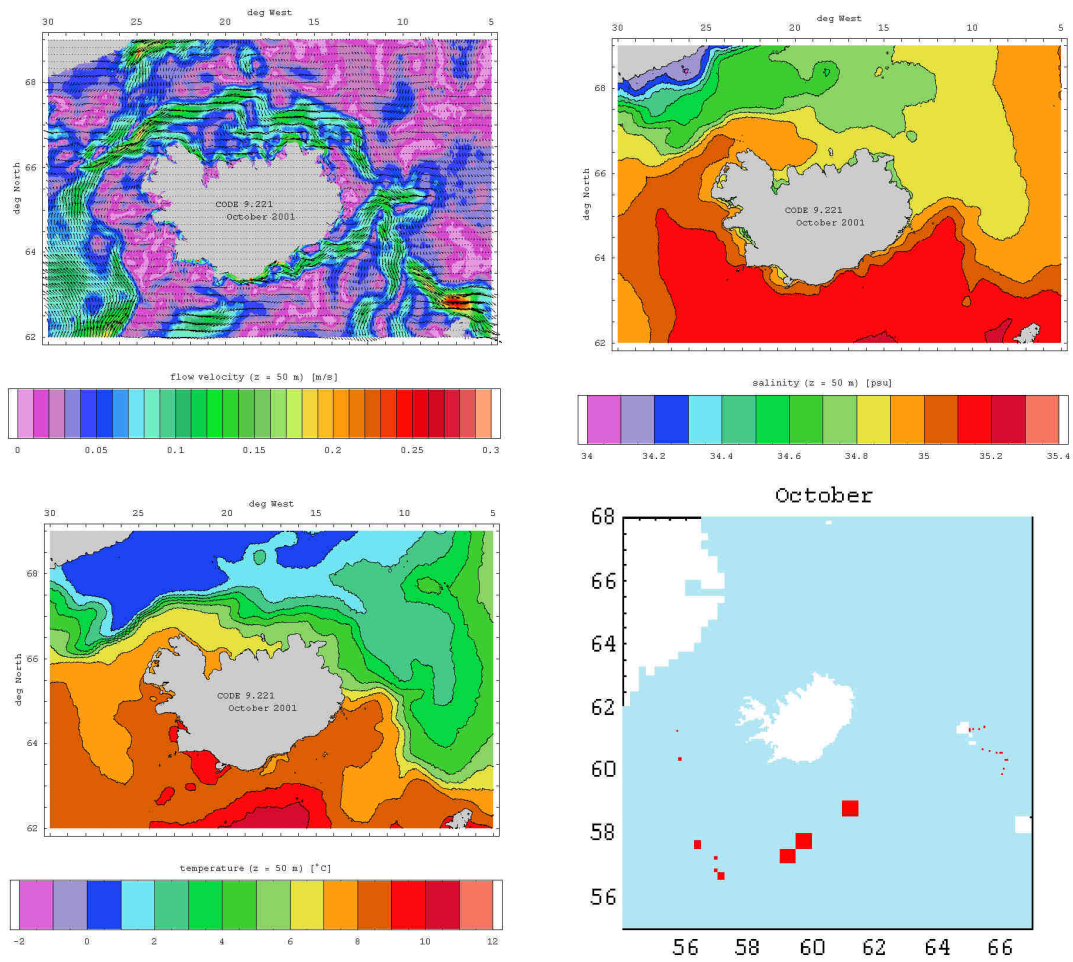


Fig. 2.118.: Monthly mean flow, salinity and temperature fields at 50 m depth and location of used CTD profiles – October 2001.



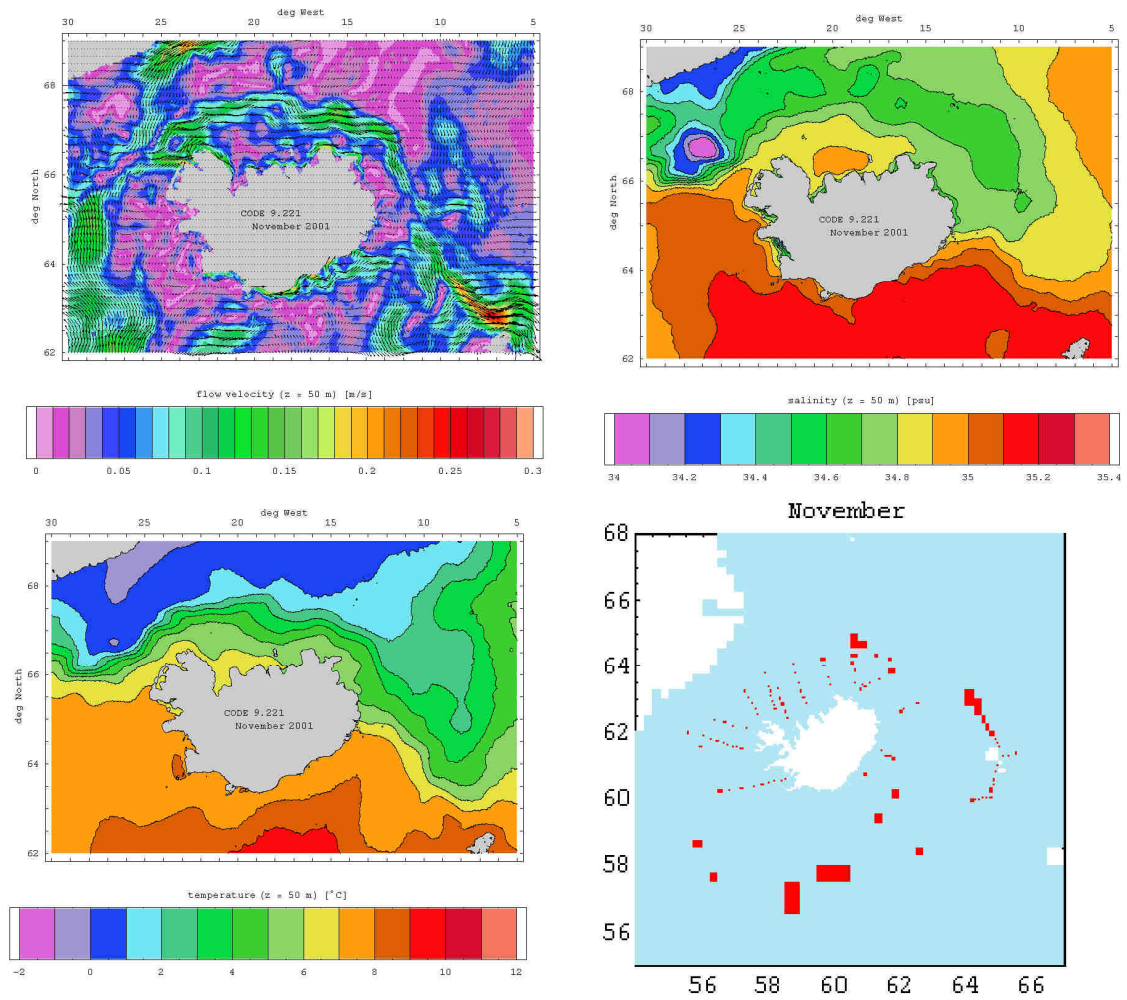


Fig. 2.119.: Monthly mean flow, salinity and temperature fields at 50 m depth and location of used CTD profiles – November 2001.

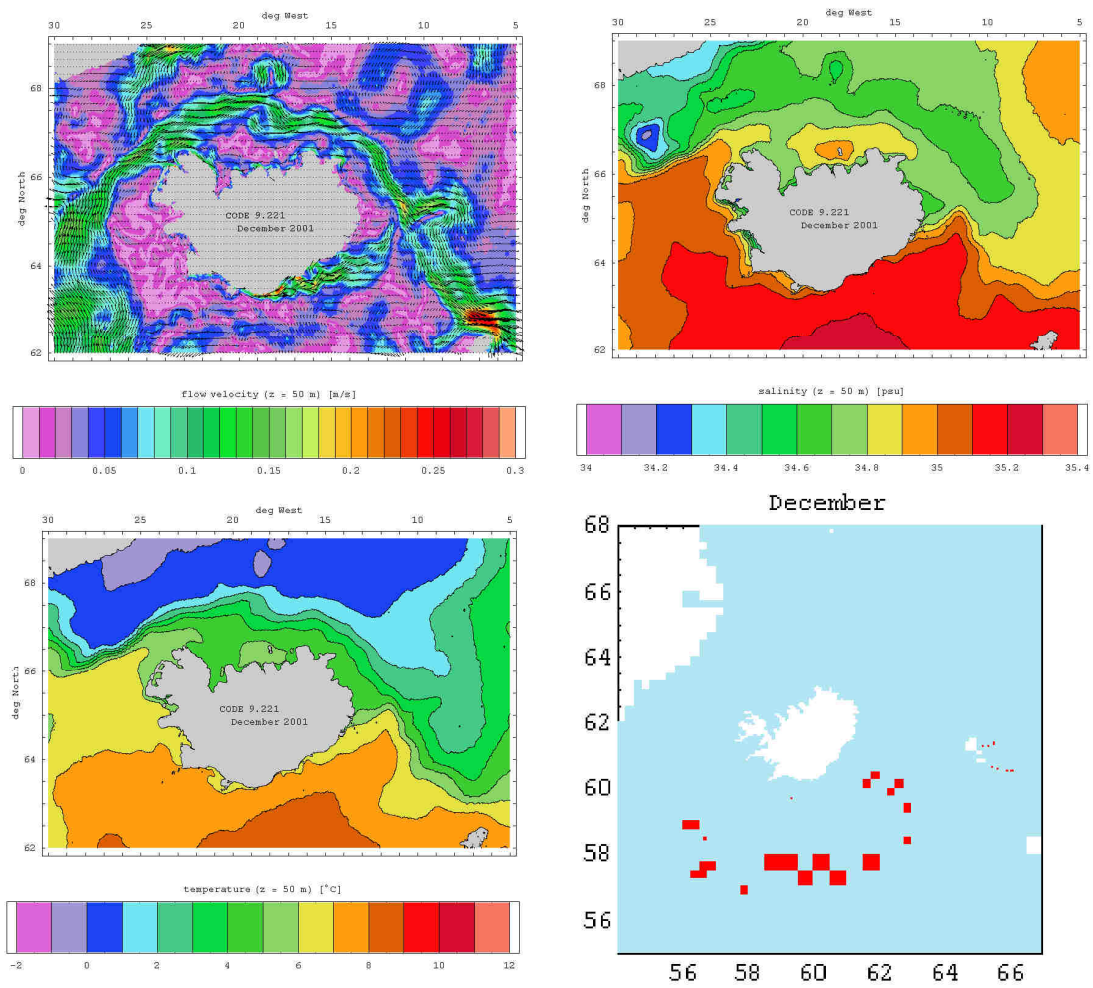


Fig. 2.120.: Monthly mean flow, salinity and temperature fields at 50 m depth and location of used CTD profiles – December 2001.

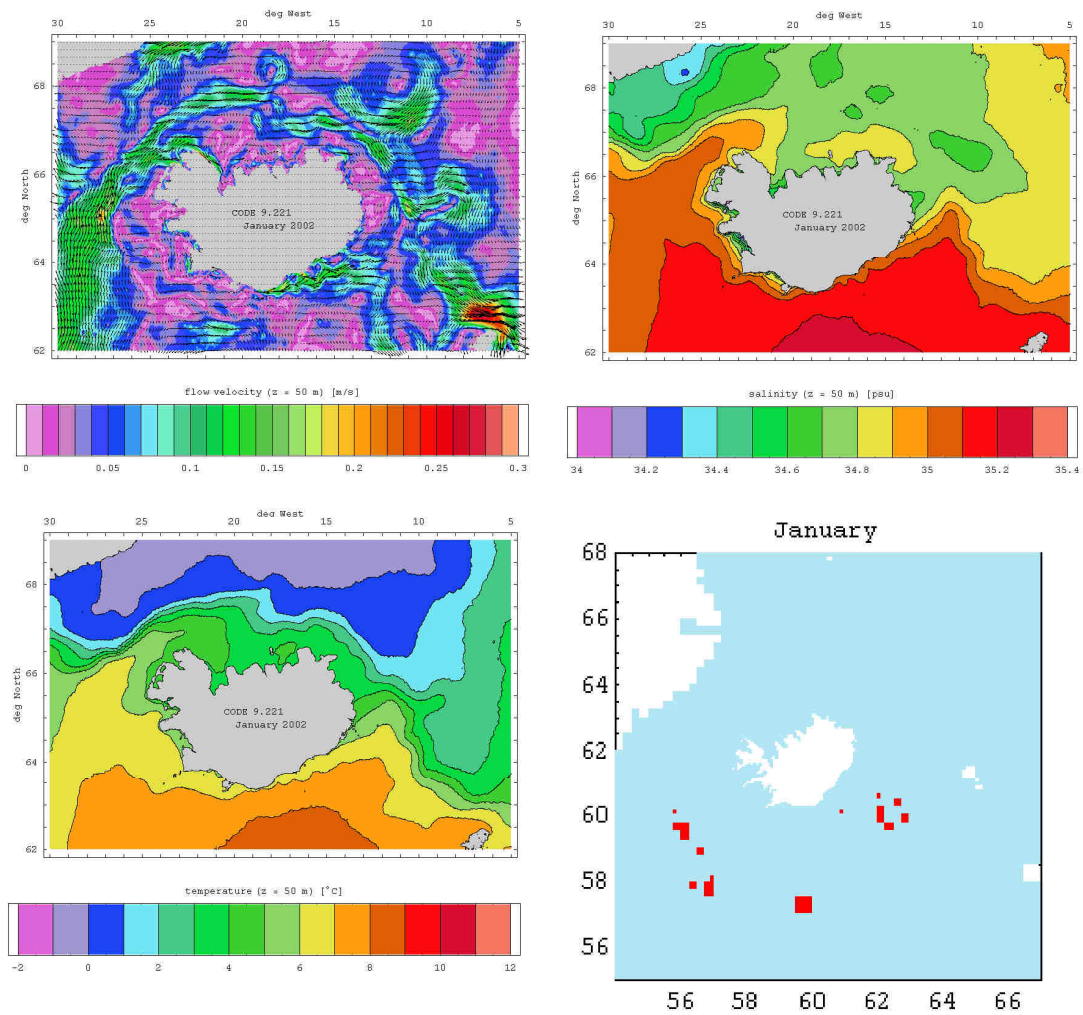


Fig. 2.121.: Monthly mean flow, salinity and temperature fields at 50 m depth and location of used CTD profiles – January 2002.

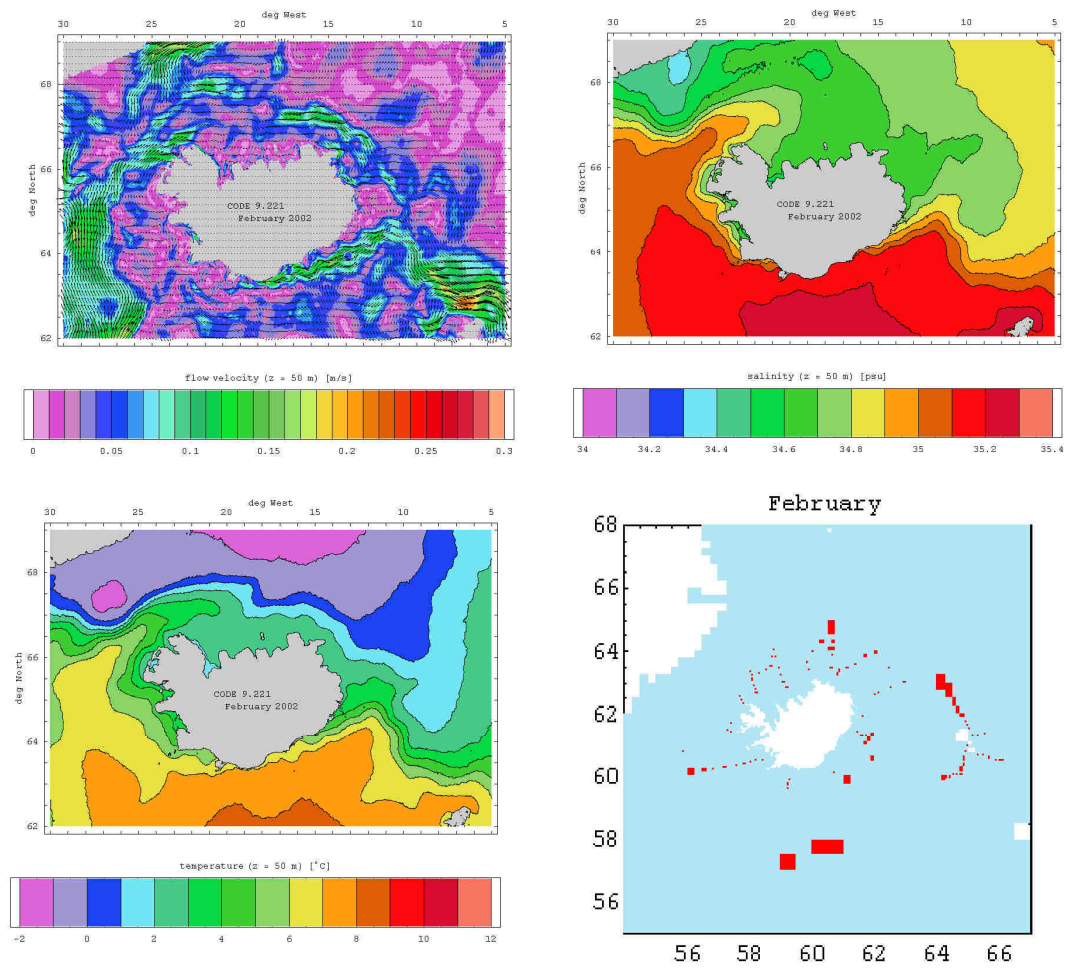


Fig. 2.122.: Monthly mean flow, salinity and temperature fields at 50 m depth and location of used CTD profiles – February 2002.

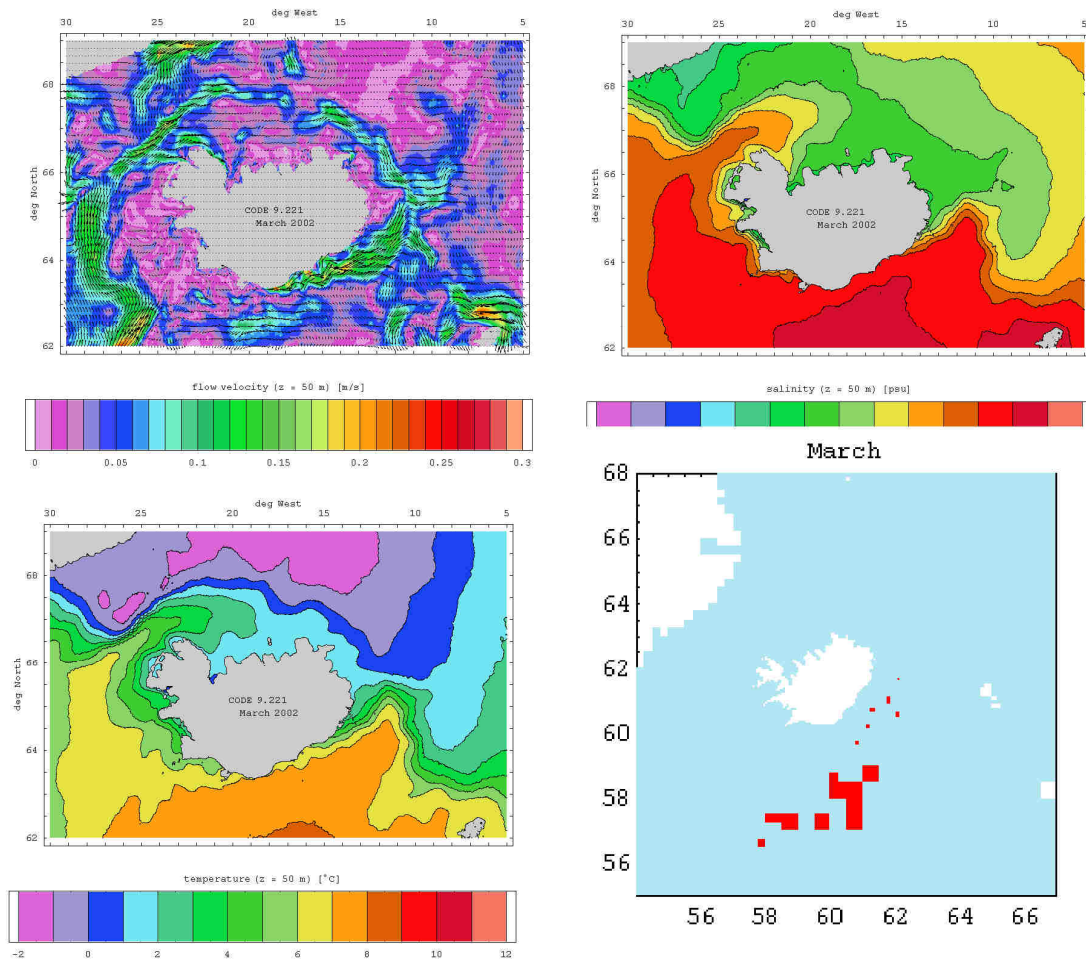


Fig. 2.123.: Monthly mean flow, salinity and temperature fields at 50 m depth and location of used CTD profiles – March 2002.



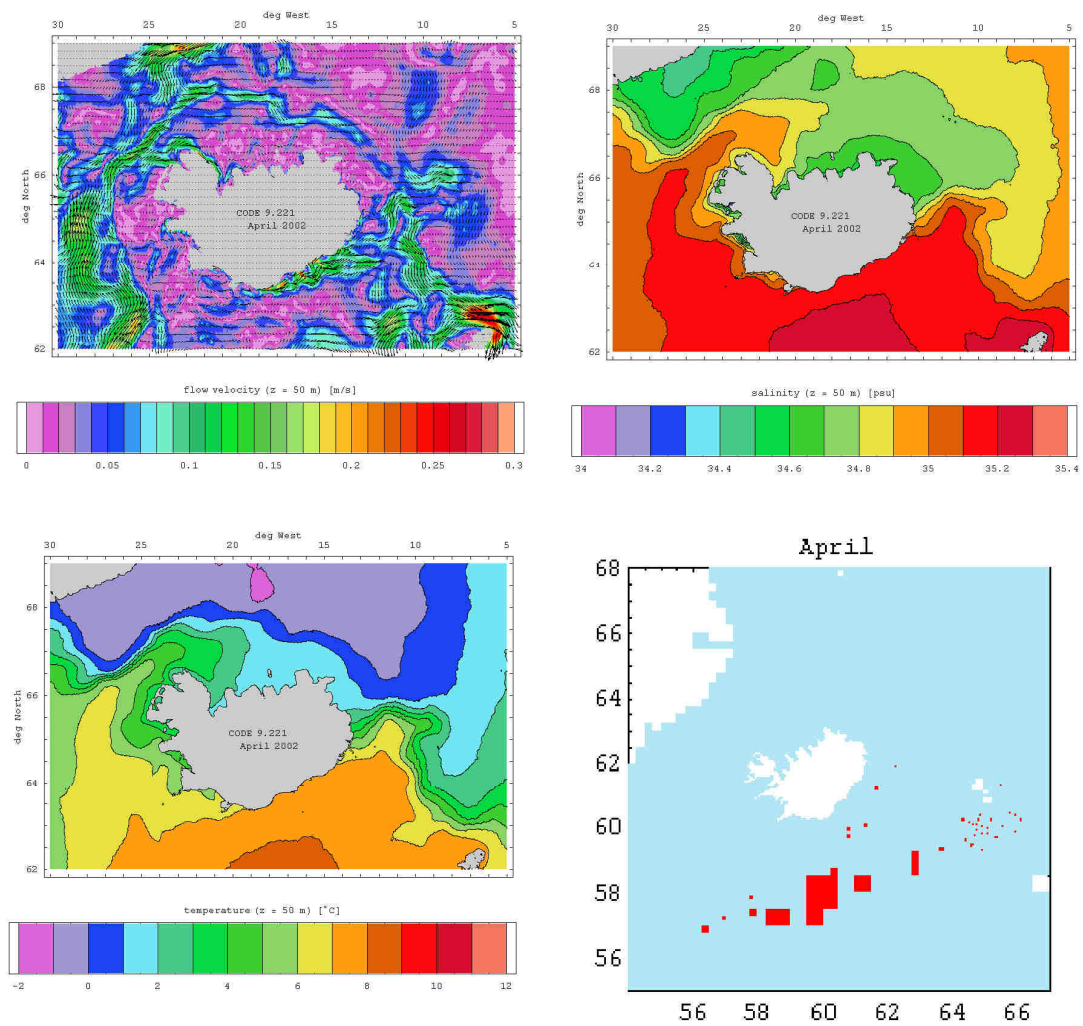


Fig. 2.124.: Monthly mean flow, salinity and temperature fields at 50m depth and location of used CTD profiles – April 2002.



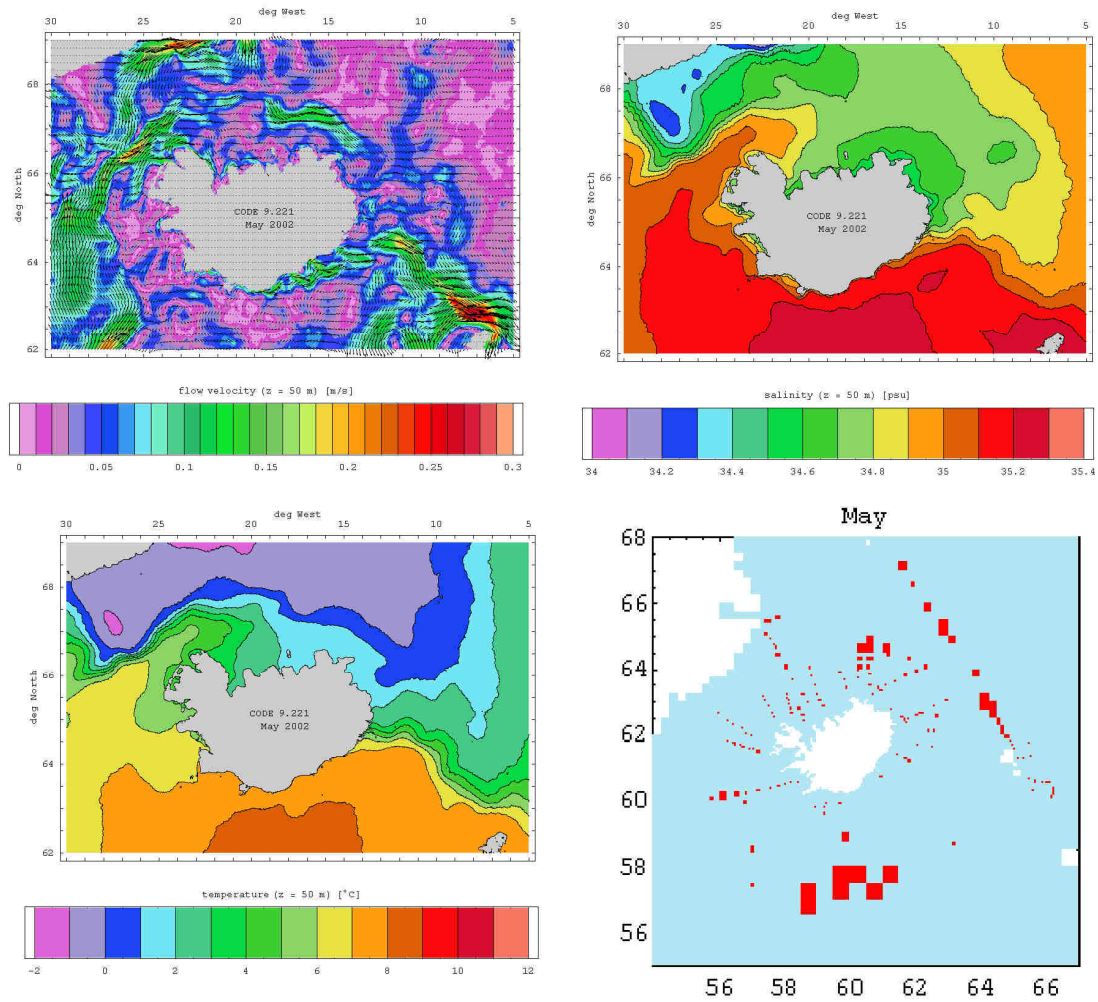


Fig. 2.125.: Monthly mean flow, salinity and temperature fields at 50 m depth and location of used CTD profiles – May 2002.

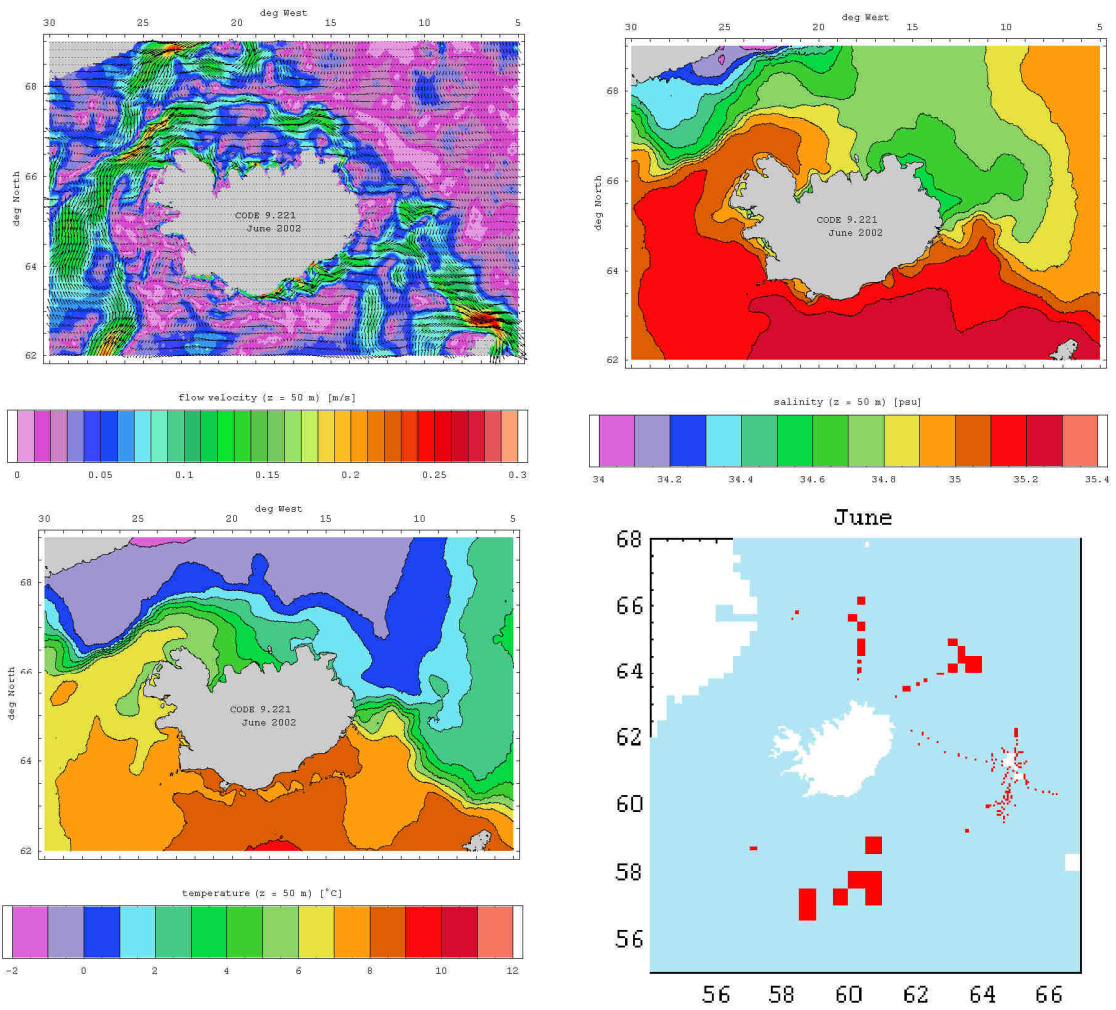


Fig. 2.126.: Monthly mean flow, salinity and temperature fields at 50 m depth and location of used CTD profiles – June 2002.

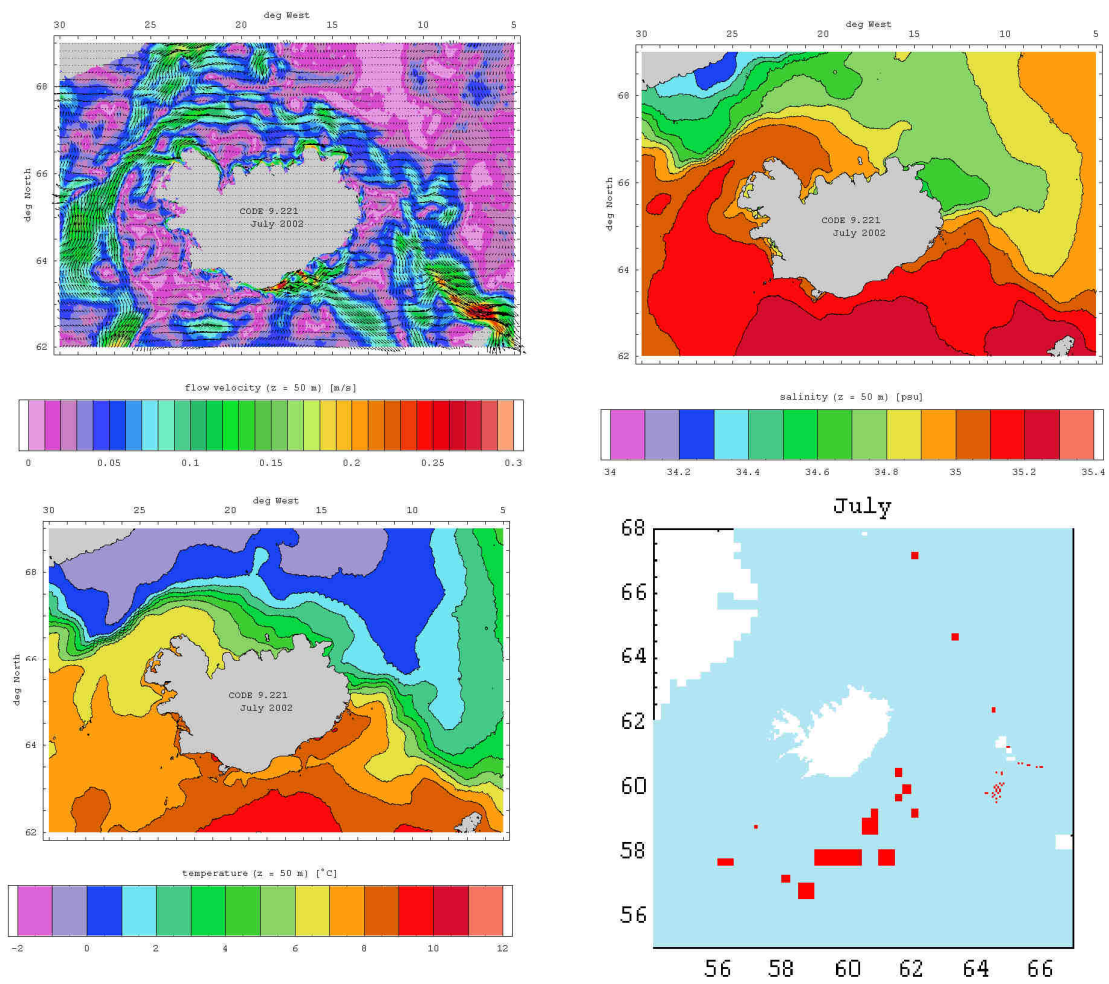


Fig. 2.127.: Monthly mean flow, salinity and temperature fields at 50 m depth and location of used CTD profiles – July 2002.

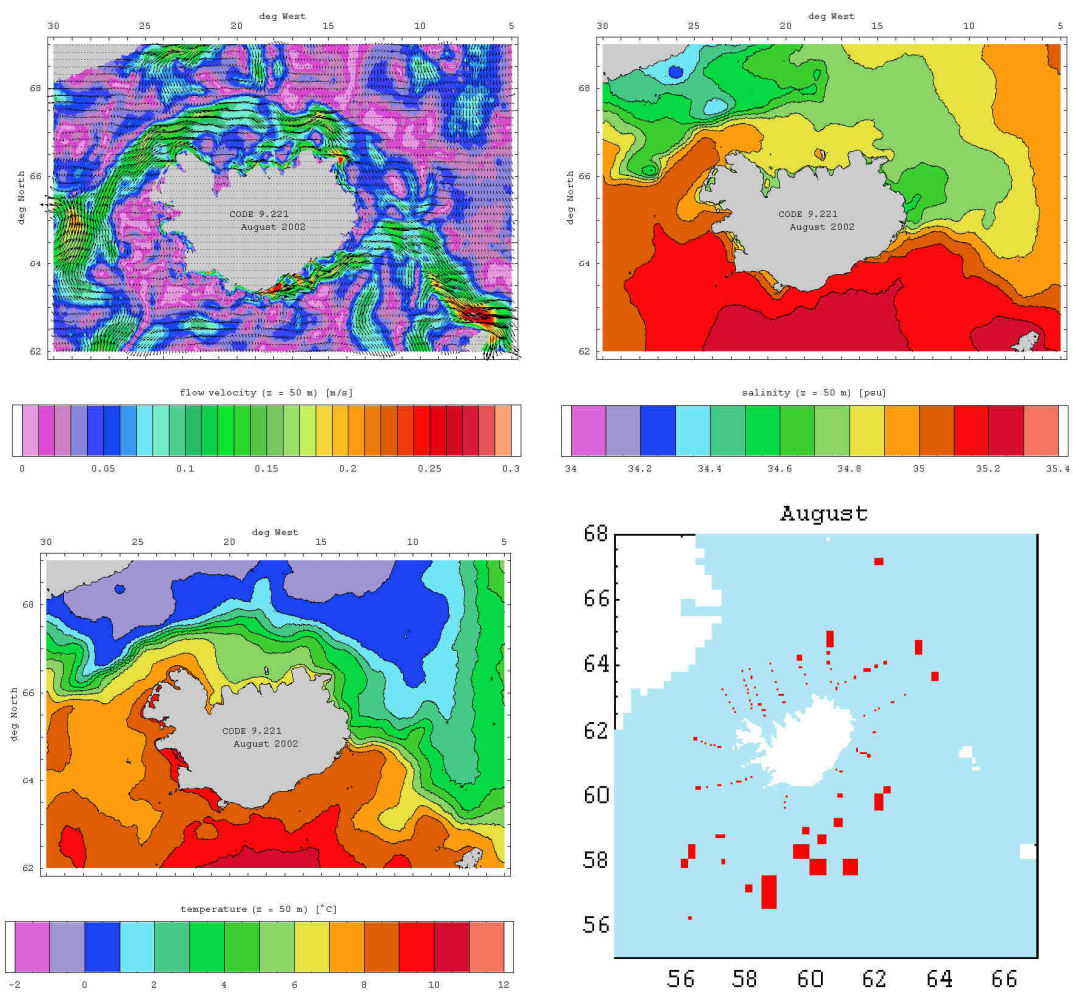


Fig. 2.128.: Monthly mean flow, salinity and temperature fields at 50 m depth and location of used CTD profiles – August 2002.

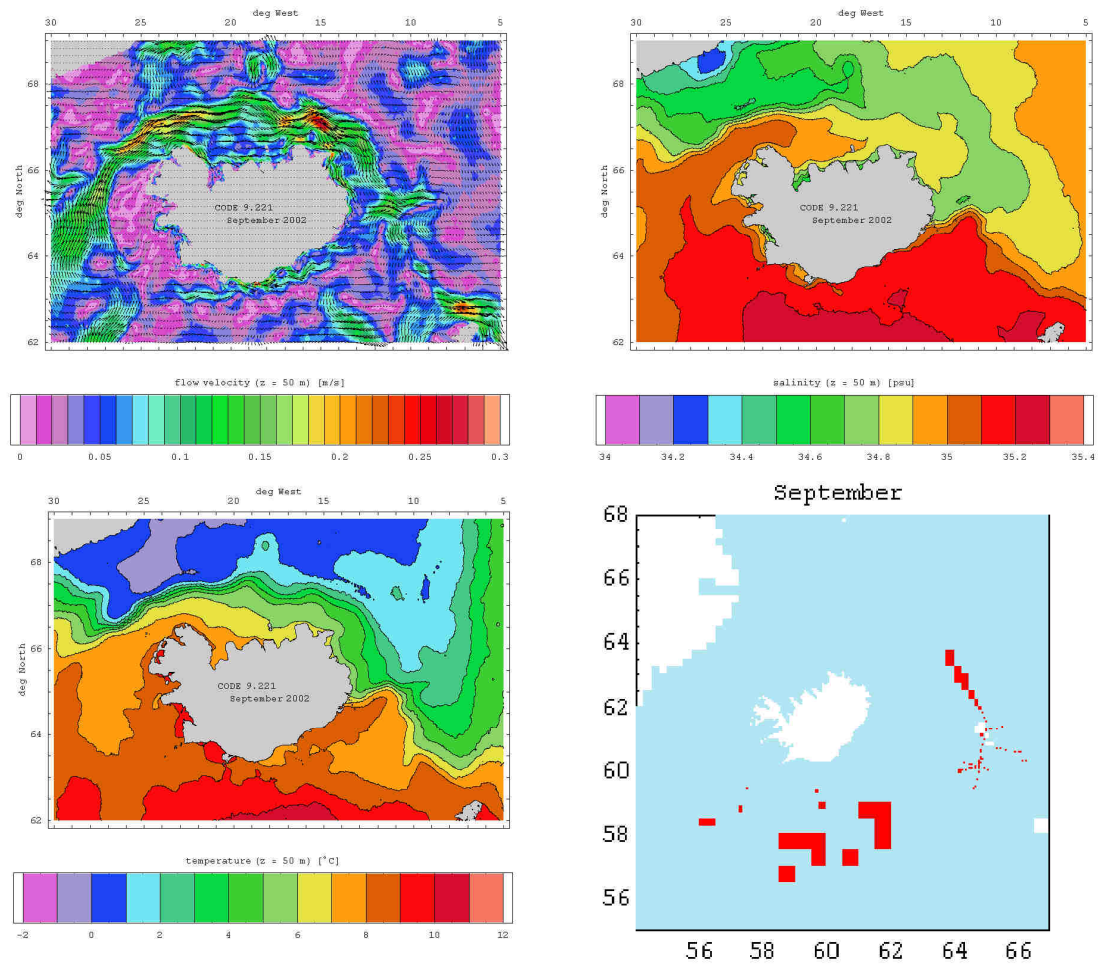


Fig. 2.129.: Monthly mean flow, salinity and temperature fields at 50 m depth and location of used CTD profiles – September 2002.



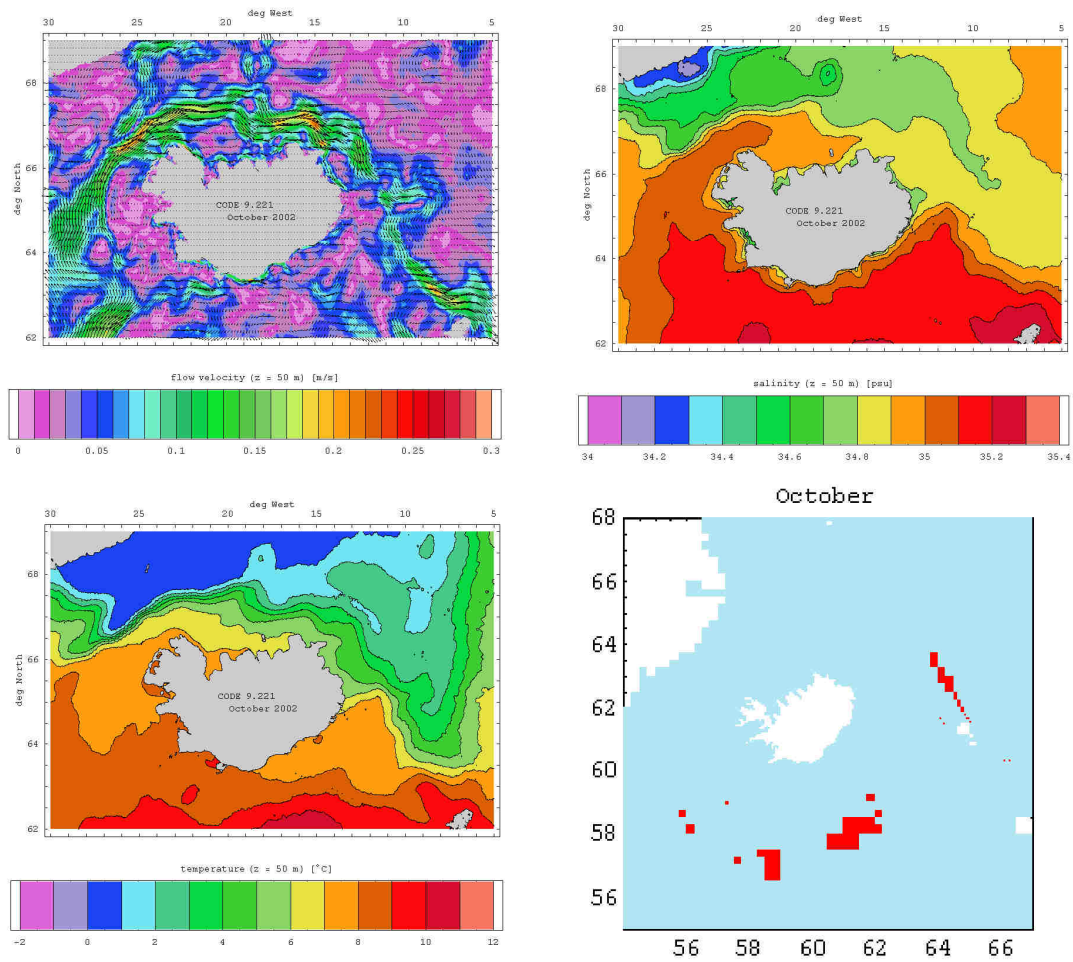


Fig. 2.130.: Monthly mean flow, salinity and temperature fields at 50 m depth and location of used CTD profiles – October 2002.



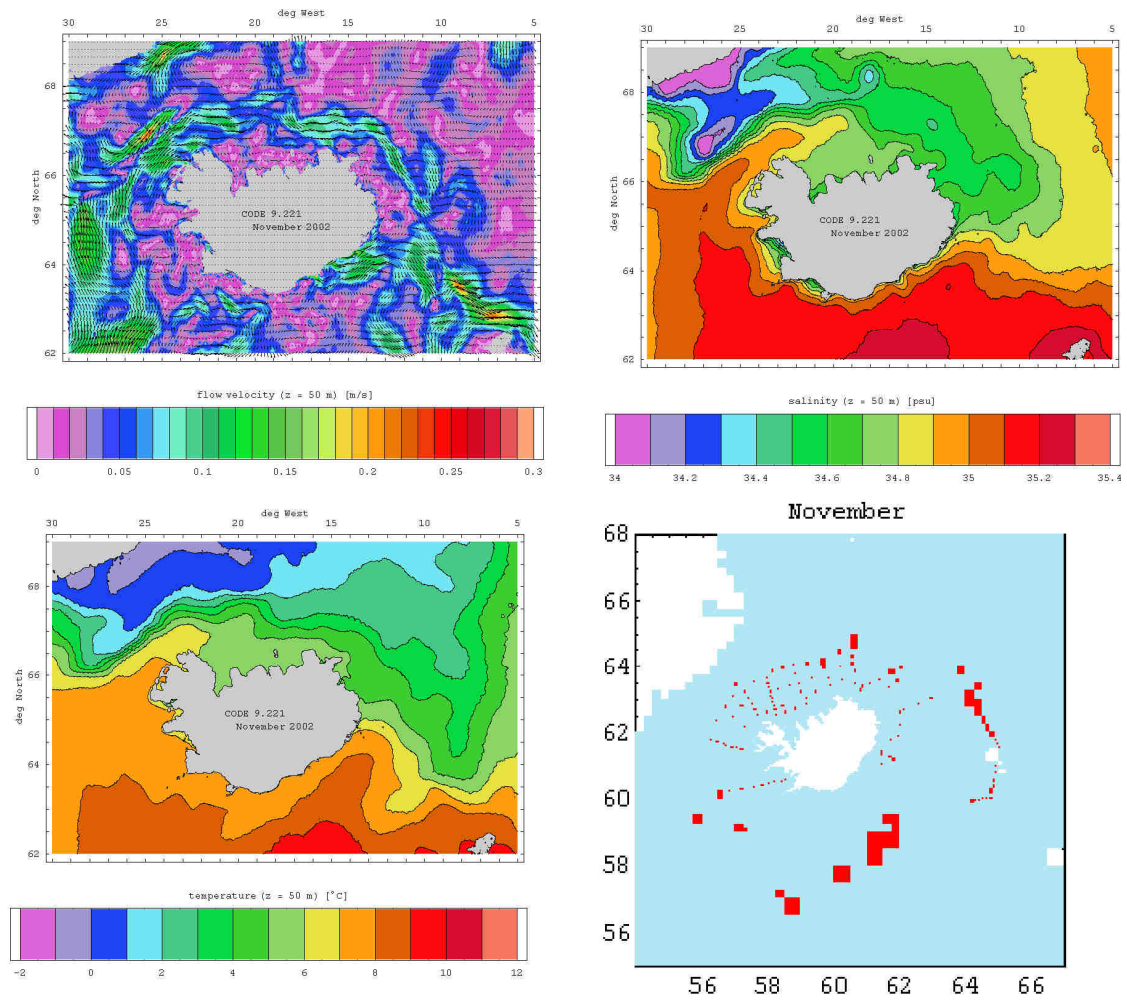


Fig. 2.131.: Monthly mean flow, salinity and temperature fields at 50 m depth and location of used CTD profiles – November 2002.

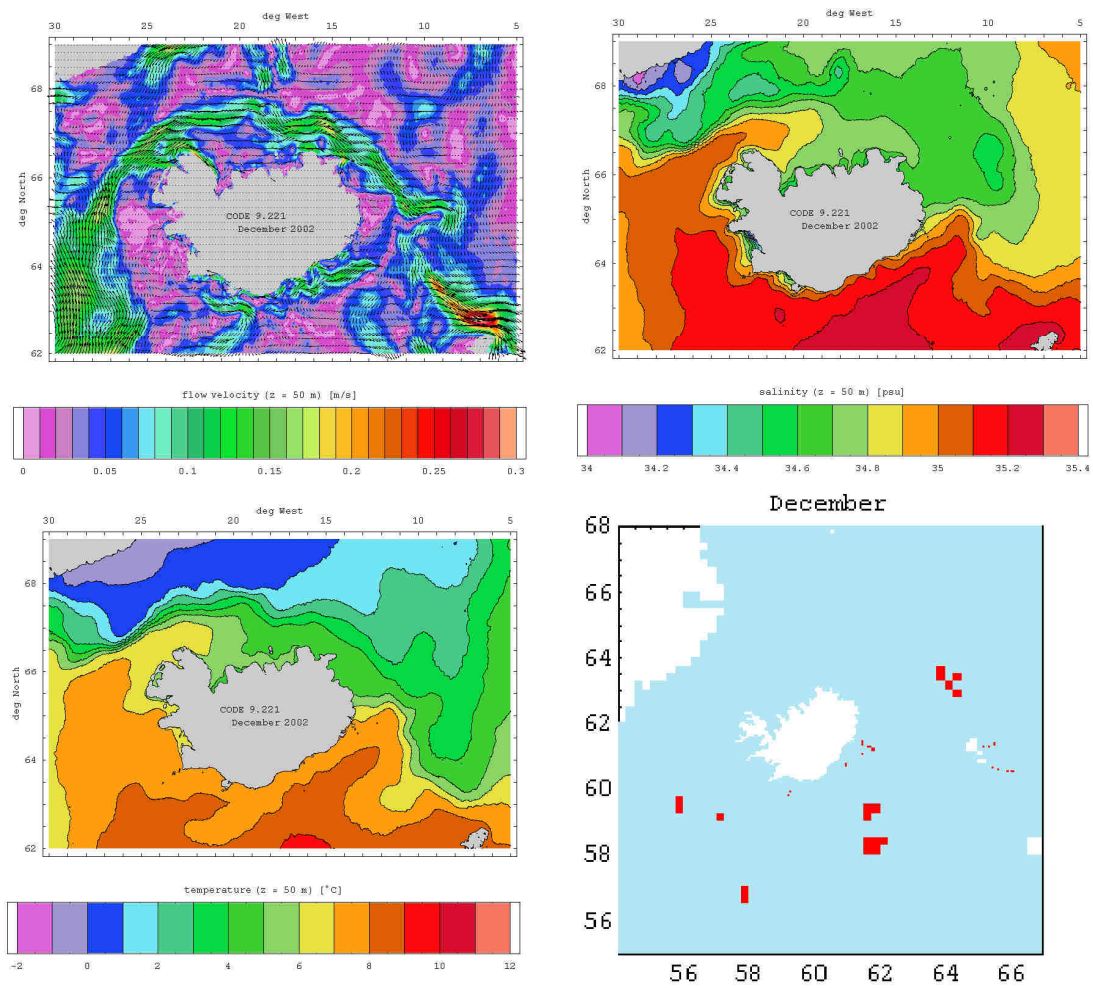


Fig. 2.132.: Monthly mean flow, salinity and temperature fields at 50 m depth and location of used CTD profiles – December 2002.

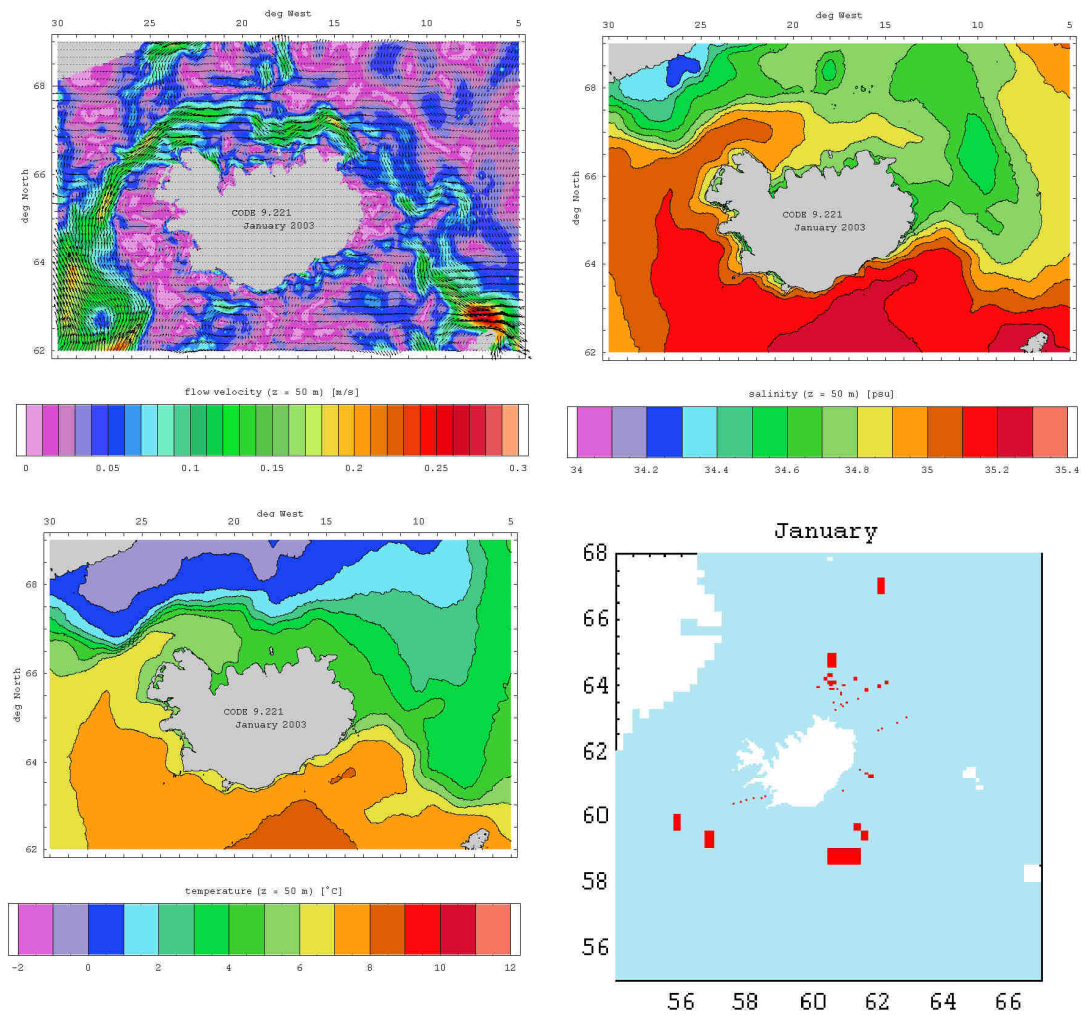


Fig. 2.133.: Monthly mean flow, salinity and temperature fields at 50 m depth and location of used CTD profiles – January 2003.

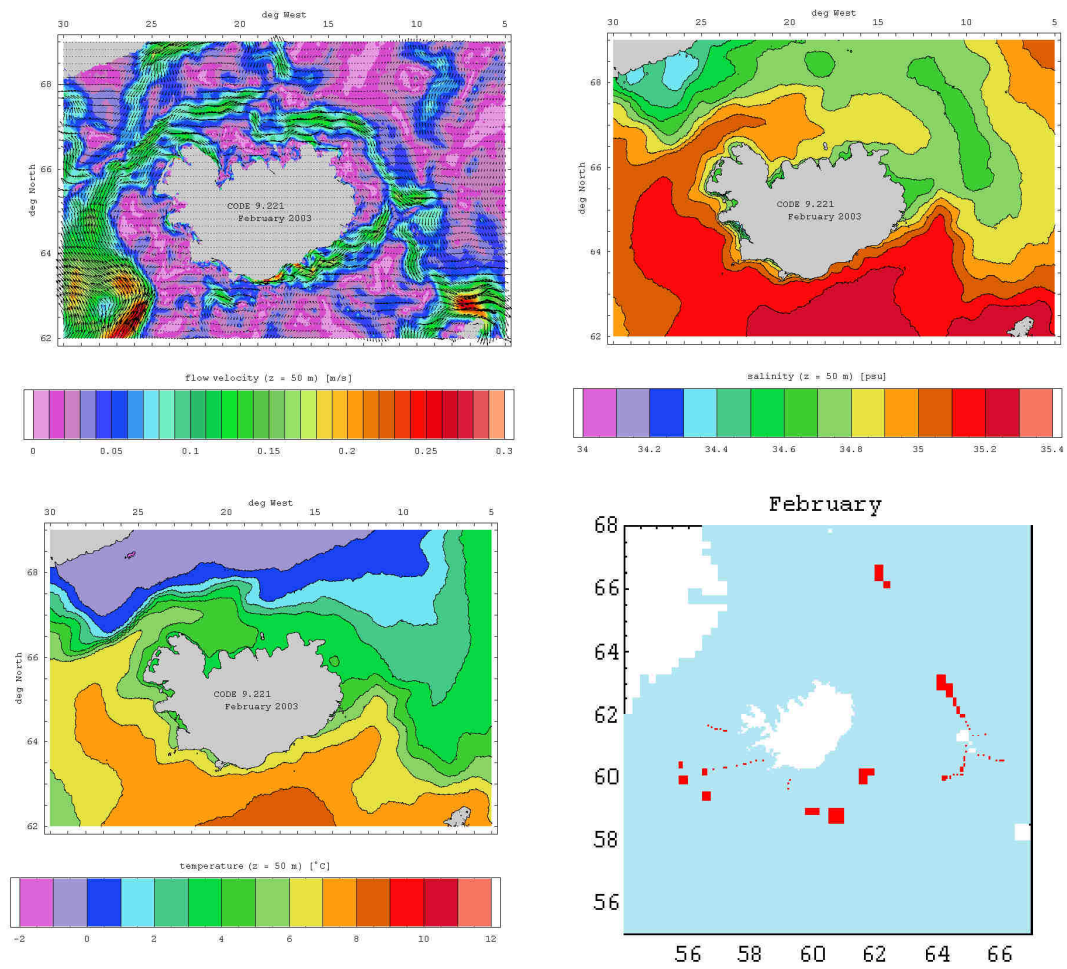


Fig. 2.134.: Monthly mean flow, salinity and temperature fields at 50 m depth and location of used CTD profiles – February 2003.

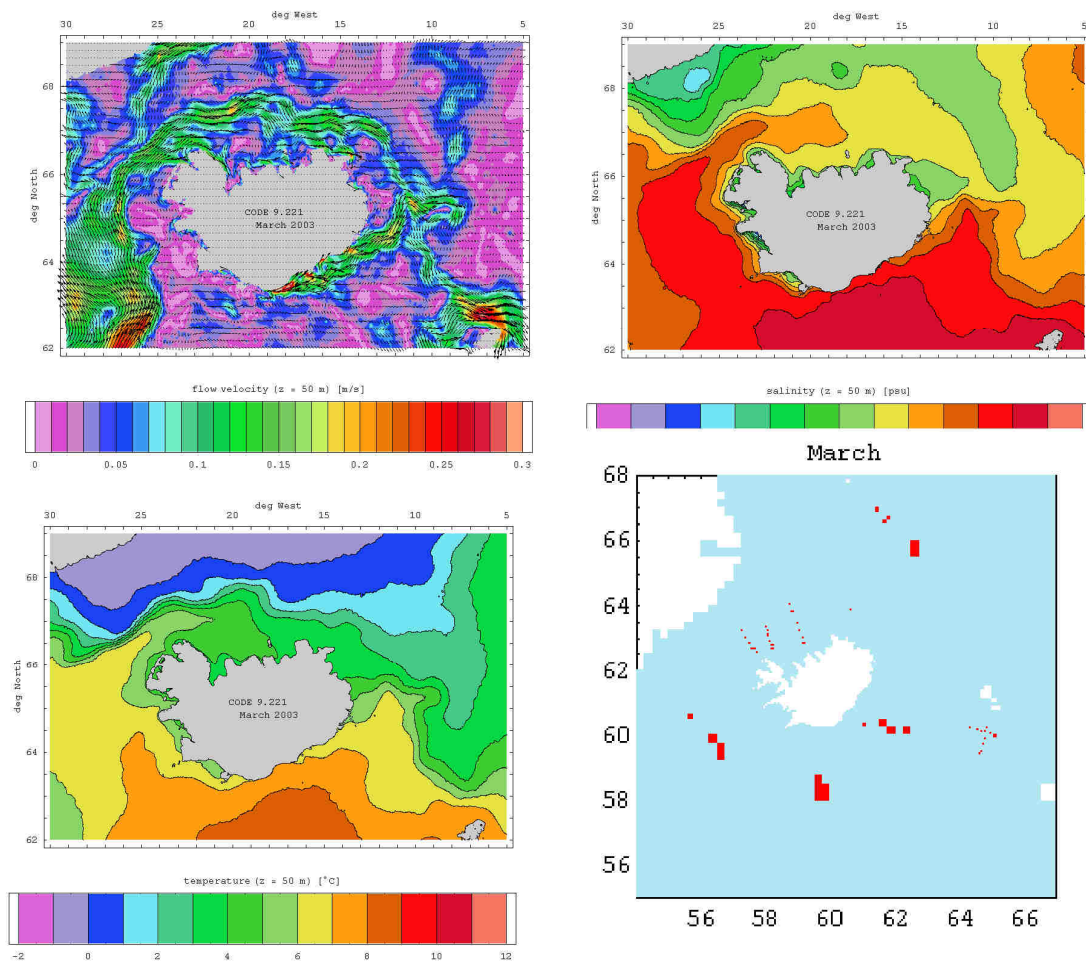


Fig. 2.135.: Monthly mean flow, salinity and temperature fields at 50 m depth and location of used CTD profiles – March 2003.



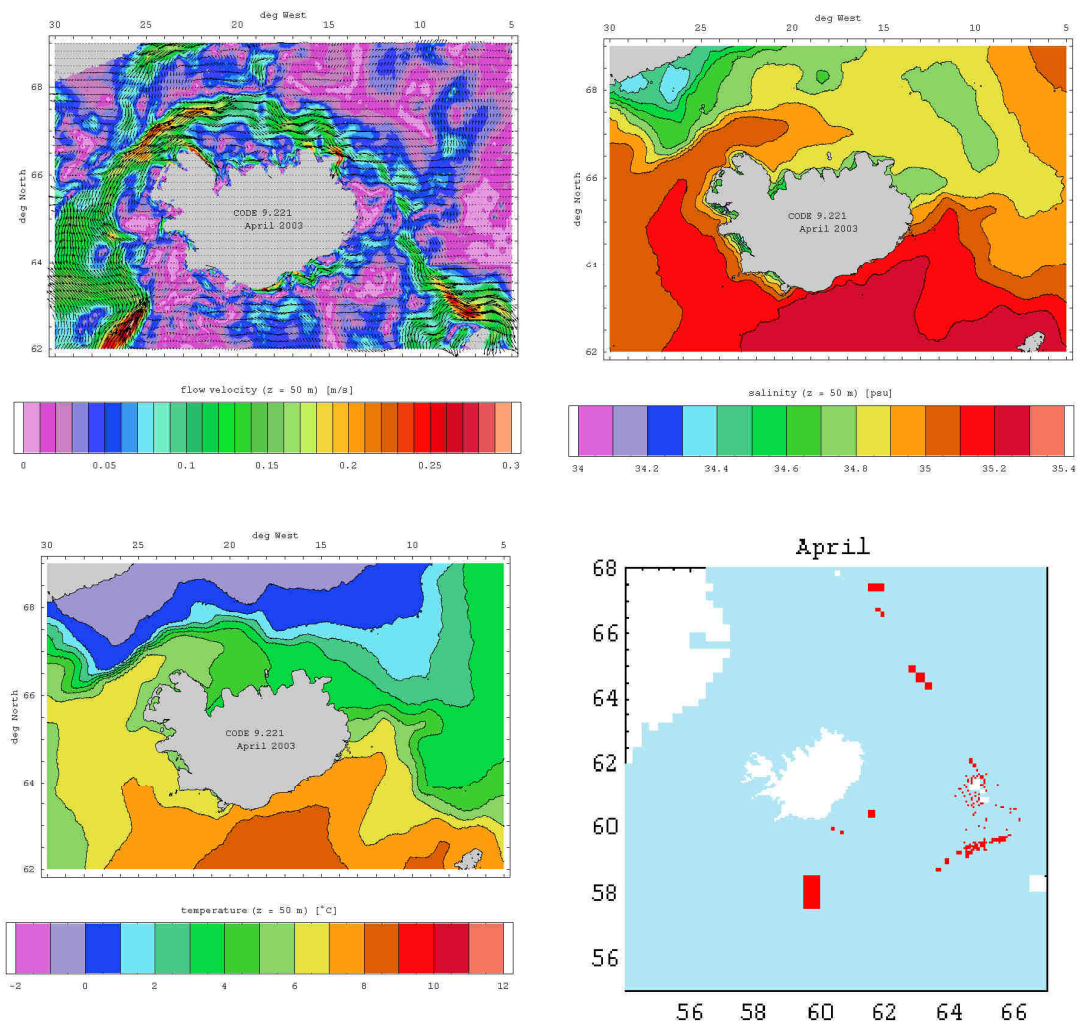


Fig. 2.136.: Monthly mean flow, salinity and temperature fields at 50 m depth and location of used CTD profiles – April 2003.

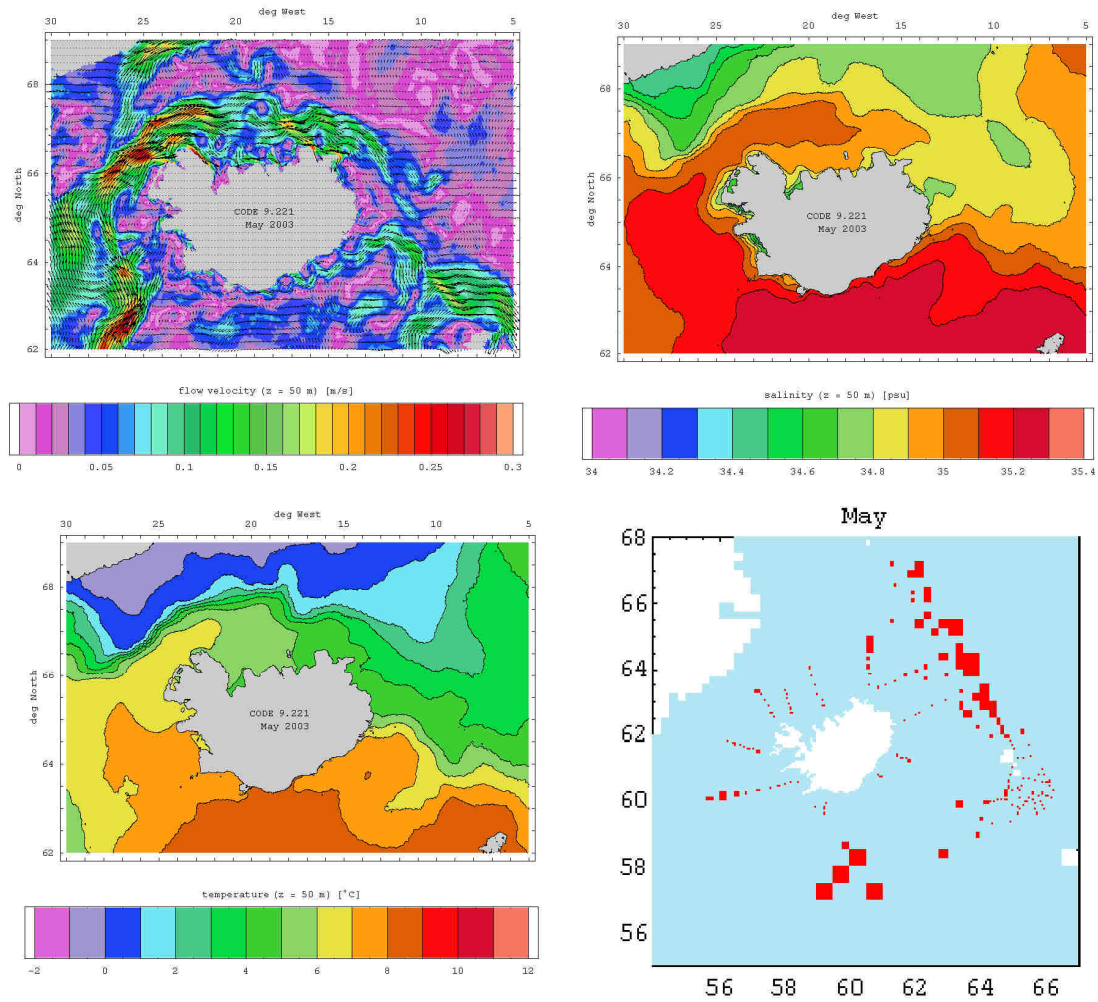


Fig. 2.137.: Monthly mean flow, salinity and temperature fields at 50 m depth and location of used CTD profiles – May 2003.

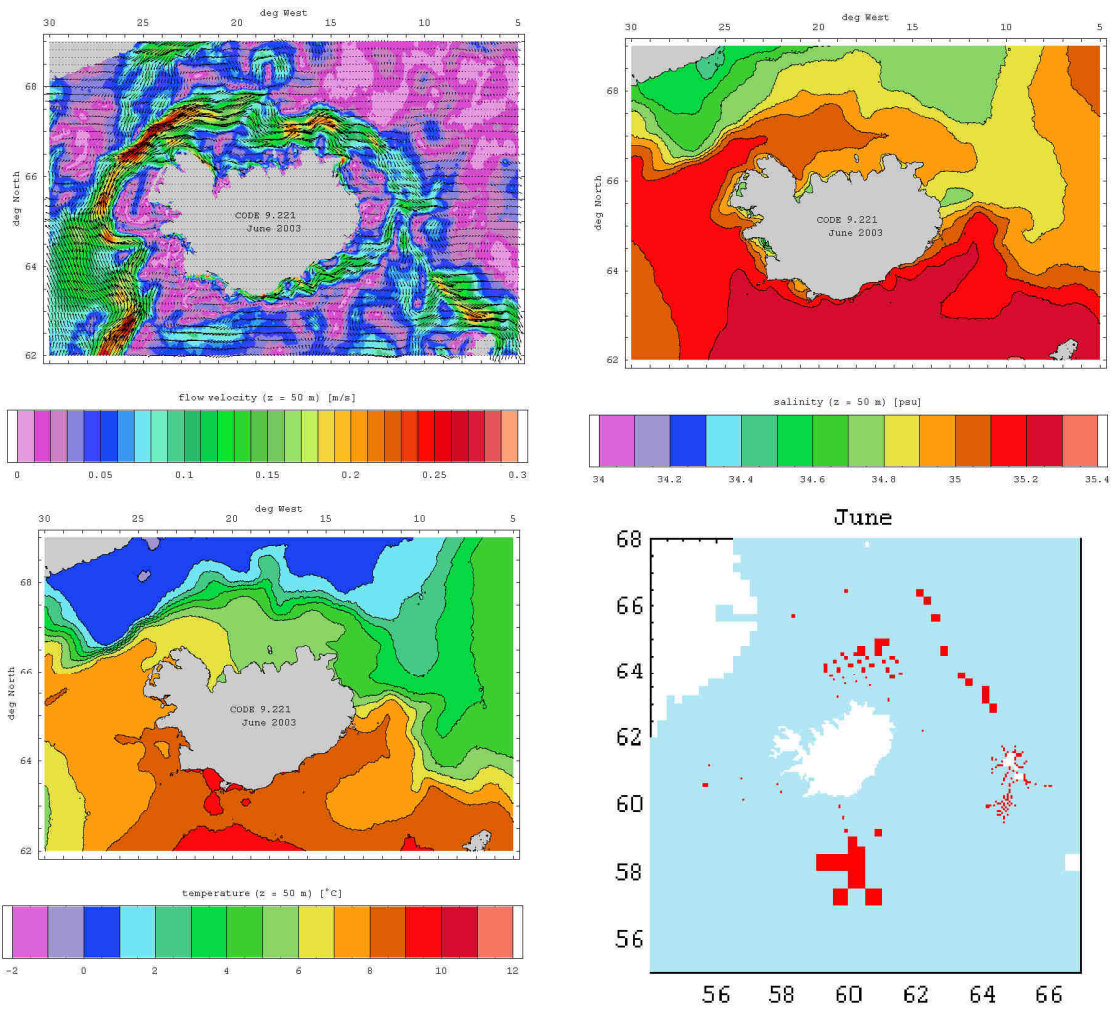


Fig. 2.138.: Monthly mean flow, salinity and temperature fields at 50 m depth and location of used CTD profiles – June 2003.

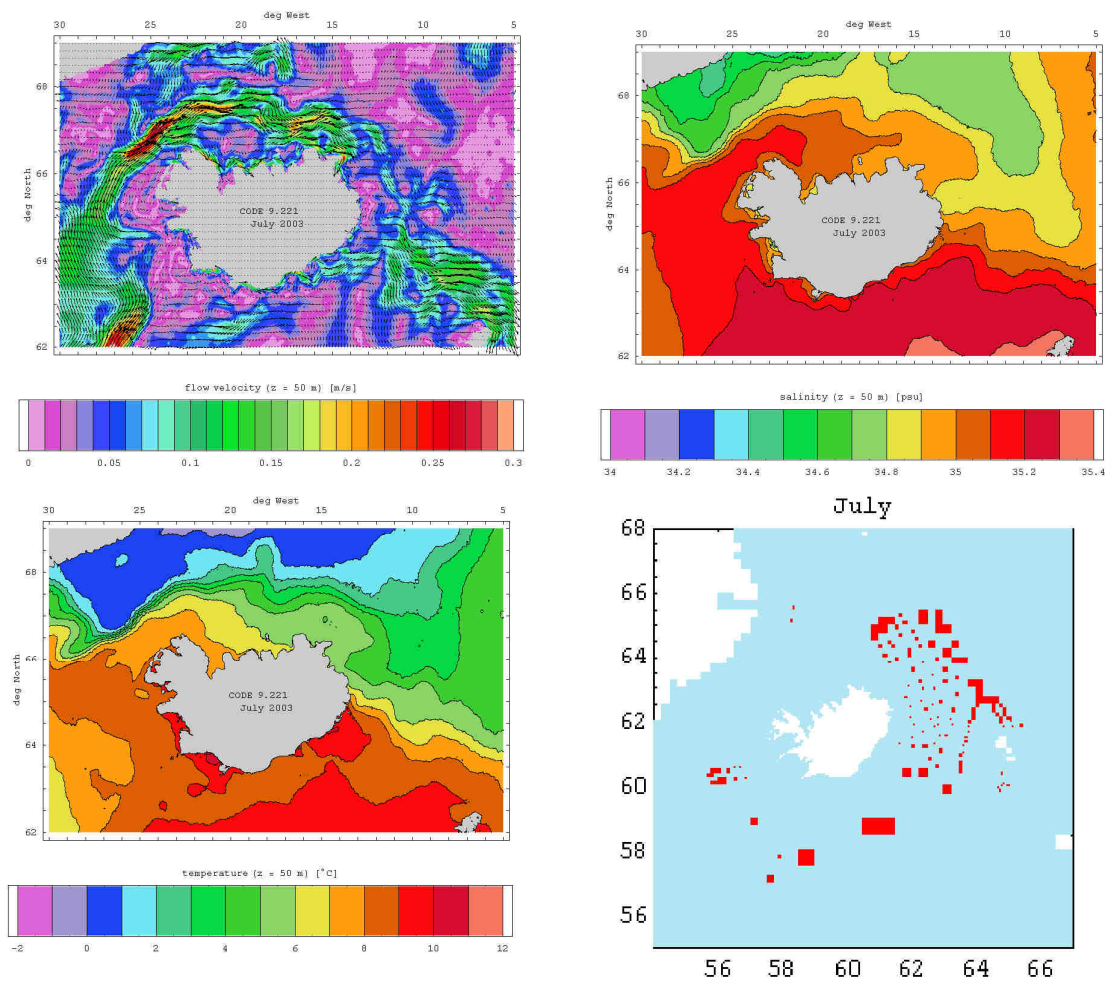


Fig. 2.139.: Monthly mean flow, salinity and temperature fields at 50 m depth and location of used CTD profiles – July 2003.

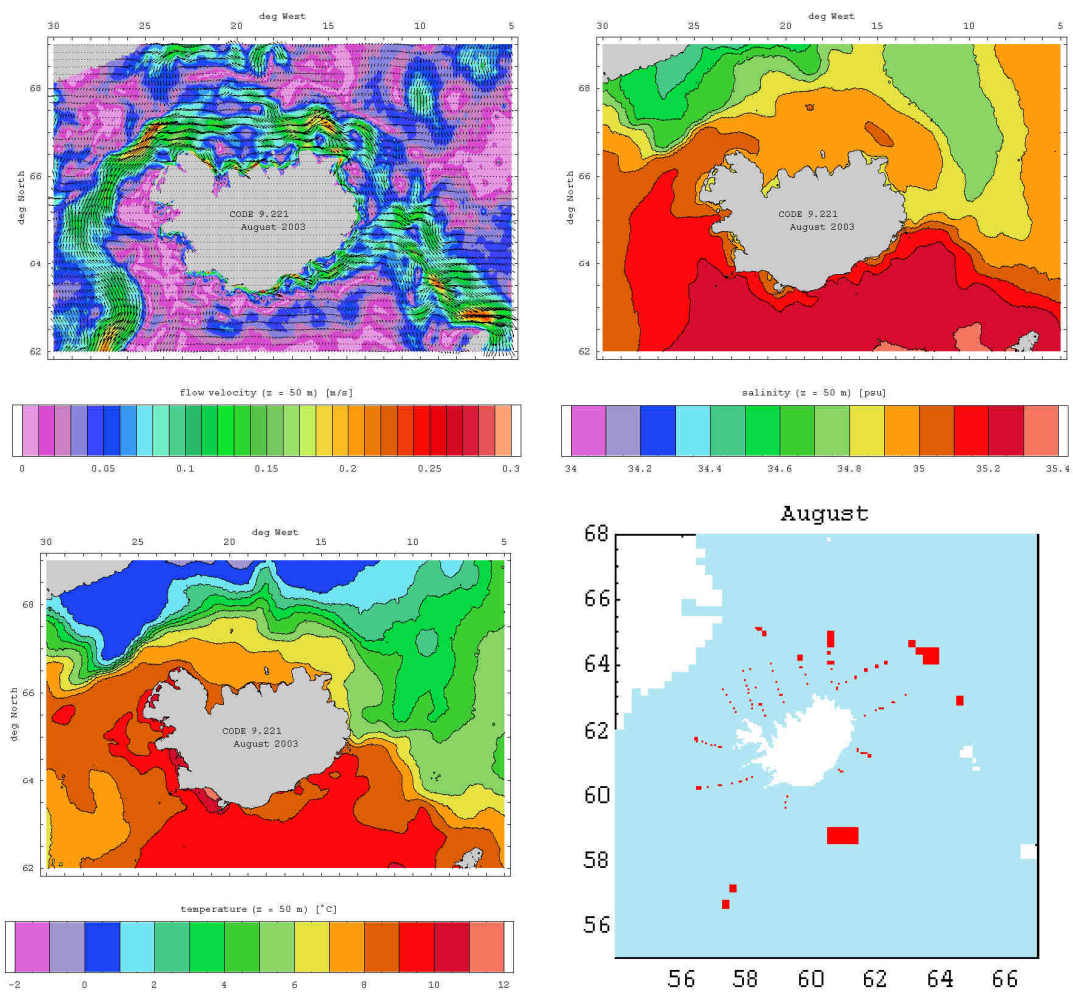


Fig. 2.140.: Monthly mean flow, salinity and temperature fields at 50 m depth and location of used CTD profiles – August 2003.



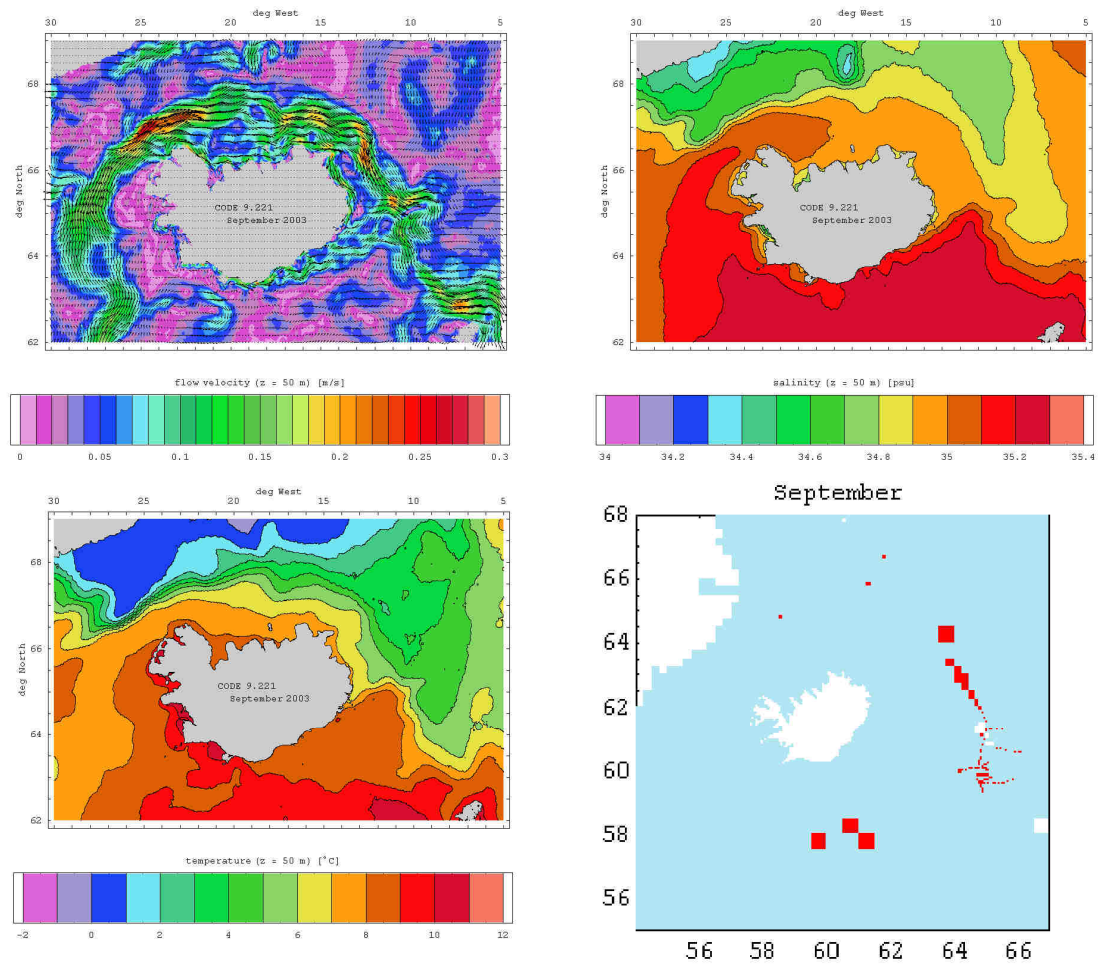


Fig. 2.141.: Monthly mean flow, salinity and temperature fields at 50 m depth and location of used CTD profiles – September 2003.

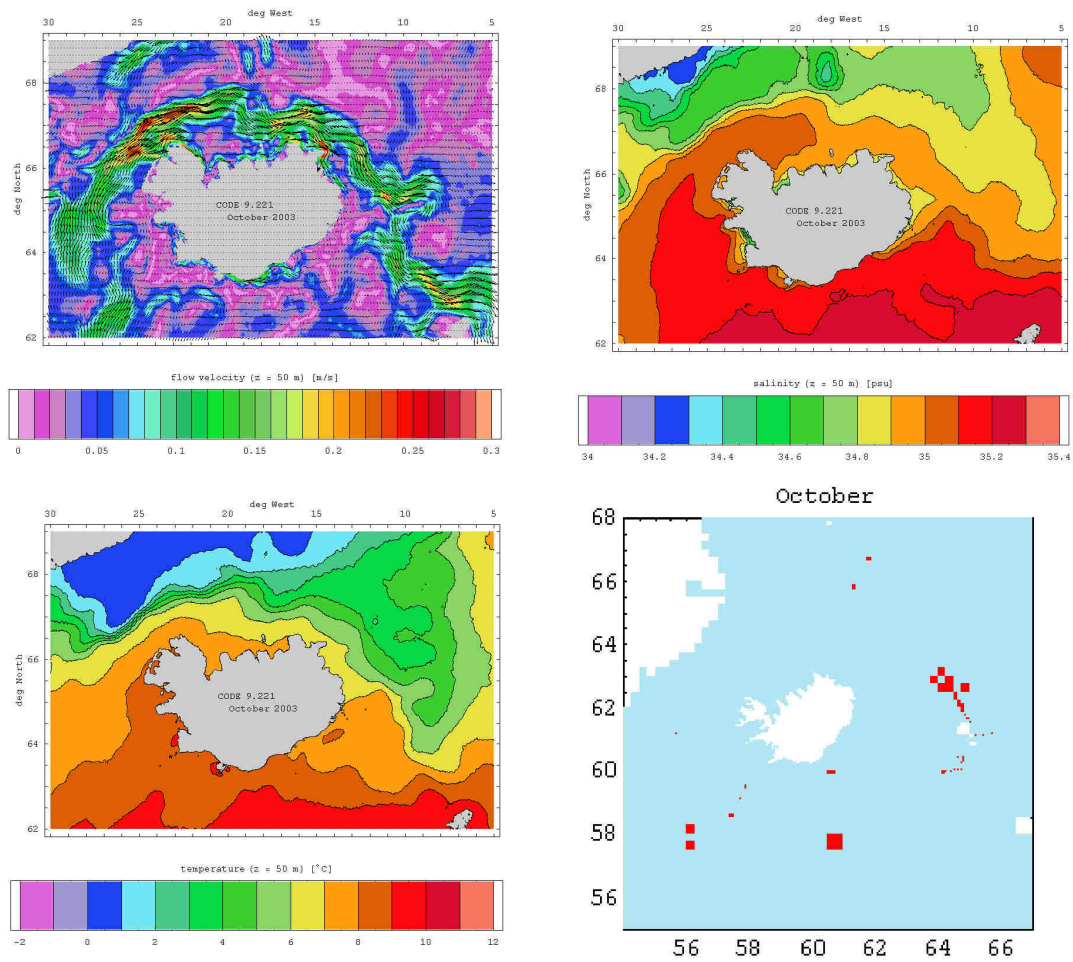


Fig. 2.142.: Monthly mean flow, salinity and temperature fields at 50 m depth and location of used CTD profiles – October 2003.

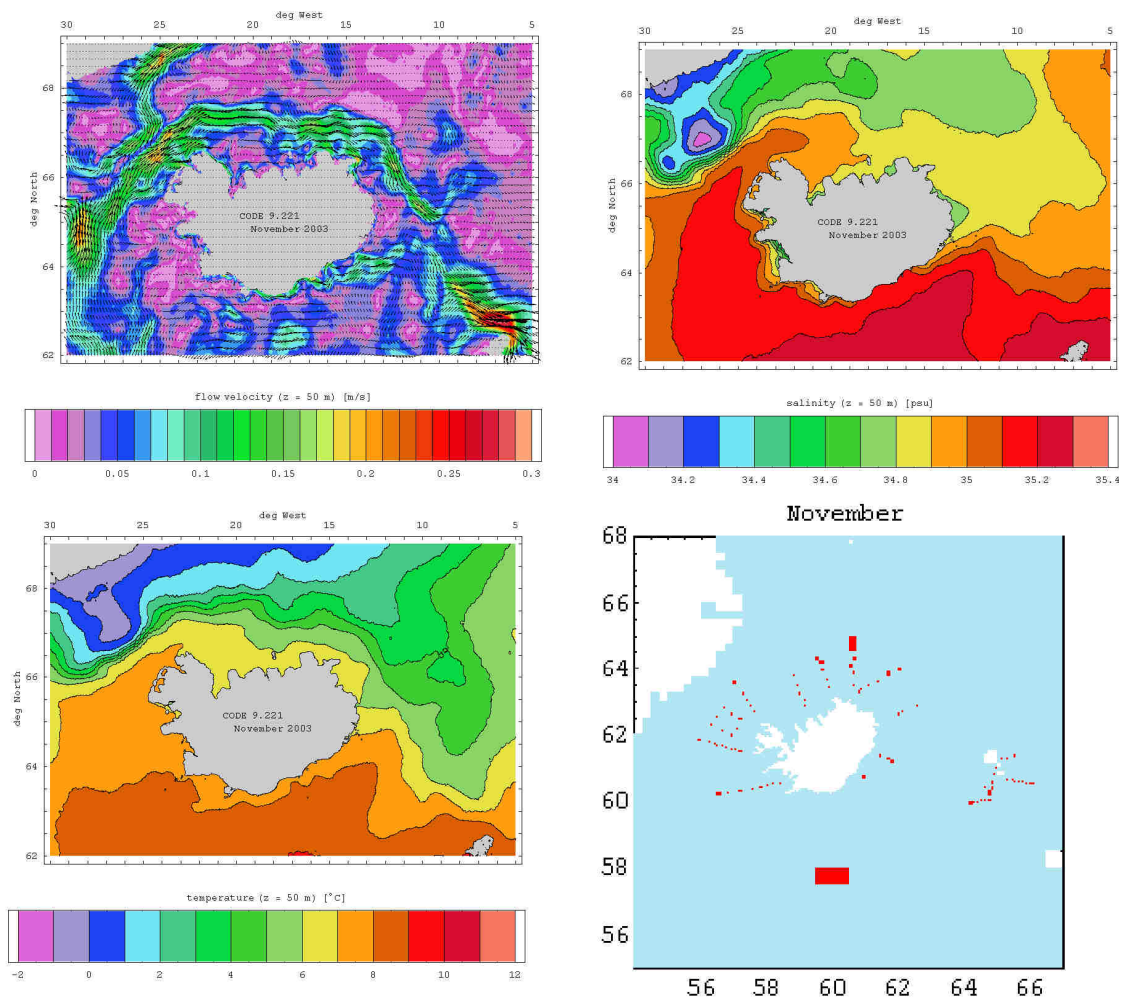


Fig. 2.143.: Monthly mean flow, salinity and temperature fields at 50 m depth and location of used CTD profiles – November 2003.

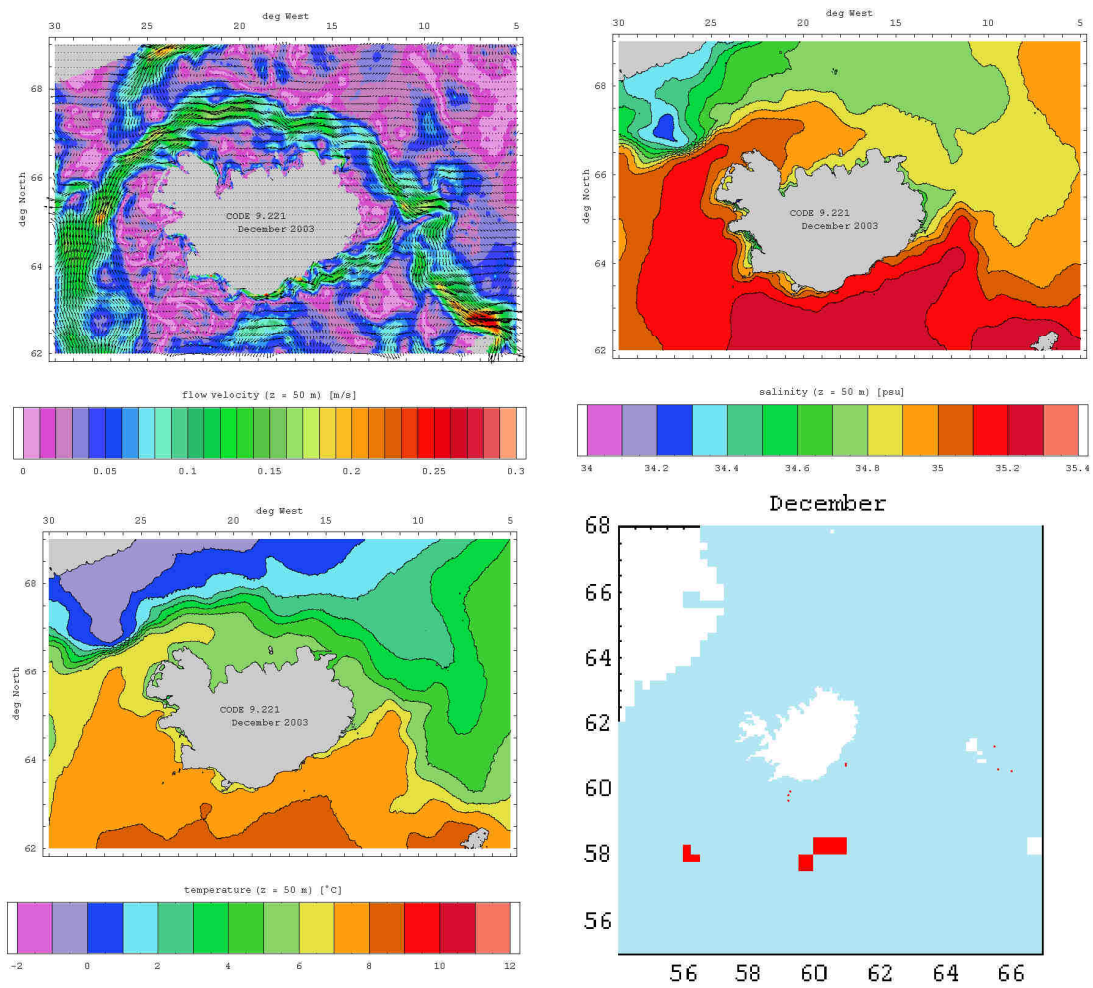


Fig. 2.144.: Monthly mean flow, salinity and temperature fields at 50 m depth and location of used CTD profiles – December 2003.

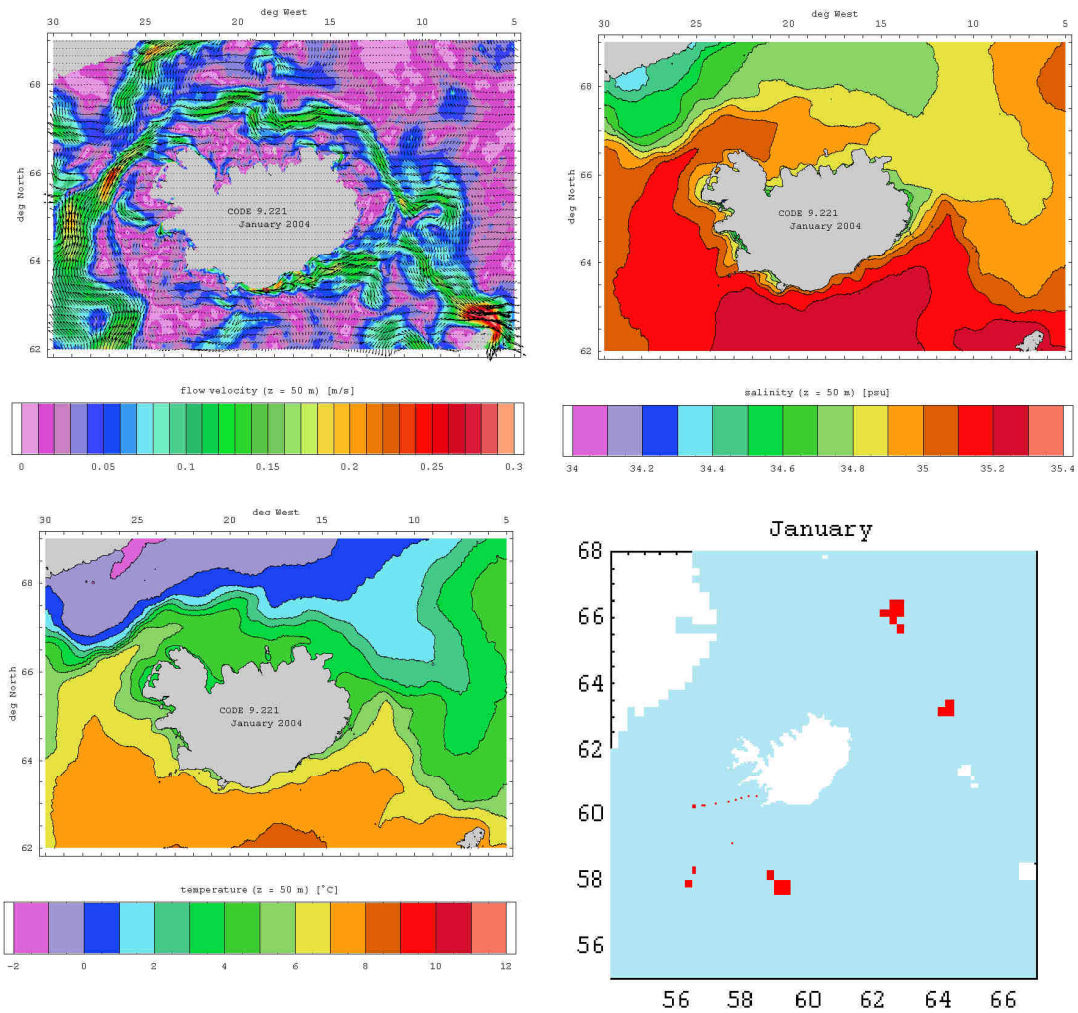


Fig. 2.145.: Monthly mean flow, salinity and temperature fields at 50 m depth and location of used CTD profiles – January 2004.



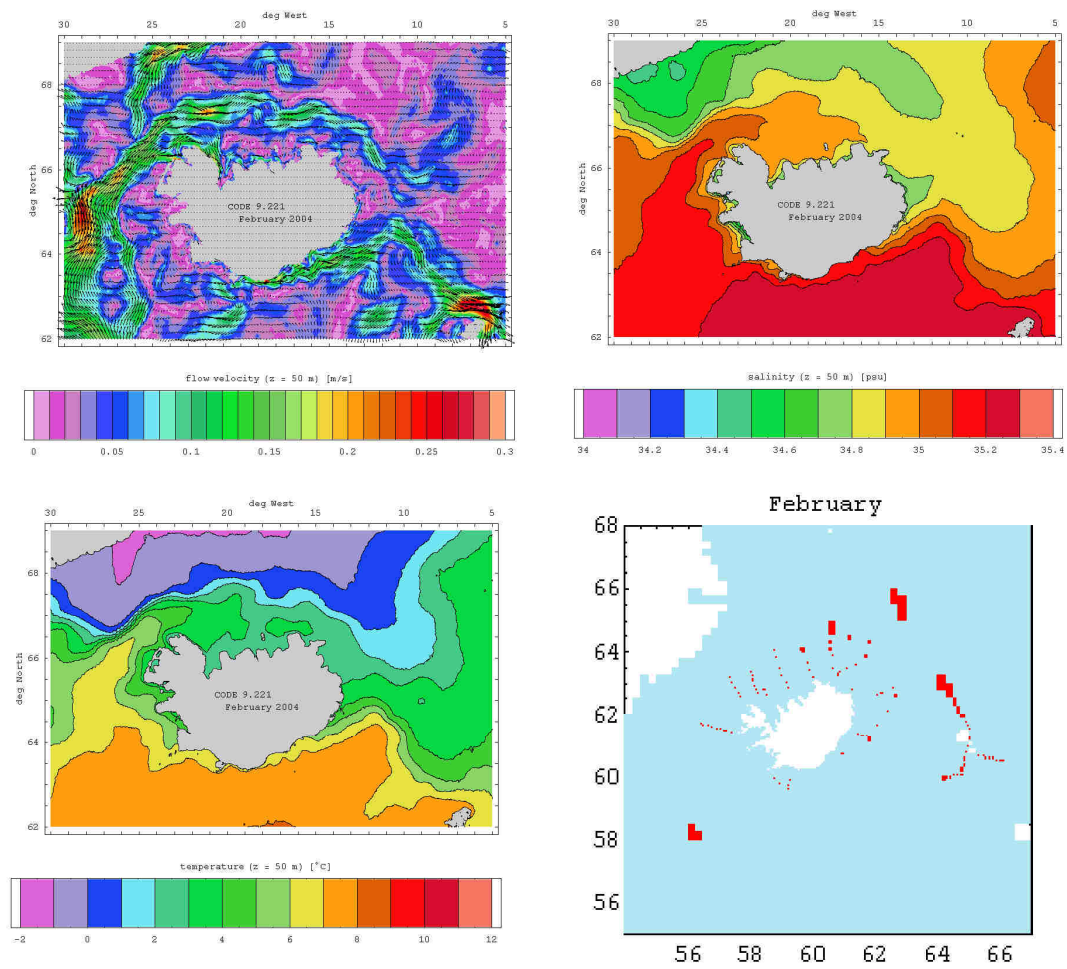


Fig. 2.146.: Monthly mean flow, salinity and temperature fields at 50 m depth and location of used CTD profiles – February 2004.

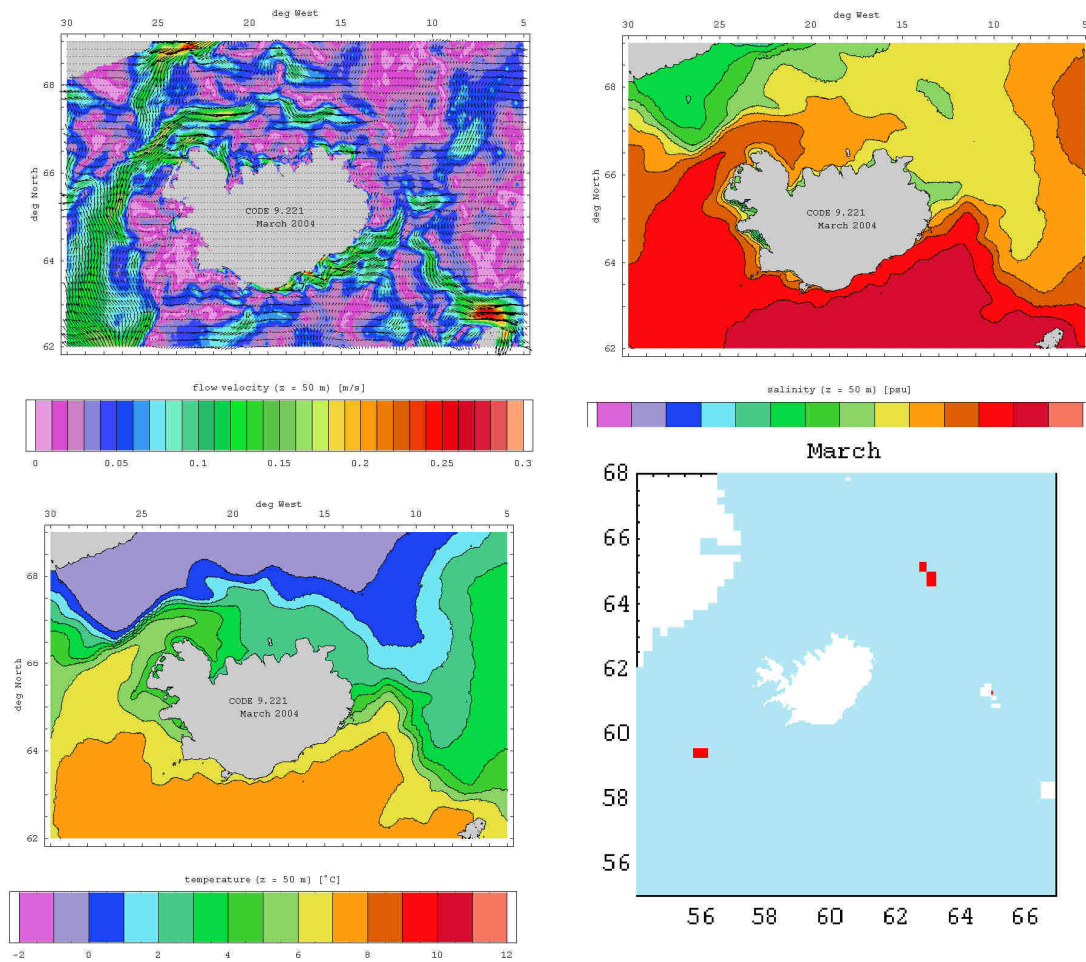


Fig. 2.147.: Monthly mean flow, salinity and temperature fields at 50 m depth and location of used CTD profiles – March 2004.

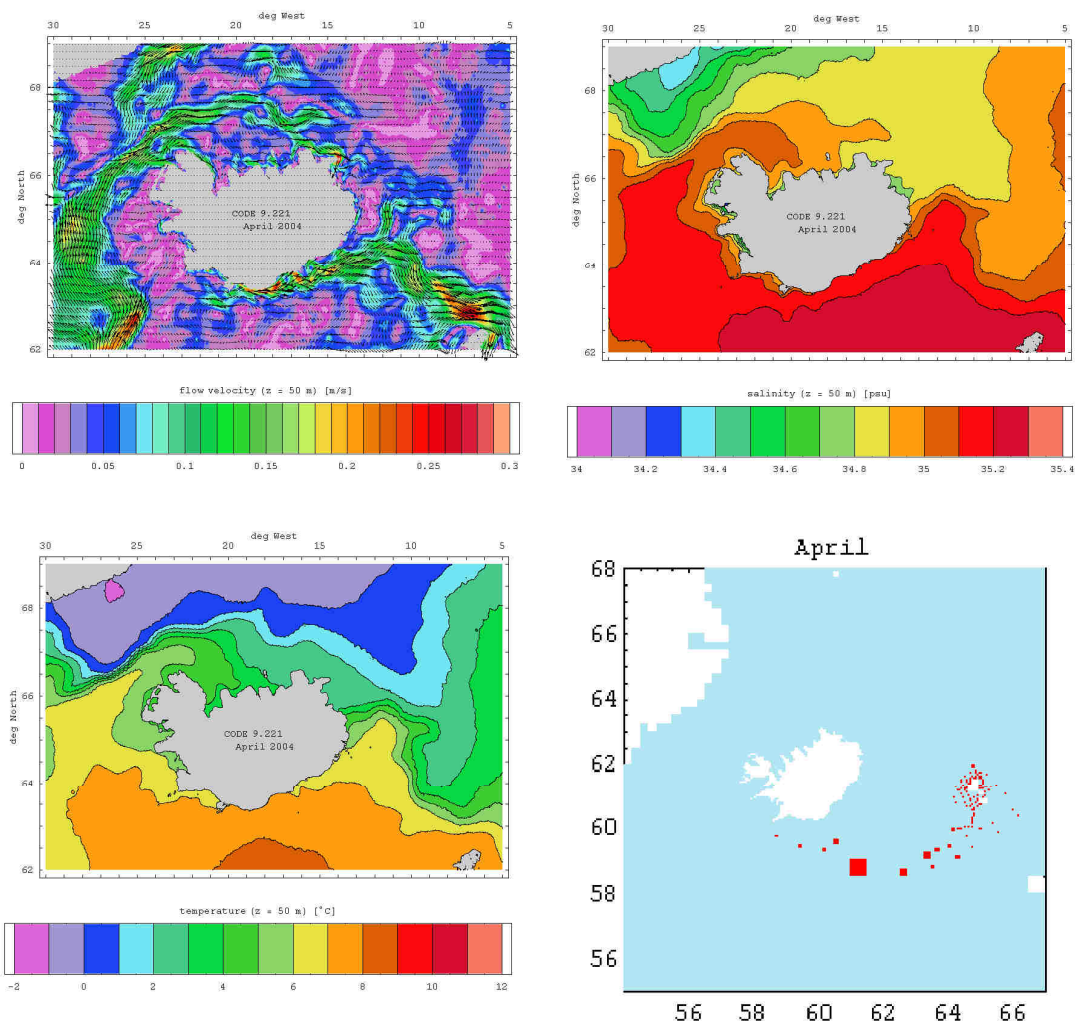


Fig. 2.148.: Monthly mean flow, salinity and temperature fields at 50 m depth and location of used CTD profiles – April 2004.

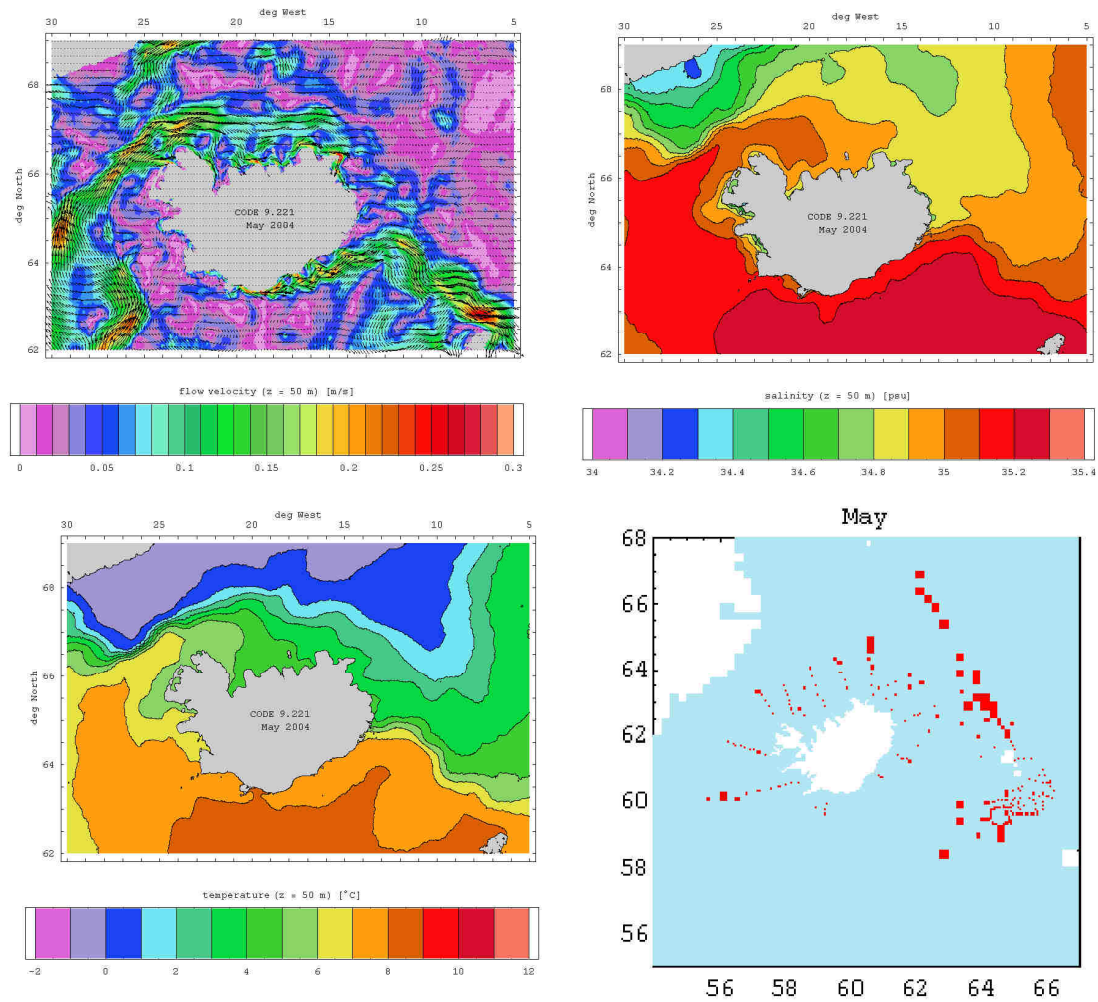


Fig. 2.149.: Monthly mean flow, salinity and temperature fields at 50 m depth and location of used CTD profiles – May 2004.

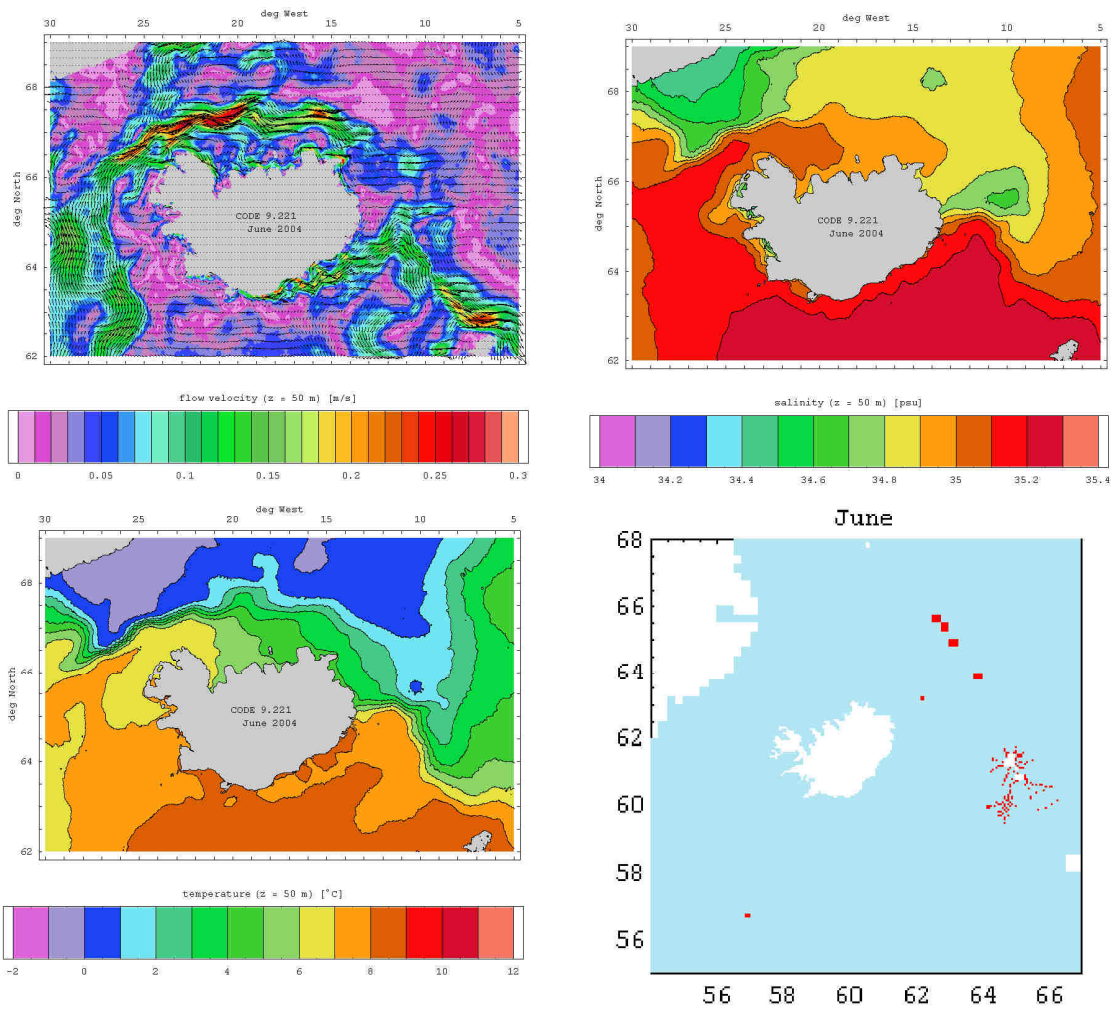


Fig. 2.150.: Monthly mean flow, salinity and temperature fields at 50 m depth and location of used CTD profiles – June 2004.



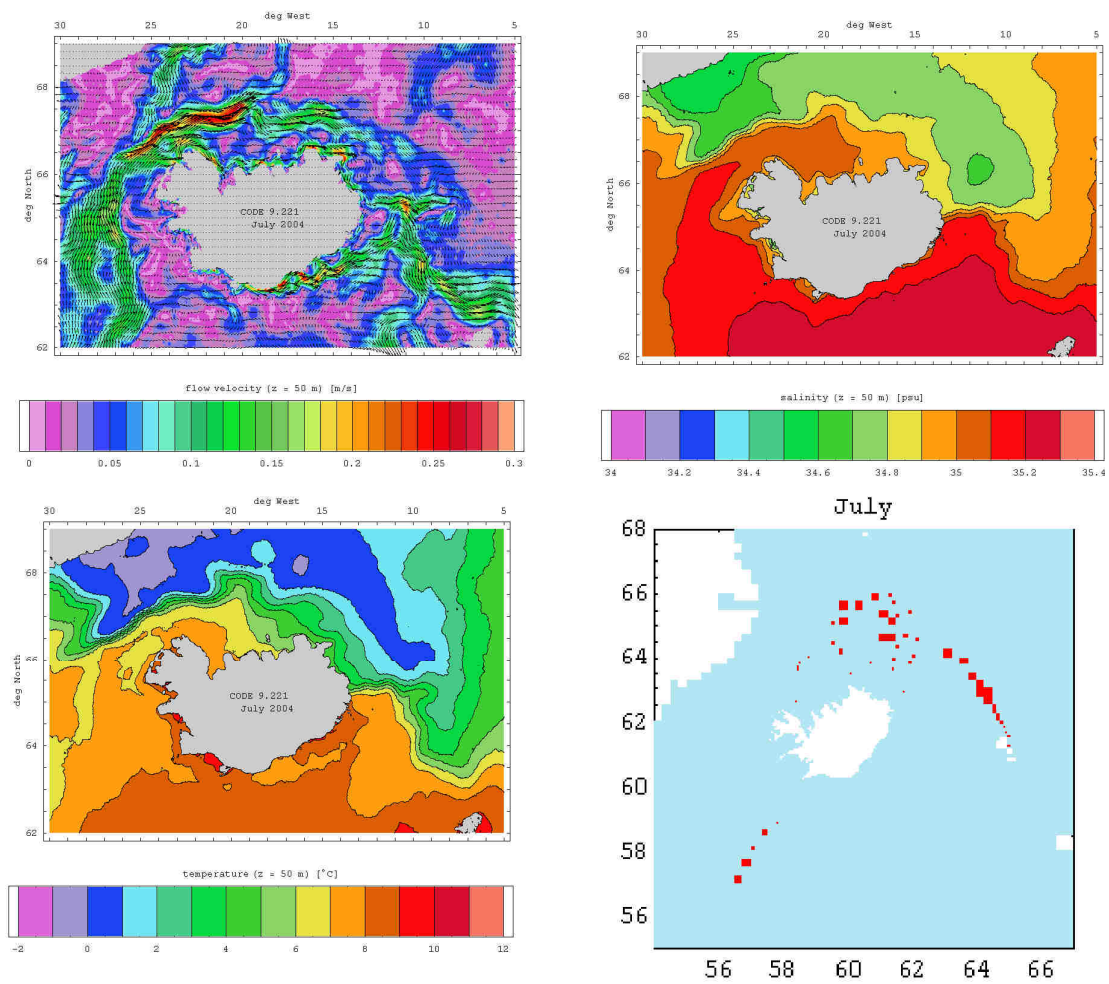


Fig. 2.151.: Monthly mean flow, salinity and temperature fields at 50 m depth and location of used CTD profiles – July 2004.

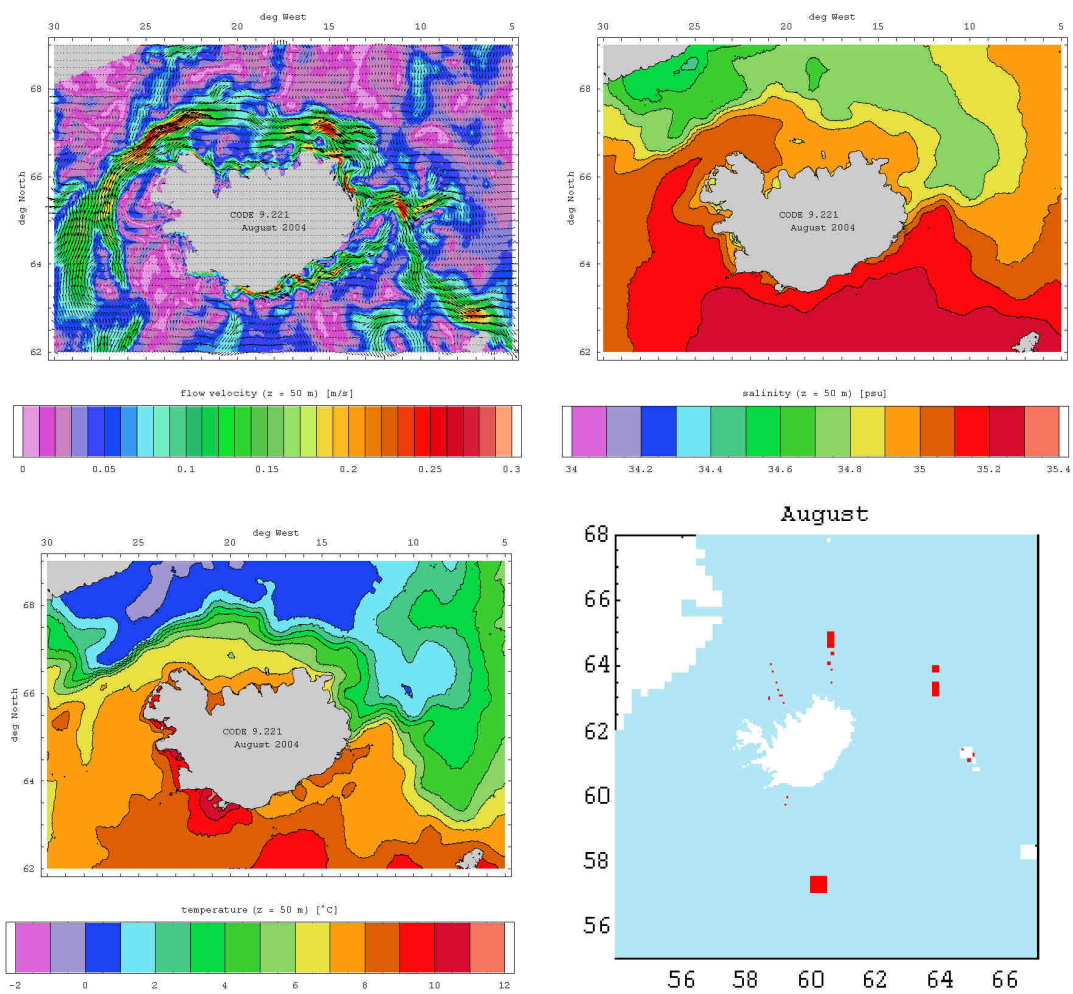


Fig. 2.152.: Monthly mean flow, salinity and temperature fields at 50 m depth and location of used CTD profiles – August 2004.

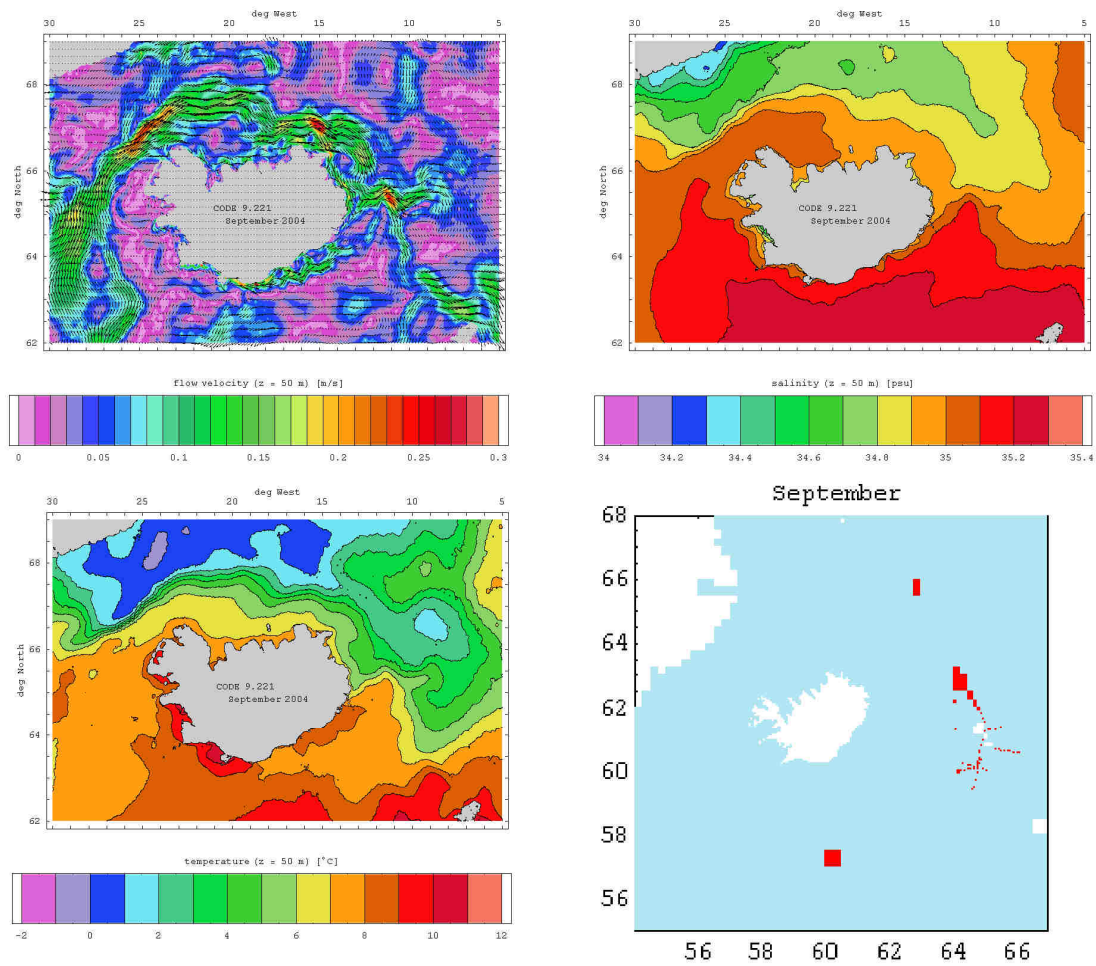


Fig. 2.153.: Monthly mean flow, salinity and temperature fields at 50 m depth and location of used CTD profiles – September 2004.

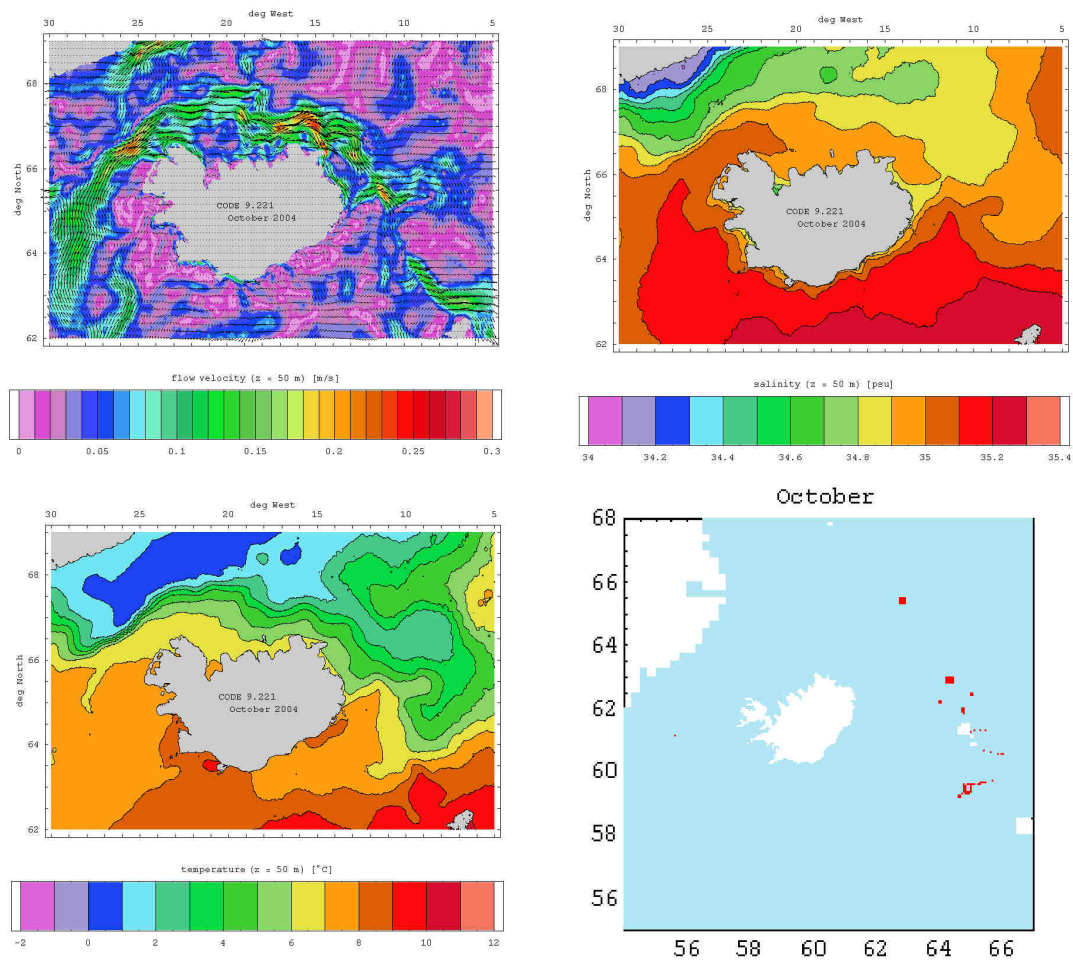


Fig. 2.154.: Monthly mean flow, salinity and temperature fields at 50 m depth and location of used CTD profiles – October 2004.

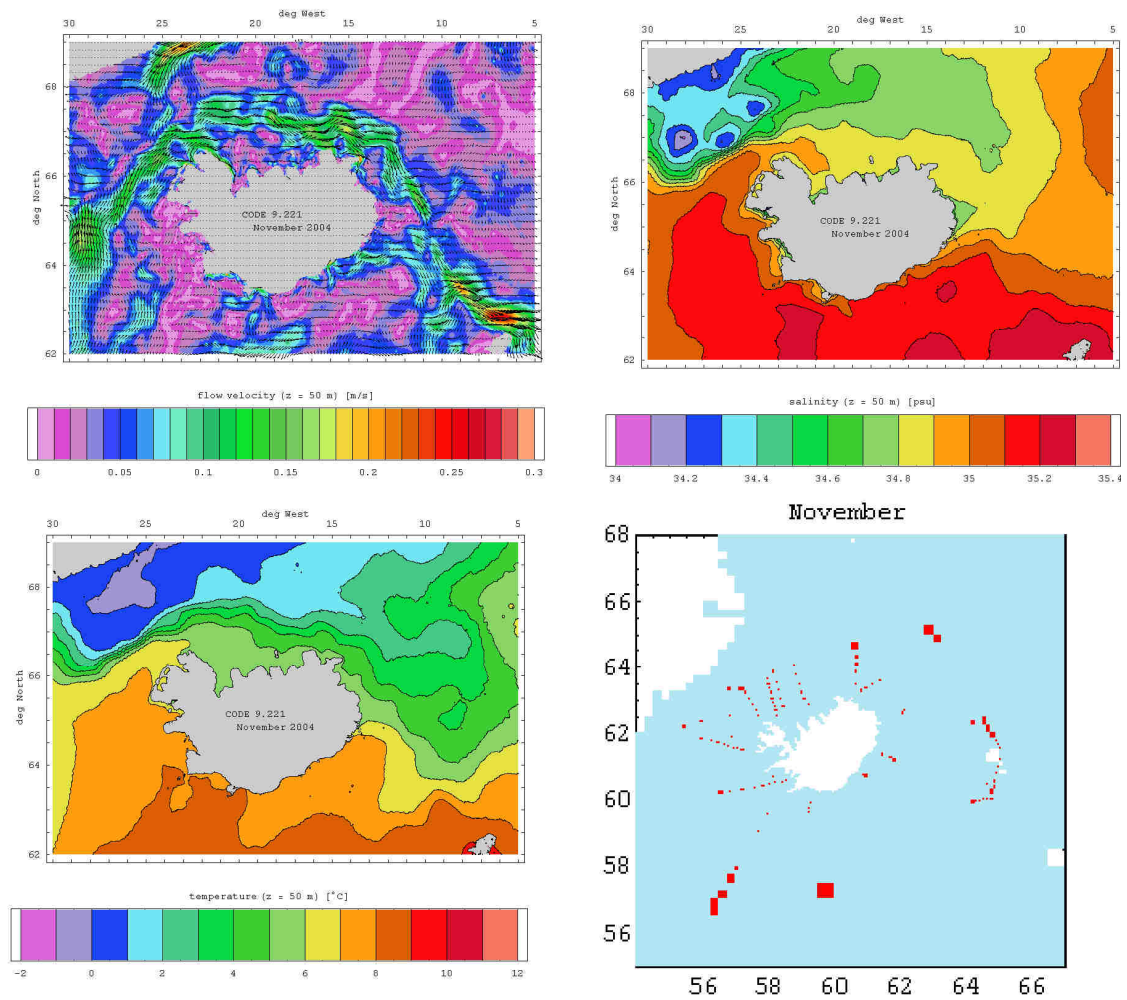


Fig. 2.155.: Monthly mean flow, salinity and temperature fields at 50 m depth and location of used CTD profiles – November 2004.



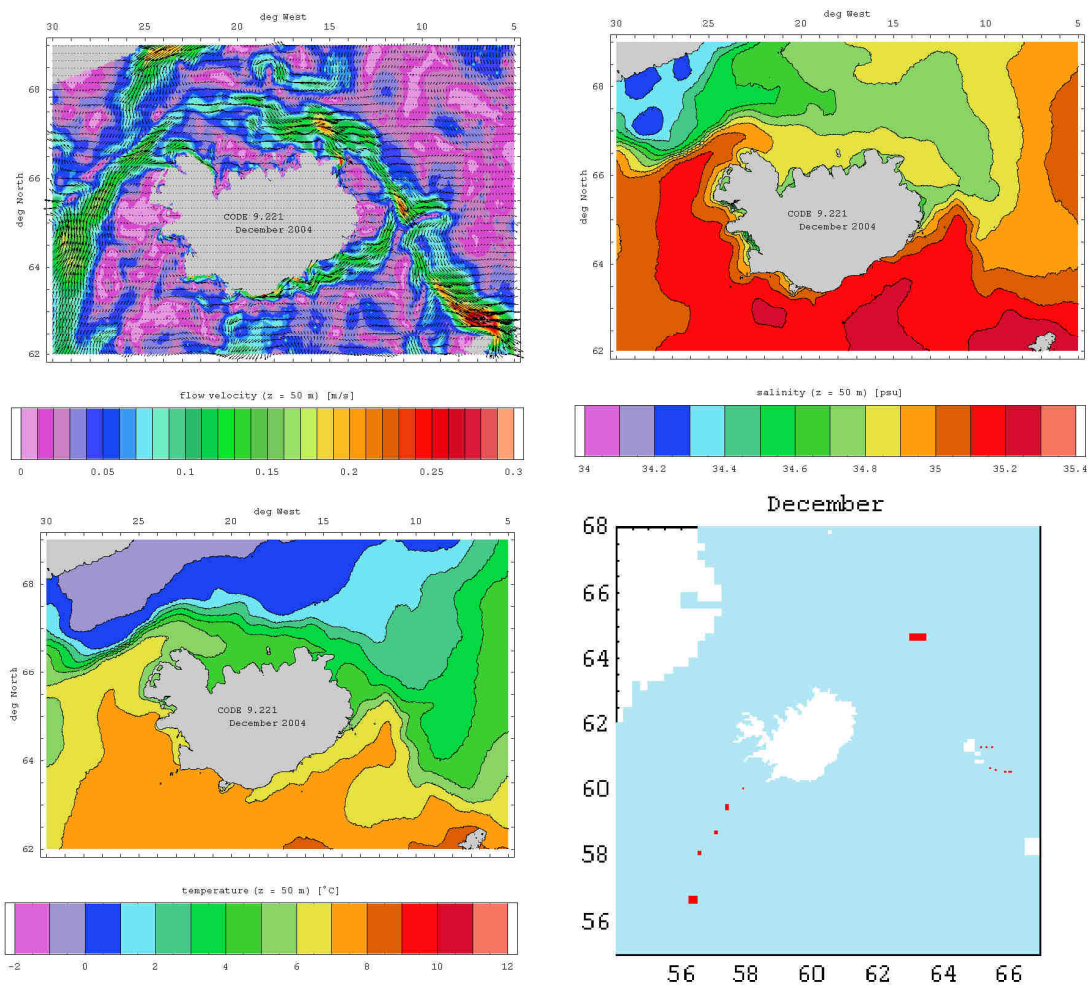


Fig. 2.156.: Monthly mean flow, salinity and temperature fields at 50 m depth and location of used CTD profiles – December 2004.

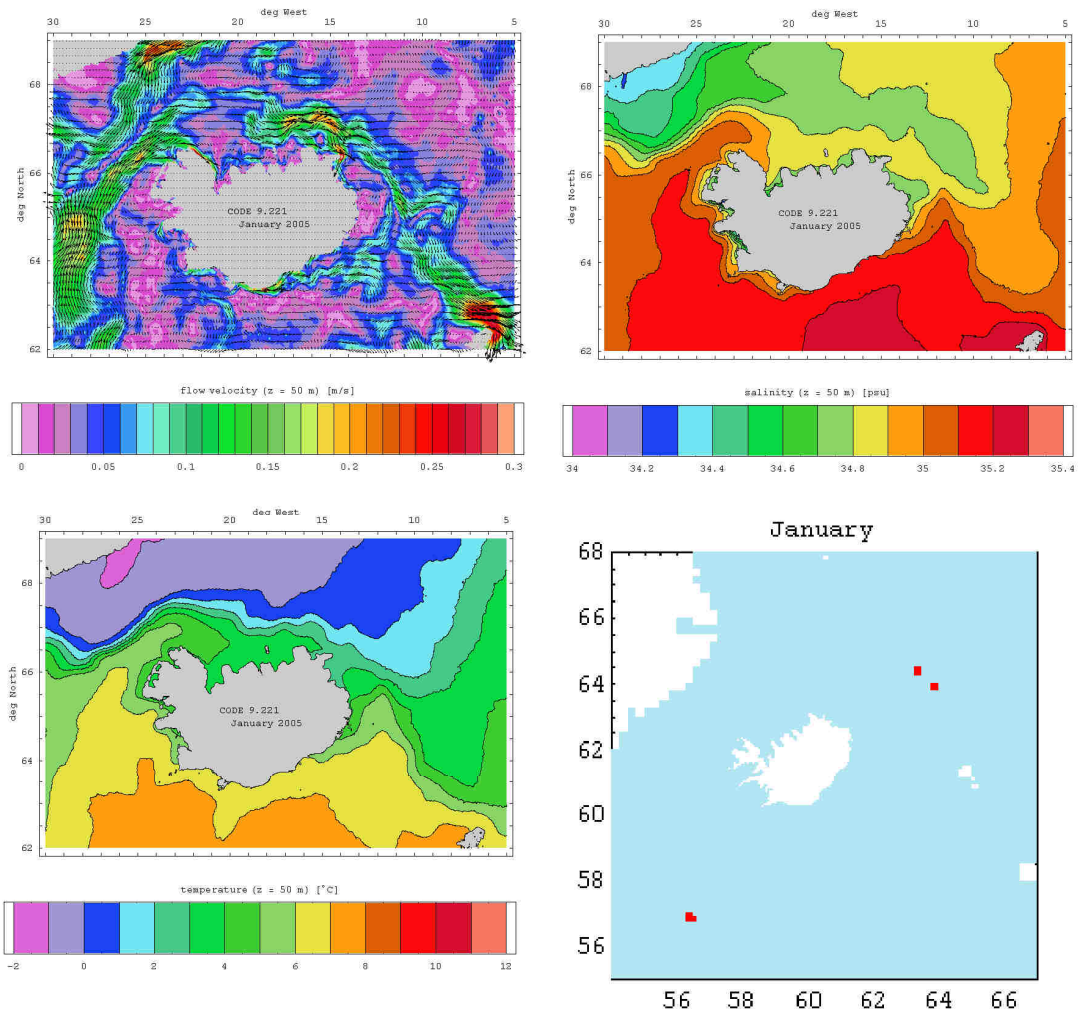


Fig. 2.157.: Monthly mean flow, salinity and temperature fields at 50 m depth and location of used CTD profiles – January 2005.

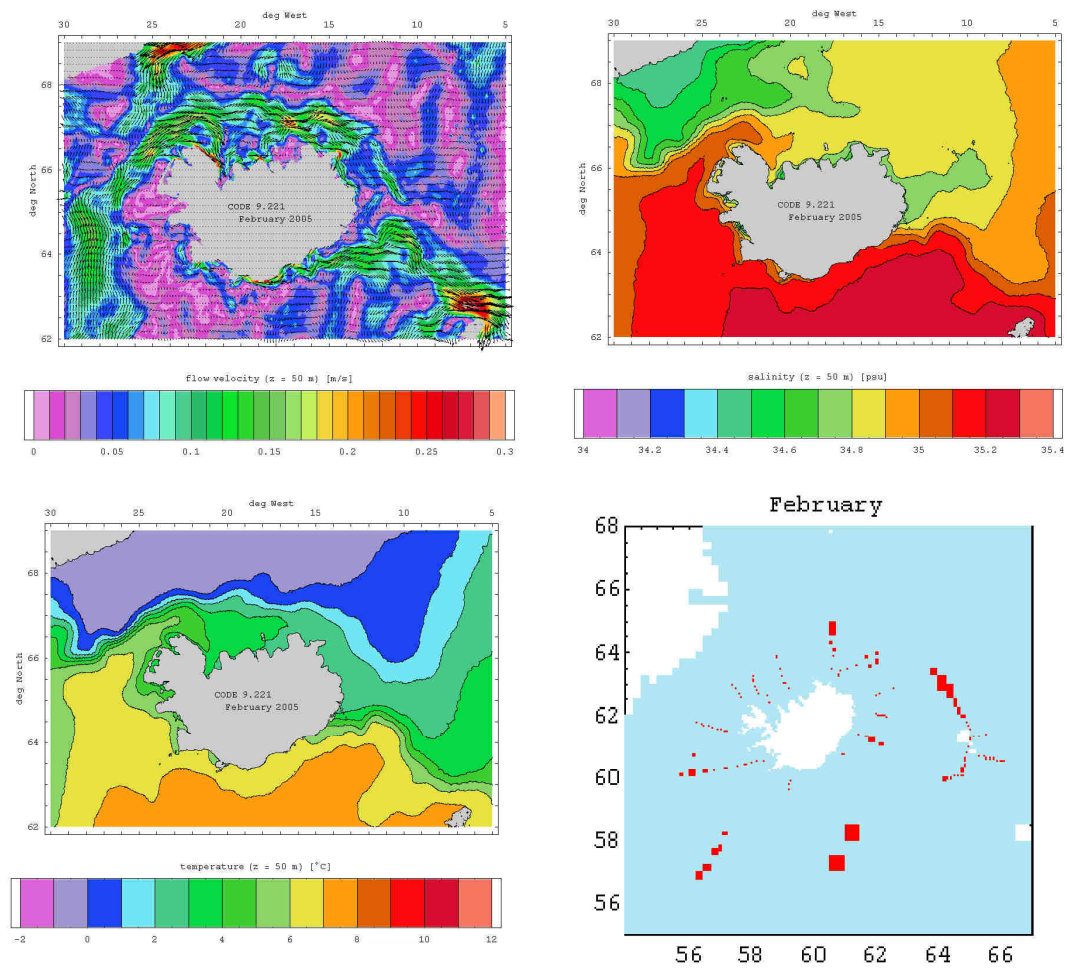


Fig. 2.158.: Monthly mean flow, salinity and temperature fields at 50 m depth and location of used CTD profiles – February 2005.

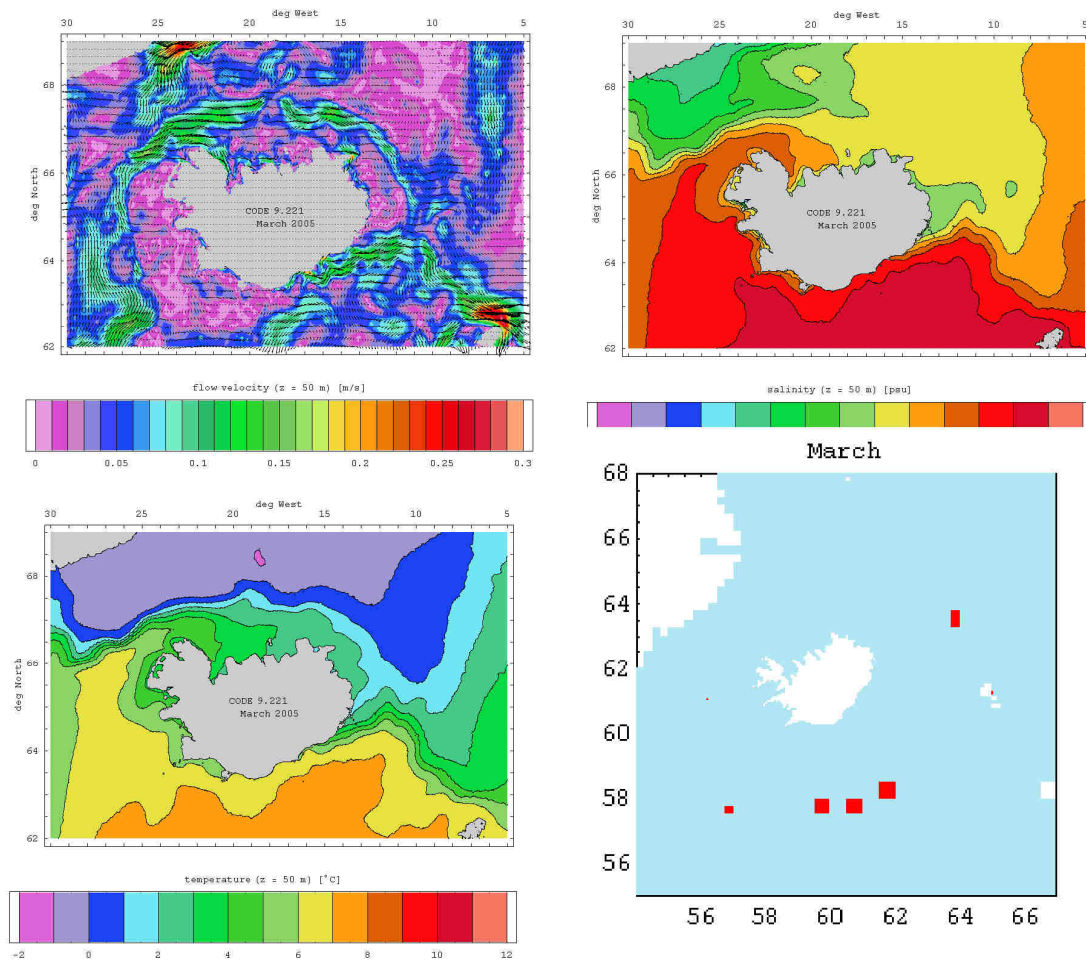


Fig. 2.159.: Monthly mean flow, salinity and temperature fields at 50 m depth and location of used CTD profiles – March 2005.

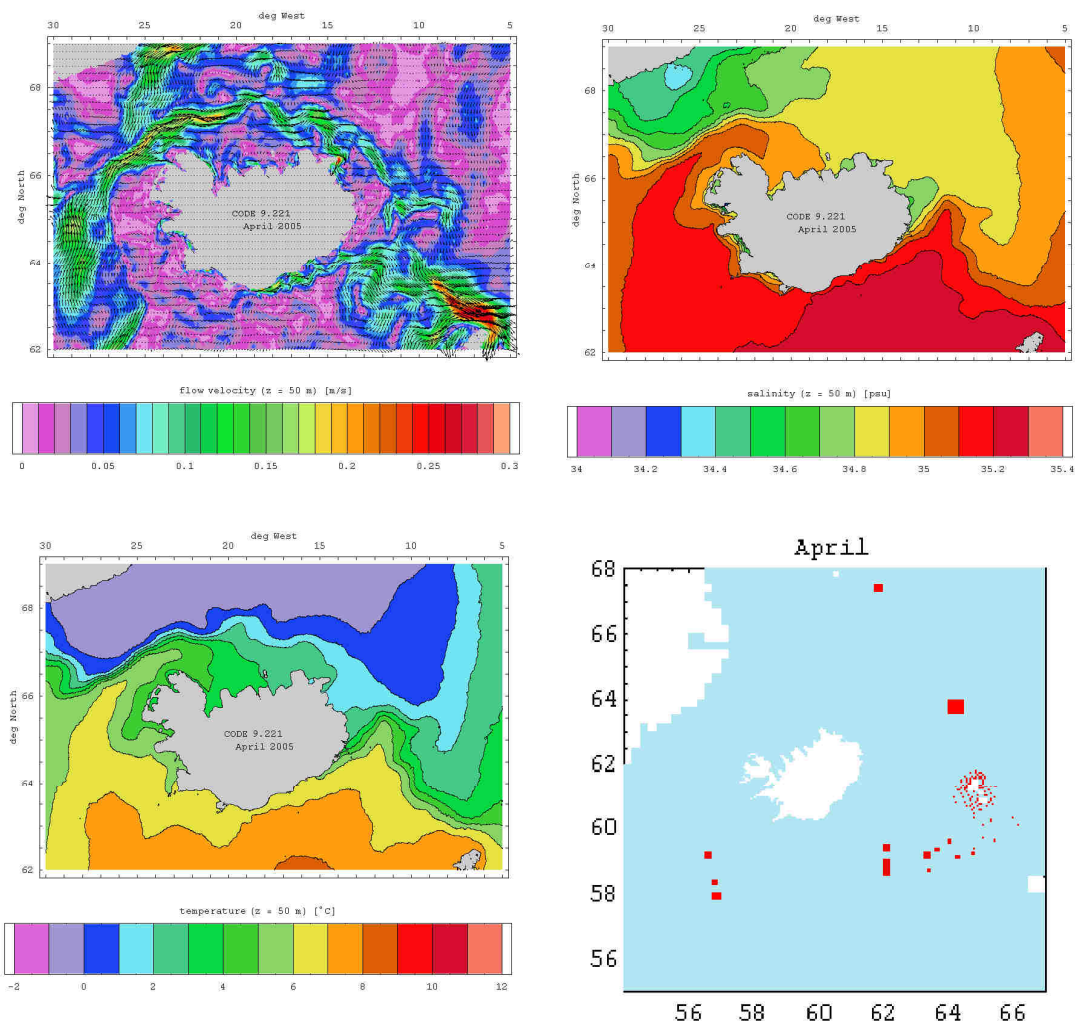


Fig. 2.160.: Monthly mean flow, salinity and temperature fields at 50 m depth and location of used CTD profiles – April 2005.



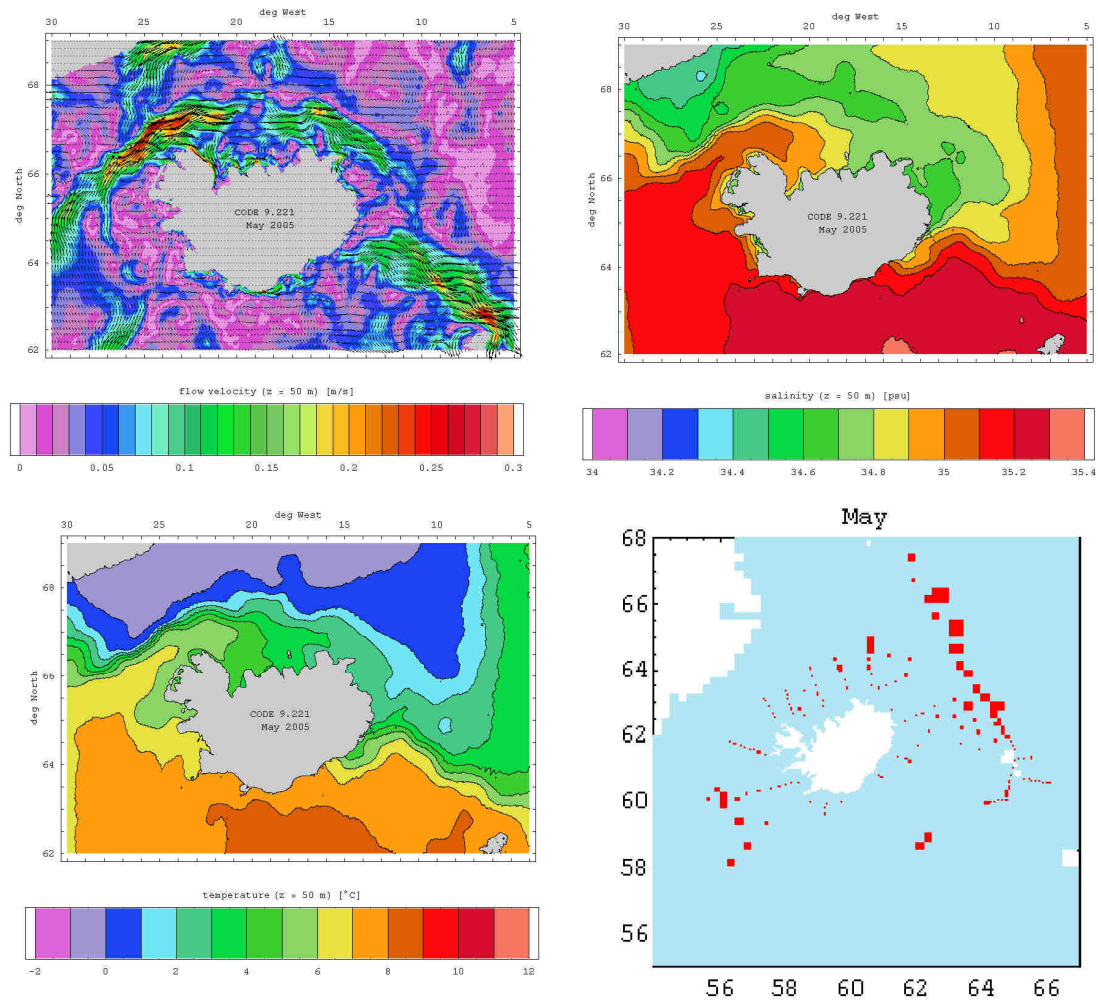


Fig. 2.161.: Monthly mean flow, salinity and temperature fields at 50 m depth and location of used CTD profiles – May 2005.

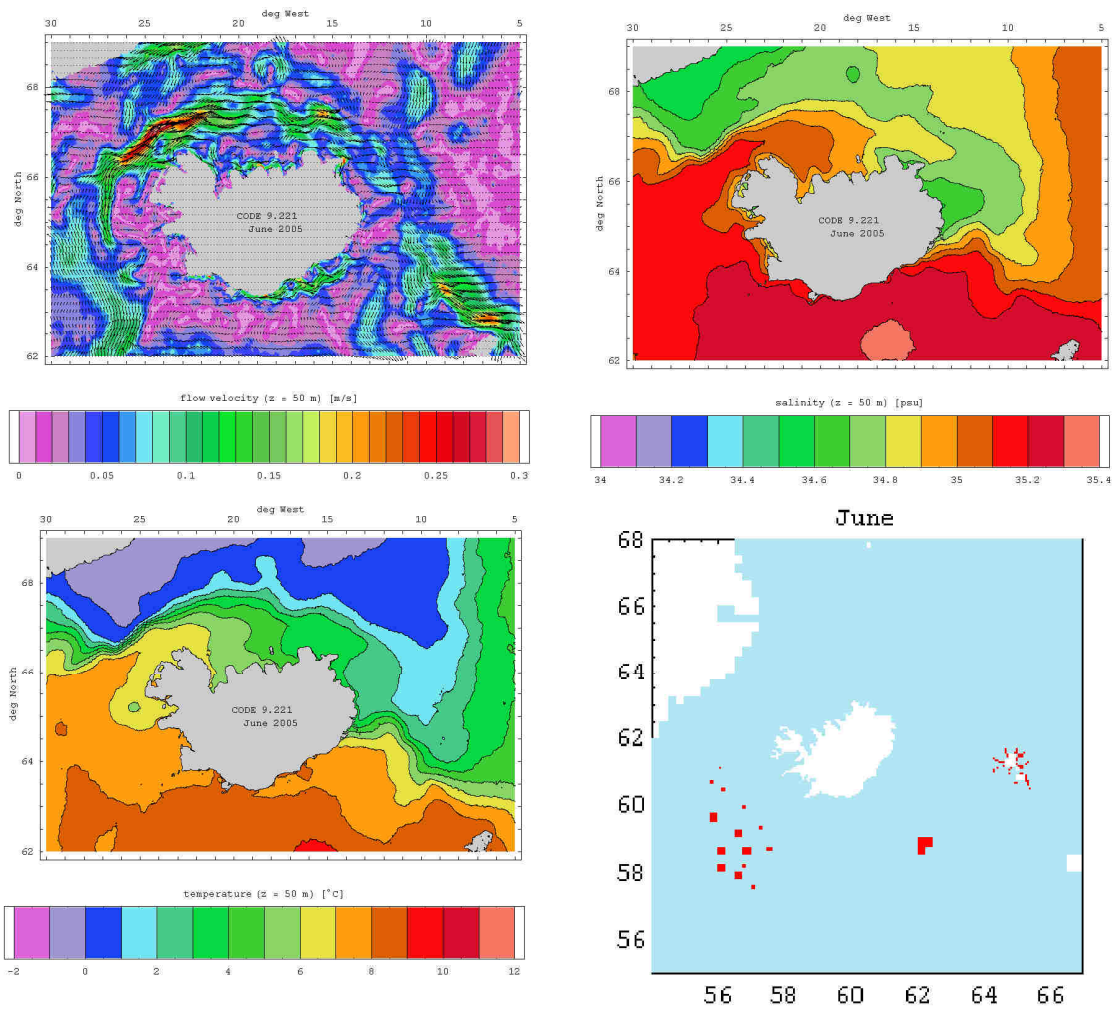


Fig. 2.162.: Monthly mean flow, salinity and temperature fields at 50 m depth and location of used CTD profiles – June 2005.

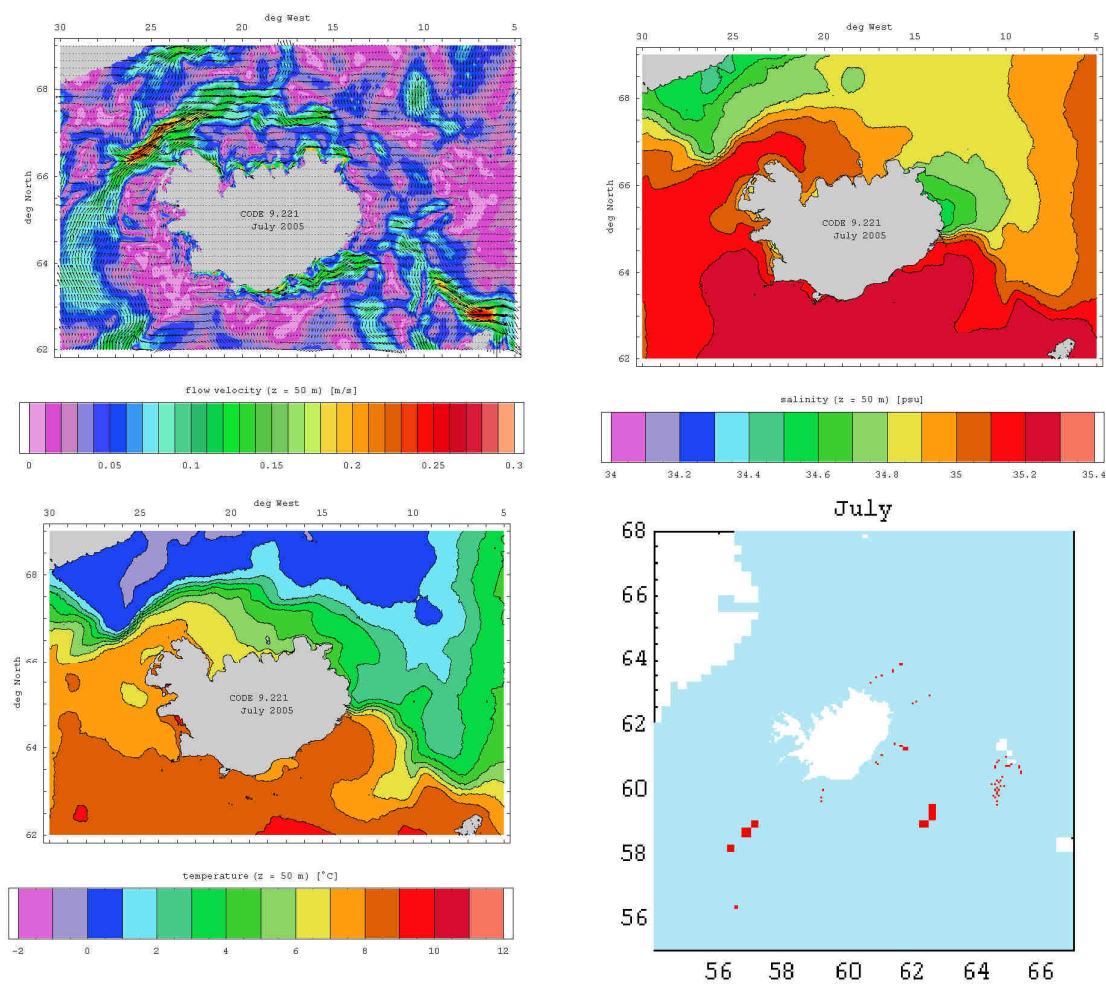


Fig. 2.163.: Monthly mean flow, salinity and temperature fields at 50 m depth and location of used CTD profiles – July 2005.

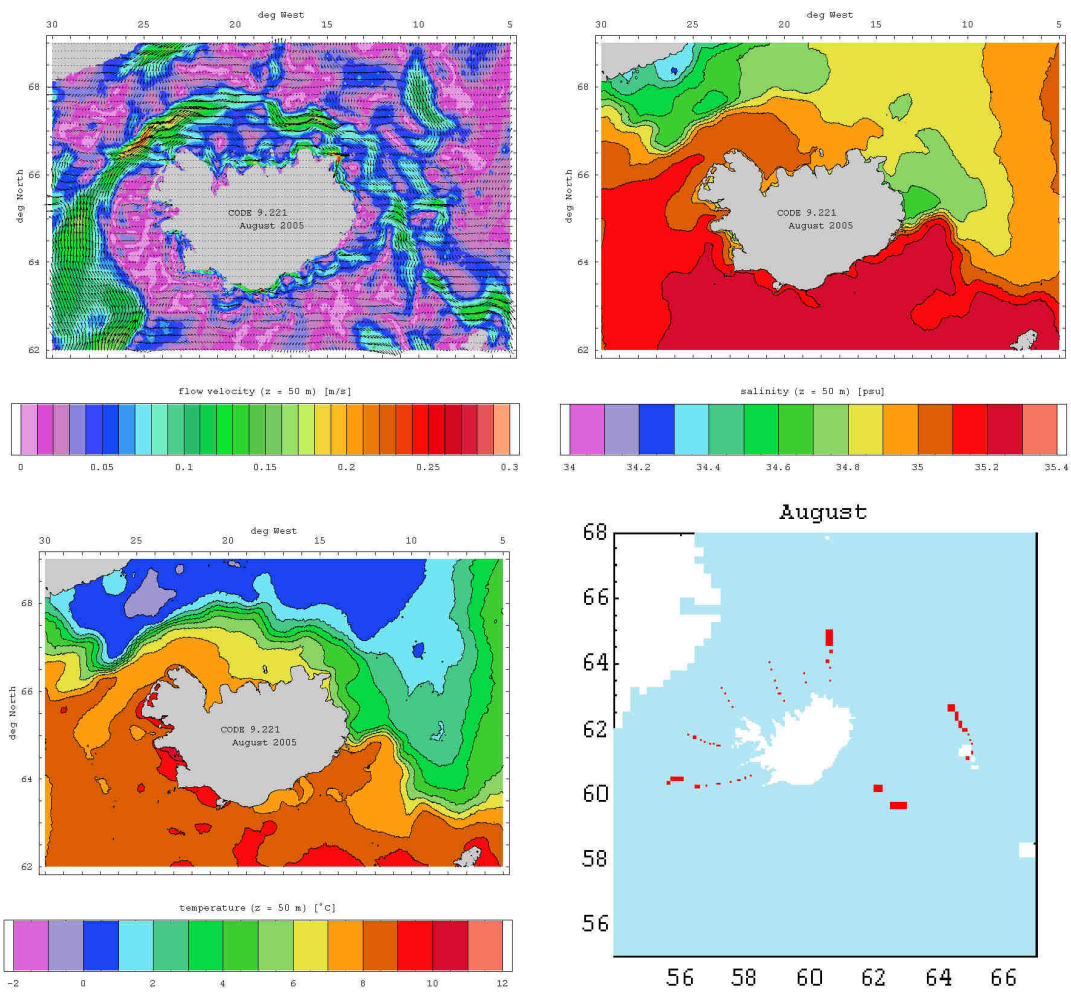


Fig. 2.164.: Monthly mean flow, salinity and temperature fields at 50 m depth and location of used CTD profiles – August 2005.

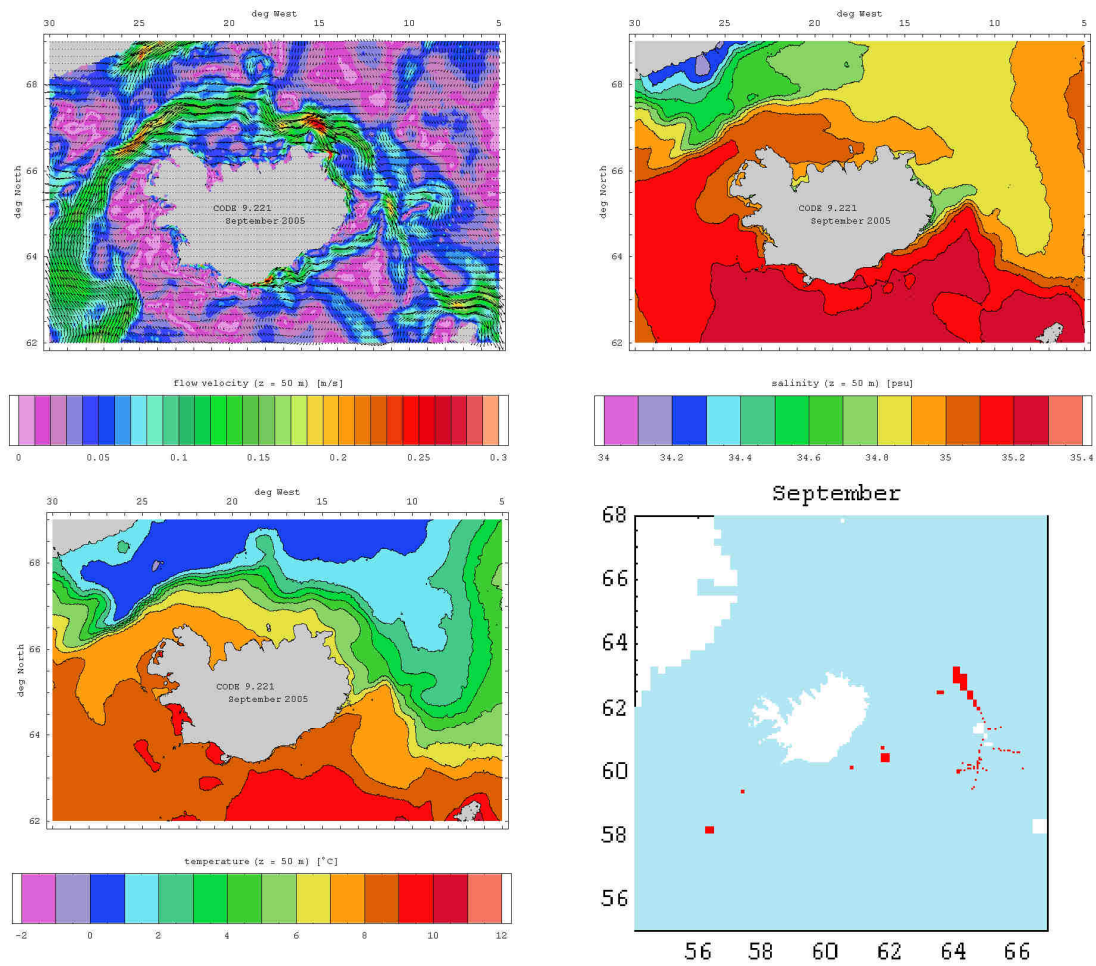


Fig. 2.165.: Monthly mean flow, salinity and temperature fields at 50 m depth and location of used CTD profiles – September 2005.



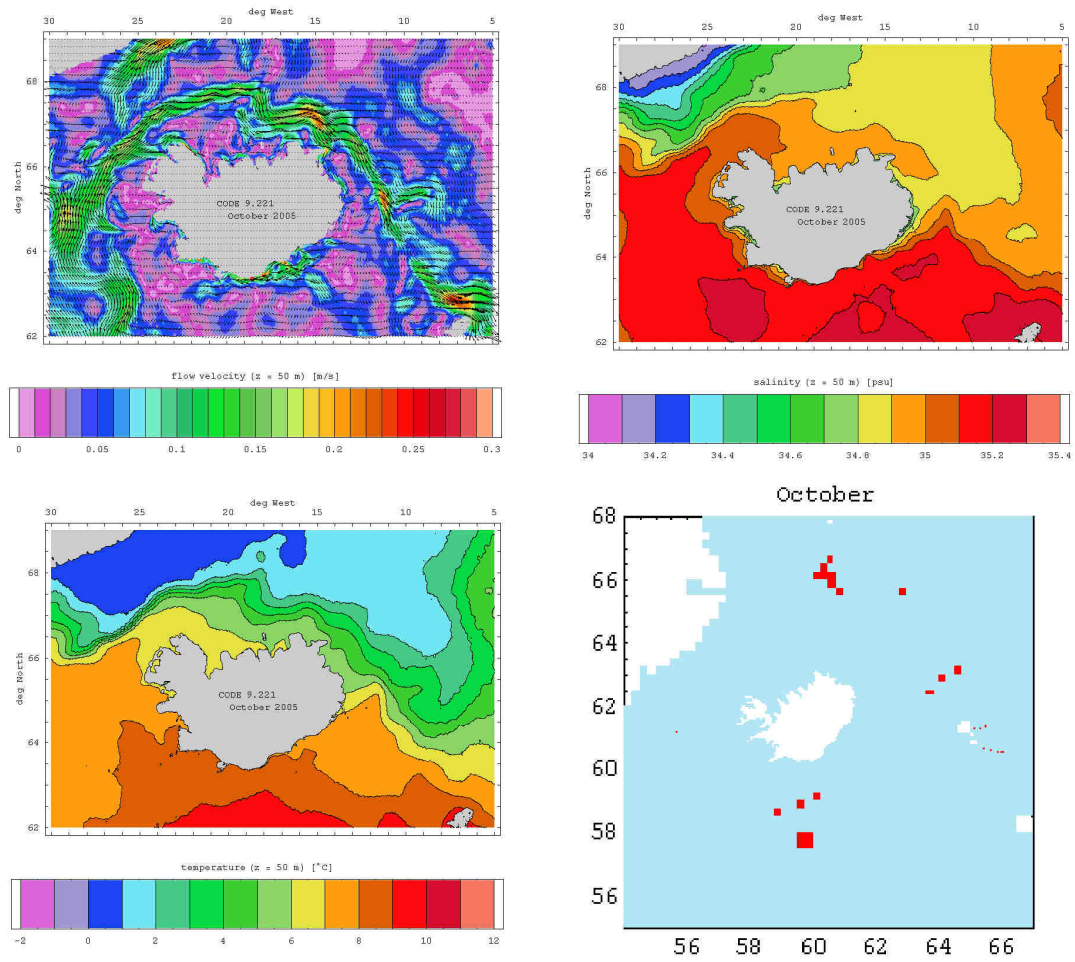


Fig. 2.166.: Monthly mean flow, salinity and temperature fields at 50 m depth and location of used CTD profiles – October 2005.

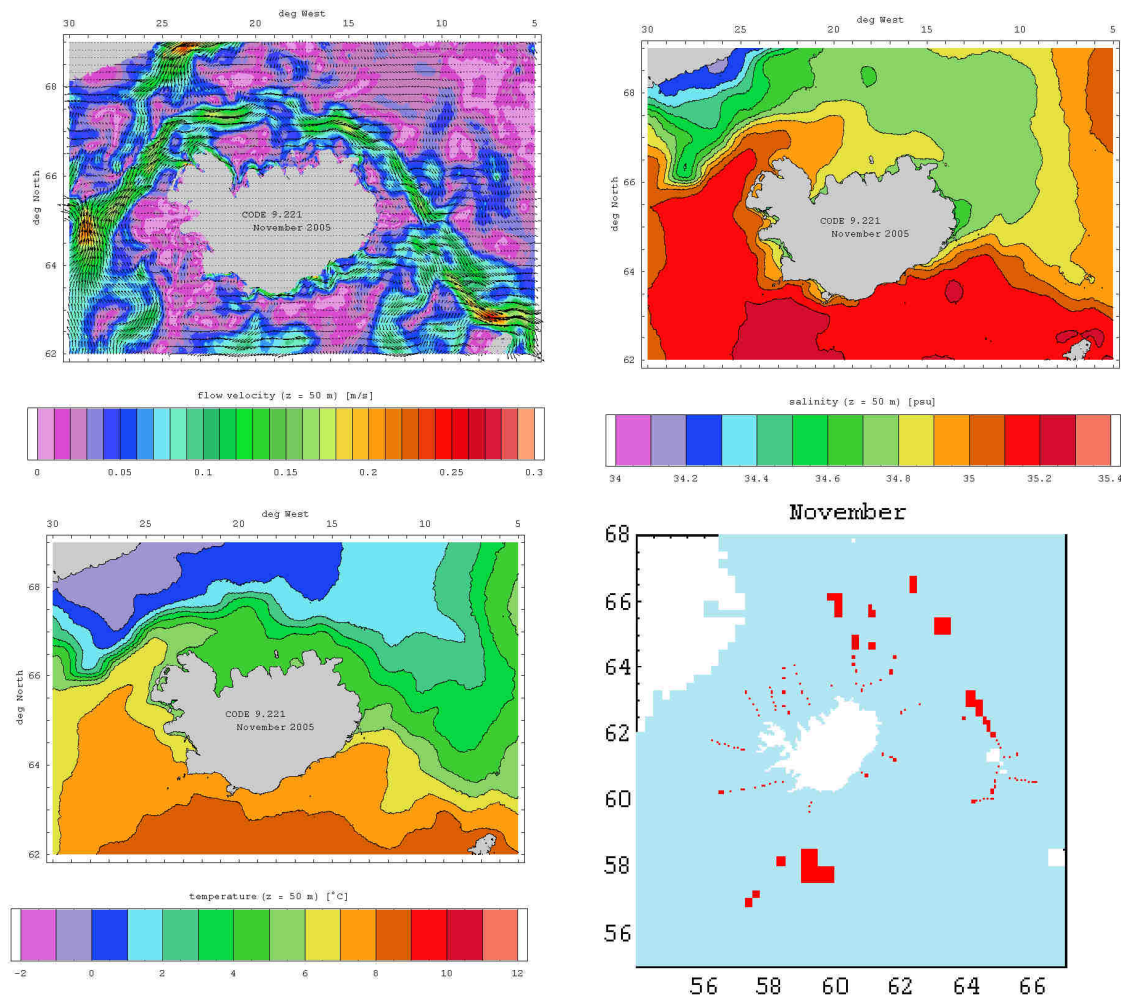


Fig. 2.167.: Monthly mean flow, salinity and temperature fields at 50 m depth and location of used CTD profiles – November 2005.

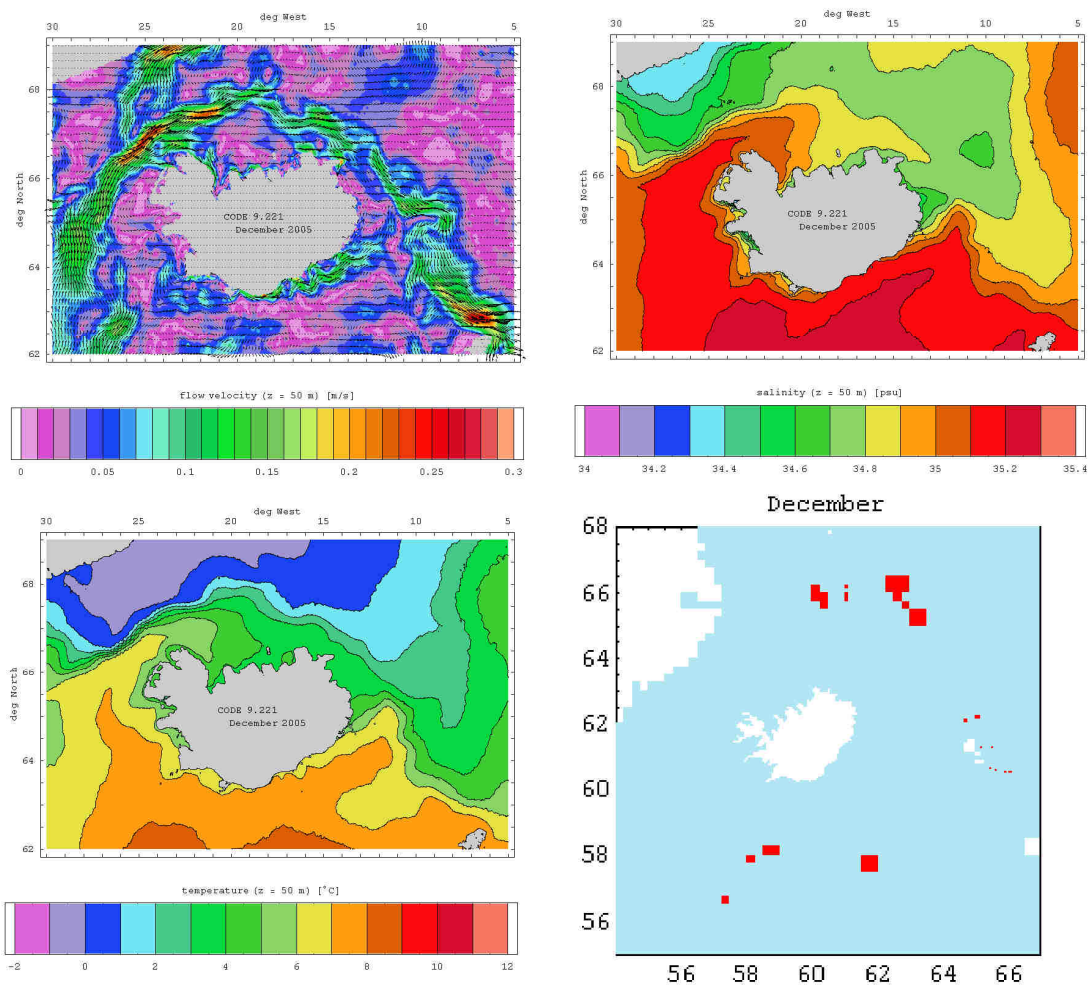


Fig. 2.168.: Monthly mean flow, salinity and temperature fields at 50 m depth and location of used CTD profiles – December 2005.

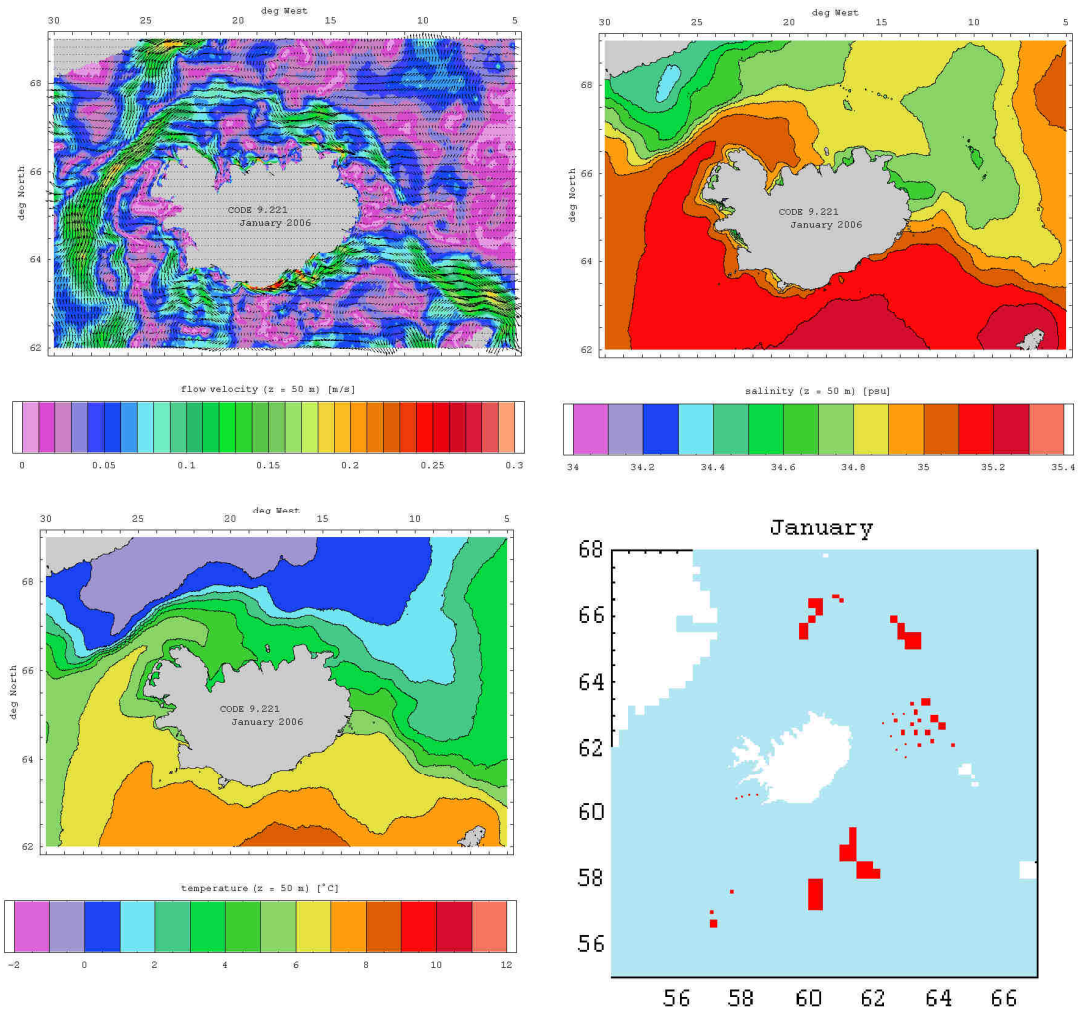


Fig. 2.169.: Monthly mean flow, salinity and temperature fields at 50 m depth and location of used CTD profiles – January 2006.

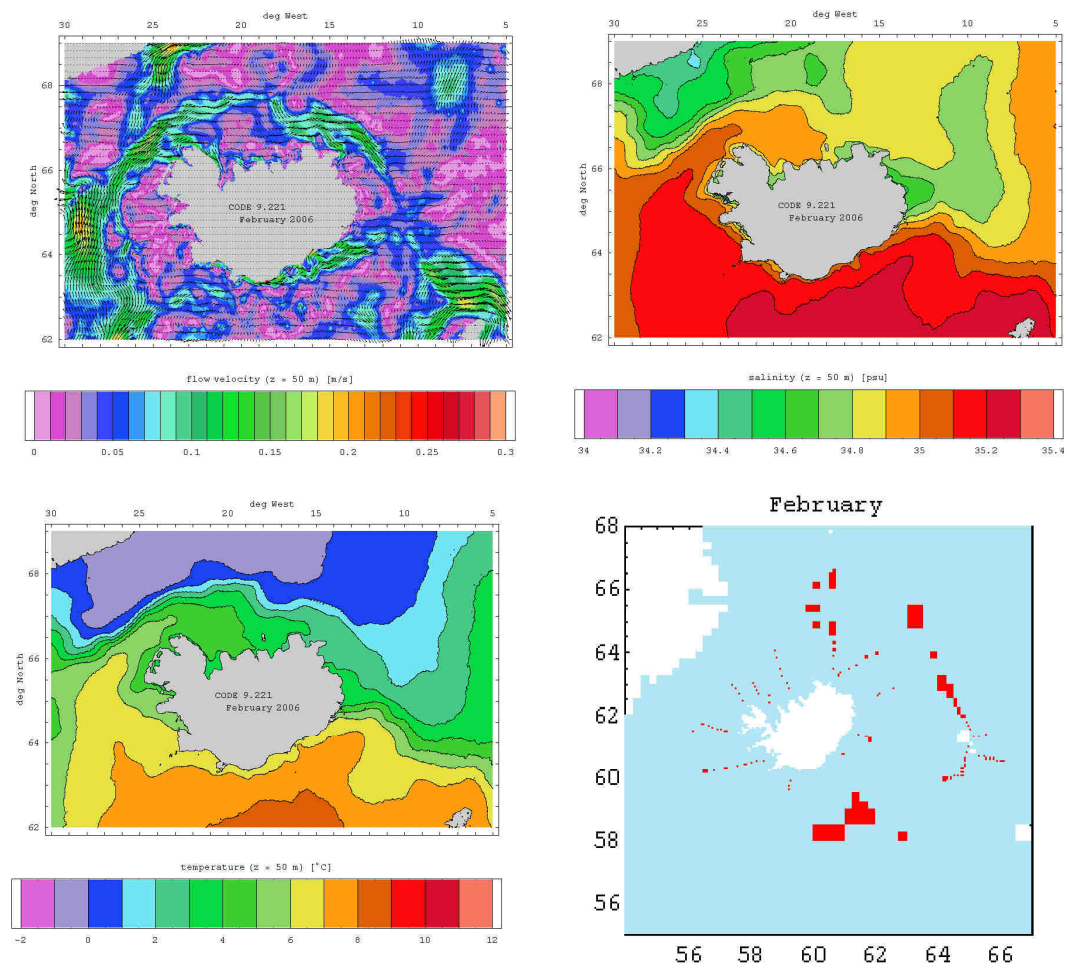


Fig. 2.170.: Monthly mean flow, salinity and temperature fields at 50 m depth and location of used CTD profiles – February 2006.



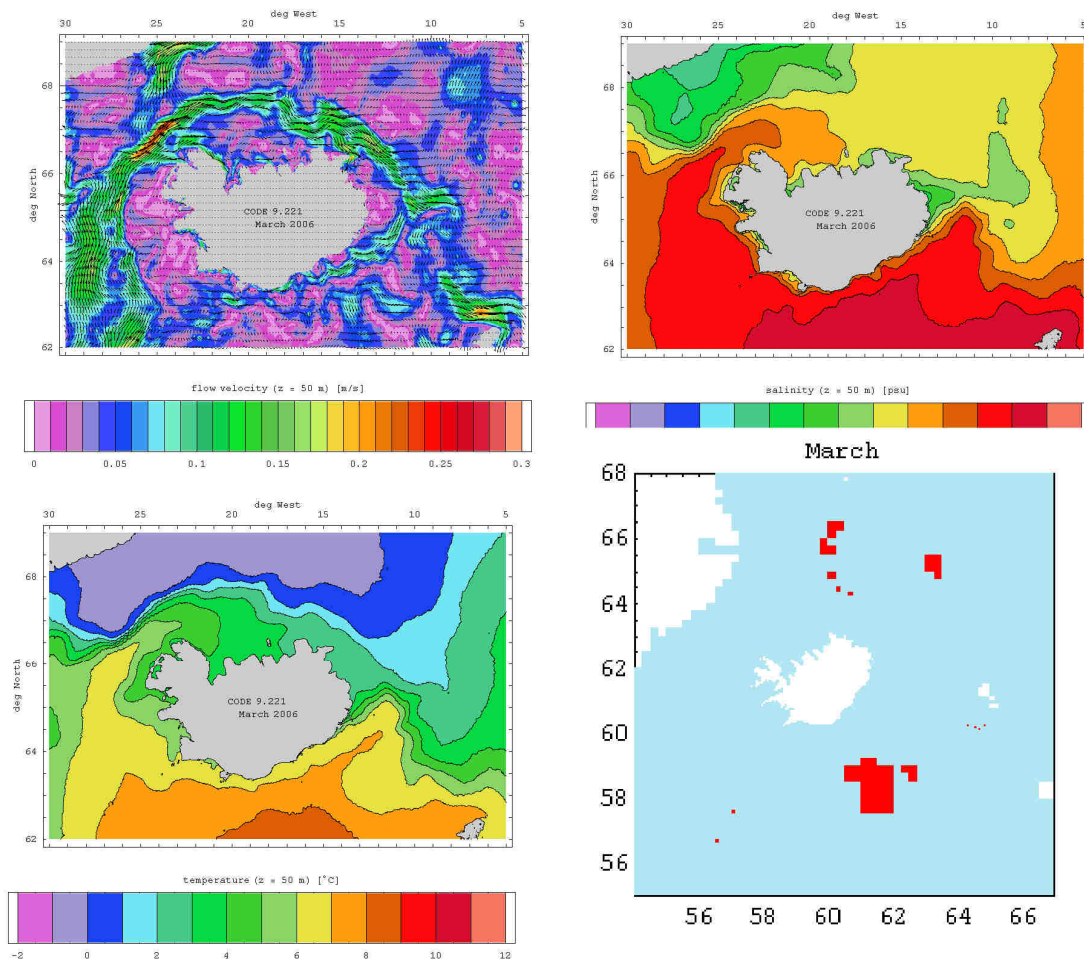


Fig. 2.171.: Monthly mean flow, salinity and temperature fields at 50 m depth and location of used CTD profiles – March 2006.

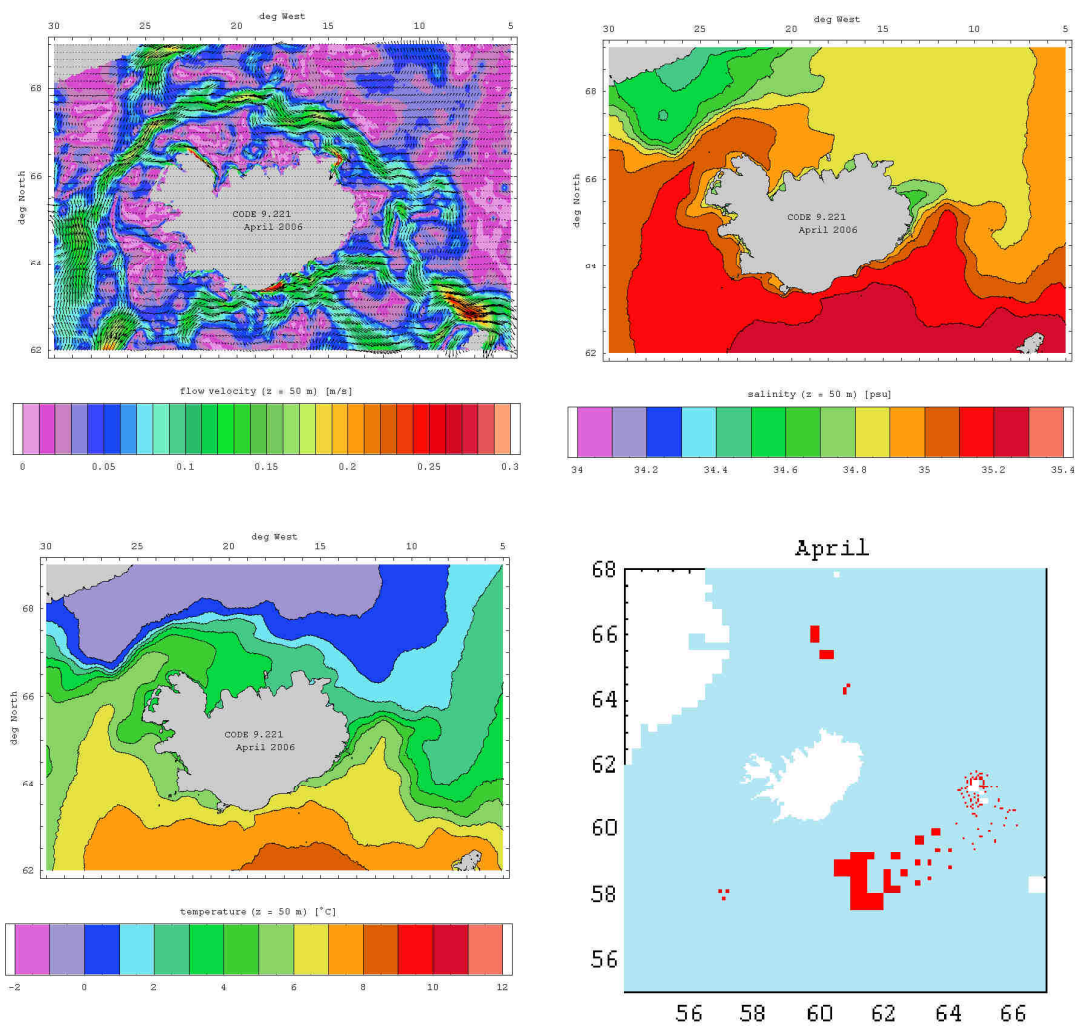


Fig. 2.172.: Monthly mean flow, salinity and temperature fields at 50 m depth and location of used CTD profiles – April 2006.

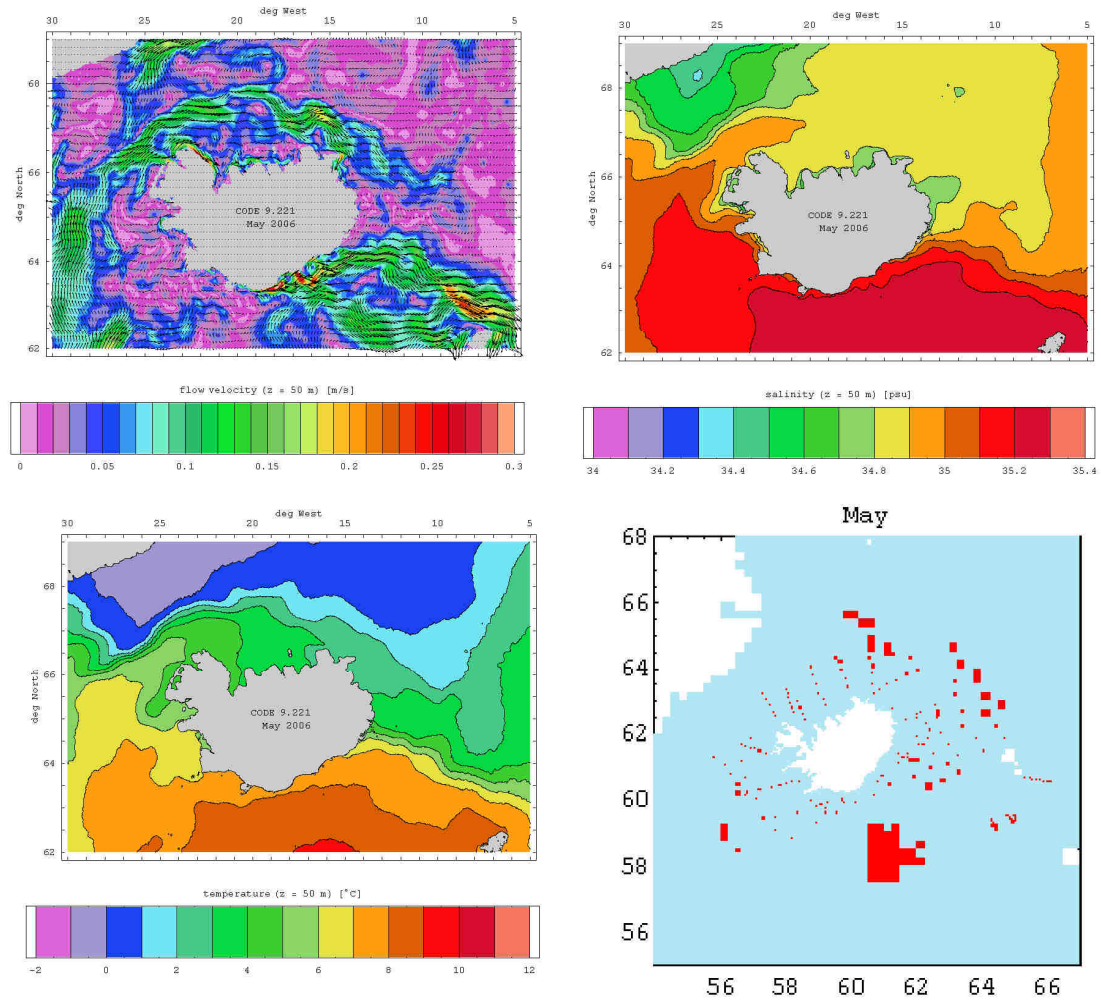


Fig. 2.173.: Monthly mean flow, salinity and temperature fields at 50 m depth and location of used CTD profiles – May 2006.

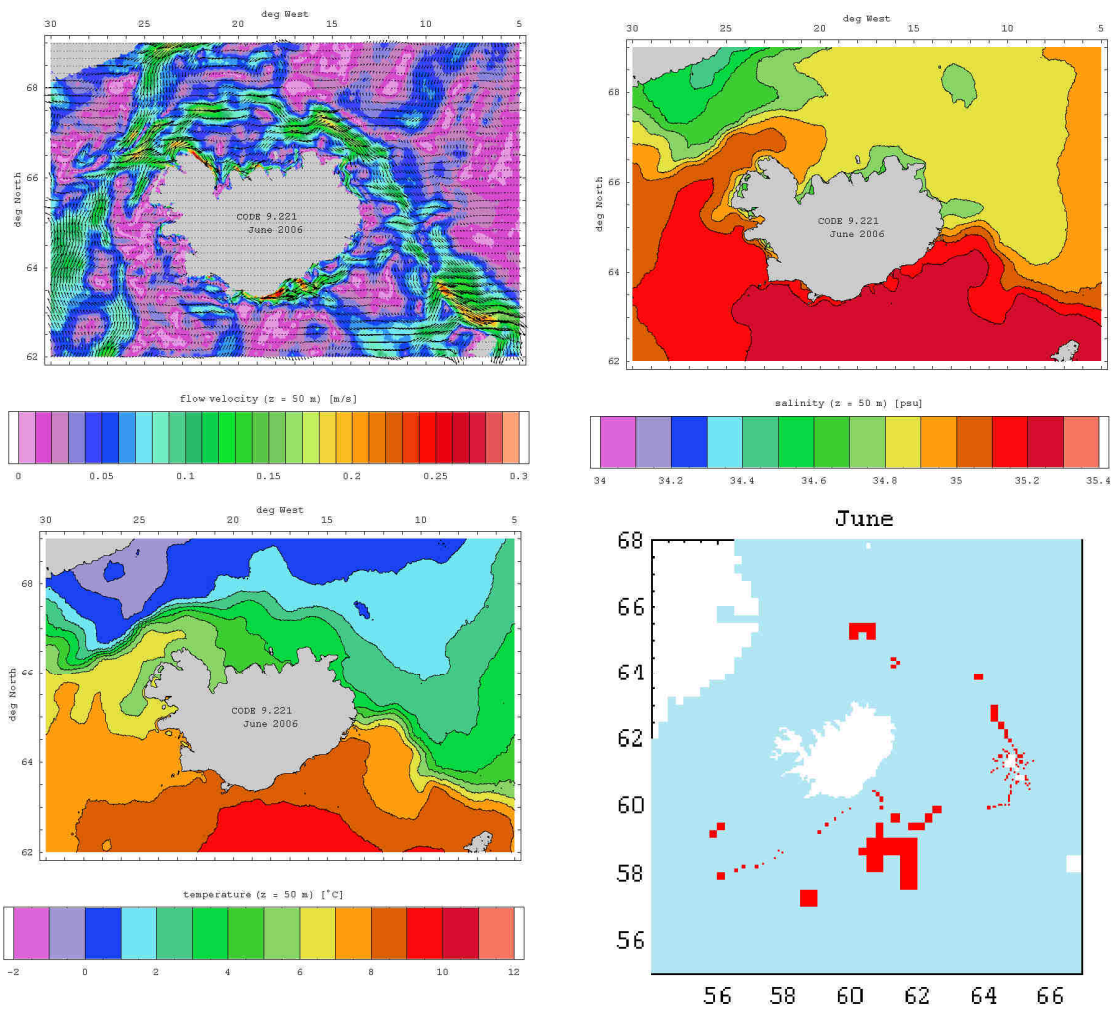


Fig. 2.174.: Monthly mean flow, salinity and temperature fields at 50 m depth and location of used CTD profiles – June 2006.

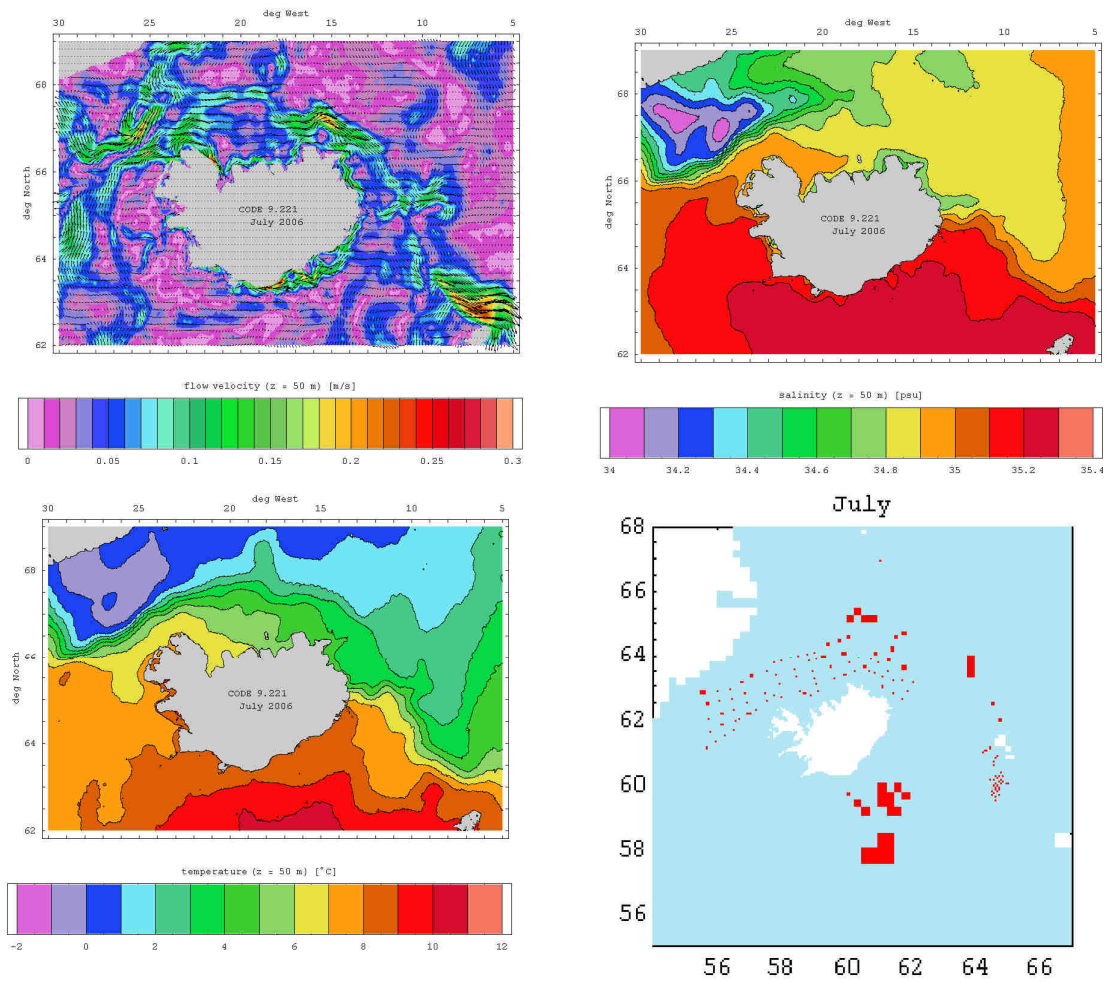


Fig. 2.175.: Monthly mean flow, salinity and temperature fields at 50 m depth and location of used CTD profiles – July 2006.



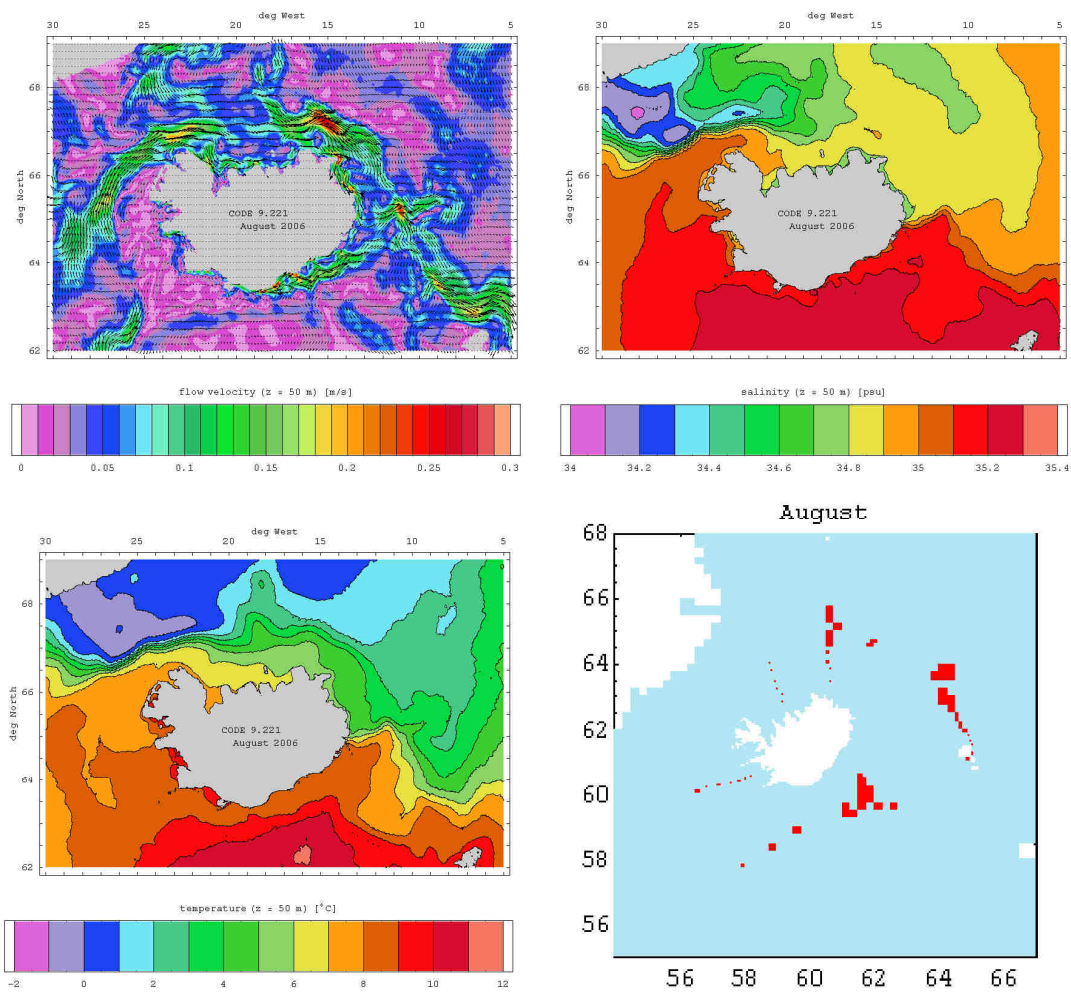


Fig. 2.176.: Monthly mean flow, salinity and temperature fields at 50 m depth and location of used CTD profiles – August 2006.

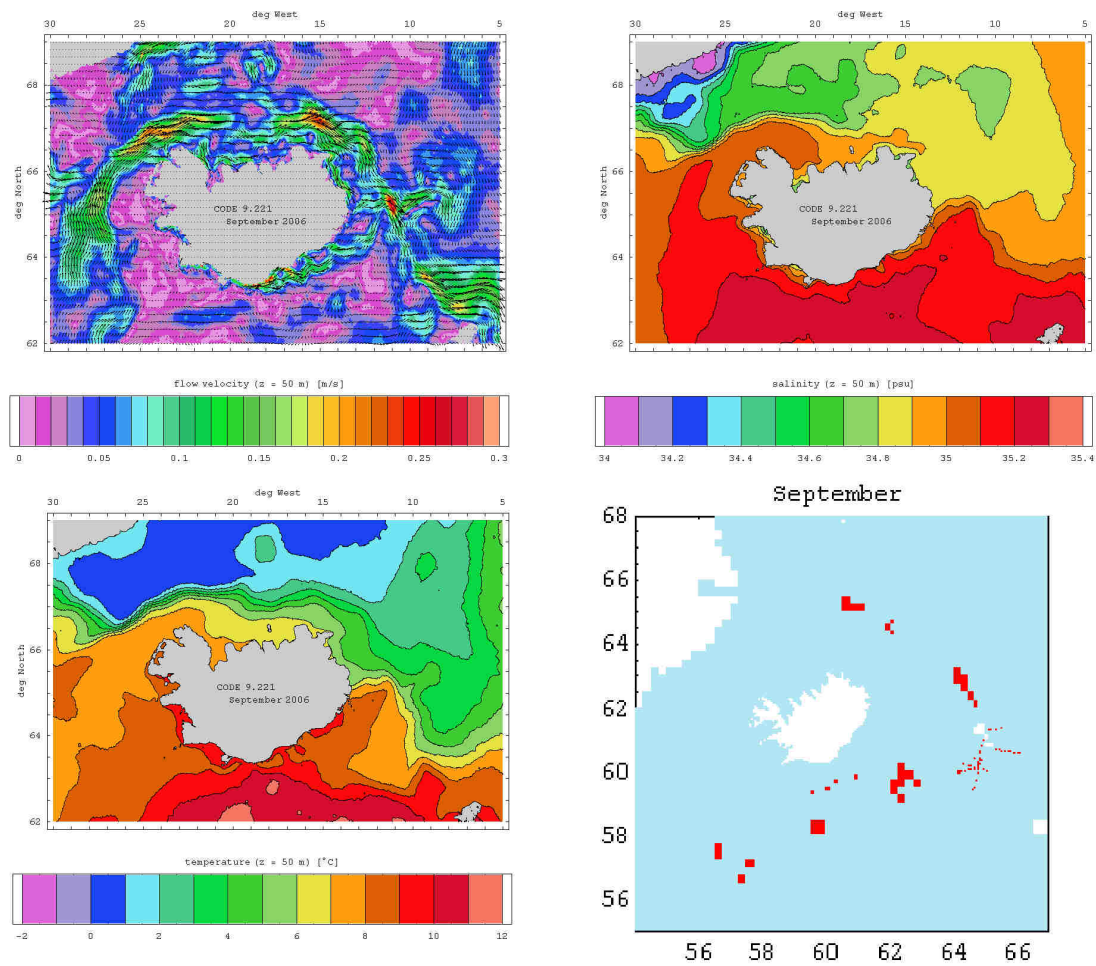


Fig. 2.177.: Monthly mean flow, salinity and temperature fields at 50 m depth and location of used CTD profiles – September 2006.

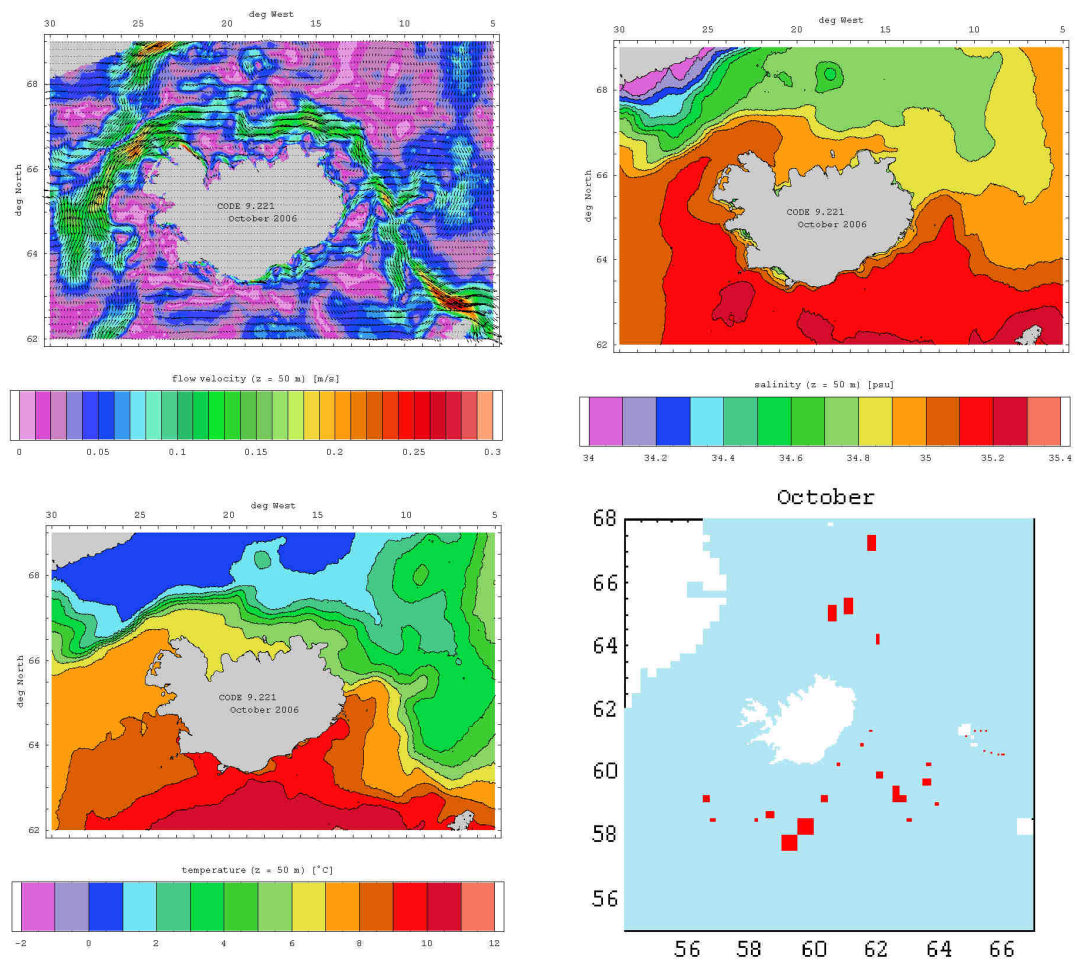


Fig. 2.178.: Monthly mean flow, salinity and temperature fields at 50 m depth and location of used CTD profiles – October 2006.

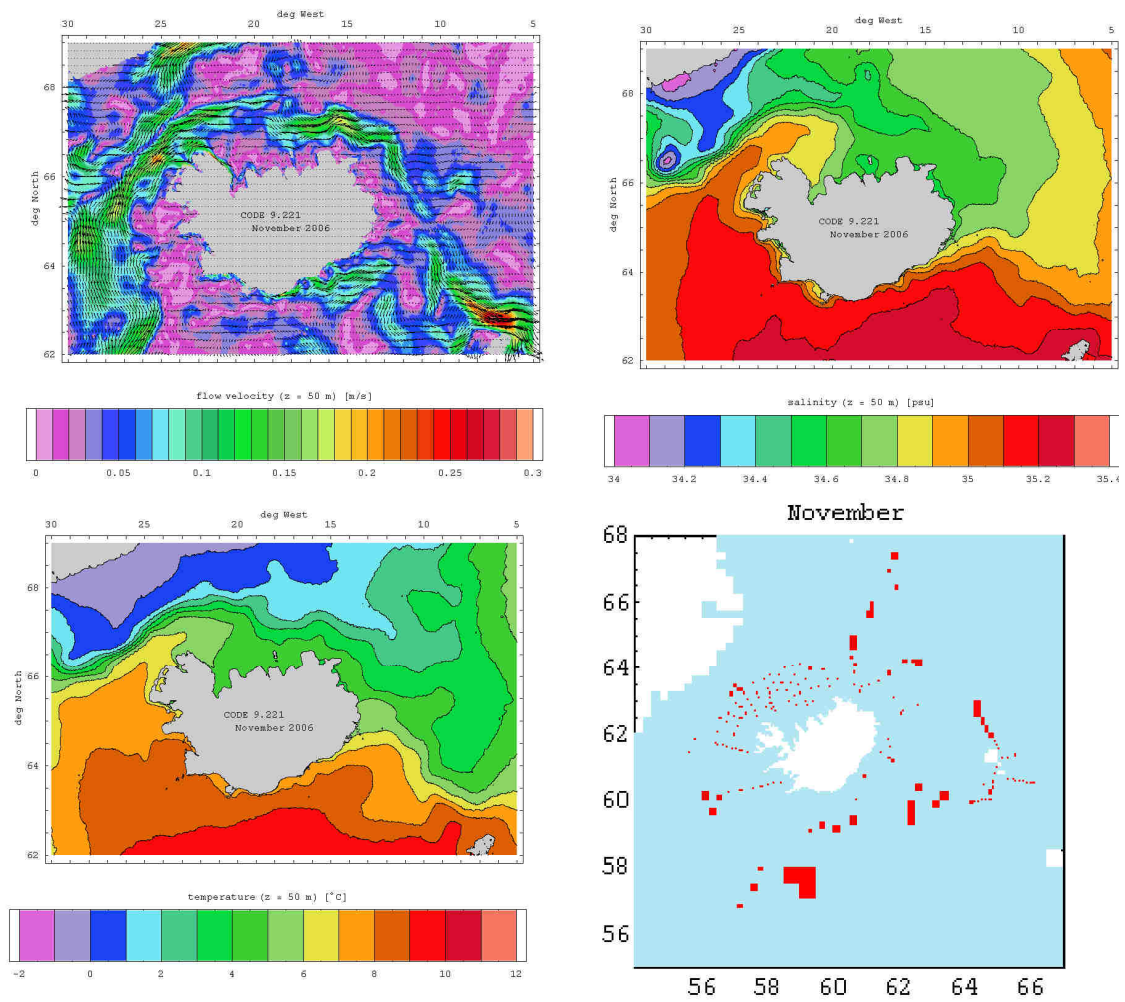


Fig. 2.179.: Monthly mean flow, salinity and temperature fields at 50 m depth and location of used CTD profiles – November 2006.

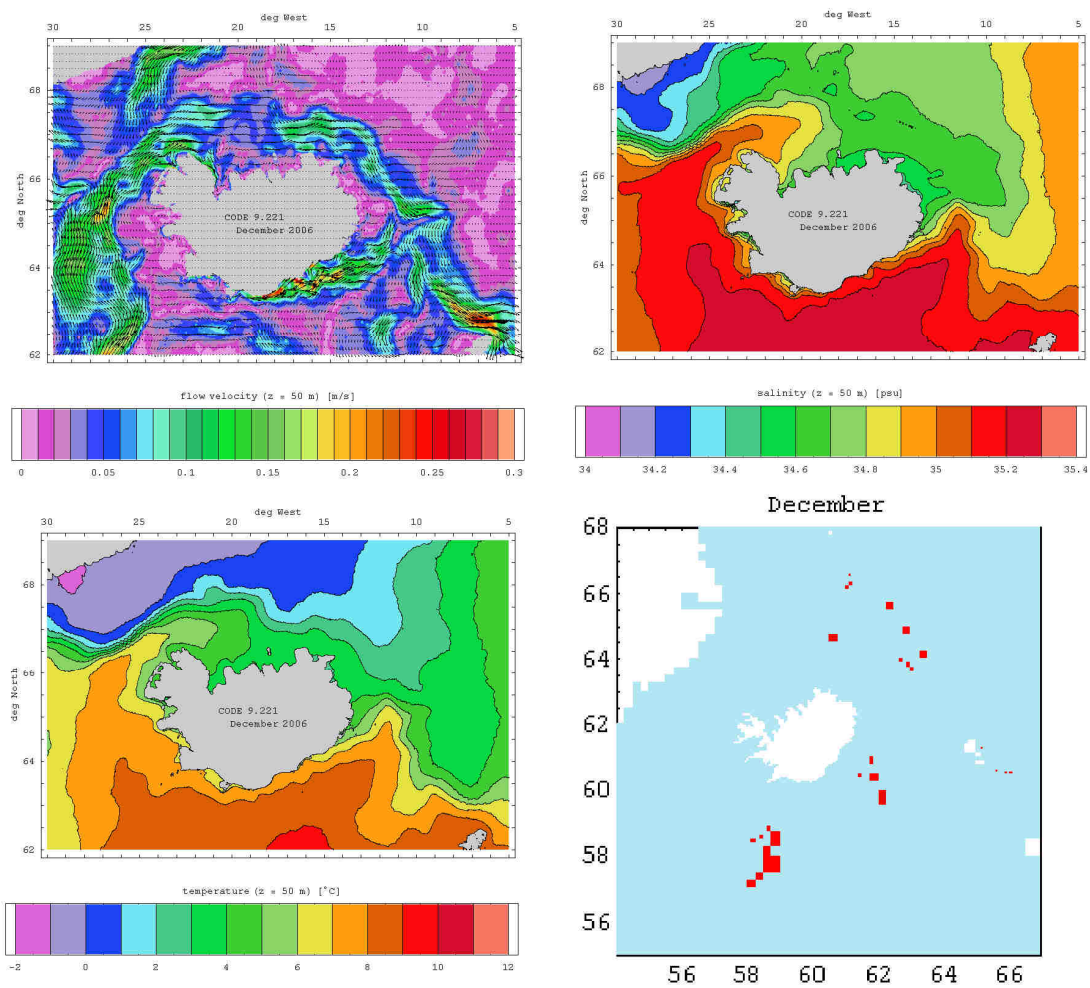


Fig. 2.180.: Monthly mean flow, salinity and temperature fields at 50 m depth and location of used CTD profiles – December 2006.



### 3. Validation

In chapter 1.3.3. the used method of temperature and salinity data assimilation is explained. There, it is also said that we assumed the available CTD measurements to be true, i.e. we neglected the measurement errors. Hence, it may surprise still to read about the temperature and salinity error of the model because this error could have been erased by the data assimilation procedure. However, the used assimilation procedure just “pushes” the simulation towards the observation. Even after three or more iterations a certain distance between the measured and the modelled value will exist, with its extend depending on the accordance of the measurements with the solution found by the model.

Another reason why we still detect temperature and salinity errors is the temporal shift of all measurements done during one month towards the 15<sup>th</sup> of this month, which allows us to save computational costs by activating the assimilation routine only once per simulated month. However, the errors discussed here are computed at the time points of the respective measurements. This way, the model assimilates temperature and salinity signals with periods equal or longer than one month whereas shorter signals contained in the CTD data cannot be considered.

If we compare the temperature and salinity errors (table 3.1.) with those of a former run which did not include the CTD data assimilation (Logemann et al. 2010, their table 3.1.) we detect a strong reduction of the median temperature and salinity error by around one order of magnitude whereas the standard deviation of the errors, which is a measure of unresolved variability, was only slightly reduced. However, in future runs, the standard deviation will be reduced by a more frequent (e.g. daily) activation of the data assimilation routine

Table 3.1.: Vertical median error profiles with their standard deviations from the mean error of the modelled temperature and salinity fields.

depth range (m)	$\Delta T_{\text{median}}$ [K]	$\sigma_T$ [K]	$\Delta S_{\text{median}}$ [psu]	$\sigma_S$ [psu]
0-10	0.09	1.27	0.004	0.562
10-20	-0.10	1.21	0.007	0.434
20-30	-0.24	1.22	0.008	0.478
30-50	-0.26	1.17	0.007	0.423
50-100	-0.23	1.08	0.001	0.335
100-150	-0.23	1.11	-0.006	0.317
150-200	-0.25	1.21	-0.008	0.327
200-300	-0.29	1.31	-0.011	0.393

Finally we compared the modelled flow fields with observations from a surface drifter experiment (Valdimarsson & Malmberg 1999) which includes 21 GPS tracks of drift at the depth of around 15 m in Icelandic waters during the years 1998 and 1999. By using a low-pass filter to remove tidal and shorter periods, 607 drift vectors could be derived. These vectors were compared with their modelled counterparts.

Comparing the flow velocity a median model error of  $-0.64 \text{ cm s}^{-1}$  with a standard deviation of  $6.54 \text{ cm s}^{-1}$  was determined (fig. 3.3., fig. 3.1. and 3.2.). The error of the modelled flow direction we found to be:  $-4^\circ \pm 67^\circ$  (fig. 3.4.). The former version without CTD assimilation

showed a velocity error of  $-2.8 \text{ cm s}^{-1} \pm 15.8 \text{ cm s}^{-1}$  (Logemann et al. 2010). Considering the fact that we did not assimilate flow measurements directly into the model the improvement is striking.

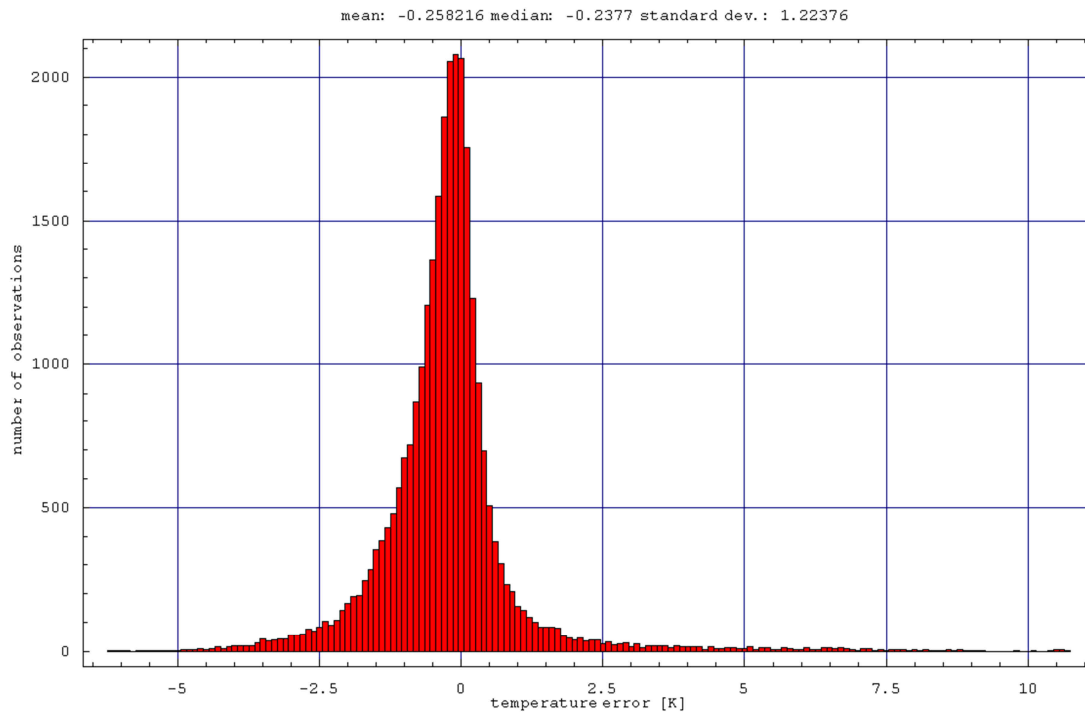


Fig. 3.1.: Bar chart of the model temperature error at a depth between 20 and 30 m.

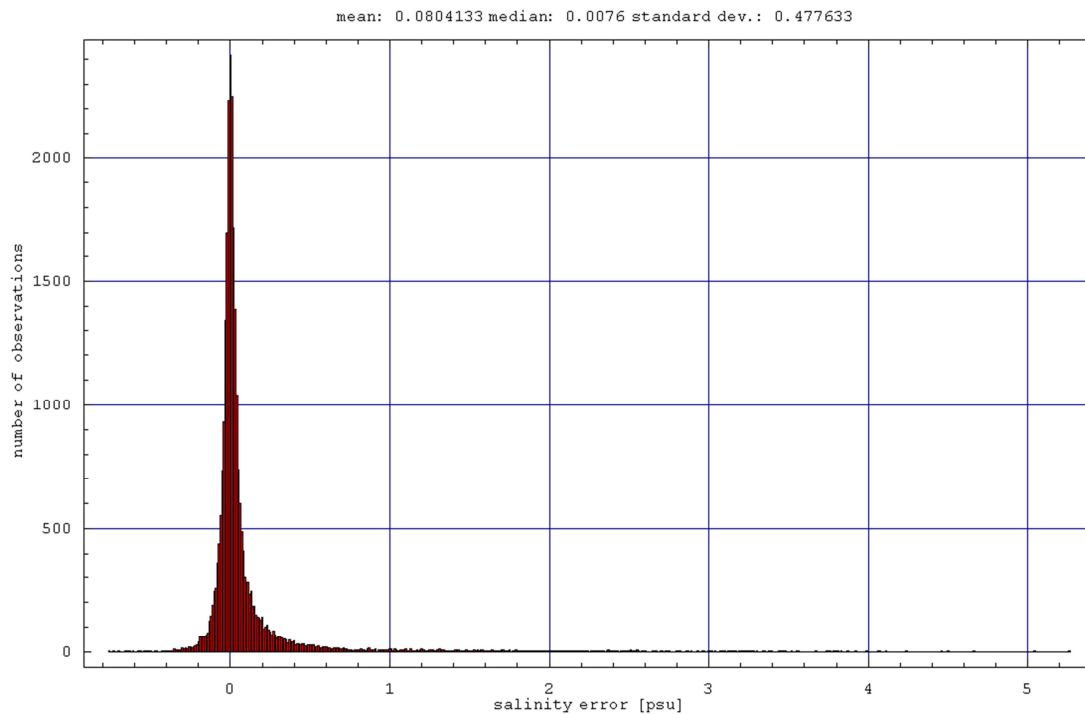


Fig. 3.2.: Bar chart of the model salinity error at a depth between 20 and 30 m.

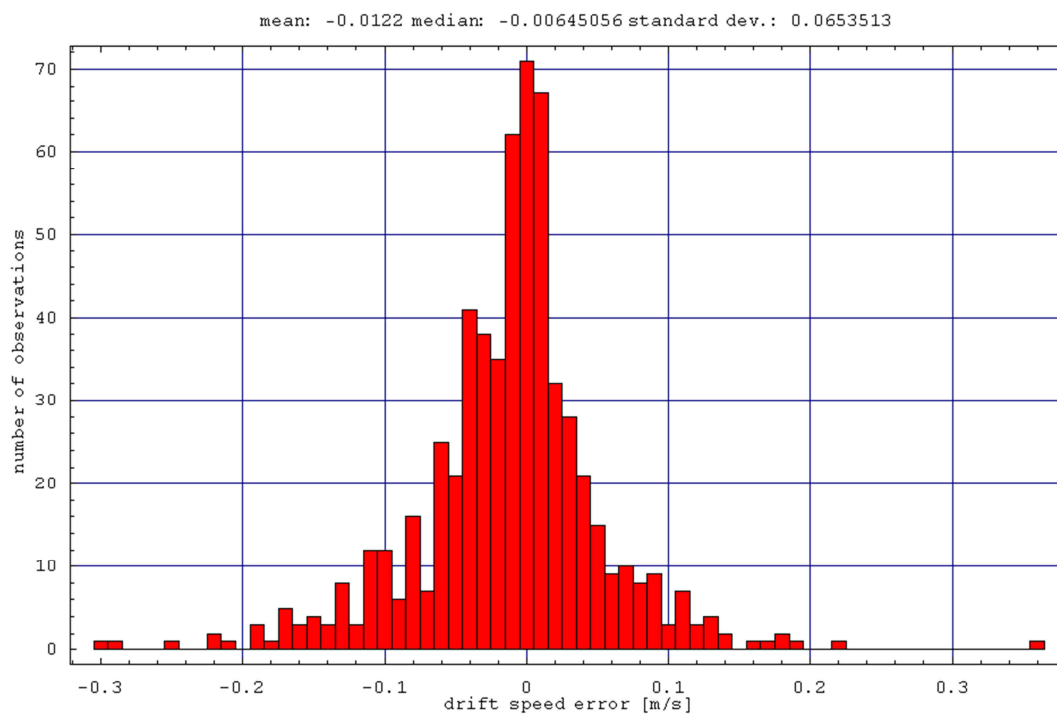


Fig. 3.3.: Bar chart of the model drift speed error at a depth of 15 m.

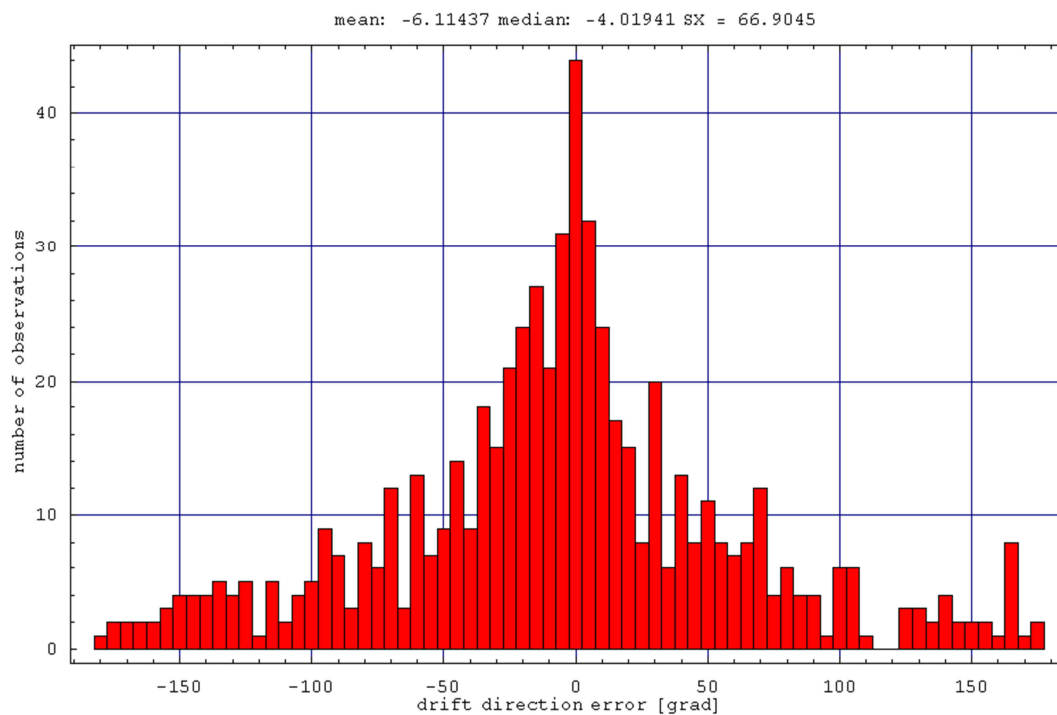


Fig. 3.4.: Bar chart of the model drift direction error at a depth of 15 m.

## 4. References

- Apel, J.R. (1987): Principles of Ocean Physics. Academic Press Limited. 209-219.
- Backhaus, J.O. (1985): A three-dimensional model for the simulation of shelf sea dynamics. Deutsche hydrographische Zeitschrift 38, 165-187.
- BODC - British Oceanographic Data Centre (2003): GEBCO Digital Atlas, General Bathymetric Chart of the Oceans, 1903 - Centenary Edition - 2003, CD-ROM, Joseph Proudman Building, Brownlow Street, Liverpool L3 5DA.
- Einarsson B. and S. Jónsson (2010): Improving groundwater representation and the parameterization of glacial melting and evapotranspiration in applications of the WaSiM hydrological model within Iceland. Report 2010-017, Icelandic Meteorological Office, pp. 29.
- Gill, A.E. (1982): Atmosphere-Ocean Dynamics. International Geophysics Series. Academic Press, London, pp. 662.
- Fofonoff, N.P. und R.C. Millard (1983): Algorithms for computation of fundamental properties of sea water. UNESCO Technical Papers in Marine Science, 44.
- Hibler, W.D. (1979): A Dynamic Thermodynamic Sea Ice Model. J. Phys. Oceanogr. 9, 815-846.
- ICES (2000): VEINS – Variability of Exchanges in the Northern Seas. EC – MAST III Project, 1997-2000, International Council for the Exploration of the Sea, CD-ROM.
- Kalnay, E., Kanamitsu, M., Kistler, R., Collins, W., Deaven, D., Gandin, L., Iredell, M., Saha, S., White, Woollen, J., Zhu, J., Chelliah, M., Ebisuzaki, W., Higgins, W., Janowiak, J., Mo, K., Ropelewski, C., Wang, J., Leetmaa, A., Reynolds, R., Jenne, R., Joseph, D. (1996): The NCEP/NCAR 40-year reanalysis project, Bull. Am. Meteorol. Soc., 77, 437-471.
- Khokhlov, A.M. (1998): Fully threaded tree algorithms for adaptive refinement fluid dynamics simulations. J. Comp. Phys. 143, 2, 519-543.
- Kochergin, V.P. (1987): Three-dimensional prognostic models. In: N.S. Heaps (ed.): Three-dimensional coastal ocean models. Coastal and Estuarine Sciences, 4, 201-208.
- Laevastu, T. (1963): Energy exchange in the North Pacific; its relations to weather and its oceanographic consequences. Part 1: Formulas and nomograms for computation of heat exchange components over the sea. Hawaii Institute of Geophysics Report No. 29, 15 pp., 11 nomograms.
- van Leer, B. (1979): Towards the Ultimate Conservative Difference Scheme. V: A Second Order Sequel to Godunov's Method. J. Comput. Phys. 32, 101-136.
- Logemann, K., J. Olafsson and G.Marteinsdóttir (2010): The ocean model CODE and its application to Icelandic waters. MARICE E-report MER-10-2010, University of Iceland, pp. 93, <http://www.marice.is/ereports/MER-10-2010.pdf>

- Maykut G.A. (1986): The surface heat and mass balance. In: N. Untersteiner (ed.), *Geophysics of Sea I*, Plenum, New York, 395-463.
- Mellor G.L. and T. Yamada (1974): A hierarchy of turbulence closure models for planetary boundary layers. *Journal of Atmospheric Sciences*, 31, pp. 1791-1806.
- Mellor G.L. and P.A. Durbin (1975): The structure and dynamics of the ocean surface mixed layer. *Journal of Physical Oceanography*, 5, pp. 718-728.
- Mesinger, F., Arakawa, A. (1976): Numerical methods used in atmospheric models. Volume I, GARP Publication Series, 17, pp. 64.
- Millero, F.J. (1978): Freezing Point of Sea Water. Eighth Report of the Joint Panel on Oceanographic Tables and Standards, UNESCO Tech. Pap. Mar. Sci. No. 28, Annex 6, UNESCO Paris.
- Millero, F.J., C.-T. Chen, A. Bradshaw und K. Schleicher (1980): A New High Pressure Equation of State for Seawater. *Deep Sea Res.*, 27, 255.
- Möller, F. (1973): Einführung in die Meteorologie. Bd. 1. BI-Wiss.-Verl., Mannheim, 423pp.
- Nilsen, J.E.Ø., H. Hatún, K.A. Mork and H. Valdimarsson (2006): The NISE Data Collection. Report published on CD-ROM, pp. 20.
- Pedlosky, J. (1987): *Geophysical Fluid Dynamics*. Springer-Verlag, New York, pp. 710.
- Pickard, G.L. and W.J. Emery (1982): *Descriptive physical oceanography: an introduction*. 5th enl. ed. (in SI units), pp. 74.
- Pohlmann, T. (1996): Predicting the thermocline in a circulation model of the North Sea - Part I: model description, calibration and verification. *Continental Shelf Research*, Vol. 16, No. 2, pp. 131-146.
- Schulla, J. and K. Jasper (2007): Model Description WaSiM-ETH. Technical report, ETH Zürich, pp. 181.
- Semtner, A.J. (1987): A Numerical Study of Sea Ice and Ocean Circulation in the Arctic. *J. Phys. Oceanogr.* 17, 1077-1099.
- Smagorinsky J. (1963): General Circulation Experiments with the Primitive Equations. I. The Basic Experiment. *Monthly Weather Review*, 91, 3, 99-106.
- Steele, M., R. Morley, and W. Ermold (2001): PHC: A global ocean hydrography with a high quality Arctic Ocean. *J. Climate* 14, 2079-2087.
- Valdimarsson, H. and Malmberg, S.A. (1999): Near-surface circulation in Icelandic waters derived from satellite tracked drifters. *Rit Fiskideildar*, 16, 23 - 39.